POLITECNICO DI MILANO
Department of Aerospace Science and Technology
Doctoral Programme In Aerospace Engineering

High order methods for Space Situational Awareness

Doctoral Dissertation of:
Alessandro Morselli

Supervisor:
Prof. Franco Bernelli Zazzera

Co-Advisors:
Dr. Roberto Armellin
Dr. Pierluigi Di Lizia

The Chair of the Doctoral Program:
Prof. Luigi Vigevano

2014–XXVII cycle

Keywords:

Printed in Italy

A common mistake that people make
when trying to design something completely foolproof
is to underestimate the ingenuity of complete fools.

Mostly Harmless
Douglas Adams, 1992

Contents

Summary

High order methods for Space Situational Awareness

Alessandro Morselli

The era of space exploration started in 1957 with the launch of the first man-made object, the soviet satellite Sputnik I. Since then a large number of man-made objects has been launched into space, and many of them are still orbiting the Earth. The large majority of objects currently orbiting the Earth is a result of fragmentations, mostly caused by collisions and explosions. These events can have catastrophic effects on the near-Earth environment: they increase the number of objects and, thus, the probability of further collisions, potentially leading to a collisional cascade. This scenario is named Kessler's syndrome after the name of the scientist who first analyzed the effects of the increasing density of resident space objects.

Mitigation guidelines have been published by various organisations such as the Inter-Agency Space Debris Coordination Committee (IADC) and the United Nations (UN). The general aim of space debris mitigation is to reduce the growth of space debris by ensuring that space systems are designed, operated, and disposed of in a manner that prevents them from generating debris throughout their orbital lifetime. In parallel specific space programs were started to build the expertise required to manage the challenges posed by the space traffic control problem.

This thesis deals with the development of new methods for the Space Surveillance and Tracking of the near-Earth environment. All the relevant aspects of the problem are addressed in this thesis: orbit propagation, orbit determination, conjunction identification, collision probability estimation, and collision avoidance manoeuvre design. The main goal is to implement innovative methods to propagate uncertainties in an efficient and accurate way, which is a major problem when dealing with a large amount of data.

In this framework, differential algebraic techniques are used to perform nonlinear propagation of uncertainties on the orbital state and to speed-up computational demanding simulations, such as Monte Carlo methods. An introduction to Differential Algebra (DA) and its tools, as well as a description of the high-order DA-based propagators developed, is given in the first part of the work. In particular, the first ever

high-accuracy DA-based numerical propagator is developed, using some of the most recent models for Earth gravitational field and atmosphere density.

Then, the problem of orbit determination is addressed. A novel algorithm based on batch least square fit that can process measurements from a bistatic radar with a multibeaming receiver is analyzed. The algorithm is capable of estimating, with a single measurement, the whole set of six orbital parameters, with a good accuracy on the orbital position. By adding optical measurements the estimate gets closer to the reference state and the ballistic coefficient can be estimated as well.

Two algorithms for the conjunction identification are proposed: the first is based on the DA-version of the analytical propagator SGP4/SDP4 and the rigorous global optimizer COSY-GO. The choice of the objective function is such that all stationary points of the relative distance between the two objects can be computed in the time window of interest with a computational time that ranges from a few to tens of seconds. The second algorithm uses the procedure for the DA expansion of the time and distance of closest approach. The advantage of this approach is that it provides the polynomial approximation of the distance of closest approach with respect to the uncertain initial states of both objects, that can be used to compute collision probabilities efficiently.

The three methods for the collision probability computation exploit the availability of the DA expansion of the distance of closest approach to perform fast Monte Carlo simulations. The numerical simulations to compute the minimum relative distance for each sample of the simulation are replaced by fast polynomial evaluations. A DA-based standard Monte Carlo method and two advanced Monte Carlo techniques, Line Sampling and Subset Simulation, are used. These advanced techniques limit the number of samples required to compute sufficiently accurate estimates of the collision probability, which is usually well below 10^{-3}. Since they are based on polynomial evaluations, the methods allow for large computational time savings. As an example when 1000 samples are required the computation time can be reduced by two orders of magnitude. Besides enabling the collision probability computation in a Monte Carlo fashion, without any assumption on relative dynamics as in the classical algorithms, the developed methods can be used with any statistics, such as uniform distribution or Gaussian mixtures.

The design of collision avoidance manoeuvres is tackled as a multi-objective optimization problem, using a particle swarm optimizer. Two approaches are analyzed, the first is based on SGP4/SDP4 and the corresponding method for conjunction identification, whereas the other one uses the DA-based numerical propagator and the expansion of the distance of closest approach with respect to the execution time and the manoeuvre velocity vector. The optimization returns a set of fuel-efficient manoeuvres that can raise the miss-distance and decrease collision probability besides being compliant with mission constraints.

Overall, the proposed algorithms can be combined in a comprehensive DA-based Space Surveillance and Tracking tool. The tool would be able to manage the uncertainties by considering the nonlinearities arising from orbit determination and orbit propagation and could produce accurate estimations of the collision probability to rank close conjunctions. More in general, the tool would support the management of space traffic, re-entry, and observation scheduling. In the scope of the mitigation guidelines, any improvement in handling such operations will have beneficial effects on space debris population control and the future exploitation of space.

1

Introduction

The era of space exploration started in 1957 with the launch of the first man-made object the soviet satellite Sputnik I. Since then the interest for space and its possible commercial exploitation has continued to grow and the number of launches per year has increased year after year. To keep track of all artificial satellites orbiting the Earth and to determine their trajectory, both the United States and URSS developed a network of radar and optical sensors to perform observations of satellites. In particular, a complete catalogue of all the detectable objects, continuously updated with satellite tracking data, was created and is still maintained by the United States Strategic Command (USSTRATCOM) [Hoo04].

In those years there was almost no concern for the continuous accumulation of man-made objects in space. In 1978 Donald Kessler presented a paper in which he analyzed the possible evolution of the population of Resident Space Object (RSO) [Kes78]. Using a model initially developed for the study of the asteroid belt formation he found that if the density of Earth orbiting objects becomes larger than a certain threshold a collisional cascade could occur. A collision between two satellites will indeed generate a huge amount of smaller fragments, due to the high relative velocity during a close approach, that can be as high as 14 km/s. In those conditions even a collision with a small object involves an high level of energy and could have catastrophic consequences. Furthermore, if the fuel tanks on board the satellite were hit, an explosion could occur. The immediate effect of a collision or explosion would be the increase of the object density. This, in turn, will increase the probability of further collisions, resulting in the formation of a dense layer of *debris* around the Earth. A debris is defined as “any man-made Earth-orbiting object which is non-functional with no reasonable expectation of assuming or resuming its intended function or any other function for which it is or can be expected to be authorized, including fragments and parts thereof” [Flu01].

The consequence of such an event would be catastrophic: at that altitude the lifetime of a satellite will be drastically reduced due to the high risk of collisions and any object launched into higher orbits should cross that region and should be protected by high-velocity impacts with smaller fragments by means of shields and reinforced surfaces.

Fortunately this scenario has not yet occurred, although in the past years two events largely contributed in increasing the number of debris. In 2007 a Chinese anti-satellite missile test was performed: the satellite Fengyun 1C was destroyed at an altitude of approximately 700 km, generating thousands of fragments. Two years later a collision between Iridium 33 and Cosmos 2251 occurred at an altitude of 789 km. At those altitudes the air drag, that is the only natural force capable of causing the re-entry of orbiting objects, has very small effects. The decrease in the semi-major axis of satellites and debris at those altitudes can be so small that hundreds of years are required for the object to re-enter. As of July 2012 more than 3,400 fragments larger than 5 cm originated by the Fengyun explosion and 2,200 collisional debris from the Iridium-Cosmos collision were catalogued by the USSTRATCOM [Joh12]. It is estimated that more than 50% of those debris could still be in orbit 20 years after the event due to the limited effect of drag.

In this framework it is clear how important the so called space surveillance activity is. The European Space Agency (ESA) has thus started the Space Situational Awareness (SSA) program to provide Europe with timely and precise information on space environment. The activity is not only focused on space debris but also on space weather and Near-Earth Objects (asteroids) detection. Inside the SSA program, the Space Surveillance and Tracking (SST) segment is targeted at tracking and maintaining the information on all orbiting objects. This activity must be performed by collecting data with dedicated radar and optical sensors, then performing orbit determination to estimate the orbital parameters of every object. These data are then used to forecast, on a daily basis, all close conjunctions between active satellites and debris. In case the relative distance is below a safety threshold and/or the collision probability exceeds the maximum allowed value a warning is issued to satellite operators to determine whether or not a collision avoidance manoeuvre must be performed. In some cases additional measurements to improve the accuracy of the debris orbit must be performed prior to the conjunction. All these activities lie in the mitigation strategies that the international community has introduced to ensure the exploitation of Earth orbits in the future.

Besides the avoidance manoeuvre, other mitigation strategies have been introduced to limit or reduce the number of man-made objects in Earth orbit. The Inter-Agency Space Debris Coordination Committee (IADC), a committee that is formed by the space agencies of Italy, France, China, Canada, Germany, India, Japan, USA, Russia, Ukraine, and UK besides ESA, issued a set of mitigation guidelines. These were then incorporated into the Space Debris Mitigation Guidelines of the United Nations Committee on the Peaceful Uses of Outer Space (UNCOPUOS), released in 2010. The identified guidelines are the following:

- Limit debris release during normal operations
- Minimise the potential for break-ups during operational phases
- Limit the probability of accidental collisions

- Avoid intentional destruction and other harmful activities
- Minimise the potential for post-mission break-ups resulting from stored energy (e.g. remaining on-board fuel)
- Limit the long-term presence of spacecraft and launch vehicle orbital stages in the low-Earth orbit region after the end of their mission
- Limit the long-term interference of spacecraft and launch vehicle orbital stages with the geosynchronous region after their end of mission

In addition, remediation strategies, such as Active Debris Removal (ADR) of non-operative satellites, are currently studied to reduce the risk of further fragmentation and proper end-of-life disposal strategies, aimed at de-orbiting the spacecraft within 25 years after the end of the mission or the injection in graveyard orbits (i.e. orbits on which the effect of perturbations is such that the evolving trajectory will not intersect orbits commonly used, such as the geostationary orbit).

The purpose of the research activity performed during the PhD was to develop new methods for orbit determination, conjunction identification, collision probability computation, and collision avoidance manoeuvre design in the framework of SST. The activity can be also grouped inside the mitigation strategies aimed at limiting the probability of accidental collisions, as described in the Space Debris Mitigation Guidelines.

In this chapter the background of this research activity is briefly described. In Section 1.1 some figures and facts concerning the population of RSO currently orbiting the Earth are given. The SST operations and activities are described in Section 1.2. The organization of the research activity and its innovative aspects are outlined in Section 1.3.

1.1 Near-Earth environment

In this section the near-Earth environment is described, focusing mainly on the detectable object population and catalogued objects. For this purpose, it is important to identify first the different orbital regimes involved. Typically an altitude-based classification is performed and four geocentric orbit types are defined:

- Low Earth Orbit (LEO), $h < 2,000$ km;
- Medium Earth Orbit (MEO), $2,000 < h < 33,000$;
- Geosynchronous Earth Orbit (GSO), $h \approx 35,786$ km, with period equal to a sidereal day;
  - Geostationary Earth Orbit (GEO), when the inclination is close to 0 deg and eccentricity is close to 0;

- High Earth orbit, $h > 38,600$ km, comprising orbits with period above 24 h.

This orbit classification is usually employed for all objects orbiting the Earth and is used throughout this work. An additional orbit class, that groups all objects whose orbit has eccentricity above 0.1, is defined. This class is named Highly Elliptical Orbit (HEO) and comprises orbits such as Molnyia and Geosynchronous Transfer Orbit (GTO). These orbits have a perigee that is usually low enough to be inside the LEO region but an apogee that could reach the GEO region.

The current population of catalogued man-made Earth-orbiting objects comprises more than 17,000 individuals [1]. Though, it is estimated that the number of objects whose diameter is greater than 10 cm could thus exceed 29,000. The number of objects larger than 1 cm could be around 670,000 whereas objects larger than 1 mm are likely more than 170 millions. The smallest size of the objects that can be currently detected by the (ground-based) space surveillance networks is equal to 10 cm in the LEO region and around 1 m for objects orbiting in GEO [Flu01]. Smaller objects are modelled statistically using population models, such as ESA's MASTER-2009 and National Aeronautics and Space Administration (NASA)'s ORDEM 3.0.

The total number of catalogued payloads (i.e. active satellites), rocket bodies, and debris for the main countries and space agencies is listed in Table 1.1. The debris category here comprises nonfunctional satellites, mission related debris (exhaust products, objects released in spacecraft deployment and operations, and refuse from manned mission), and fragmentation debris (explosion fragments, collision fragments, and products of deterioration). The two nations that pioneered the space exploration during the Cold War, United States of America (USA) and the Commonewalth of Independent Sates (CSI), i.e. the former URSS, are responsible of more than 50% of larger objects currently in orbit. Notwithstanding a small number of payloads, the Public Republic of China (PRC) is accounted for nearly 3,500 debris due to the anti-satellite missile test of 2007. All other countries are responsible for the remaining 11% of the total number of RSO larger than 10 cm.

The distribution of the RSO is not uniform: the large majority of these objects is concentrated in two orbital regimes, LEO and GEO. The histogram of the number of objects as function of the semi-major axis is plotted in Figure 1.1 for the LEO and in Figure 1.2 for altitudes above LEO. Both plots are obtained using the information publicly available from the Space-Track catalogue. For what concerns the LEO regime, it can be observed that the most populated altitude is between 700 and 1000 km. As highlighted in the previous section here the effect of air drag is lower and the two main catastrophic events, the explosion of Fengyun 1C and the Iridium-Cosmos collision, occurred. For altitudes above LEO, it can be clearly observed the peak corresponding to the GEO ring at 42,164 km. In addition, the 12-hour revolution orbits (26,562 km) have an higher concentration, due to the presence of objects on Molnyia orbit or upper stages on GTO. Both Monlyia and GTO orbits can be also classified

---

[1] Source: Space-Track, www.space-track.org

Country/Organization	Payloads	Rocket bodies	Debris	TOTAL
CIS	1491	1014	3913	6418
USA	1215	661	3189	5065
PRC	161	80	3485	3726
FR	60	135	316	511
JPN	141	44	37	222
IND	58	21	100	179
ESA	55	7	39	101
Others	785	37	85	907
TOTAL	3966	1999	11164	17129

Table 1.1. Number of orbiting objects divided by country. The objects are divided into active satellites (payloads), upper stages of launchers and fairings (rocket bodies), and debris. Epoch: 2014-08-19 16:00:0 GMT. Source: Space-Track.

as HEO, due to their high eccentricity. Because of their low pericentre, that in some cases can be as low as 150 km, they also experience orbital decay.

The LEO region is used for a large variety of missions, e.g. Earth observation and Earth science, meteorology, communication, remote sensing, reconnaissance, astrophysics and space science. The GEO orbit is instead mainly used for communication purposes, since the satellite ground track can be maintained on the same latitude and longitude box. Other uses include Earth observation, surveillance, and meteorology. It is thus clear that in the future the use of both LEO and GEO will increase or

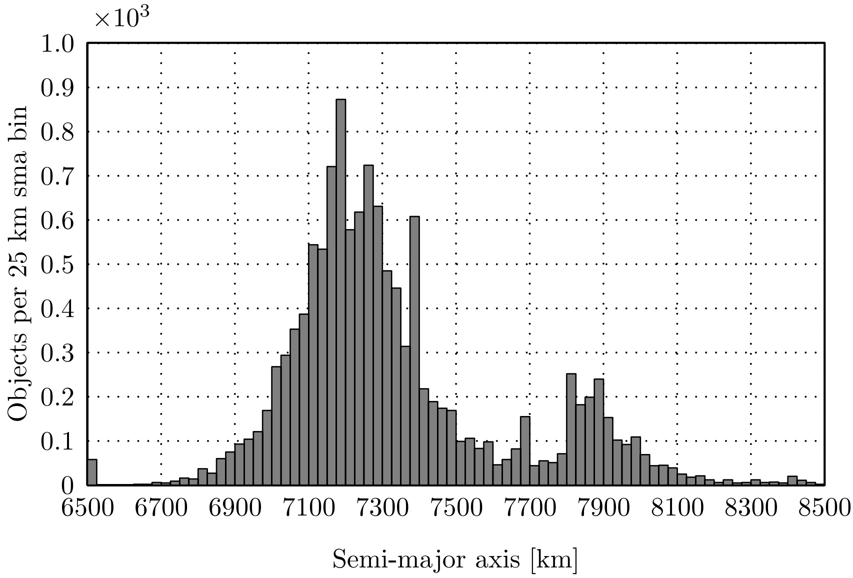

Figure 1.1. Histogram of the semi-major axis distribution of catalogued LEO objects as of September 2014 (bin size $\Delta a = 25$ km). Source: Space-Track.

remain at the present level. In addition, there is an increasing interest for the MEO region, with plans for the creation of satellite constellations for navigation purposes such as the European Galileo program.

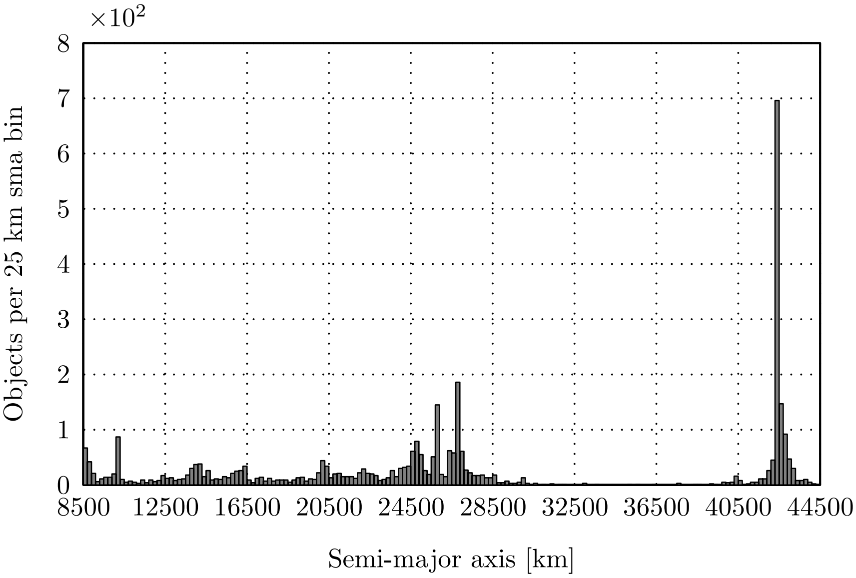

Figure 1.2. Histogram of the semi-major axis distribution of catalogued super-LEO objects as of September 2014 (bin size $\Delta a = 200$ km). Source: Space-Track.

The histogram of the eccentricity distribution is plotted in Figure 1.3. The large majority of objects is on a circular or nearly-circular orbit and only a few are found at high eccentricity, between 0.5 and 0.7. Those objects are the ones orbiting in Monlyia and GTOs identified before on the semi-major axis plots.

For what concerns the inclination of the currently catalogued population of detectable objects, an histogram plot is given in Figure 1.4. It can be observed that many objects are found at inclinations above 60 degrees. These are mainly objects in LEO that are on Sun-Synchronous Orbit (SSO), so that illumination conditions are the same for each orbit. This is particularly useful for Earth observation and meteorological satellites that have instruments to take images of Earth's surface. The small peak at zero inclination is instead associated to the objects in the GEO region. In addition, non-operative satellites and debris at that altitude are influenced by the Moon's attraction, resulting in a 53-year cyclic inclination variation that could reach 15 deg [Kli06].

A detailed and continuous monitoring of the near-Earth environment is thus required to forecast close conjunctions and plan, when possible, the appropriate counteraction. The next section provides a description of the SST framework, which is aimed at surveying and identifying risky situations for in-orbit satellites.

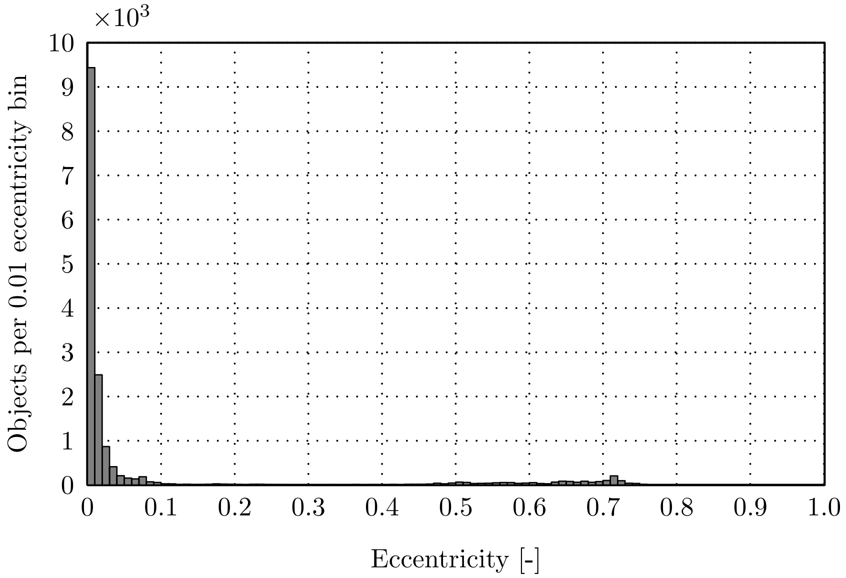

Figure 1.3. Histogram of the eccentricity distribution of catalogued objects as of September 2014 (bin size $\Delta e = 0.01$). Source: Space-Track.

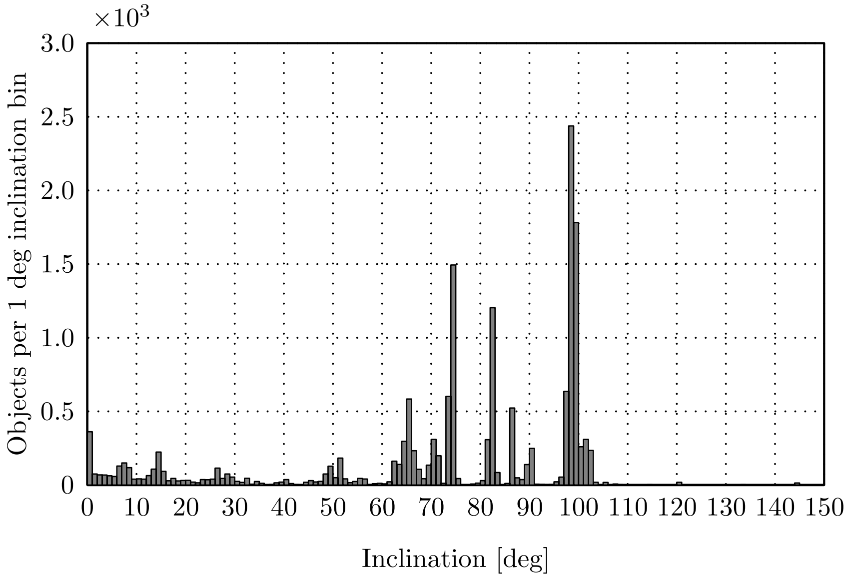

Figure 1.4. Histogram of the inclination distribution of catalogued objects as of September 2014 (bin size $\Delta I = 1$ deg). Source: Space-Track.

1.2 Space surveillance and tracking

The Space Surveillance and Tracking (SST) is the set of operations to be performed in order to maintain the awareness of the population of man-made space objects. Some of its main goals are to support safe and secure operations of space assets, risk management and liability assessment, to characterize physical properties of space objects. Besides the observations of RSO by means of optical and radar networks, the information on launches (date, country, payload, etc.), re-entered objects, and owner/operator of each objects must be considered in the SST activities. In addition, for cooperative objects, the station keeping and/or orbital manoeuvres that are performed must be determined to correctly represent the trajectory. All gathered information is used to build and maintain a comprehensive space catalogue, where all detected objects orbital states and properties are listed. The surveillance data should indeed support different applications

- launch and early operations, by confirming separation of satellite from launcher and providing information on initial orbit for tracking operations;
- contingencies, by tracking malfunctioning or passive satellites;
- collision warnings, by detecting conjunctions between satellites and other objects;
- search for released or lost objects;
- controlled and uncontrolled re-entry, by estimating trajectory, re-entry time and location, and risk to ground;
- identification of new objects, detection and characterization of in-orbit fragmentations.

In this work the focus is mainly on the SST activities required to determine collision warnings, going from observations to the collision avoidance manoeuvre design. A possible scheme of the related activities and their interconnections is represented in Figure 1.5. The first block is the observation block, coloured in light blue. The observation and measuring is a key activity for any SST: without observations it is indeed not possible to characterize the population of man-made objects. The data obtained from observations (mainly radar and optical) is then processed to determine the orbital elements that are required to forecast the future trajectory of the object, through the algorithms contained in the *orbit determination* block. Besides a set of six orbital elements, the orbit determination usually estimates also ballistic coefficients or the area-to-mass ratio required to correctly model solar radiation pressure and air drag.

The obtained information is then stored in a catalogue, to be readily available for any further activity or study. The catalogue is also useful to schedule new observations

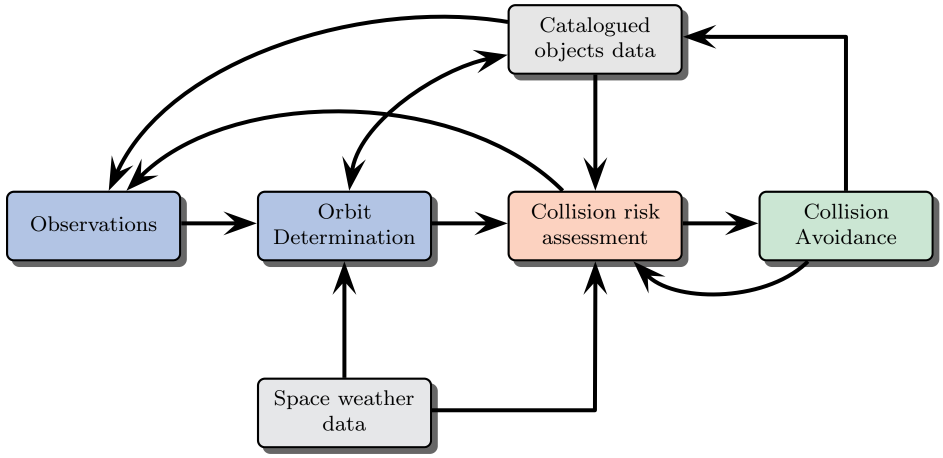

Figure 1.5. Space surveillance and tracking: scheme of activities involved.

and perform tracking of known objects. This activity is particularly important for those objects whose trajectory is highly influenced by perturbations, such as objects at lower altitudes that are about to re-enter in a few weeks or days. Also note that the information contained in the catalogue could be used during the orbit determination phase.

The schedule of new observations must guarantee sufficiently small uncertainties on the estimated orbital state for the data to be useful during the *collision risk assessment*. The risk determination is usually performed daily and can be divided into two phases: first all conjunctions occurring in the following days or week are identified. Those conjunctions whose minimum distance is below a warning threshold are retained and the collision probability is computed for each one. Even in this case a warning threshold is defined from engineering experience. A warning is issued to satellite operators for all the conjunctions with a high collision probability (i.e. above 10^{-3}) and a small minimum relative distance (i.e. a few hundreds metres). In case the orbit uncertainties on one of the two objects are too high, further observation of the object can be decided in order to obtain more accurate estimates of the minimum relative distance and collision probability.

For those close conjunctions with an high risk of collision, an *avoidance manoeuvre* must be designed. The aim of the manoeuvre is to reduce the collision probability and increase the objects separation. Fuel-optimal strategy can be adopted or station-keeping manoeuvre can be anticipated. This second approach has the advantage of reducing collision risk without the need of a recover manoeuvre, aimed at restoring the original trajectory after an avoidance manoeuvre has been carried out. It is also important to perform a new collision risk assessment with the orbital state after the manoeuvre to exclude the appearance of new close conjunctions. The new trajectory can indeed increase the relative distance for the considered conjunction but it is not guaranteed that other conjunctions with different objects will remain unaltered.

1.3 Research activity organization

In this section a brief description of the activity and algorithms developed in the thesis is provided. The goal of the research activity is to develop new, fast, accurate, and efficient methods to support the SST activity in the determination of close conjunctions, the computation of the associated risk level, and the design of fuel-optimal strategy for collision avoidance. This is performed by means of Differential Algebra (DA), described in Chapter 2. Instead of working with real-numbers, DA operates directly on functions. In a computer environment this is achieved by approximating these functions with Taylor polynomials. All operations on standard floating points number are theoretically replicable within a DA framework. As an example, the polynomial approximation of the orbital state at any epoch as function of the initial state can be obtained. Given the resulting polynomials, any variation of the initial condition in the surroundings of the nominal state can be mapped at future epochs by simple polynomial evaluations. When many propagations are required, the availability of such an expansion reduces drastically the computational effort, since each numerical propagation is substituted by the evaluation of polynomials. In addition, the order of the Taylor approximation is arbitrary and can be selected according to the required accuracy. This is particularly helpful when the dynamic of the problem is highly nonlinear or nonlinear effects arise from long-term propagations or large uncertainties. This situation is quite common for orbit propagation in the near-Earth environment. For instance, the period of a LEO orbit could be around 90 minutes. The identification of conjunctions is usually performed over a time window of one week: more than 100 revolutions are performed by a LEO object in this window. The common assumption of Gaussian distribution for the uncertainties on the orbital state used for the collision probability computation could be violated even if initial uncertainties were small.

It is clear that any new algorithm that requires a DA polynomial expansions of the orbital state requires an orbit propagator capable of providing it. A key role of the whole activity was thus to develop orbit propagators that can operate in a DA framework. Two DA-based propagators were developed: an high-fidelity numerical propagator and an analytical propagator replicating SGP4/SDP4. A description of the two propagators, the details of their implementation, and the way to perform a high-order expansion of the flow of the differential equations is given in Chapter 3. It is worth noting that both DA-based propagators are the first high-order propagators tailored for accurate propagation of Earth-orbiting objects ever developed.

The following research topics are investigated in this work:

- orbit determination, tailored for bistatic radars and optical measures
- conjunction identification procedures

- collision probability computation
- collision avoidance manoeuvre design.

The algorithms developed for each topic and their interactions are represented in Figure 1.6, together with the two DA-based propagators. The gray lines that connects the propagators to the blocks are used to indicate in which block the DA-version of the propagator is used. The only source of information for the analysis presented in this work are the Two-Line Element set (TLE) from the Space-Track catalogue. These are directly used as inputs for the SGP4/SDP4 propagator, whereas a pseudo orbit-determination on a set of states generated from a single TLE is performed to obtain the initial state for the numerical propagator.

The TLE are also used as input for the simulator of optical and radar measurements, that was developed to provide the inputs for the orbit determination block. Both the simulators and the algorithms for orbit determination are described in Chapter 4. Besides using a batch least square fit, the peculiarity of the orbit determination algorithm is the kind of radar measurement that can be processed. Tailored algorithm were indeed developed to manage data from a bistatic radar system with a multibeaming receiver in collaboration with the Italian Institute for Radioastronomy (IRA). In addition, tests were made to verify the capability of mixed orbit determinations with both radar and optical measurements.

For what concerns the conjunction identification process, two algorithms were developed. The first uses the DA version of SGP4/SDP4 and tackles the problem as a global optimization. The rigorous global optimizer COSY-GO, that exploits the properties of DA, is used for this purpose. The second algorithm, instead, exploits the Taylor expansion of the orbital state obtained with the DA-based numerical propagator to compute the Taylor expansion of the time and distance of closest approach. Given a first guess of these two quantities, e.g. from the other conjunction identification algorithm, their analytical approximation can be computed. The true minimum of the relative distance is then quickly obtained by means of a polynomial evaluation. The algorithms and the performances of the new methods are described in Chapter 5.

The collision risk assessment phase (represented by the red blocks in Figure 1.6) is the collision probability computation. Three DA-based Monte Carlo methods were developed. Due to the availability of the Taylor expansion of the relative distance at the closest approach, it is possible to perform fast Monte Carlo computations, since the numerical propagation is replaced by polynomial evaluations. Besides a standard Monte Carlo method, two advanced methods are proposed to deal with low collision probability and reduce the number of samples required to obtain sufficiently accurate estimates in that case. The methods exploit the polynomial expansion up to high-order and are not influenced by the initial uncertainty distribution, that is not restricted to be Gaussian. With respect to the classical methods for collision probability computation, no assumptions on the relative motion are made, and the

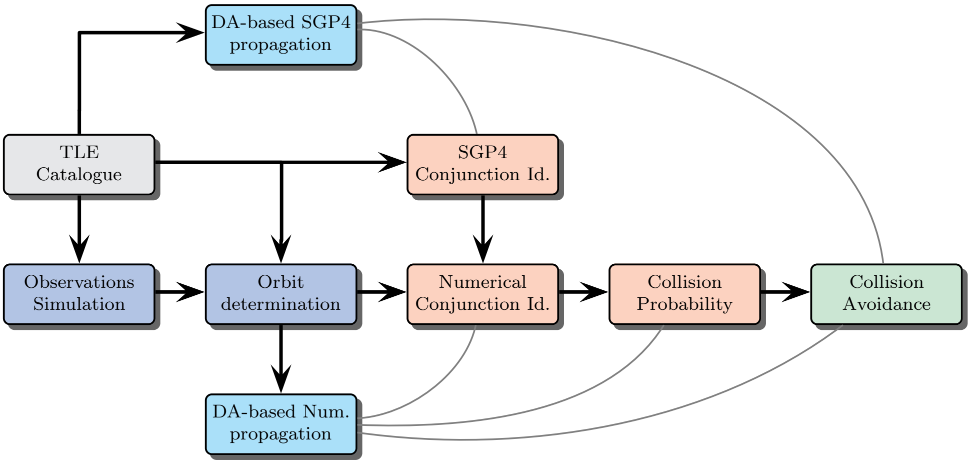

Figure 1.6. Research activity: workflow and interconnections between developed algorithms

complete dynamics is considered. Although the outputs of the orbit determination block should be used for the numerical conjunction identification, it was not possible to perform it in this work since the observation simulators and orbit determination algorithms were the last to be developed. The details and performances of the methods are described in Chapter 6.

The last block of Figure 1.6 is the collision avoidance algorithm. The manoeuvre design is tackled as a multi-objective optimization, using a particle swarm optimizer. Besides searching for a fuel-optimal manoeuvre, the optimization takes into account the mission constraints. The optimization can be performed by propagating with SGP4/SDP4 or the numerical propagator. In the latter case, the DA expansion of the relative distance at the closest approach is obtained as function of the manoeuvre time and $\Delta \boldsymbol{v}$. In this way it is possible to speed up the execution of the code, since polynomial evaluations are used in place of numerical propagations. The algorithms for conjunction identification are also used to compute the conjunctions during the manoeuvre optimization. The details on the implementation of the collision avoidance algorithms and some tests performed on LEO and GEO objects are given in Chapter 7.

Overall, the methods developed in the thesis exploit Differential Algebra to perform fast and accurate computation for collision risk assessment and collision avoidance manoeuvre design. The proposed approaches tackle the classical limitations of numerical simulations and Monte Carlo methods, since fast polynomial evaluations are used instead of any numerical propagation, drastically reducing the computational effort. In addition, algorithms for the orbit determination of space debris with optical and radar sensors are developed, tailored for new and innovative bistatic radar systems. The achieved results and conclusions are summarized in Chapter 8 together with the possible developments and future works.

1.3.1 Advancements with respect to the state of the art

The work presented in this thesis was developed in the framework of the research on the use of DA for the solution of astrodynamics problems performed by the Space Mission Engineering Lab of the Politecnico di Milano. The original contributions to the background know-how of the research group are summarized in Table 1.2.

Research topic	**State of the art**	**Original contributions**
DA orbit propagation	DA expansion of the flow for • two-body dynamics • n-body dynamics	DA expansion of the flow using • SGP4/SDP4 • High-fidelity numerical propagator
Orbit determination	• preliminary orbit determination of NEO based on DA	• Orbit determination algorithms for RSO (suitable also for NEO) • Investigation of radar-based orbit determination • Development of tailored algorithms for multibeaming receiver antenna • Mixed orbit determination with radar and optical measurements using batch least-square optimization
Conjunction identification	• Rigorous global optimization with keplerian dynamics for NEO (MOID, solution of geometrical problem) • Expansion of MOID wrt. orbital parameters	• Rigorous global optimization with SGP4/SDP4 for RSO • Computation of all stationary points wrt. time (geometrical problem and phasing) • TCA&DCA expansion wrt. time and initial state
Collision probability	• DA-based Monte Carlo for NEO	• Advanced DA Monte Carlo methods
Collision avoidance	• Multi-objective optimization of space trajectories	• Problem formulation and tailoring for collision avoidance design

Table 1.2. Original contributions of this thesis with respect to the background of the research group.

2

Differential Algebra and Taylor Models

The theory of differential algebra presented in this chapter has been developed by Martin Berz in the late 80's, and the short summary given in the followings takes advantage of his book *Modern Map Methods in Particle Beam Physics* [Ber99c].

Differential Algebra (DA) techniques find their origin in the attempt to solve analytical problem by an algebraic approach. Historically, treatment of functions in numerics has been based on the treatment of numbers, and the classical numerical algorithms are based on the mere evaluation of functions at specific points. DA techniques are based on the observation that it is possible to extract more information on a function rather than its mere values. The basic idea is to bring the treatment of functions and the operations on them to the computer environment in a similar way as the treatment of real numbers. Referring to Figure 2.1, consider two real numbers a and b. In order to operate on them in a computer environment, they are usually transformed in their floating point (FP) representation, $\overline{a}$ and $\overline{b}$ respectively. Then, given any operation $*$ in the set of real numbers, an adjoint operation $\circledast$ is defined in the set of FP numbers such that the diagram commutes. Consequently, transforming the real numbers a and b in their FP representation and operating on them in the set of FP numbers returns the same result as carrying out the operation in the set of real numbers and then transforming the achieved result in its FP representation. In a similar way, suppose two sufficiently regular functions f and g are given. In the framework of differential algebra, the computer operates on them using their Taylor series expansions, F and G respectively. Therefore, the transformation of real numbers in their FP representation is now substituted by the extraction of the Taylor expansions of f and g. For each operation in the function space, an adjoint operation in the space of Taylor polynomials is defined such that the corresponding diagram commutes: extracting the Taylor expansions of f and g and operating on them returns the same result as operating on f and g in the original space and then extracting the Taylor expansion of the resulting function. Differential algebra can be effectively implemented in a computer environment. In this way, the Taylor coefficients of a function can be obtained up to a specified order k, along with the function evaluation, with a fixed amount of effort. The Taylor coefficients of order k for sums and product of functions, as well as scalar products with reals, can be computed from those of

$$\begin{tikzcd}
a, b \in R \arrow[r, "\mathcal{T}"] \arrow[d, "*"'] & \overline{a}, \overline{b} \in FP \arrow[d, "\circledast"] \\
a * b \arrow[r, "\mathcal{T}"'] & \overline{a} \circledast \overline{b}
\end{tikzcd}
\qquad
\begin{tikzcd}
f, g \arrow[r, "\mathcal{P}"] \arrow[d, "*"'] & F, G \arrow[d, "\circledast"] \\
f * g \arrow[r, "\mathcal{P}"'] & F \circledast G
\end{tikzcd}$$

Figure 2.1. Analogy between the floating point representation of real numbers in a computer environment (left figure) and the introduction of the algebra of Taylor polynomials in the differential algebraic framework (right figure).

summands and factors; therefore, the set of equivalence classes of functions can be endowed with well-defined operations, leading to the so-called truncated power series algebra (TPSA) [Ber86, Ber87].

Similarly to the algorithms for floating point arithmetic, the algorithm for functions followed, including methods to perform composition of functions, to invert them, to solve nonlinear systems explicitly, and to treat common elementary functions [Ber91, Ber99b]. In addition to these algebraic operations, also the analytic operations of differentiation and integration have been developed on these function spaces, defining a differential algebraic structure.

As DA represents the core of the algorithms developed in the frame of this work, some useful notes to get familiar with these techniques are given in the followings. In particular, the minimal differential algebra for 1-dimensional functions and their first order expansion is explained in details, and some hints on its extension to functions of n variables and to k-th order are given. Two important applications of DA techniques are then presented in section 2.3, pertaining the solution of parametric implicit equations. The validated extension of differential algebra into the Taylor model method concludes the chapter in section 2.5.

2.1 The Minimal Differential Algebra

The simplest nontrivial differential algebra is here described. Consider all ordered pairs (q_0, q_1), with q_0 and q_1 real numbers. The addition, scalar multiplication, and vector multiplication are defined as follows:

$$\begin{aligned}
(q_0, q_1) + (r_0, r_1) &= (q_0 + r_0,\ q_1 + r_1) \\
t \cdot (q_0, q_1) &= (t \cdot q_0,\ t \cdot q_1) \\
(q_0, q_1) \cdot (r_0, r_1) &= (q_0 \cdot r_0,\ q_0 \cdot r_1 + q_1 \cdot r_0),
\end{aligned} \tag{2.1}$$

where $t \in \mathbb{R}$. The ordered pairs with the above arithmetic are called ${}_1D_1$. The first two operations are the familiar vector space structure of $\mathbb{R}^2$, whereas the multiplication is similar to that in the complex numbers; except here $(0,1)\cdot(0,1)$ does not equal $(-1,0)$, but rather $(0,0)$. The multiplication of vectors is seen to have $(1,0)$ as the unity element. The multiplication is commutative, associative, and distributive with respect to addition. Together, the three operations defined in Eq. (2.1) form an algebra. Furthermore, they do form an extension of real numbers, as $(r,0)+(s,0)=(r+s,0)$ and $(r,0)\cdot(s,0)=(r\cdot s,0)$, so that the reals can be included.

However ${}_1D_1$ is not a field, as (q_0,q_1) has a multiplicative inverse in ${}_1D_1$ if and only if $q_0 \neq 0$. If $q_0 \neq 0$ then

$$(q_0,q_1)^{-1} = \left(\frac{1}{q_0}, -\frac{q_1}{q_0^2}\right). \tag{2.2}$$

If q_0 is positive, then $(q_0,q_1) \in {}_1D_1$ has a root

$$\sqrt{(q_0,q_1)} = \left(\sqrt{q_0}, \frac{q_1}{2\sqrt{q_0}}\right), \tag{2.3}$$

as simple arithmetic shows.

One important property of this algebra is that it has an order compatible with its algebraic operations. Given two elements (q_0,q_1) and (r_0,r_1) in ${}_1D_1$, the following is defined

$$\begin{aligned}
(q_0,q_1) < (r_0,r_1) \quad &\text{if} \quad q_0 < r_0 \quad \text{or} \quad (q_0 = r_0 \text{ and } q_1 < r_1) \\
(q_0,q_1) > (r_0,r_1) \quad &\text{if} \quad (r_0,r_1) < (q_0,q_1) \\
(q_0,q_1) = (r_0,r_1) \quad &\text{if} \quad q_0 = r_0 \text{ and } q_1 = r_1.
\end{aligned} \tag{2.4}$$

As for any two elements (q_0,q_1) and (r_0,r_1) only one of the three relation holds, ${}_1D_1$ is said totally ordered. The order is compatible with the addition and multiplication; for all $(q_0,q_1),(r_0,r_1),(s_0,s_1) \in {}_1D_1$, it follows $(q_0,q_1) < (r_0,r_1) \Rightarrow (q_0,q_1)+(s_0,s_1) < (r_0,r_1)+(s_0,s_1)$; and $(s_0,s_1) > (0,0) = 0 \Rightarrow (q_0,q_1)\cdot(s_0,s_1) < (r_0,r_1)\cdot(s_0,s_1)$.

The number $d = (0,1)$ has the interesting property of being positive but smaller than any positive real number; indeed

$$(0,0) < (0,1) < (r,0) = r. \tag{2.5}$$

For this reason d is called an infinitesimal or a differential. In fact, d is so small that its square vanishes in ${}_1D_1$. Since for any $(q_0,q_1) \in {}_1D_1$

$$(q_0,q_1) = (q_0,0) + (0,q_1) = q_0 + d \cdot q_1, \tag{2.6}$$

the first component is called the real part and the second component the differential part.

The algebra in ${}_1D_1$ becomes a differential algebra by introducing a map ∂ from

${}_1D_1$ to itself, and proving that the map is a derivation. Define $\partial : {}_1D_1 \to {}_1D_1$ by

$$\partial(q_0, q_1) = (0, q_1). \tag{2.7}$$

Note that

$$\begin{aligned} \partial\{(q_0, q_1) + (r_0, r_1)\} &= \partial(q_0 + r_0, q_1 + r_1) = (0, q_1 + r_1) \\ &= (0, q_1) + (0, r_1) = \partial(q_0, q_1) + \partial(r_0, r_1) \end{aligned} \tag{2.8}$$

$$\begin{aligned} \partial\{t \cdot (q_0, q_1)\} &= \partial(t \cdot q_0, t \cdot q_1) = (0, t \cdot q_1) \\ &= t \cdot (0, q_1) = t \cdot \partial\{(q_0, q_1)\} \end{aligned} \tag{2.9}$$

$$\begin{aligned} \partial\{(q_0, q_1) \cdot (r_0, r_1)\} &= \partial(q_0 \cdot r_0, q_0 \cdot r_1 + r_0 \cdot q_1) = (0, q_0 \cdot r_1 + r_0 \cdot q_1) \\ &= (0, q_1) \cdot (r_0, r_1) + (0, r_1) \cdot (q_0, q_1) \\ &= \partial\{(q_0, q_1)\} \cdot (r_0, r_1) + (q_0, q_1) \cdot \partial\{(r_0, r_1)\}. \end{aligned} \tag{2.10}$$

This holds for all $(q_0, q_1), (r_0, r_1) \in {}_1D_1$. Therefore ∂ is a derivation and $({}_1D_1, \partial)$ is a differential algebra.

The most important aspect of ${}_1D_1$ is that it allows the automatic computation of derivatives. As an example, assume to have two functions $f, g \in \mathcal{C}^1(D)$, with $D \subseteq \mathbb{R}$. Put their values and their derivatives at $x \in D$ in the form $(f(x), f'(x))$ and $(g(x), g'(x))$ as two vectors in ${}_1D_1$; and consider the product

$$(f(x), f'(x)) \cdot (g(x), g'(x)) = \left(f(x) \cdot g(x), f(x) \cdot g'(x) + f'(x) \cdot g(x)\right). \tag{2.11}$$

As it can be seen, if the derivative of the product $f \cdot g$ at x is of interest, one has just to look at the second component of the resulting pair in Eq. (2.11); whereas the first component gives the value of the product of the functions. Therefore, if two vectors contain the values and the derivatives of two functions, their product contains the values and the derivatives of the product function.

Defining the operation [ ] from the space of differential functions to ${}_1D_1$ via

$$[f] = (f(x), f'(x)), \tag{2.12}$$

and using Eq. (2.2), it holds

$$\begin{aligned} [f + g] &= [f] + [g] \\ [t \cdot f] &= t \cdot [f] \\ [f \cdot g] &= [f] \cdot [g], \end{aligned} \tag{2.13}$$

where $t \in \mathbb{R}$, and

$$[1/g] = [1]/[g] = 1/[g] \tag{2.14}$$

for all g with $g(x) \neq 0$. This observation can be used to compute derivatives of many kinds of functions algebraically by merely applying arithmetic rules on ${}_1D_1$, starting from the value and the derivative of the identity function $f(x) = x$, i.e., $[f] = [x] = (x, 1)$. Consider the example

$$f(x) = \frac{1}{x + 1/x} \tag{2.15}$$

and its derivative

$$f'(x) = \frac{(1/x^2) - 1}{(x + (1/x))^2}. \tag{2.16}$$

The function value and its derivative at the point $x = 3$ are

$$f(3) = \frac{3}{10}, \quad f'(3) = -\frac{2}{25}. \tag{2.17}$$

The same result can be obtained by replacing x with $[x]$ evaluated at $x = 3$, i.e., $(3, 1)$. Performing all the operations of (2.15) in the algebraic framework defined in (2.1) and (2.2) yields

$$\begin{aligned} f([x]) &= \frac{1}{[x] + 1/[x]} = \frac{1}{(3,1) + 1/(3,1)} = \frac{1}{(3,1) + (1/3, -1/9)} \\ &= \frac{1}{(10/3, 8/9)} = \left(\frac{3}{10}, -\frac{8}{9} \Big/ \frac{100}{9}\right) = \left(\frac{3}{10}, -\frac{2}{25}\right). \end{aligned} \tag{2.18}$$

Thus, the real part of the result is the value of the function at $x = 3$, whereas the differential part is the value of the derivative of the function at $x = 3$. This is expected as, by applying the relations (2.13) and (2.14) to compute the ${}_1D_1$ representative of f,

$$\begin{aligned} [f] &= \left[\frac{1}{x + 1/x}\right] = \frac{1}{[x + 1/x]} \\ &= \frac{1}{[x] + [1/x]} = \frac{1}{[x] + 1/[x]} \\ &= f([x]). \end{aligned} \tag{2.19}$$

It is worth highlighting that DA circumvents the analytical derivation of $f'(x)$ as performed in Eq. (2.16) to compute the derivative of f at $x = 3$.

The method can be generalized to allow the treatment of common intrinsic functions, like trigonometric or exponential functions, by setting

$$\begin{gathered} g_i([f]) = [g_i(f)] \quad \text{or} \\ g_i\left((q_0,\, q_1)\right) = \left(g_i(q_0),\; q_1\, g_i'(q_0)\right). \end{gathered} \tag{2.20}$$

By virtue of equations (2.1) and (2.20) any function f representable by finitely many additions, subtractions, multiplications, divisions, and intrinsic functions in ${}_1D_1$ satisfies the important relationship

$$[f(x)] = f([x]). \tag{2.21}$$

Note that $f(r+d) = f(r) + d \cdot f'(r)$ resembles $f(x+\Delta x) \approx f(x) + \Delta x \cdot f'(x)$, in which the approximation becomes increasingly more refined for smaller Δx.

2.2 The Differential Algebra ${}_kD_n$

This section extends the algebra ${}_1D_1$ to the general ${}_kD_n$ case, which enables the computation of the derivatives of functions in n variables up to order k. Similarly as before, it is based on taking the space $\mathcal{C}^k(D)$, i.e. the collection of k times continuously differentiable functions on $D \subseteq \mathbb{R}^n$. On this space an equivalence relation is introduced. For $f, g \in \mathcal{C}^k(D)$, $f =_k g$ if and only if $f(x) = g(x)$ with $x \in D$ and all the partial derivatives of f and g agree at x up to order k. The relation $=_k$ satisfies

$$\begin{aligned} f =_k f \quad & \text{for all} \quad f \ \in \mathcal{C}^k(D), \\ f =_k g \Rightarrow g =_k f \quad & \text{for all} \quad f, g \ \in \mathcal{C}^k(D), \text{ and} \\ f =_k g \text{ and } g =_k h \Rightarrow f =_k h \quad & \text{for all} \quad f, g, h, \in \mathcal{C}^k(D). \end{aligned} \tag{2.22}$$

Thus, $=_k$ is an equivalence relation. All the elements that are related to f can be grouped together in one set, the equivalence class $[f]$ of the function f. The resulting equivalence classes are often referred to as DA vectors or DA numbers. Intuitively, each of these classes is then specified by a particular collection of partial derivatives in all n variables up to order k. This set of these classes is called ${}_kD_n$.

If the values and the derivatives of two functions f and g are known, the corresponding values and derivatives of $f+g$ and $f \cdot g$ can be inferred. Therefore, the arithmetics on the classes in ${}_kD_n$ can be introduced via

$$\begin{aligned} [f+g] &= [f] + [g] \\ [t \cdot f] &= t \cdot [f] \\ [f \cdot g] &= [f] \cdot [g], \end{aligned} \tag{2.23}$$

where $t \in \mathbb{R}$. Under this operations, ${}_kD_n$ becomes an algebra. Note that the algebra ${}_1D_1$ is a particular case of ${}_kD_n$. This is justified by the fact that the equivalence relation in (2.22) holds for the special case $k = n = 1$; moreover, the algebra in Eq. (2.23) is identical to the ${}_1D_1$ counterpart in Eq. (2.13). Thus, the definition of ${}_1D_1$ in Section 2.1 is compatible with its ${}_kD_n$ extension; therefore, no difference in notation is made. For each $v \in 1, \ldots, n$, define the map ∂_v from ${}_kD_n$ to ${}_kD_n$ for f via

$$\partial_v[f] = \left[p_v \cdot \frac{\partial f}{\partial x_v} \right], \tag{2.24}$$

where

$$p_v(x_1, \ldots, x_n) = x_v \tag{2.25}$$

projects out the v-th component of the identity function. It's easy to show that, for all $v = 1, \ldots, n$ and for all $[f], [g] \in {}_kD_n$,

$$\begin{aligned} \partial_v([f] + [g]) &= \partial_v[f] + \partial_v[g] \\ \partial_v(t \cdot [f]) &= t \cdot \partial_v[f] \\ \partial_v([f] \cdot [g]) &= [f] \cdot (\partial_v[g]) + (\partial_v[f]) \cdot [g], \end{aligned} \tag{2.26}$$

where $t \in \mathbb{R}$. Therefore, ∂_v is a derivation for all v, and hence $({}_kD_n, \partial_1, \ldots, \partial_v)$ is a differential algebra.

The dimension of ${}_kD_n$ is now assessed. Define the special numbers d_v as follows:

$$d_v = [x_v]. \tag{2.27}$$

Observe that f lies in the same class as its Taylor polynomial T_f of order k around the origin; they have the same function values and derivatives up to order k. Therefore,

$$[f] = [T_f]. \tag{2.28}$$

Denoting the Taylor coefficients of the Taylor polynomial T_f of f as $c_{j_1,\ldots,j_n}$, it follows

$$T_f(x_1, \ldots, x_n) = \sum_{j_1+\cdots+j_n \leq k} c_{j_1,\ldots,j_n} \cdot x_1^{j_1} \cdots x_n^{j_n} \tag{2.29}$$

with

$$c_{j_i}, \ldots, c_{j_n} = \frac{1}{j_1! \cdots j_n!} \cdot \frac{\partial^{j_1+\cdots+j_n} f}{\partial x_1^{j_1} \cdots \partial x_n^{j_n}} \tag{2.30}$$

and thus

$$\begin{aligned} [f] = [T_f] &= \left[\sum_{j_1+\cdots+j_n \leq k} c_{j_1,\ldots,j_n} \cdot x_1^{j_1} \cdots x_n^{j_n} \right] \\ &= \sum_{j_1+\cdots+j_n \leq k} c_{j_1,\ldots,j_n} \cdot d_1^{j_1} \cdots d_n^{j_n}, \end{aligned} \tag{2.31}$$

where, in the last step, the properties $[a + b] = [a] + [b]$ and $[a \cdot b] = [a] \cdot [b]$ have been used. Therefore, the set $\{1, d_v : v = 1, 2, \ldots, n\}$ generates ${}_kD_n$, as any element of

${}_kD_n$ can be obtained from 1 and the d_v via addition and multiplication. Therefore, as an algebra, ${}_kD_n$ has $(n+1)$ generators, and the terms $d_1^{j_1}\cdots d_n^{j_n}$ form a basis for the vector space ${}_kD_n$. It is shown in [Ber99c] that the number of basic elements is $(k+n)!/(k!\,n!)$, which is the dimension of ${}_kD_n$.

Similarly to the structure ${}_1D_1$, ${}_kD_n$ can be ordered, and the d_v, being smaller than any real number, are infinitely small or infinitesimal. Furthermore, a fixed point theorem for contracting operators in ${}_kD_n$ exists, which enables the evaluation of square roots, the quotient, and the inversion of Taylor polynomials through iterative processes based on a finite number of steps [Ber99c]. Once the function composition and the elementary functions, like trigonometric or exponential functions, are introduced in ${}_kD_n$, the derivatives of any function f belonging to $\mathcal{C}^k(\mathbb{R}^n)$ can be computed up to order k in a fixed amount of effort by applying

$$[f(x_1,\dots,x_n)] = f([x_1,\dots,x_n]) = f(x_1+d_1,\dots,x_n+d_n). \tag{2.32}$$

The differential algebra sketched in this section was implemented by M. Berz and K. Makino in the software COSY INFINITY [Ber06a]. [1]

2.3 Solution of Parametric Implicit Equations

DA techniques can be effectively used to identify the solution of parametric implicit equations. Well-established numerical techniques (e.g. Newton's method) exist, which can effectively identify the solution of a classical implicit equation

$$f(x) = 0. \tag{2.33}$$

Without loss of generality, suppose an explicit dependence on a vector of parameter $\boldsymbol{p}$ can be highlighted in the previous function f, which leads to the parametric implicit equation

$$f(x,\boldsymbol{p}) = 0. \tag{2.34}$$

Suppose the previous equation is to be solved, whose solution is represented by the function $x(\boldsymbol{p})$ returning the value of x solving Eq. (2.34) for any value of $\boldsymbol{p}$. Thus, the dependence of the solution of the implicit equation on the vector of parameters $\boldsymbol{p}$ is of interest. DA techniques can effectively handle the previous problem by identifying the function $x(\boldsymbol{p})$ in terms of its Taylor expansion with respect to $\boldsymbol{p}$. The DA-based algorithm is presented in the followings for the solution of the scalar parametric implicit equation (2.34); the generalization to a system of parametric implicit equations is straightforward.

The solution of (2.34) is sought, where sufficient regularity is assumed to charac-

---

[1] The software and all the related documentations are available free of charge for non-commercial use online at `http://bt.pa.msu.edu/index_cosy.htm`.

terize the function f, i.e. $f \in \mathcal{C}^{k+1}$. This means that $x(\boldsymbol{p})$ satisfying

$$f(x(\boldsymbol{p}), \boldsymbol{p}) = 0 \tag{2.35}$$

is to be identified. The first step is to consider a reference value $\boldsymbol{p}^0$ of the vector of parameters $\boldsymbol{p}$ and to compute the value of the solution x^0 of the corresponding implicit equation by means of a classical numerical method, e.g. a Newton's method. The variable x and $\boldsymbol{p}$ are then initialized as k-th order DA variables, i.e.,

$$\begin{aligned} [x] &= x^0 + \delta x \\ [\boldsymbol{p}] &= \boldsymbol{p}^0 + \delta \boldsymbol{p}. \end{aligned} \tag{2.36}$$

A DA-based evaluation of the function f in (2.34) delivers the k-th order expansion of f with respect to x and $\boldsymbol{p}$:

$$\delta f = \mathcal{M}_f(\delta x, \delta \boldsymbol{p}). \tag{2.37}$$

where $\mathcal{M}_f$ denotes the Taylor map for f. Note that the map has no constant part as x^0 is the solution of the implicit equation for the nominal value $\boldsymbol{p}^0$; thus, δf represents the deviation of f from its reference value 0, resulting from deviations of x and $\boldsymbol{p}$ from x^0 and $\boldsymbol{p}^0$. The map (2.37) is then augmented by introducing the map corresponding to the identity function on $\boldsymbol{p}$, i.e. $\delta \boldsymbol{p} = \mathcal{I}_{\boldsymbol{p}}(\delta \boldsymbol{p})$, ending up with

$$\begin{bmatrix} \delta f \\ \delta \boldsymbol{p} \end{bmatrix} = \begin{bmatrix} \mathcal{M}_f \\ \mathcal{I}_{\boldsymbol{p}} \end{bmatrix} \begin{bmatrix} \delta x \\ \delta \boldsymbol{p} \end{bmatrix}. \tag{2.38}$$

The k-th order map (2.38) is inverted using COSY INFINITY built-in tools (based on fixed point iterations), obtaining

$$\begin{bmatrix} \delta x \\ \delta \boldsymbol{p} \end{bmatrix} = \begin{bmatrix} \mathcal{M}_f \\ \mathcal{I}_{\boldsymbol{p}} \end{bmatrix}^{-1} \begin{bmatrix} \delta f \\ \delta \boldsymbol{p} \end{bmatrix} \tag{2.39}$$

As the goal is to compute the k-th order Taylor expansion of the solution manifold $x(\boldsymbol{p})$ of (2.34), the map (2.39) is evaluated for $\delta f = 0$:

$$\begin{bmatrix} \delta x \\ \delta \boldsymbol{p} \end{bmatrix} = \begin{bmatrix} \mathcal{M}_f \\ \mathcal{I}_{\boldsymbol{p}} \end{bmatrix}^{-1} \begin{bmatrix} 0 \\ \delta \boldsymbol{p} \end{bmatrix}. \tag{2.40}$$

The first row of map (2.40)

$$\delta x = \mathcal{M}_f^{-1}(\delta \boldsymbol{p}), \tag{2.41}$$

can be written as

$$\delta x = \mathcal{M}_{x, \delta f = 0}(\delta \boldsymbol{p}), \tag{2.42}$$

where $\mathcal{M}_f^{-1}$ has been written as $\mathcal{M}_{x,\delta f=0}$ to stress the imposed constraint. Equation

(2.42) express how a variation of the vector of parameters $\delta\boldsymbol{p}$ affects the solution of the implicit equation as a k-th order Taylor polynomial. In particular, by plugging map (2.42) into the first of Eq. (2.36) we obtain

$$[x] = x^0 + \mathcal{M}_{x,\delta f=0}(\delta\boldsymbol{p}), \tag{2.43}$$

which is the k-th order Taylor expansion of the solution manifold. For every value of $\boldsymbol{p}$ the approximate solution of $f(x,\boldsymbol{p}) = 0$ can be easily computed by evaluating the Taylor polynomial (2.43) at $\delta\boldsymbol{p} = \boldsymbol{p} - \boldsymbol{p}^0$. Apparently, the solution obtained by means of (2.43) is a Taylor approximation of the exact solution of equation (2.34) and the accuracy of the approximation depends on the order of the Taylor expansion and the displacement $\delta\boldsymbol{p}$ from the reference value $\boldsymbol{p}^0$.

A classical example of parametric implicit equation in Astrodynamics is Kepler's equation

$$f(E) = E - e\sin E - M = 0, \tag{2.44}$$

where E is the eccentric anomaly, e the orbit eccentricity, and M is the mean anomaly. The solution of Kepler's equation (or its variants) is necessary to compute the orbital position and velocity of an object along its orbit at a certain time in many analytical solutions for satellite motion. As an example, SGP4/SDP4 requires the solution of a slightly different formulation in the variable $u = E + \omega$ [Hoo04]:

$$f(u) = (M + \omega) - a_{yN}\cos u + a_{xN}\sin u - u = 0, \tag{2.45}$$

where ω is the argument of pericentre and the two coefficients a_{yN} and a_{xN} are related to orbit eccentricity and long-period periodic effects of Earth gravity. Within this work the algorithm for the solution of parametric implicit equations is used for expanding the solution of Kepler's equation and its variants.

2.4 High Order Expansion of the Flow

Differential algebra allows the derivatives of any function f of n variables to be computed up to an arbitrary order k, along with the function evaluation. This has an important consequence when the numerical integration of an Ordinary Differential Equation (ODE) is performed by means of an arbitrary integration scheme. Any integration scheme is based on algebraic operations, involving the evaluation of the ODE right hand side at several integration points. Therefore, carrying out all the evaluations in the DA framework allows differential algebra to compute the arbitrary order expansion of the flow of a general ODE with respect to the initial condition.

Without loss of generality, consider the scalar initial value problem

$$\begin{cases} \dot{x} = f(x,t) \\ x(t_0) = x_0 \end{cases} \tag{2.46}$$

and the associated phase flow $\varphi(t; x_0)$. We now want to show that, starting from the DA representation of the initial condition x_0, differential algebra allows us to propagate the Taylor expansion of the flow in x_0 forward in time, up to the final time t_f.

To this aim, replace the point initial condition x_0 by the DA representative of its identity function up to order k, which is a $(k+1)$-tuple of Taylor coefficients. (Note that x_0 is the flow evaluated at the initial time; i.e, $x_0 = \varphi(t_0; x_0)$.) As for the identity function only the first two coefficients, corresponding to the constant part and the first derivative respectively, are non zeros, we can write $[x_0]$ as $x_0 + \delta x_0$, where x_0 is the reference point for the expansion. If all the operations of the numerical integration scheme are carried out in the DA framework, the phase flow $\varphi(t; x_0)$ is approximated, at each fixed time step t_i, as a Taylor expansion in x_0.

For the sake of clarity, consider the forward Euler's scheme

$$x_i = x_{i-1} + f(x_{i-1})\Delta t \tag{2.47}$$

and substitute the initial value with the DA identity $[x_0] = x_0 + \delta x_0$. At the first time step we have

$$[x_1] = [x_0] + f([x_0]) \cdot \Delta t. \tag{2.48}$$

If the function f is evaluated in the DA framework, the output of the first step, $[x_1]$, is the k-th order Taylor expansion of the flow $\varphi(t; x_0)$ with respect to x_0 at $t = t_1$. Note that, as a result of the DA evaluation of $f([x_0])$, the $(k+1)$-tuple $[x_1]$ may include several non zero coefficients corresponding to high order terms in δx_0. The previous procedure can be inferred through the subsequent steps. The result of the final step is the k-th order Taylor expansion of $\varphi(t; x_0)$ in x_0 at the final time t_f. Thus, the flow of a dynamical system can be approximated, at each time step t_i, as a k-th order Taylor expansion in x_0 in a fixed amount of effort. In addition, the high order expansion of the flow with respect to the final time is obtained when the final time is initialized as DA variable. Consider the last step of the forward Euler's scheme where the initial value $[x_0]$ is a DA variable and f is evaluated in a DA environment:

$$[x_N] = [x_{N-1}] + f([x_{N-1}])\Delta t. \tag{2.49}$$

Since the final time is initialized as a DA variable, i.e.

$$[t_f] = t_f + \delta t_f, \tag{2.50}$$

the last time step Δt will be a DA variable as well, yielding

$$[x_N] = [x_{N-1}] + f([x_{N-1}])[\Delta t] = [x_{N-1}] + f([x_{N-1}])\left([t_f] - t_{n-1}\right). \tag{2.51}$$

As a result, the high order expansion of the flow with respect to final time variation is obtained.

The conversion of any standard integration scheme to its DA counterparts is straightforward both for explicit and implicit solvers. This is essentially based on the substitution of the operations on real numbers with those on DA numbers. In addition, whenever the integration scheme involves iterations (e.g. iterations required in implicit and predictor-corrector methods), step size control, and order selection, a measure of the accuracy of the Taylor expansion of the flow needs to be included.

Integration schemes based on DA pave the way to the algorithms presented in this work. A first example is given hereafter about the propagation of uncertainties on initial conditions. The Taylor polynomials resulting from the use of DA-based numerical integrators expand the solution of the initial value problem presented in Eq. (2.46) with respect to the initial condition. Thus, the dependence of the solution $x(t)$ on the initial condition is available, at a time t_i, in terms of a k-th order polynomial map $\mathcal{M}_{x_0}(\delta x_0)$, where δx_0 is the displacement from the reference initial condition. The evaluation of the map $\mathcal{M}_{x_0}(\delta x_0)$ for a selected value of δx_0 supplies the k-th order Taylor approximation of the solution at t_i corresponding to the perturbed initial condition. The accuracy of the result depends on the function f, the expansion order k, and the value of the displacement δx_0.

The main advantage of the DA-based approach is that there is no need to write and integrate variational equations in order to obtain high order expansions of the flow. This result is basically obtained by the substitution of operations between real numbers with those on DA numbers, and therefore the method is ODE independent. Furthermore, the efficient implementation of the differential algebra in COSY INFINITY allows us to obtain high order expansions with limited computational time.

2.5 Taylor Models

This section is devoted to the introduction of the Taylor Model (TM) method, which plays a key role in the conjunction identification algorithms described in chapter 5. Some notes on Taylor Models are presented first based on the Ph.D. thesis of Kyoko Makino [Mak98].

2.5.1 Differential Algebra and Interval Arithmetic

While DA methods can provide the derivatives of functional dependencies and the expansion of the solution of ODEs up to high orders, in a rigorous sense they fail to provide information about the range of the function. A simple example that dramatically illustrates this phenomenon is the function shown in Figure 2.2

$$f(x) = \begin{cases} 0 & \text{if } x = 0 \\ \exp(-1/x^2) & \text{else.} \end{cases} \tag{2.52}$$

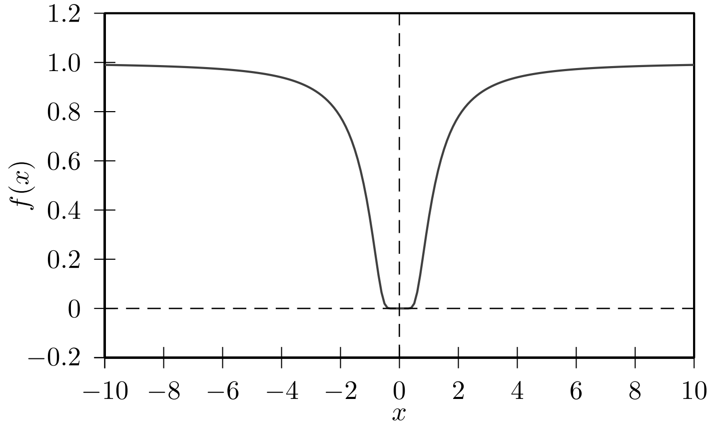

Figure 2.2. Function $f(x) = \exp(-1/x^2)$ if $x \neq 0$; 0 else, and its Taylor polynomial, which vanishes identically.

The value of the function and all the derivatives at $x = 0$ are 0. Thus the Taylor polynomial at the reference point $x = 0$ is just the constant 0. In particular, this also implies that the Taylor expansion of f converges everywhere, but it fails to agree with $f(x)$ everywhere but at $x = 0$.

Rigorous bounds of the range of functions can be obtained instead using the method of Interval Arithmetic (IA) [Moo66]. Both extended domains of numbers as well as individual real numbers are represented via rigorous inclusions of floating point intervals. Arithmetic operations are introduced on intervals such that, for any two real numbers in two different intervals, a real arithmetic operation on the two real numbers always leads to a result that is contained in the interval obtained from the corresponding arithmetic operation on the two intervals. Table 2.1 lists some elementary properties of interval arithmetic. By evaluating a function in interval arithmetic, it is thus possible to carry rigorous bounds information through the operations, and in the end obtain rigorous bounds of the function.

$I_1 + I_2 = [a_1 + a_2, b_1 + b_2]$

$-I_1 = [-b_1, -a_1]$

$I_1 \cdot I_2 = [\min(a_1a_2, a_1b_2, b_1a_2, b_1b_2), \max(a_1a_2, a_1b_2, b_1a_2, b_1b_2)]$

If $0 \notin I_1$, $1/I_1 = [1/b_1, 1/a_1]$

Table 2.1. Elementary properties of interval arithmetic; $I_1 = [a_1, b_1], I_2 = [a_2, b_2]$.

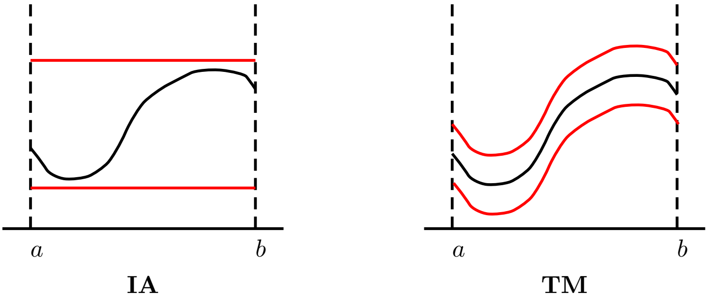

Figure 2.3. Comparison between Interval Arithmetic and Taylor Model

However, while reasonably fast in practice, interval methods have some severe disadvantages, which limit their applicability for complicated functions. First, the width of the resulting intervals scales with the width of the original intervals; and second, artificial blow-up usually occurs in extended calculations. To illustrate the blow-up phenomenon with a trivial example, consider the interval $I = [a, b]$, which has the width $b - a$. Compute the addition of I to itself and its subtraction from itself:

$$\begin{aligned} I + I &= [a, b] + [a, b] = [a + a, b + b] = [2a, 2b] \\ I - I &= [a, b] - [a, b] = [a, b] + [-b, -a] = [a - b, b - a]. \end{aligned}$$

In both cases the resulting width is $2(b-a)$, which is twice the original width, although we know that regardless of what unknown quantity x is characterized by I, certainly $x - x$ should equal zero.

The TM method is a method that combines the advantage of rigor of the interval approach, while largely avoiding the blow-up problem through the use of DA techniques. The key idea is to describe the bulk of the functional dependence through a Taylor polynomial, and bound the deviation of the original function from the Taylor polynomial by an interval. Therefore a TM represents a hybrid between formula manipulation, interval methods, and methods of computational differentiation [Gri91, Ber96]. As can be seen in Figure 2.3, TM supply a more accurate enclosure of a function over an interval $[a, b]$ with respect to IA.

In this endeavor, the Taylor theorem plays an important role.

Theorem 1 (Taylor's Theorem)**.** *Suppose that a function* $f : [\boldsymbol{a}, \boldsymbol{b}] \subset \mathbb{R}^n \to \mathbb{R}$ *is* $(k+1)$ *times continuously partially differentiable on* $[\boldsymbol{a}, \boldsymbol{b}]$*. Assume* $\boldsymbol{x}_0 \in [\boldsymbol{a}, \boldsymbol{b}]$*. Then for each* $\boldsymbol{x} \in [\boldsymbol{a}, \boldsymbol{b}]$*, there is* $\theta \in \mathbb{R}$ *with* $0 < \theta < 1$ *such that*

$$f(\boldsymbol{x}) = \sum_{\nu=0}^{k} \frac{1}{\nu!} \left((\boldsymbol{x} - \boldsymbol{x}_0) \cdot \boldsymbol{\nabla}\right)^{\nu} f(\boldsymbol{x}_0) + \frac{1}{(k+1)!} \left((\boldsymbol{x} - \boldsymbol{x}_0) \cdot \boldsymbol{\nabla}\right)^{k+1} f\left(\boldsymbol{x}_0 + (\boldsymbol{x} - \boldsymbol{x}_0)\theta\right),$$

where the partial differential operator $(\boldsymbol{h}\cdot\boldsymbol{\nabla})^v$ *operates as*

$$(\boldsymbol{h}\cdot\boldsymbol{\nabla})^v = \sum_{\substack{0\le i_1,\cdots,i_n\le v\\ i_1+\cdots+i_n=v}} \frac{v!}{i_1!\cdots i_n!}\, h_1^{i_1}\cdots h_n^{i_n}\, \frac{\partial^v}{\partial x_1^{i_1}\cdots\partial x_n^{i_n}}.$$

Depending on the situation at hand, the remainder term also can be cast into a variety of well-known other forms. Taylor's theorem allows a quantitative estimate of the error that is to be expected when approximating a function by its Taylor polynomial. Furthermore, it even offers a way to obtain bounds for the error in practice, based on bounding the $(k+1)$st derivative, a method that has sometimes been employed in interval calculations.

For notational convenience, we introduce a parameter α to describe the details of a given Taylor expansion, namely, the order of the Taylor polynomial k, and the reference point of expansion $\boldsymbol{x}_0$. For the purpose to derive bounds for the remainder, it is also necessary to include the domain interval $[\boldsymbol{a},\boldsymbol{b}]$ on which the function is to be considered; altogether

$$\alpha = (k, \boldsymbol{x}_0, [\boldsymbol{a},\boldsymbol{b}]). \tag{2.53}$$

Consider now a $(k+1)$ times continuously partially differentiable function $f : [\boldsymbol{a},\boldsymbol{b}] \subset \mathbb{R}^n \to \mathbb{R}$ and write it as a sum of its Taylor polynomial $P_{\alpha,f}$ of k-th order and a remainder $\varepsilon_{\alpha,f}$ as

$$f(\boldsymbol{x}) = P_{\alpha,f}(\boldsymbol{x}-\boldsymbol{x}_0) + \varepsilon_{\alpha,f}(\boldsymbol{x}-\boldsymbol{x}_0),$$

where $\varepsilon_{\alpha,f}(\boldsymbol{x}-\boldsymbol{x}_0)$ is continuous (even continuously differentiable) on the domain interval and thus bounded. Let the interval $I_{\alpha,f}$ be such that

$$\forall \boldsymbol{x}\in[\boldsymbol{a},\boldsymbol{b}], \quad \varepsilon_{\alpha,f}(\boldsymbol{x}-\boldsymbol{x}_0)\in I_{\alpha,f}.$$

Then

$$\forall \boldsymbol{x}\in[\boldsymbol{a},\boldsymbol{b}], \quad f(\boldsymbol{x})\in P_{\alpha,f}(\boldsymbol{x}-\boldsymbol{x}_0) + I_{\alpha,f}. \tag{2.54}$$

Because of the special form of the Taylor remainder term $\varepsilon_{\alpha,f}$, in practice the remainder usually decreases as $|\boldsymbol{x}-\boldsymbol{x}_0|^{k+1}$. Hence, if $|\boldsymbol{x}-\boldsymbol{x}_0|$ is chosen to be small, the interval $I_{\alpha,f}$, which, from now on, will be referred to as the interval remainder bound, can become so small that even the effect of considerable blow-up is not detrimental. The set $P_{\alpha,f}(\boldsymbol{x}-\boldsymbol{x}_0) + I_{\alpha,f}$ containing f consists of the Taylor polynomial $P_{\alpha,f}(\boldsymbol{x}-\boldsymbol{x}_0)$ and the interval remainder bound $I_{\alpha,f}$, and it rigorously bounds the range of the function f over the interval $[\boldsymbol{a},\boldsymbol{b}]$. The pair $(P_{\alpha,f}, I_{\alpha,f})$ of a Taylor polynomial $P_{\alpha,f}(\boldsymbol{x}-\boldsymbol{x}_0)$ and an interval remainder bound $I_{\alpha,f}$ is said to be a Taylor model of f if and only if Eq. (2.54) is satisfied. In this case, the Taylor model is denoted by

$$T_{\alpha,f} = (P_{\alpha,f}, I_{\alpha,f}).$$

Altogether, the Taylor Model approach has the following important properties:

1. The ability to provide enclosures of any function given by a finite computer code list by a Taylor polynomial and a remainder bound with a sharpness that scales with order $(k+1)$ of the width of the domain.

2. The computational expense increases only moderately with order, allowing the computation of sharp range enclosures even for complicated functional dependencies with a significant dependency problem.

3. The computational expense of higher dimensions increases only very moderately, significantly reducing the "curse of dimensionality".

The implementation of the method in the code COSY Infinity [Mak98, Ber06a] supports binary operations and standard intrinsic functions, as well as the antiderivative operation which widens the applications of the method. In the following section a few details concerning Taylor Models operations are given.

2.5.2 Operations on Taylor Models

In this section, tools that allow to efficiently calculate Taylor models for all functions representable on a computer are briefly described. Similarly to differential algebra, the key is to begin with the Taylor model for the identity function, which is trivial, and then successively build up Taylor models for the total function from its pieces. This requires methods to determine Taylor models for sums and products from those of the summands or factors, as well as from intrinsics applied to functions with known Taylor models.

For illustration purposes, details about how Taylor models can be rigorously summed are reported hereafter. Let the functions $f, g : [\boldsymbol{a}, \boldsymbol{b}] \subset \mathbb{R}^n \to \mathbb{R}$ have Taylor models

$$T_{\alpha,f} = (P_{\alpha,f}, I_{\alpha,f}) \quad \text{and} \quad T_{\alpha,g} = (P_{\alpha,g}, I_{\alpha,g}),$$

which entails that

$$\begin{aligned} \forall \boldsymbol{x} \in [\boldsymbol{a}, \boldsymbol{b}], \quad & f(\boldsymbol{x}) \in P_{\alpha,f}(\boldsymbol{x} - \boldsymbol{x}_0) + I_{\alpha,f} \qquad \text{and} \\ & g(\boldsymbol{x}) \in P_{\alpha,g}(\boldsymbol{x} - \boldsymbol{x}_0) + I_{\alpha,g}. \end{aligned}$$

Then it is straightforward to obtain a Taylor model for $f+g$; in fact, for any $\boldsymbol{x} \in [\boldsymbol{a}, \boldsymbol{b}]$,

$$\begin{aligned} f(\boldsymbol{x}) + g(\boldsymbol{x}) &\in (P_{\alpha,f}(\boldsymbol{x} - \boldsymbol{x}_0) + I_{\alpha,f}) + (P_{\alpha,g}(\boldsymbol{x} - \boldsymbol{x}_0) + I_{\alpha,g}) \\ &= (P_{\alpha,f}(\boldsymbol{x} - \boldsymbol{x}_0) + P_{\alpha,g}(\boldsymbol{x} - \boldsymbol{x}_0)) + (I_{\alpha,f} + I_{\alpha,g}), \end{aligned}$$

so that a Taylor model $T_{\alpha,f+g}$ for $f+g$ can be obtained via

$$P_{\alpha,f+g} = P_{\alpha,f} + P_{\alpha,g} \quad \text{and} \quad I_{\alpha,f+g} = I_{\alpha,f} + I_{\alpha,g}. \tag{2.55}$$

Thus we define

$$T_{\alpha,f} + T_{\alpha,g} = (P_{\alpha,f} + P_{\alpha,g}, I_{\alpha,f} + I_{\alpha,g}),$$

and we obtain that $T_{\alpha,f} + T_{\alpha,g} = (P_{\alpha,f+g}, I_{\alpha,f+g})$ is a Taylor model for $f + g$. Note that the above addition of Taylor models is both commutative and associative. The procedure to multiply two Taylor models is similarly introduced and it is detailed in [Mak98].

Having introduced addition and multiplication, the computation of any polynomial of Taylor models can be performed, which turns out to be crucial when intrinsic functions are of interest. In particular, the key idea behind the computation of Taylor models for intrinsic functions is to employ Taylor's theorem of the function under consideration. As an example, consider the exponential function. Assume the Taylor model of the function f, $T_{\alpha,f} = (P_{\alpha,f}, I_{\alpha,f})$, is already available. Write the constant part of the function f around $\boldsymbol{x}_0$ as $c_{\alpha,f}$, which agrees with the constant part of the Taylor polynomial $P_{\alpha,f}$, and write the remaining part as $\bar{f}$; that is,

$$f(\boldsymbol{x}) = c_{\alpha,f} + \bar{f}(\boldsymbol{x}).$$

A Taylor model of $\bar{f}$ is then $T_{\alpha,\bar{f}} = (P_{\alpha,\bar{f}}, I_{\alpha,\bar{f}})$, where

$$P_{\alpha,\bar{f}}(\boldsymbol{x} - \boldsymbol{x}_0) = P_{\alpha,f}(\boldsymbol{x} - \boldsymbol{x}_0) - c_{\alpha,f} \qquad \text{and} \qquad I_{\alpha,\bar{f}} = I_{\alpha,f}.$$

Now we can write

$$\begin{aligned} \exp\left(f(\boldsymbol{x})\right) &= \exp\left(c_{\alpha,f} + \bar{f}(\boldsymbol{x})\right) = \exp(c_{\alpha,f}) \cdot \exp\left(\bar{f}(\boldsymbol{x})\right) \\ &= \exp(c_{\alpha,f}) \cdot \left\{ 1 + \bar{f}(\boldsymbol{x}) + \frac{1}{2!}\left(\bar{f}(\boldsymbol{x})\right)^2 + \cdots + \frac{1}{k!}\left(\bar{f}(\boldsymbol{x})\right)^k + \right. \\ &\qquad \left. + \frac{1}{(k+1)!}\left(\bar{f}(\boldsymbol{x})\right)^{k+1} \exp\left(\theta \cdot \bar{f}(\boldsymbol{x})\right) \right\}, \end{aligned}$$

where $0 < \theta < 1$. Taking $v \geq k$, where k is the order of the Taylor model, the part

$$\exp(c_{\alpha,f}) \cdot \left\{ 1 + \bar{f}(\boldsymbol{x}) + \frac{1}{2!}(\bar{f}(\boldsymbol{x}))^2 + \cdots + \frac{1}{k!}(\bar{f}(\boldsymbol{x}))^k \right\}$$

is a polynomial of $\bar{f}$, of which we can obtain the Taylor model using addition and multiplication rules. The remainder part of $\exp(f(\boldsymbol{x}))$,

$$\exp(c_{\alpha,f}) \cdot \left\{ \frac{1}{(k+1)!}(\bar{f}(\boldsymbol{x}))^{k+1} + \cdots + \frac{1}{(v+1)!}(\bar{f}(\boldsymbol{x}))^{v+1} \exp\left(\theta \cdot \bar{f}(\boldsymbol{x})\right) \right\}, \quad (2.56)$$

will be bounded by an interval. The reader is remanded to Makino's Ph.D. thesis [Mak98] for further details.

Similar procedures can be used to obtain Taylor models for other elementary functions. Altogether, it is now possible to compute Taylor models for any function that can be represented in a computer environment along with the mere evaluation of the function by simple operator overloading, in much the same way as the mere computation of derivatives and Taylor polynomials in the DA framework, or interval bounds in interval arithmetic.

2.6 COSY-GO

In this section a few hints concerning interval based Global Optimization (GO) are given. After a brief description of Taylor-model-based bounders, the main characteristic of COSY-GO are outlined.

Verified GO needs the determination of rigorous upper and lower bounds of the objective function in order to implement a branch and bound method [Kea96]. The commonly used interval approach has excelled in solving this problem elegantly from both a formal and an implementational viewpoint. However, as outlined in section 2.5.1, there are situations where the method has limitations for extended or complicated calculations because of the dependency problem, which is characterized by a cancellation of various sub-parts of the function that cannot be detected by direct use of interval methods. This effect often leads to pessimism and sometimes even drastic overestimation of range enclosure. Furthermore, the sharpness of intervals resulting from calculations typically scales linearly with the sharpness of the initial discretization intervals. For complicated problems, and in particular higher dimensions, this sometimes significantly limits the sharpness of the resulting answer that can be obtained [Mak99].

The Taylor model approach enables the computation of fully mathematically rigorous range enclosures while largely avoiding many of the limitations of the conventional interval method [Mak98].

The structure of Taylor models naturally represents a rich resource of information. In particular, the coefficients of the polynomial part P of a Taylor model are closely related to derivatives. That means when representing a function f by a Taylor model (P, I) on a computer, we also obtain the local slope, Hessian and higher order derivatives almost free. When a task is focused on range bounding, those pieces of information become particularly useful.

While range bounding of Taylor Model with interval arithmetic in the naive sense [Mak03] already exhibits superiority over mere interval arithmetic and the more advanced centered form [Mak98], the active utilization of those additional pieces of information in Taylor models has a lot of potential of developing efficient range bounders. Based on this observation, various kinds of Taylor-model-based range bounders have been developed [Ber06b], and among them the Linear Dominated Bounder (LDB) and the Quadratic Fast Bounder (QFB) are the backbones of Taylor model based verified global optimizer COSY-GO.

The linear dominated bounder is based on the fact that, for Taylor models with sufficiently small remainder bound, the linear part of the Taylor model dominates the behavior; this is also the case for range bounding. The linear dominated bounder utilizes the linear part as a guideline for iterative domain reduction to bound Taylor models. Around an isolated interior minimizer, the Hessian of a function f is positive definite, so the purely quadratic part of a Taylor model (P, I) which locally represents f, has a positive definite Hessian matrix H. The quadratic fast bounder provides a lower bound of a Taylor model cheaply when the purely quadratic part is positive definite. More details on polynomial bounders are given in [Mak05].

COSY-GO [Ber06b, Arm10b] is a branch-and-bound optimization code employing local domain reduction techniques exploiting the bounding performances assured by TM methods. Should the global minimum of a sufficiently regular scalar function f on a given domain $A \subseteq \mathbb{R}^m$ wished to be evaluated, the algorithm starts with an initial value for the global optimum, the *cutoff* value, and then proceeds on analyzing at each step a subdomain for possible elimination or reduction. At each step the following tasks are performed

1. A rigorous lower bound l of the objective function is obtained on the subdomain of interest using various bounding schemes hierarchically with the hope of showing that l lies above the already established cutoff value, which will allow to eliminate of the subdomain. A first assessment is made whether the remainder bound of the Taylor model at hand is sufficiently small; if it is not, then the underlying function exhibits too much detail for modeling by local estimators, and the subdomain is split in the direction of fastest change of the function.

2. If the remainder bound is sufficiently small, as a first test the polynomial part of the objective function is evaluated in interval arithmetic. When it fails to eliminate the box, the LDB bounder is applied. If it also fails to eliminate the box, and if the quadratic part of the polynomial representation of the objective function P is positive semi-definite, the QFB bounder is applied.

3. If the just studied subdomain of interest cannot be eliminated, but is seen to have a lower bound close to the current cutoff values, domain reduction techniques are brought to bear based on the LDB and QFB algorithms to reduce the subdomain in size. Once these methods are applicable, they will allow to cut the subdomain of interest and rapidly reduce the active volume.

4. The cutoff value is updated using various schemes. At first, the linear and quadratic parts of the Taylor polynomial are utilized to obtain a potential cutoff update. In particular, if the quadratic part of the polynomial is positive definite, the minimizer of the quadratic polynomial is tested. If the quadratic part is not positive definite, the minimizer of the quadratic part in the direction of the negative gradient is tested. For objective functions of nontrivial cost, as in the example at hand, also more sophisticated local searches within and near the current subdomain may be carried out.

The algorithm continues to reduce and examine the domain until the minimum dimension allowed is reached. The result of the optimization is the validated enclosure of the minimum of the problem.

COSY-GO has been used in this work with the aim of computing Minimum Orbital Intersection Distance (MOID) between a Keplerian orbit and a perturbed orbit. To achieve this result, the square distance between two points belonging to the one of the two orbits respectively was used as objective function. In the following chapter this application is described and the most relevant results are reported.

3

High-order orbit propagation using Differential Algebra

The propagation of spacecraft trajectories and the associated uncertainties play an important role in the field of Space Situational Awareness. The procedures and the algorithms for orbit determination, conjunction identification, and risk assessment all depend on orbit propagation. The more accurately the trajectory is described the more reliable the performed analysis will be. To this aim the more important orbital perturbations must be taken into account by the selected orbit propagator, according to the current orbital regime. As an example, the Moon's gravitational force plays an important role for satellites in GEO, whereas its effects are nearly negligible for a satellite at a really low altitude, where the atmospheric drag is by far the most important perturbing force.

In addition, the time required to perform an orbit propagation must be taken into account. Modeling more perturbations than the ones required will result in longer simulations, producing only minor changes in the final position or trajectory. Moreover, the additional computational effort is magnified when a large set of objects has to be propagated: this is the case of conjunction identification where, on a daily basis, the close encounter between a satellite and all orbiting objects must be computed. From the Engineer's point of view it is thus important to select (or design) the orbit propagator for a certain application by considering the requirements on accuracy and computational effort.

Three different approaches exists for orbit propagation of satellites: *analytical*, *numerical*, and *semi-analytical*. Analytical theories, also known as *general perturbations*, use methods such as variation of parameters, averaging techniques, and canonical transformation to simplify the equation of motion when perturbations are present, since no closed form solution of the motion can be obtained. With this approach the orbital elements can be expressed as functions of time, hence reducing the computation of the orbital state to an evaluation of known functions, drastically reducing the computational effort. However, simplification are necessary to obtain an analytical solution and, therefore, some coupling effects are sometimes neglected or certain perturbations are not considered. As a consequence, the propagation error can rapidly increase with propagation time.

The numerical methods, also referred to as *special perturbations*, consist in integrating numerically the equation of motion. The advantage of these approaches is that all secular and periodic perturbations are retained and coupling effects are automatically considered. Besides being, in general, more accurate than analytical methods the numerical integration of the perturbed equations of motion requires longer time.

Semi-analytical methods have been developed to combine the speed of analytical methods and the accuracy of special perturbations. The short periodic contributions are separated from long-periodic and secular effects, obtaining a system where three groups of equations are present: 1) equation of motion for mean elements; 2) equations for short-period periodic coefficients; 3) Fourier series (which allows the construction of short periodic motion in the elements given short-periodic coefficients). This enables the use of larger time steps (e.g. days) to integrate the equations of motion of the mean elements, thus reducing the time required for an integration. Semi-analytical methods are often used to study the long-term evolution of the space debris environment, space debris clouds resulting from explosions or fragmentation, and stability of graveyard orbits.

In general, given the initial set of orbital elements $\boldsymbol{e}^0$ at epoch t^0, the state of a body at time t can be expressed as

$$\boldsymbol{x} = \boldsymbol{f}(\boldsymbol{e}^0, t), \tag{3.1}$$

where $\boldsymbol{x} = (\boldsymbol{r}, \boldsymbol{v})$ and $\boldsymbol{f}$ is a nonlinear function that maps the initial orbital elements in the final state. Thus, $\boldsymbol{f}$ includes both coordinate transformations and the forward propagation of the state up to time t. In a DA environment it is thus possible to obtain a polynomial approximation of this nonlinear function for any orbit propagation method. As a consequence, the evolution of orbit state uncertainty can be studied and high-order effects are captured using an expansion order $k > 1$ [Val13c]. The availability of these polynomial maps is used as a starting point for the algorithms developed in this work, in particular for conjunction identification and collision probability computation.

In this chapter the orbit propagators used throughout this work are described. In Section 3.1 two analytical solution for satellite motion are introduced. Section 3.1.3 illustrates the procedure to compute the state transition matrix using the DA automatic differentiation techniques. Then, in Section 3.2 a numerical propagator tailored for Earth orbiting object, written in COSY INFINITY, is described.

3.1 Analytical orbit propagation

In this section two analytical solutions are briefly described. The Keplerian propagator used in 6.3.1 to validate the DA-based collision probability algorithms is first described, Then SGP4/SDP4, used in Chapter 5 to perform conjunction identification, is introduced. The section ends with the description of the procedure to compute the state transition matrix and propagate the covariance matrix, tailored for SGP4/SDP4 with uncertainty in the Radial Transverse Normal (RTN) frame.

3.1.1 Universal variables formulation of Keplerian motion

The solution to two-body problem is formulated using universal variables, which may be used for elliptical, parabolic, and hyperbolic orbits [Her65, Der96]. Given position $\boldsymbol{r}_0$ and velocity $\boldsymbol{v}_0$ at reference epoch t_0, the position and velocity evolve according to the equation of motion

$$\frac{d^2\boldsymbol{r}}{dt^2} = -\frac{\mu}{r^3}\boldsymbol{r}. \tag{3.2}$$

An analytic solution of the form

$$\boldsymbol{r} = f(t, \boldsymbol{r_0}, \boldsymbol{v_0})\boldsymbol{r_0} + g(t, \boldsymbol{r_0}, \boldsymbol{v_0})\boldsymbol{v_0} \tag{3.3}$$

$$\boldsymbol{v} = \dot{f}(t, \boldsymbol{r_0}, \boldsymbol{v_0})\boldsymbol{r_0} + \dot{g}(t, \boldsymbol{r_0}, \boldsymbol{v_0})\boldsymbol{v_0} \tag{3.4}$$

is obtained by using the universal variable X, i.e. the universal anomaly or generalized anomaly. Kepler's equation becomes

$$r_0 X\left(1 - \alpha X^2 c_3(\alpha X^2)\right) + \frac{\boldsymbol{r}_0 \cdot \boldsymbol{v}_0}{\sqrt{\mu}} X^2 c_2(\alpha X^2) + X^3 c_3(\alpha X^2) - \sqrt{\mu}\,(t - t_0) = 0, \tag{3.5}$$

where α is computed using vis-viva equation

$$\alpha = \frac{2}{r_0} - \frac{v_0^2}{\mu}$$

and $c_2(\alpha X^2)$ and $c_3(\alpha X^2)$ are Stumpff's functions, i.e. generalizations of sine and cosine. Once solved for X Kepler's equation (e.g. using Newton's method using a proper initial guess X_0 for the universal anomaly) the functions f, g, and their derivatives are readily obtained as

$$f = 1 - \frac{X^2 c_2}{r_0} \qquad \dot{f} = X\left(\alpha X^2 c_3 - 1\right)\frac{\sqrt{\mu}}{r r_0}$$

$$g = (t - t_0) - \frac{X^3 c_3}{\sqrt{\mu}} \qquad \dot{g} = 1 - \frac{X^2 c_2}{r}.$$

By substituting f and g in Eq. (3.3) and, similarly, $\dot{f}$, and $\dot{g}$ in Eq. (3.4) the position and velocity of the spacecraft at time t are obtained.

The DA implementation of the analytical solution of the two-body problem is obtained by initializing as DA variables the initial position and velocity and, in case, time. Kepler's equation (3.5) can be solved by means of a standard Newton's method or using the procedure for the solution of parametric implicit equations described in

Section 2.3.

The accuracy of the polynomial expansion of the final position $\boldsymbol{r}_f(\delta\boldsymbol{r}_0, \delta\boldsymbol{v}_0)$ with respect to a variation of the initial position components on the equatorial plane is given in Figure 3.1. A regular grid is defined on the area of the equatorial plane IJ bounded by the intervals $\pm 3\sigma$ and centred at the reference initial position components r_I and r_J. Each node of the grid represents a set of initial conditions that can be propagated to the final time t using the universal variables solution described above. The resulting final position is then compared with the one obtained by evaluating the polynomial approximation $\boldsymbol{r}_f(\delta\boldsymbol{r}_0, \delta\boldsymbol{v}_0)$. Even after 100 revolutions the error of the expansion of the final position remains below 10^{-4} km for the considered initial uncertainties: this is the largest error that is indeed observed in Figure 3.1(b) and is obtained only for displacement from the reference position close to 3σ in both components.

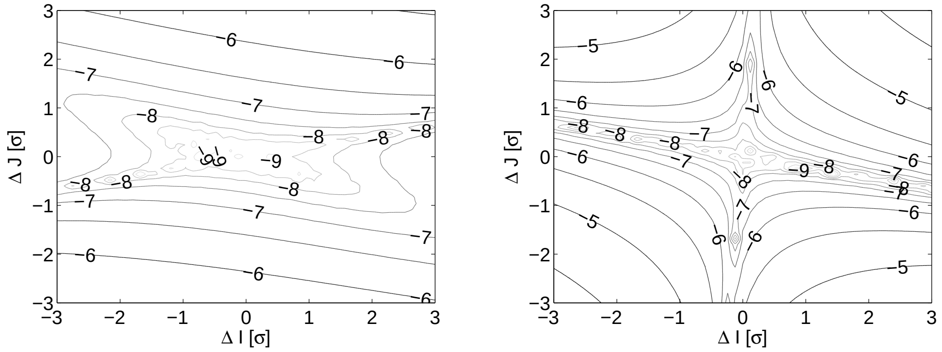

(a) Contour lines of the common logarithm of the position error in km after $t = 37.75$ revolutions.

(b) Contour lines of the common logarithm of the position error in km after $t = 100$ revolutions.

Figure 3.1. Fifth order expansion of the final position of satellite AGILE with respect to uncertain initial position $\boldsymbol{r}_0$ and velocity $\boldsymbol{v}_0$. Considered standard deviations σ at reference epoch on the equatorial plane are $\sigma_I = 16$m and $\sigma_J = 46$m.

3.1.2 SGP4/SDP4

The Simplified General Perturbations #4 (SGP4) model is one of the orbit propagators developed during the 1970s by NORAD and U.S. Air Force Space Command. The source code of the model was made public at the end of the 1980s [Hoo80] and nowadays it is one of the most used propagators for Earth orbit satellite. The code is optimized to work with TLE released by the USSTRATCOM. The USSTRATCOM also maintains a catalogue containing TLEs for all resident space objects together with launch (and/or decay) date information which is available to public from the Space-Track website[1].

---

[1] www.space-track.org

The SGP4 model is tailored for orbits whose period is less than 225 minutes and accounts for secular effects of air drag, long- and short-period periodic effects of zonal harmonics from J_2 to J_5. For "deep-space" satellites, i.e. those with orbital period of more than 225 minutes, the Simplified Deep Space Perturbations #4 (SDP4) was developed, adding the lunar and solar perturbations and some geopotential resonance effects for orbits with periods of 12 and 24 hours with tesseral harmonics $J_{2,2}$, $J_{3,1}$, and $J_{3,3}$. The two models were later unified and the combined code is usually referred to as SGP4/SDP4. A complete documentation of all equations, including the deep space portion, is found in [Hoo04] and a comprehensive collection of bug fixes and modifications to the code are in [Val06]. The SGP4/SDP4 code has been rewritten in COSY INFINITY following the details presented in these two papers, replicating the "official" version of the code (as those downloadable from CelesTrak website[1]).

The accuracy of the SGP4/SDP4 model greatly depends on the orbit type and can vary from object to object. The epoch uncertainty for LEO and Navigation Satellite Orbit (NSO) satellites is about 1 km, 1-2 km for MEO, between 2 and 4 km for GEO and 6-8 km for GTO and HEO [Val13a]. The uncertainty can rapidly increase with propagation time, reaching tens of kilometres after a few days. Thus, the confidence on SGP4/SDP4 propagation is guaranteed only in a time interval of a few days in the surrounding of the TLE epoch. In addition, no information on orbital uncertainty is provided with TLEs and the presence of manoeuvre after the TLE epoch can result in considerable error in the propagated orbital state [Val12].

For SGP4/SDP4 algorithm, $\boldsymbol{e}^0 = (t_0, n_0, e_0, I_0, \omega_0, \Omega_0, M_0, B^*)$ is the vector of mean elements included in the TLE, where t_0 is the epoch time, n_0 is the mean motion, e_0 the eccentricity, I_0 the inclination, ω_0 the argument of perigee, Ω_0 the right ascension of the ascending node, M_0 the mean anomaly, and B^* is the atmospheric drag coefficient. The procedure to compute the state $\boldsymbol{x} = (\boldsymbol{r}, \boldsymbol{v})$ is more complicated with respect to Keplerian assumption and it can be summarized in

1. Recover Brouwer mean motion from the Kozai mean motion included in the TLE.
2. Update orbital elements at time t adding secular effects of Earth's zonal harmonics and luni-solar perturbations.
3. Compute resonance effect of Earth's gravity through numerical integration.
4. Add long-period periodic perturbation due to Moon's, Sun's, and Earth's gravity.
5. Solve Kepler's equation for $U = E + \omega$.
6. Update for short-periodic effects of Earth's gravity.
7. Compute $\boldsymbol{r}$ and $\boldsymbol{v}$ from the updated Keplerian elements.

---

[1] http://celestrak.com/software/vallado-sw.asp

Note that although the evaluation of $\boldsymbol{x}$ is more complicated for the SGP4/SDP4 case, both analytical approximations require explicit algebraic computations (including also the Euler-Maclaurin scheme for the resonance effects for SGP4/SDP4) with the only exception of the solution of Kepler's equation. For standard floating point computation this is not an issue (with the exception of some cases as described in [Val06]), as the solution can be found by few iterations of a Newton method. When validated computations are necessary, the problem becomes much more complex and it requires an ad-hoc algorithm presented in [Arm12].

The accuracy of the expansion of the final state obtained with the DA implementation of SGP4/SDP4 with respect to time is here analyzed for various expansion order. In Figure 3.2 the expansion is performed after one revolution from the initial epoch for orders $n = 1, 3, 5$. The polynomial approximation of the final position and velocity is then evaluated on a time grid centred around the reference epoch $t = T$, where T is the orbital period of the satellite and compared with a SGP4/SDP4 propagation up to the same final time. Around the reference point of DA expansion, i.e. $t = T$, the error between standard and DA SGP4/SDP4 evaluations is really small, namely comparable to machine precision. The error then increases when moving away from the reference epoch. The error becomes smaller for both position and velocity for increasing expansion order n. In particular, the error remains below 1km and 10^{-3}km/s inside the interval $[-0.1, 0.1]T$ for a fifth-order expansion.

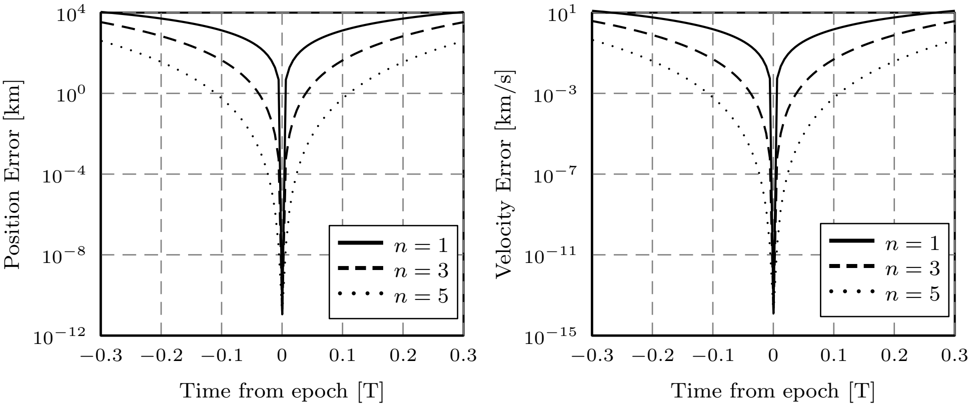

(a) Position error for $t \in T + [-0.3, 0.3]T$. **(b)** Velocity error for $t \in T + [-0.3, 0.3]T$.

Figure 3.2. Expansion with respect to time of position and velocity at time $t = T$ using SGP4/SDP4 for different expansion orders n.

The analysis is repeated considering an expansion around $t = 50T$. The same considerations of Figure 3.2 can be applied to Figure 3.3.

The Taylor approximation of the final state with respect to the initial position and velocity can be used to quickly assess the high-order effects resulting from uncertainty propagation. As an example, the orbit of the LEO satellite AGILE is considered. The orbit, plotted in Figure 3.4 is almost circular and nearly equatorial. For illustration

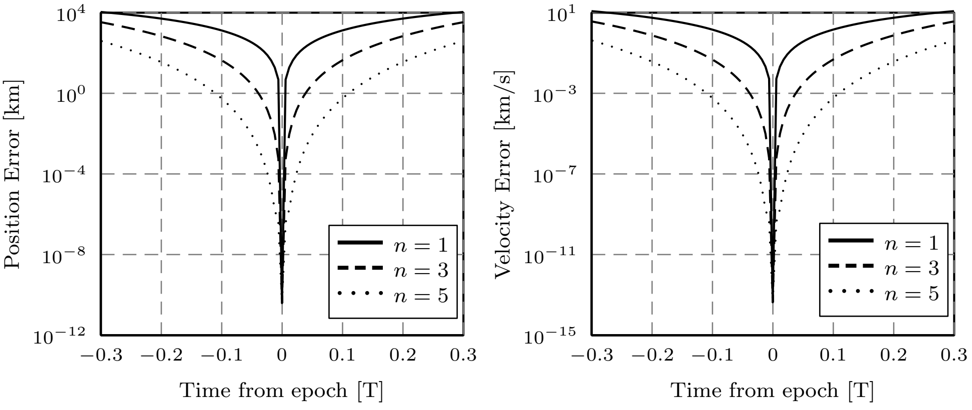

(a) Position error for $t \in 50T + [-0.3, 0.3]T$. **(b)** Velocity error for $t \in 50T + [-0.3, 0.3]T$.

Figure 3.3. Expansion with respect to time of position and velocity at time $t = 50T$ using SGP4/SDP4 for different expansion orders n.

purposes, only uncertainties on the two position components lying on the equatorial plane are considered. A set of samples is generated at the reference epoch from a multivariate Gaussian distribution, by considering a diagonal covariance matrix with standard deviations $\sigma = 100$km. Please note that such a high uncertainty is chosen only to highlight non-linear effects resulting from propagation. The positions on the equatorial plane of the virtual objects (i.e. the samples) at four different time

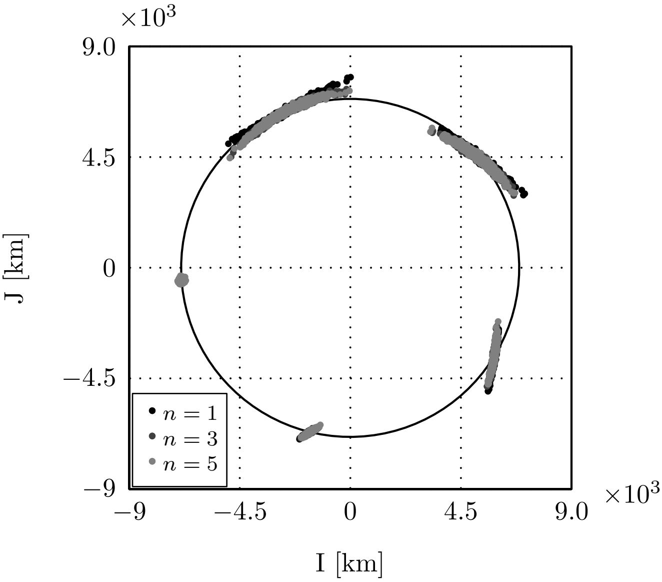

Figure 3.4. Uncertainty propagation using different expansion orders n with SGP4/SDP4 for satellite AGILE

instants are then computed evaluating the polynomial expansion of order $n = 1, 3, 5$ at those times and plotted. The black dots refer to expansion order $n = 1$, whereas dark gray and gray dots are associated to $n = 3$ and $n = 5$ respectively. It can be observed how the higher order expansion can capture the dispersion of the samples around the trajectory, that results in a non-Gaussian distribution that resembles a “boomerang”. Instead, when the first-order expansion is used the samples are still normally distributed. It is worth noting that the fifth and third order clouds are almost indistinguishable so no additional information is retrieved in this case by using order $n = 5$.

3.1.3 State transition matrix computation

The covariance matrix can be easily computed at any propagation time by means of the automatic differentiation techniques made available by COSY INFINITY. In this section the procedure to compute the coefficients of the state transition matrix is described. The method is general and can be applied to compute the partial derivatives of any set of orbital parameters with respect to another set of initial orbital elements.

The first step consists in choosing an orbital element set and perform a DA initialization of these uncertain variables. As an example, consider an SGP4/SDP4 propagation with uncertainty of TLE expressed in the RTN reference frame [Kli05, Flo09b]. According to Figure 3.5, the first unit vector of the reference frame $\hat{\boldsymbol{r}}$ is aligned with the position vector $\boldsymbol{r}$, the third unit vector $\hat{\boldsymbol{n}}$ is perpendicular to the orbital plane, and the second unit vector , or transverse unit vector, $\hat{\boldsymbol{t}}$ completes the frame. Note that this unit vector is aligned with satellite velocity only for circular orbits.

Since TLE and SGP4/SDP4 are written in classical mean orbital elements, the relations between RTN state vector and mean Keplerian orbital elements is found through the following steps:

1. Compute TEME state vector $\boldsymbol{x} = [\boldsymbol{r}; \boldsymbol{v}]$ at TLE epoch. This is achieved with

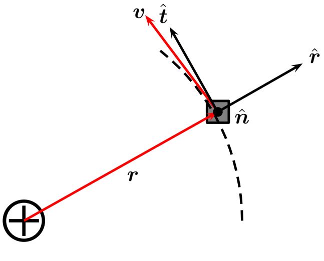

Figure 3.5. RTN reference frame, radial $\hat{\boldsymbol{r}}$, transverse $\hat{\boldsymbol{t}}$, and normal $\hat{\boldsymbol{n}}$ vectors.

an evaluation of SGP4/SDP4 at time 0.0

$$[\delta \boldsymbol{x}_0] = [\mathcal{M}_{\mathrm{TEME}}]\,[\delta \boldsymbol{\kappa}_0]\,, \tag{3.6}$$

where $\boldsymbol{\kappa}_0$ is the classical orbital element vector $\boldsymbol{\kappa} = \{a, e, I, \Omega, \omega, M\}^T$

2. Convert TEME vectors into ECI J2000 vectors, retrieving

$$[\delta \boldsymbol{x}_{0,\mathrm{ECI}}] = [\mathcal{M}_{\mathrm{ECI}}]\,[\delta \boldsymbol{\kappa}_0] \tag{3.7}$$

3. Transform ECI J2000 state vector into RTN orbital frame, obtaining

$$[\delta \boldsymbol{x}_{0,\mathrm{RTN}}] = [\mathcal{M}_{\mathrm{RTN}}]\,[\delta \boldsymbol{\kappa}_0] \tag{3.8}$$

This map provides the RTN initial state deviation as function of classical orbital elements variation.

4. Invert the DA map with DA tools, retrieving

$$[\delta \boldsymbol{\kappa}_0] = [\mathcal{M}_{\mathrm{RTN}}]^{-1}\,[\delta \boldsymbol{x}_{0,\mathrm{RTN}}] \tag{3.9}$$

The obtained DA map describes the deviation of the mean orbital elements used in SGP4/SDP4, as function of deviation from position and velocity in RTN frame. By plugging this transformation in the SGP4/SDP4 initialization phase, it is possible to compute the object position $\boldsymbol{r}_f$ and velocity $\boldsymbol{v}_f$ in TEME reference frame as a function of initial uncertainties by simply evaluating the COSY INFINITY implementation of SGP4/SDP4 at the desired time t. It is then straightforward to assembly the state transition matrix by computing the first derivatives with respect to the initial uncertain variables within the DA framework

$$\boldsymbol{\Phi}(t_0, t) = \begin{bmatrix} \dfrac{\partial \boldsymbol{r}_f}{\partial \boldsymbol{r}_{0,\mathrm{RTN}}^T} & \dfrac{\partial \boldsymbol{r}_f}{\partial \boldsymbol{v}_{0,\mathrm{RTN}}^T} \\ \dfrac{\partial \boldsymbol{v}_f}{\partial \boldsymbol{r}_{0,\mathrm{RTN}}^T} & \dfrac{\partial \boldsymbol{v}_f}{\partial \boldsymbol{v}_{0,\mathrm{RTN}}^T} \end{bmatrix}. \tag{3.10}$$

The covariance matrix $\boldsymbol{C}_0$ at reference epoch t_0 is then mapped at time t by means of

$$\boldsymbol{C}(t) = \boldsymbol{\Phi}(t_0, t)\; \boldsymbol{C}_0(t_0)\; \boldsymbol{\Phi}^T(t_0, t). \tag{3.11}$$

3.2 Numerical propagator AIDA

The numerical propagator AIDA (Accurate Integrator for Debris Analysis) is a numerical propagator tailored for space debris analysis within a DA framework. The perturbations included in AIDA are the geopotential acceleration, atmospheric drag, solar radiation pressure, and third body gravity. Details on the modeling of these sources of perturbation are given in the following. For the numerical integrations presented in this work, a DA version of the Dormand-Prince (8-th order solution for propagation, 7-th order solution for step size control) implementation of the Runge-Kutta scheme is used. A weighted norm of the resulting Taylor polynomials is computed within the step size control procedure, where the weights are selected to scale the polynomial variables by the size of their initial uncertainty. The propagator AIDA is used in this work to perform high-order uncertainty propagations, the expansions of time and distance of closest approach (see Sect. 5.3), and orbit determination.

In the following some details on the modeled perturbations are given.

3.2.1 Geopotential acceleration

The acceleration due to Earth's gravity potential can be written as

$$\boldsymbol{a}_{\text{Harm}} = \boldsymbol{\nabla} \frac{GM_E}{r} \sum_{n=0}^{\infty} \sum_{m=0}^{n} \frac{{R_E}^n}{r^n} \overline{P}_{nm} \left(\sin\phi\right) \left(\overline{C}_{nm} \cos\left(m\lambda\right) + \overline{S}_{nm} \sin\left(m\lambda\right)\right) , \quad (3.12)$$

where GM_E is Earth's gravitational constant, R_E is Earth's radius, $\overline{C}_{nm}$ and $\overline{S}_{nm}$ are the normalized geopotential coefficients, $\overline{P}_{nm}$ are the normalized associated Legendre functions, r is the object distance from the centre of the Earth, and ϕ and λ are the geocentric latitude and longitude.

The default gravitational model selected for the numerical propagator is EGM2008 [Pav12]. The model combines gravitational information from GRACE with surface data and is complete to spherical harmonic degree and order 2160. The field model was downloaded from the International Centre for Global Earth Models (ICGEM) website [1].

The default degree n and order m in Eq. (3.12) are set to 10 for the simulations performed in this work using Accurate Integrator for Debris Analysis (AIDA).

3.2.2 Atmospheric drag

The perturbing acceleration due to atmospheric drag on a satellite is

$$\boldsymbol{a}_{\text{Drag}} = -\frac{1}{2} C_D \frac{A}{M} \rho \, v_r \boldsymbol{v}_r , \quad (3.13)$$

where C_D is the drag coefficient, A is the satellite's cross-sectional area and M its mass, $\boldsymbol{v}_r$ is the satellite velocity relative to the atmosphere , and ρ is the atmospheric density at satellite's position.

The drag coefficient and area to mass ratio are often grouped in a parameter

---

[1] http://icgem.gfz-potsdam.de/ICGEM/

known as ballistic coefficient, B, defined as

$$B = C_D \frac{A}{M}. \tag{3.14}$$

The atmospheric density is computed using the Naval Research Laboratory's Mass Spectrometer and Incoherent Scatter Radar of year 2000 (NRLMSISE-00) model [Pic02]. This model includes the anomalous oxygen component together with Helium, atomic and molecular Oxygen, atomic and molecular Nitrogen, Argon, and Hydrogen. The model requires as inputs the solar and geomagnetic activity, geodetic altitude and latitude, longitude, year, day, and time of day in UT. Solar and geomagnetic data are read from up-to-date space weather files that are automatically downloaded from CelesTrack [1].

3.2.3 Third body perturbations

The gravitational attraction of the Sun and the Moon is the main source of perturbation among all third bodies. The perturbing acceleration acting on the orbiting object is given by

$$\boldsymbol{a}_{\text{3rdB}} = GM_{\text{3rdB}} \left(\frac{\boldsymbol{s}}{s^3} - \frac{\boldsymbol{r}_{\text{3rdB}}}{{r_{\text{3rdB}}}^3} \right), \tag{3.15}$$

where the relative position of the satellite, $\boldsymbol{s}$, is defined as

$$\boldsymbol{s} = \boldsymbol{r}_{\text{3rdB}} - \boldsymbol{r}_{\text{obj}}, \tag{3.16}$$

where $\boldsymbol{r}_{\text{3rdB}}$ and $\boldsymbol{r}_{\text{obj}}$ are the position vectors of the third body and the object, respectively. The position of the third bodies, i.e. the Sun and the Moon, are computed using NASA JPL's DE405 ephemeris [Sta98].

3.2.4 Solar radiation pressure

The absorption or reflection of photons exerts a small force on the satellite. This perturbing acceleration depends on the object area and on the mass as well as on the intensity of the solar flux Φ, that is approximately 1367 W/m^2 at 1 AU. The solar radiation pressure, P_S, is given, assuming full absorption, by

$$P_S = \frac{\Phi}{c} = \frac{L_S}{4\pi r^2 c}, \tag{3.17}$$

where the speed of light is indicated as c, the distance from the Sun as r, and L_S is the solar luminosity.

The information regarding shape and attitude of operative satellites are usually available, at least for satellite owners and operators. Unfortunately, in general, this

---

[1] `http://celestrak.com/SpaceData/SpaceWx-format.asp`

is not the case for space debris. Therefore, the debris is modeled as a sphere in this work, removing the need for attitude information. The resulting acceleration, which is in the direction of the Sun-satellite vector, is equal to

$$\boldsymbol{a}_{\mathrm{SRP}} = \frac{L_S}{4\pi\, c}\,\frac{A}{M}\,(1+\varepsilon)\,\frac{\boldsymbol{r}_{\mathrm{obj}} - \boldsymbol{r}_S}{||\boldsymbol{r}_{\mathrm{obj}} - \boldsymbol{r}_S||^3}\,\nu, \tag{3.18}$$

where A is the debris area and M its mass, ε is body reflectivity, and ν is the shadow function. The position of the Sun, $\boldsymbol{r}_S$, is in ECI J2000 reference frame and is obtained from JPL's DE405 ephemeris. The acceleration $\boldsymbol{a}_{\mathrm{SRP}}$ decreases as Sun's distance increases.

Area-to-mass ratio can be estimated from the object ballistic coefficient, assuming a drag coefficient $C_D = 2.2$. The reflectivity ε, if not otherwise specified, is set to 0.31. This value lies in the range typical of materials used for satellite construction, i.e. $[0.2; 0.9]$ [Mon00].

The shadow function ν is zero when the object is in shadow, one when it is in light, and varies within these two values when the object is in penumbra. The value of this function is computed by comparing the satellite position with the one of the occulting body and the Sun [Mon00]. Three options to model the shadow of an occulting body are implemented in AIDA: no shadow, cylindrical shadow, and dual-cone shadow. Dual-cone shadow model is the default model.

3.3 High-Order Numerical Propagation

In this section the performances of the numerical propagator AIDA are assessed, focusing on the computational cost and accuracy of the expansion of the flow, aimed at the selection of the expansion order.

The six objects listed in Table 3.1 (either active spacecraft or debris) are considered for these analyses. The first three objects are classified as LEO objects, since their altitude is below 2,000 km. In particular the altitude of the first two objects is comprised between 750 and 800 km, whereas for object 3 it is approximately 1400 km. Object 4 is on an HEO since it has an altitude of 1340 km at its perigee and at its apogee is at 5700 km above the Earth's surface. Objects 5 and 6 instead are on a GEO since their orbit is almost circular, with a low inclination, and an orbital period of nearly 24 hours.

The initial conditions for the numerical propagation are computed from TLEs, using the procedure described in [Val12]. The method consists of performing an Orbit Determination (OD) process on a set of pseudo-observations generated over a certain time span. In our case we generated one measure, i.e. position and velocity of the satellite, every hour over a time span of 24 h, centred at the reference epoch of the selected TLE. The resulting state vectors were then transformed from TEME of epoch to ECI J2000 [Val01], that is the reference frame of AIDA. A nonlinear least

ID	Sat. No.	Sat. Name	a [km]	e [-]	I [deg]	Orbit
1	11510	COSMOS 1125	7161	1.15E-3	74.04	LEO
2	21574	ERS 1	7149	3.49E-3	98.25	LEO
3	20237	COSMOS 2043	7787	4.19E-4	82.57	LEO
4	23820	OPS 0856 DEB	9895	2.20E-1	87.62	HEO
5	36744	COMS 1	42165	7.88E-5	0.01	GEO
6	28194	RADUGA 1-7	42166	1.21E-4	5.28	GEO

Table 3.1. Selected objects

square fit of the pseudo-observations was then performed using AIDA, to compute the initial position and velocity of the object, and its ballistic coefficient and area-to-mass ratio for Solar Radiation Pressure (SRP). The (6×6) covariance matrix of initial position and velocity was also obtained after this process.

The values of initial conditions, covariance matrices, and ballistic coefficients of the objects used for the following analyses are reported in Appendix A.1. All computations are performed on an Intel Core i5 2500 @3.30GHz, 8Gb RAM processor running Sabayon Linux (kernel version 3.11.0).

3.3.1 Performances of the DA numerical propagation

The selection of the expansion order requires a trade-off between accuracy and computational time. This analysis is performed by propagating the objects for a time window of 7 days (which is the time window for conjunction identification) with uncertainties on initial states compatible with the estimated covariance matrices.

The computational time required for each run of AIDA is reported in Table 3.2 for zeroth (i.e., pointwise integration) to fourth order expansions. Only one test case for each orbital regime is given, since similar results are obtained for objects in similar orbits. The computational time required to propagate each object for one orbit is also given in Table 3.2. It can be observed that the computational time per revolution is

Order	Computational time [s]			Comp. time per rev. [s]		
	LEO	HEO	GEO	LEO	HEO	GEO
0	63.53	37.65	6.45	0.63	0.61	0.91
1	98.81	55.87	9.38	0.98	0.90	1.33
2	176.31	98.19	15.85	1.75	1.59	2.26
3	443.77	234.87	41.38	4.41	3.80	5.90
4	1391.02	690.77	110.80	13.84	11.19	15.79

Table 3.2. Computational costs for 7 days propagation and for each revolution with AIDA for different expansion orders

nearly the same for each of the three orbits for a given order of truncation. The total computational time for 7 days propagation clearly depends on the orbital period of the orbits, i.e. on the number of orbital revolutions completed in the considered time span.

It is worth highlighting that the computational time of pointwise integrations is not the main focus of the following analysis, since it depends on the details of the implementation of the dynamical model, programming language, compiler, and machine. The significant figure to be investigated is the time of a k-th order computation compared to a pointwise one. For this reason, the computational times can be normalized using the pointwise integration as reference value. The ratios are plotted, for each orbital regime, in Figure 3.6. It is clear that the computational time increases exponentially with the order, but it is remarkable that a fourth order expansion is roughly only ten times slower than a pointwise integration.

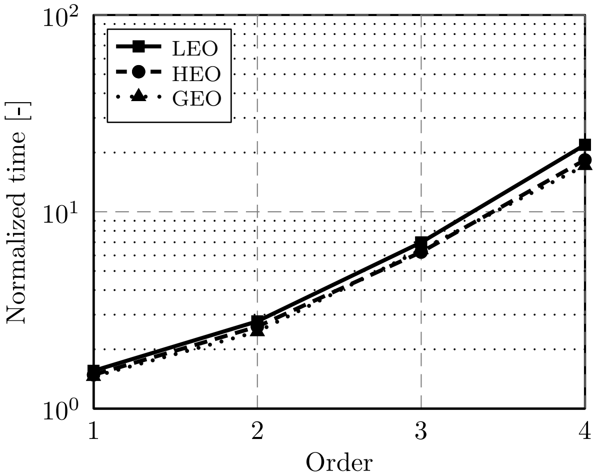

Figure 3.6. Normalized computational time for three classes of orbits

The accuracy of maps (5.9) with respect to uncertainties in the initial states (thus neglecting variation in the final time) is reported in Figure 3.7. The final positions are computed by evaluating the polynomial

$$[\boldsymbol{r}_f] = \boldsymbol{r}_f + \mathcal{M}_{\boldsymbol{r}_f}\left(\delta\boldsymbol{r}_0, \delta\boldsymbol{v}_0\right), \tag{3.19}$$

which is obtained by the DA-based integration in AIDA for a given time window up to 7 days. Then, they are compared with pointwise propagations of the same perturbed initial states. For each of the three orbital regimes 10^9 samples were generated considering the normalized full state covariance matrix obtained with the OD process described in Sect. 3.3. Since the accuracy of the map decreases with the distance of the sample from the reference point, the 100 samples with the largest displacement from the reference position and velocity were selected. This represents an

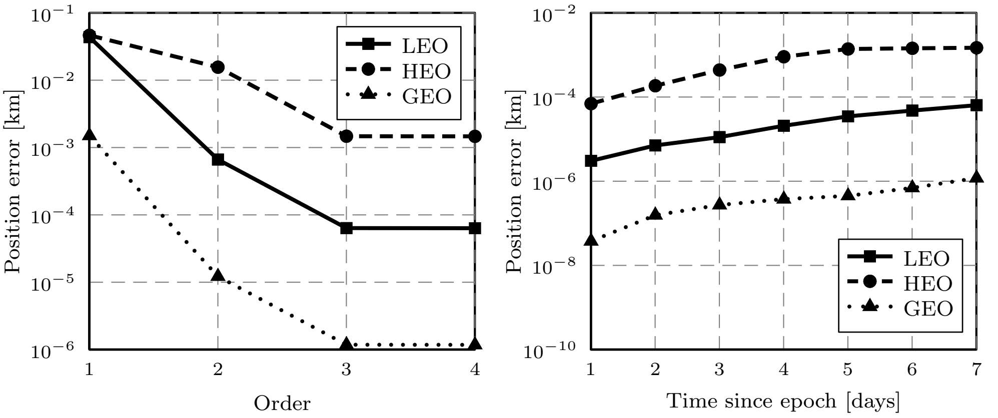

(a) Final position error versus DA expansion order

(b) Final position error versus propagation time using order $k = 3$

Figure 3.7. Accuracy of the DA map of final position $\boldsymbol{r}_f(\boldsymbol{r}_0, \boldsymbol{v}_0)$ obtained with AIDA against DA expansion order and propagation time

accurate estimation of the worst cases that can be encountered if collision probability is computed using Monte Carlo based on the polynomial approximation of the final position. Realistically, at least one billion samples would be required to estimate a collision probability of 10^{-6} with a reasonable confidence level [Dag00].

The maximum differences between Taylor polynomials evaluations and pointwise integrations over a time window of 7 days are plotted in Figure 3.7(a) for different expansion orders. The error on the final position is lower for the GEO orbit, due to the lower number of revolutions, and higher for the HEO. For the latter, the reason is mainly the higher values of the states covariances and the particular environment encountered by the objects during their motion. The influence of perturbations changes along the orbit, with an increasing relative importance of atmospheric drag near the pericenter and of third body gravity and solar radiation pressure at the apogee. In addition, the area to mass ratio is the highest among the considered orbits. Note that in all cases the maximum error on position after 7 days is approximately 1 meter for the HEO, less than 0.1 m for the LEO, and 1 mm for the GEO.

To provide more insight on the expansion error, Figure 3.7(b) illustrates the maximum differences between the polynomial evaluations and pointwise integration of the final position for different propagation time using an expansion order $k = 3$.

The results of the same analysis focused on the final velocity are plotted in Figure 3.8(a) and Figure 3.8(b). The figures confirm the behaviour found for the final position. The maximum error is found again for HEO and is approximately 1 mm/s.

According to these results, a third order expansion is a good compromise between computational time and expansion accuracy for the selected test cases.

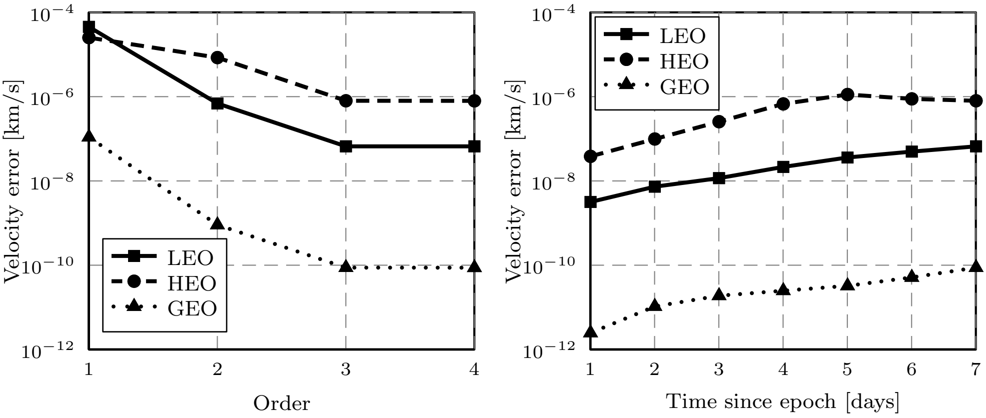

(a) Final velocity error versus DA expansion order

(b) Final velocity error versus propagation time using order $k = 3$

Figure 3.8. Accuracy of the DA map of final velocity $\boldsymbol{v}_f(\boldsymbol{r}_0, \boldsymbol{v}_0)$ obtained with AIDA against DA expansion order and propagation time

In the following analysis, the effects of orbital perturbations on the final position are studied to assess

1. the effect of the perturbations in the considered cases;
2. how well these effects are captured by the Taylor expansion.

For point 1) the final position obtained by considering the gravitational model of degree and order 10, atmospheric drag, solar radiation pressure with dual-cone shadow model, and third body perturbation from Sun and Moon is used as reference. Starting from a Keplerian orbital model (labeled as K in the figure), perturbations are gradually added and the displacement between the resulting final position and the reference value are computed. The results for a 7-day propagation are represented by the black curves in Figures 3.9(a), 3.9(b), 3.9(c). As before, the error curves are obtained considering the 100 samples with the largest displacement from the reference initial state selected from a set of 10^9 samples.

For the LEO regime, the largest effect is due to the gravitational model. The reason is that the orbital perigee is high enough to limit the effect of drag, whereas the high inclination results in a large effect of Earth oblateness. For the HEO regime no significant improvements are obtained by adding solar radiation pressure or atmospheric drag to Keplerian model. Nevertheless, the combined effects of gravitational harmonics, solar radiation pressure, and drag reduce considerably the displacement with the reference position. Even in the GEO regime, the combined effect of third body and gravitational harmonics is necessary to obtain a displacement on the final position of less than 10 km.

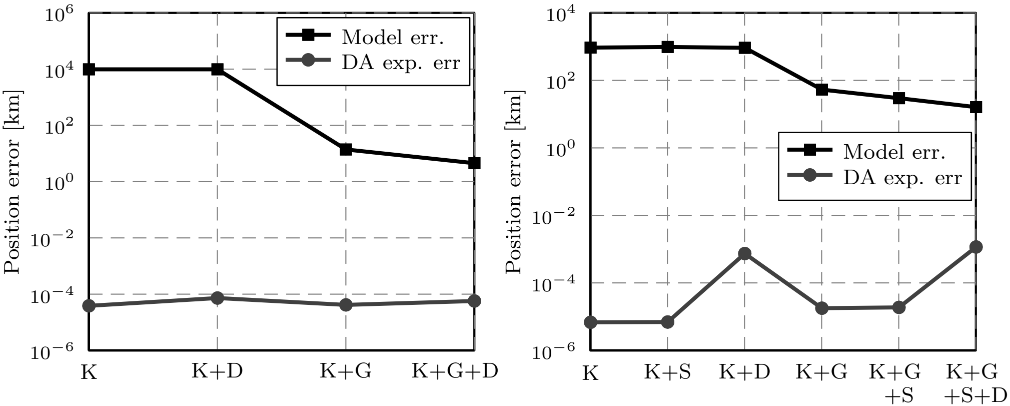

(a) LEO **(b)** HEO

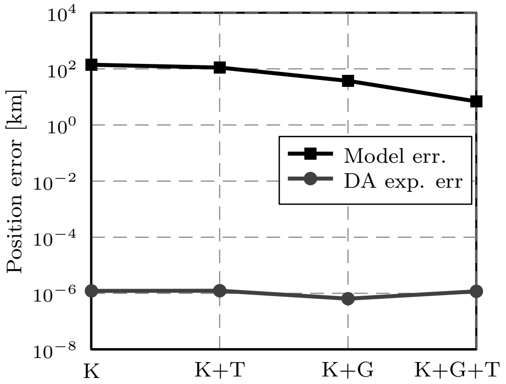

(c) GEO

Figure 3.9. Analysis of model and DA expansion error with different perturbations for the three orbital regimes for a 7-day propagation. K=Keplerian, G=Gravitational harm., D=air Drag, S=Solar rad. pressure, T=Third body

The accuracy of the DA expansions for the different orbital regimes and dynamical models is also analyzed in Figure 3.9 to highlight the contribution of the different sources of perturbation in the expansion error budget. The analysis is again obtained by comparing pointwise integrations with map evaluations for 100 virtual debris selected with the procedure used throughout this section. The curves are obtained considering 7-days propagations with an expansion order of the flow $k = 3$. For the LEO and GEO regimes the error remains almost constant with the introduction of the different sources of perturbation. In particular, the expansion error remains below 0.1 m for the LEO and is approximately 1 mm for the GEO, confirming the figures obtained previously in the position accuracy analysis with respect to order of the expansion and propagation time. For the HEO test case the largest contribution to final position error comes from atmospheric drag. The orbit is highly eccentric, with a perigee of 1340 km and an apogee of 5700 km. In addition, the area to mass ratio estimated by the OD process is 2.94 m^2/kg. After each revolution, the virtual debris will distribute along the trajectory. Due to the eccentricity of the orbit, debris can experience different air densities since they are found at different altitudes. This behaviour has to be captured by the DA expansion of the density, which is a function of altitude that in turn is a function of the current satellite position. As a result, the accuracy of the air drag perturbation is lower due to the large range of altitude that is captured by the Taylor expansion of the satellite position at each integration step within the atmosphere bound of 2,000 km. Nevertheless, the expansion error of the HEO remains always below 1 m after 7 days of propagation.

4

Orbit determination

In this chapter the Orbit Determination (OD) of space debris and satellites is studied. A regular survey and observation campaigns are performed to keep track of the evolution of the satellite and debris population. This operation is fundamental to provide up-to-date orbital elements for conjunction assessment. In addition, the uncertainty on the orbital state, usually expressed in terms of covariance matrix, is also determined with an OD process. The uncertainty information are the input required by any method for the computation of the collision probability between two objects.

Nowadays radar and telescopes are the main instruments used for the observation of space debris. The telescopes, usually equipped with a Charge-Coupled Device (CCD), are mainly used to monitor objects in GEO and GTO whereas the radars for objects in LEO [Sch07]. The USSTRATCOM operates a network of radar and optical sensors, that provides all the information required to maintain the Space-Track catalogue [Sri98].

The problem of estimating the orbital state of an Earth orbiting object is usually divided into two phases: the initial (or preliminary) orbit determination and the orbit estimation [Mon00]. In the first phase one has to deal with the linking of observations: it is indeed fundamental to associate measures belonging to a large database of uncorrelated observations taken in different days to the same object.

The classical algorithms for the initial orbit determination are based only on angles observations. The reason is that in the past most of the observations of celestial bodies were obtained with telescopes. The Laplace's and Gauss' methods, developed respectively in 1780 and 1801, use three sets of angular observations. Both methods return the position and velocity of the object. The Gibbs and Herrick-Gibbs methods extend the Gauss method to enable the computation of velocity besides object position. The Double R-iteration method, instead, is particularly suitable for spread observations, where the Gauss' and Laplace's methods fail to converge to a good solution [Esc65].

An algorithm that allows for several possible solutions also starting from a set of three angular observations was developed by Gooding. The method requires again three observations but also two initial guesses of the range for the first and third observation [Goo93].

The *admissible region* theory, developed initially for asteroids and Near-Earth Objects (NEO) preliminary orbit determination [Mil04] was extended to the case of space debris [Tom07]. Another method that uses maps of the admissible region in the Delaunay orbital element space was developed [Mar09]. Another technique correlates multiple optical observations by means of probability distributions defined by the admissible region expressed in Poincaré orbit element space [Fuj12]. Another approach exploits the multiple hypothesis filtering approach to determine how well the space debris orbits can be recovered for short-arc data in near real-time and autonomously [DM12].

Typically when more observations are available another commonly used approach for orbit determination is the least square solution. A set of correlated observations, i.e. belonging to the same object, is considered and the trajectory that minimizes the sum of the squares of the calculated observation residuals is computed [Tap04]. The advantage of the method is that any type of measurement can be processed. In addition, it can be used in the orbit estimation process and it provides the uncertainty of the estimated states.

In this chapter the least square method is used to perform the orbit determination from optical and radar measurements. It is assumed that all observations are already correlated and no initial orbit determination is required. A tailored algorithm is developed for the orbit determination of RSO using one bistatic radar measurement only. The innovative aspect of the algorithm is that it copes with a multibeaming receiver. The number of beams inside the field of view could vary and it is also insensitive from the distribution of beams in the Field Of View (FoV).

A common sensor reference frame is defined for both optical and radar instruments. This frame is defined starting from a topocentric reference frame located on the observer. This frame is the North-West-Zenith (NWZ) topocentric reference frame, where the first axis points north, the second axis towards west, and the third is the zenith direction. The azimuth Az and elevation El angles are used to define the pointing direction $\hat{\rho}$ of the instrument (telescope or antenna). The sensor frame is defined as follows: the sensor axis is supposed to be aligned with $\hat{\rho}$ and two directions

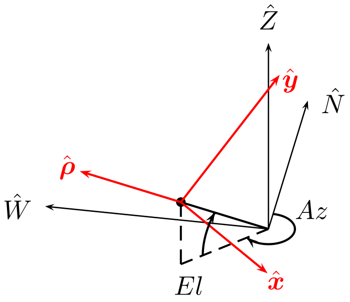

Figure 4.1. Sensor frame referred to a topocentric North-West-Zenith reference frame.

perpendicular to it are defined. The first axis $\hat{x}$ lies on a plane whose normal is the zenith and the axis $\hat{y}$ is perpendicular to both $\hat{x}$ and $\hat{\rho}$. The NWZ frame and the sensor frame are represented in Figure 4.1. The relative orientation of the sensor frame is described with Euler's angle, using the set of rotation 3-2-3. The first rotation is equal to $-Az$ around the zenith axis, the second rotation to $\pi/2 - El$ around the second axis, and the last rotation is always equal to $\pi/2$ to align the $\hat{x}$ axis as in Figure 4.1.

4.1 Optical observations

Optical observations of satellites and space debris are used to estimate positional data of satellites since the launch of Sputnik 1 in 1957. The optical techniques used are the same of NEOs and asteroids. Similarly to those objects, spacecraft and debris are not self-illuminated and, as a consequence, they can be only visible when illuminated by the Sun. Due to the relatively small size of space debris and satellites and the difficulty of obtaining intensive illumination, optical observation must be performed against a dark-sky background. When the RSO is bright enough to be visible (at the naked-eye or with the help of a telescope) information on the trajectory of the object, such as its right ascension and declination, can be determined.

Because of their high relative velocity with respect to the stellar background, space debris appear as fast moving objects. CCDs are usually connected to a telescope to take pictures of the sky. When the telescope points toward a fixed right ascension and declination the stars on the background will appear as points whereas the satellite will trace a trail on the CCD elements. The longer is the exposure time the longer is the resulting trail. Alternatively, for higher satellites such as GEO and GTO, the telescope can track the object: in this case the stars will appear as trails and the object as a fixed point. From each image it is possible to estimate not only right ascension and declination but also their derivatives by looking at the relative motion between the observed object and the stellar background. Optical observations can be also used to determine other parameters like the area to mass ratio and attitude of the spacecraft.

In this section the modelling of optical observation used to generate simulated data is described. First the illumination conditions are introduced and the assumptions required to perform the computation of the object magnitude are defined in Section 4.1.1 and 4.1.2 respectively. The simple telescope and CCD model are then introduced in Section 4.1.3.

4.1.1 Illumination conditions for optical observability

The following conditions must be satisfied to perform an optical observation of a debris or satellite [Vei63]:

- the object must be above the horizon of the station
- the object must be illuminated by the Sun (or an artificial light source)
- its brightness must exceed that of the background sky by a certain margin.

The case of a cylindrical Earth shadow is considered to assess the illumination condition of the target object. The illumination condition can be determined by considering the projection on a plane containing the Earth's and Sun's centres and the satellite, as represented in Figure 4.2.

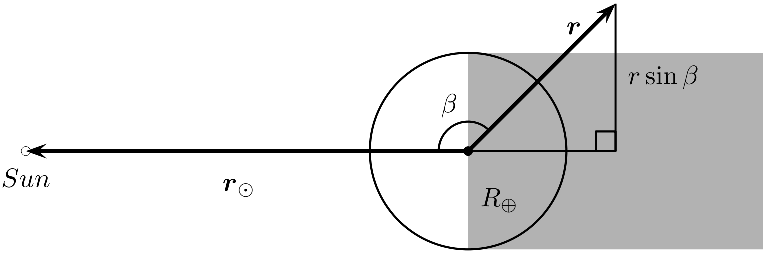

Figure 4.2. Entry-exit geometry for a cylindrical Earth shadow model.

To determine if the object is or not inside the shadow of the planet one has to look at the angle β that lies between the Sun position vector, $\boldsymbol{r}_\odot$, and the satellite position vector, $\boldsymbol{r}$, defined as

$$\beta = \arccos\left(\frac{\boldsymbol{r}\cdot\boldsymbol{r}_\odot}{r\, r_\odot}\right) \tag{4.1}$$

Given the Earth's radius $R_\oplus$, the object is inside the Earth shadow when both conditions in Eq. (4.2) are satisfied

$$\left.\begin{aligned}\beta &> \frac{\pi}{2}\\ r\sin\beta &< R_\oplus\end{aligned}\right\} \Rightarrow \quad \text{in shadow.} \tag{4.2}$$

For what concerns the other two conditions for satellite observability it is sufficient to look at the elevation of the target object and Sun. For bright objects the nautical twilight ($El_\odot < -12$ deg) can be taken as a reference, whereas for fainter objects it is preferable to consider the astronomical twilight ($El_\odot < -18$ deg). The elevation of the target object instead should be above 15 deg, in order to limit the effect of light pollution and occultation from surrounding, mountains, trees or buildings.

As a result, LEO satellites are visible only for a few hours in the proximity of twilight periods. In addition, for faint low-altitude objects the observation period is even shorter since a darker background is required to distinguish them. Higher satellites are visible for longer times, and observation windows could last almost all night for GEO objects.

4.1.2 Object magnitude computation

The equation for the visual magnitude m_v of an object of area A and albedo ς located at a distance ρ from the observer is computed by means of

$$m_v = -26.78 - 2.5 \log_{10} \left[\frac{A \varsigma F(\varphi)}{\rho^2} \right], \tag{4.3}$$

where the reference magnitude is the one of the Sun and $F(\varphi)$ is a function of the phase angle φ. The phase angle is defined as the angle between the direction of the observer and the direction of the Sun as seen from the spacecraft. Under the hypothesis of a spherical object, the phase function can be computed as [Vei63, Tou57]

$$F(\varphi) = \begin{cases} \dfrac{1}{4\pi} & \text{specular reflection} \\ \dfrac{2}{3\pi^2} \left[(\pi - \varphi) \cos\varphi + \sin\varphi \right] & \text{diffuse reflection.} \end{cases} \tag{4.4}$$

The magnitude is then corrected for the air mass, since the light reflected by the satellite crosses the atmosphere and is attenuated by absorption. A simplified model can be defined given the zenith angle ζ, by computing the observed magnitude m_o as

$$m_o = m_v + 0.04 \sec\zeta. \tag{4.5}$$

This simplified relation for atmospheric correction is indeed singular for $\zeta = 90$ deg, but can be safely used since objects with elevation below 15 deg are excluded from observations.

4.1.3 Telescope and sensor model

In this section the telescope and CCD sensor model are detailed. A telescope for optical survey of space debris should have a large FoV, fast optics and tracking velocity to follow objects rapidly moving in the sky, and a frame rate of several frames per minute. The optical performances of a telescope can be determined by knowing its aperture and focal ratio. According to the simplified telescope scheme of Figure 4.3 the objective collects the light coming from the faraway objects and projects its image onto the sensor. The distance between the objective and the focal point C (i.e. the point where all light rays from one object converge) is the focal length f. The aperture of the telescope is D and the focal ratio is defined as $F = f/D$. The FoV of a telescope

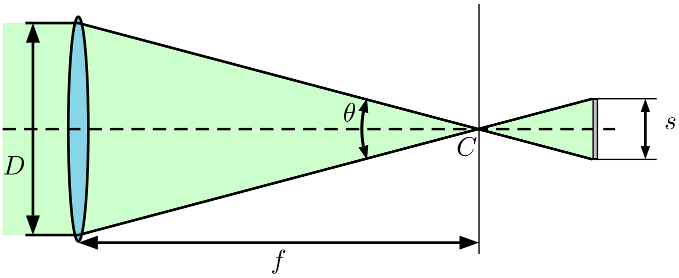

Figure 4.3. Simple telescope model. D is the telescope aperture, C indicates the focal point, f is the focal length, and S is the size of the CCD or photographic plate

depends on the focal length f and the size of the sensor s:

$$\theta = 2 \arctan \frac{s}{2f}, \tag{4.6}$$

where θ is the telescope field of view.

An important parameter to consider is the Visual Limiting Magnitude (VLM), that is the faintest apparent magnitude that is detectable by the telescope. It is a function of the aperture of the instrument:

$$VLM = 2.5 + 5 \log_{10} D, \tag{4.7}$$

where D is in millimetres. When the magnitude of the object is above the VLM the

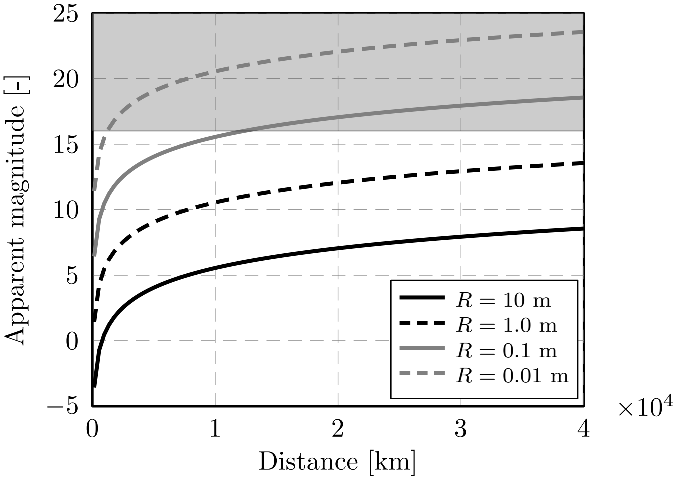

Figure 4.4. Apparent (visual) magnitude as function of range for spherical objects of different radius. Diffuse reflection, albedo $\varsigma = 0.2$, and phase angle $\varphi = 30$ deg. Non-observable region for a telescope with $D = 0.5$ m (VLM>16) is the shaded area.

object cannot be observed by the instrument. The visual magnitude for objects of different radius R is plotted in Figure 4.4 as function of range ρ. The magnitude increases with range (fainter object) and decreases when the radius increases. For a 0.5 m aperture telescope the VLM is 16. As a consequence, those objects whose size and illumination conditions result in larger magnitudes (upper part of the graph) are not detectable. It is worth noting that objects smaller than 10 cm can only be observed in LEO, whereas the smaller detectable objects in GEO measure tens of centimetres.

The CCD camera model used in this work is sketched in Figure 4.5. The model is that of a pinhole camera, although the focus f is the one of the telescope. The light rays coming from source A crossing the focus are projected onto the sensor plane, and photons impact pixels around point A'.

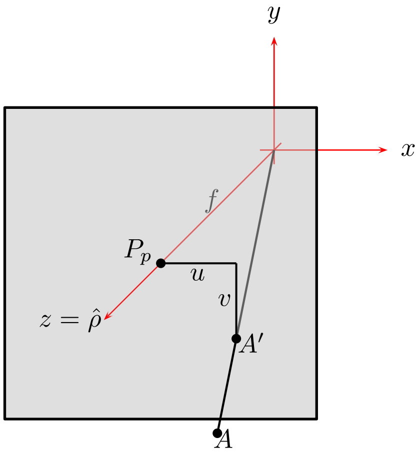

Figure 4.5. Pinhole camera model for CCD sensor.

The coordinates (u, v) of the illuminated pixels are referred to the principal point P_p (i.e. the intersection of the optical axis and the image plane) and are computed from the coordinates of the object position in the sensor frame (x, y, z):

$$\begin{cases} u & = f\,\dfrac{x}{z} \\ u & = f\,\dfrac{y}{z} \\ z & = f \end{cases} \tag{4.8}$$

The illuminated pixel coordinates (u, v) are rounded toward the nearest integer and the intensity of the signal is related to the visual magnitude of the object. An example of the resulting image is given in Figure 4.6. The image is obtained by simulating the transit of the object inside the field of view of the telescope, pointed at a fixed azimuth and elevation, and determining the illuminated pixel coordinates using Eq. (4.8). The pixels are then coloured according to the object magnitude during the transit.

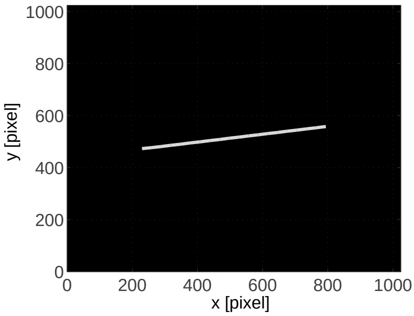

Figure 4.6. Example of simulated debris trail of a LEO object. The telescope field of view is 1.5 deg and exposure time is 1 s.

4.2 Radar observations

Ground-based radars provide a powerful tool for the characterization of the orbital debris environment [Meh97]. Radars can in fact irradiate at any time a satellite or space debris in Earth orbit with a microwave beam. The scattered wave can be detected by a receiver that may be the same transmitting antenna (*monostatic radar*) or a different one located at a distance of up to several hundreds of kilometres away (*bistatic radar*). When more than two antennas with common spatial coverage are employed and data from each site is combined at a central location, the system is called a *multistatic radar*.

Due to the high sensitivity and the capability to operate almost independently of the weather, day-night conditions and illumination of the target by sunlight, radar observations have been used to statistically sample the population of space debris in Earth orbit down to a few centimetres in size [Meh04, Fos05]. The observation modes that are usually employed are:

- **Tracking** mode: the object is followed for a certain amount of time during its transit in the sky region that is visible from the radar station;

- **Beam-park** mode: the antenna points toward a fixed direction and collects the echoes reflected by the objects transiting inside the FoV;

- Mixed mode (**stare-and-chase**): the antenna is initially in beam-park mode and shifts to tracking mode when an object is detected.

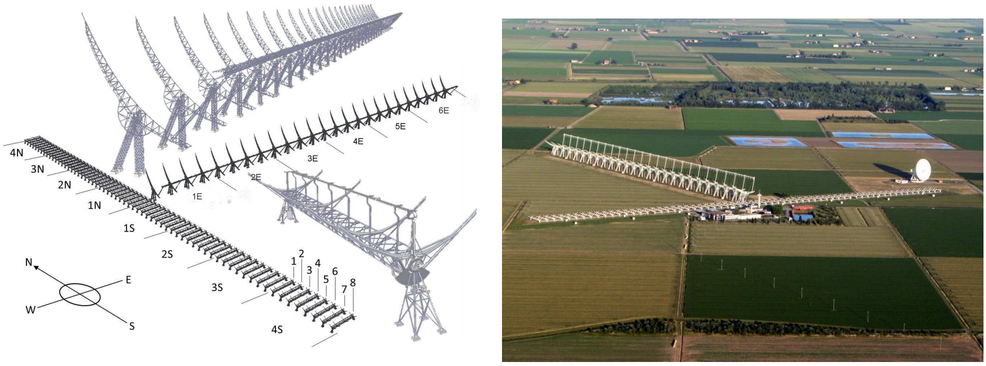

(a) A scheme of the Northern Cross antenna divided by channels. In the foreground and in the background, in gray, a detailed drown of one antenna of the N-S arm and of the whole E-W arm, respectively.

(b) A top view of the Medicina Radioastronomical Station. In the foreground the Northern Cross T-shaped array.

Figure 4.7. The Northern Cross antenna

Range, velocity (Doppler), azimuth, and elevation and object size, expressed in terms of Radar Cross-Section (RCS), are some of the information that can be derived from radar measurements [Kno04].

A collaboration with the Medicina observatory of the Istituto di Radioastronomia (IRA) (part of INAF, the Italian Istituto Nazionale di Astrofisica) was started in order to develop algorithms for the orbit determination of space debris and satellites, tailored for a bistatic radar system in which the Northern Cross (NC) plays the role of the receiver. The Northern Cross radio telescope is a T-shaped array that was designed and built during the 60's. It operates at UHF-band (408 MHz) with a bandwidth from approximately 2.5 MHz (old part) up to 16 MHz (upgraded part). It is a transit instrument, steerable in declination only, and therefore able to point at objects that transit over the local celestial meridian. The radio telescope is composed of two perpendicular branches (see Fig. 4.7): the first arm is aligned in an East-West direction and the second one in a North-South direction.

The East-West branch is a unique antenna with a 564 m long and 29.4 m wide cylindrical-parabolic reflector surface (for a total geometrical collecting area of 16,600 m^2). It is supplied with 1536 dipoles that lie out along the focal axes and transform the incident radio waves to measurable voltages.

The North-South arm is composed of 64 parallel cylindrical-parabolic shaped antennas. Each antenna is 22.6 m long and 7.5 m wide and it is set at a distance of 10 m from the next one (total geometrical collecting area of 10,800 m^2). Currently, each antenna is equipped with 64 dipoles for a total of 4096 receivers for the whole N-S arm.

The cylindrical-parabolic shape of the Northern Cross reflectors allows the incoming radiation to converge on the antenna's focus and to keep the phase unmodified after its reflection. The reflector is composed of a number of steel wires aligned at a distance of approximately 2 cm from each other. At the typical observing wavelengths (73.5 cm), the mechanical precision of this structure results sufficient to guarantee unaltered the instrument performances.

With its 27,400 square meters of total collecting area the Northern Cross represents the largest UHF-capable antenna in the Northern hemisphere, with an aperture efficiency of 60%, and second only to Arecibo in the world wide scale. Such a wide area potentially allows the constant monitoring of a large number of space debris.

A simulator of the bistatic radar configuration described above was developed to support analysis and estimate the system performances, that has also the capability of generating data resembling those that could be measured in reality. The simulator is designed so that different kind of transmitter and multibeam geometry can be easily defined by the user. In the following sections a description of radar measurements is given, together with some details on bistatic radar geometry and range relations and the multibeaming receiver for the Northern Cross developed with Oxford and Malta universities.

4.2.1 Radar measurements

The detectability of an object by means of radar observation depends on the radar power budget. It is thus important to determine the Signal-to-Noise Ratio (SNR) at the receiver to determine whether or not an object can be observed. By considering the more general case of a bistatic configuration, with transmitter and receiver located in different places, the radio waves produced by the transmitter will follow the path represented in Figure 4.8.

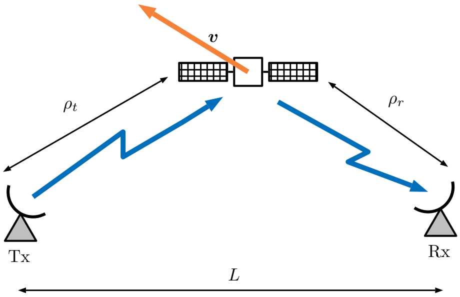

Figure 4.8. Scheme of bistatic radar mesurement

Given the power transmitted by the transmitter, P_t, the antenna gain G_t and directivity function $f(\theta, \phi)$ of the transmitter, the power density S at distance ρ_t from the transmitter is

$$S_t = \frac{G_t P_t}{4\pi\rho_t^2} f(\theta_t, \phi_t). \tag{4.9}$$

An object that is illuminated by the radio source is capable of collecting the radiated power depending on its electrical characteristics. The RCS σ is a parameter that defines the effective area of the scatterer, and, although having the dimensions of an area, is not only related with the physical dimensions of the object. The intercepted power can be thus computed using the RCS:

$$P_i = S_t \sigma. \tag{4.10}$$

Assuming that no absorption occurs and that the object is spherical (i.e. an isotropic radiation source), the power density re-reflected by the object becomes

$$S_i = \frac{1}{4\pi\rho_r^2} S_t \sigma. \tag{4.11}$$

The power that is collected at the receiver will be equal to

$$P_r = S_i A_e g(\theta, \phi), \tag{4.12}$$

where A_e is the effective area of the antenna and $g(\theta, \phi)$ its directivity function. The effective area can be related to the physical area by means of the aperture efficiency k_a, since $A_e = k_a A$. The antenna gain and effective area can be related by means of the wavelength λ

$$\frac{G}{A_e} = \frac{4\pi}{\lambda^2}. \tag{4.13}$$

By replacing the receiver effective area in Eq. (4.12) and using Equations (4.9) and (4.11), the power at the receiver becomes

$$P_r = \frac{P_t G_t G_r \lambda^2 \sigma}{(4\pi)^3 \rho_r^2 \rho_t^2} f(\theta_t, \phi_t) g(\theta_r, \phi_r) \tag{4.14}$$

Assuming that the object is exactly at the intersection of the two beam axis, the received power becomes

$$P_r = \frac{P_t G_t G_r \lambda^2 \sigma}{(4\pi)^3 \rho_r^2 \rho_t^2}, \tag{4.15}$$

since $f(\theta_t, \phi_t) = g(\theta_r, \phi_r) = 1$. Equation (4.15) is known as bistatic radar equation. System losses and propagation losses, such as free space losses and atmospheric losses, contributes in the attenuation of the received power and should be accounted for in precise modeling of such system.

In case of a monostatic radar the radar equation becomes

$$P_r = \frac{P_t G^2 \lambda^2 \sigma}{(4\pi)^3 \rho_r^4}, \tag{4.16}$$

The object is detected when the received power is higher than the noise, that is computed by means of noise equation

$$N = k_B B_n T_0, \tag{4.17}$$

where k_B is Boltzmann's constant (J/K), B_n is the bandwidth of the instrument (Hz), and T_0 is the noise temperature of the receiver (K). The signal to noise ratio, expressed in decibels, is defined as

$$SNR_{dB} = 10 \log_{10} \left(\frac{P_r}{k_B B_n T_0} \right). \tag{4.18}$$

When SNR is larger than 0 dB the reflected wave exceeds noise and it is thus possible to measure other quantities such as range and range-rate.

The range can be measured using different techniques, depending on the type of signal that is transmitted. When the signal is a continuous wave, frequency modulation can be used and ranging can be performed by analyzing the spectra of the reflected signal. For pulsed radar instead, it is sufficient to measure the delay between the transmission and reception of the signal. Since the waves travels at the speed of light the length covered by the radio waves can be easily computed. For a monstatic radar the range is equal to

$$\rho = \frac{1}{2} c \Delta t, \tag{4.19}$$

where c is the speed of light and Δt the delay.

For a bistatic radar there are two ways of determining the range [Wil05]. The *direct* method consists in measuring the time between the reception of the carrier and the scattered signal, yielding

$$\rho_t + \rho_r = L + c\Delta t, \tag{4.20}$$

where the baseline L is a known distance. In this case the carrier must be detected by the receiver, otherwise no ranging can be performed. The *indirect* method instead requires that both receiver and transmitter are equipped with synchronized clocks and the bistatic slant range, i.e. the sum of receiver and transmitter range ρ_t and ρ_r is similar to that of the monostatic radar:

$$\rho_t + \rho_r = c\Delta t. \tag{4.21}$$

The range-rate is determined from the Doppler shift, i.e. the variation in the frequency due to the motion of the target also known as Doppler effect. The frequency shift can be computed as

$$\Delta f = f_r - f_t = \frac{1}{\lambda} \left[\frac{d}{dt} (\rho_t + \rho_r) \right] = \frac{1}{\lambda} \left[\boldsymbol{v} \cdot \hat{\rho}_t + \boldsymbol{v} \cdot \hat{\rho}_r \right], \tag{4.22}$$

where $\boldsymbol{v}$ is the relative distance of the target with respect to transmitter and receiver, that are supposed to be fixed (or moving at the same velocity) and $\hat{\rho}_t$ and $\hat{\rho}_r$ are the unit vectors on transmitter to object and receiver to object direction. For monostatic radars the frequency shift is instead related to the range direction, being transmitter and the receiver the same antenna. In this case the Doppler shift becomes

$$\Delta f = \frac{2}{\lambda}\dot{\rho}. \tag{4.23}$$

The relations given in this section can be used to simulate radar measurements. Given the trajectory of an object, e.g. computed using TLE and SGP4/SDP4, the ranges ρ_t and ρ_r can be computed with respect to the location of transmitter and receiver. An elliptic cone model can then be used to represent the antenna beams. Given the beamwidths in two perpendicular directions, BW_α and BW_δ respectively, and the nominal antenna gain in decibels, G_{dB0}, the gain can be expressed as function of the angular displacement from the cone axis, $\Delta\alpha$ and $\Delta\delta$ as

$$G_{dB} = G_{dB0} - 12\left[\left(\frac{\Delta\alpha}{BW_\alpha}\right)^2 + \left(\frac{\Delta\delta}{BW_\delta}\right)^2\right]. \tag{4.24}$$

Note that this function is consistent with the definition of beamwidth, that is the angle between the half power points of the main lobe. Indeed, when the angular displacement is $\Delta\alpha = BW_\alpha/2$ or $\Delta\delta = BW_\delta/2$ the gain is 3 dB lower. Knowing the antenna directions and the spacecraft position it is possible to compute the two angular displacements and, in turn, the receiver and transmitter gains. At this, point, once the SNR is positive, the time and Doppler shift can be estimated from Equations (4.22) and (4.20) or (4.21).

4.2.2 Bistatic radar geometry

A sketch of the geometric configuration of the bistatic radar system is given in Figure 4.9. A plane that contains the two relative distance vectors from Tx and Rx, ρ_t and ρ_r respectively, and the baseline L can be defined. This plane is usually indicated as *bistatic plane* and it allows for easy computations of all range relationships. As an example, the range between the target and the transmitter ρ_t can be written as

$$\rho_t^2 = L^2 + \rho_r^2 - 2L\rho_r\cos\left(\frac{\pi}{2} + \theta_r\right), \tag{4.25}$$

where ρ_r is the range between receiver and target, L the baseline of the bistatic radar, and θ_r the look angle at the receiver. From Eq. 4.25 above it is possible to obtain the range from the receiver, ρ_r, as function of the slant range as

$$\rho_r = \frac{(\rho_t + \rho_r)^2 - L^2}{2\left(\rho_t + \rho_r + L\sin\theta_r\right)}. \tag{4.26}$$

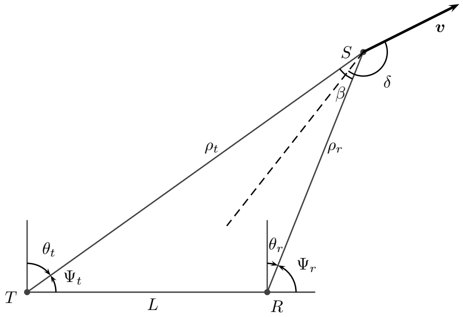

Figure 4.9. Geometry of the bi-static radar system on the bistatic plane. Point T is the transmitter, point R is the receiver and the target is point S. The transmitter and receiver look angles are θ_t and θ_r, L is the baseline, and β the bistatic angle. Ranges from receiver and transmitter are ρ_r and ρ_t respectively.

The bistatic plane is identified in a three-dimensional space, that can be referred at the receiver topocentric NWZ frame, as sketched in Figure 4.10. Since azimuth Az_t and elevation El_t of the transmitting antenna T, measured at the receiver R, are usually known it is possible to estimate the look angle of the receiver from azimuth Az and elevation El of the target [Wil05]:

$$\theta_r = -\arcsin\left[\cos El \cos El_t \cos(Az - Az_t) + \sin El \sin El_t\right]. \tag{4.27}$$

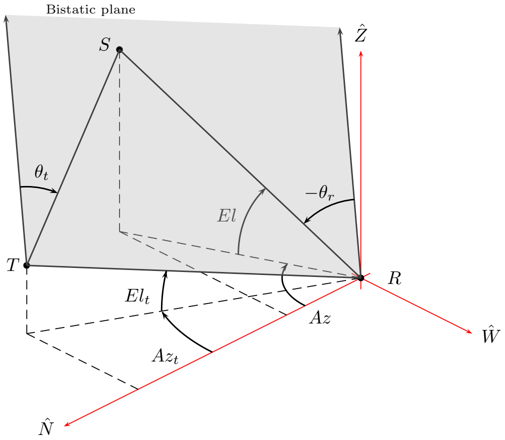

Figure 4.10. General geometry of the bistatic plane with respect to a topocentric North-West-Zenith frame centred at the receiver R. Azimuth and elevation of transmitter T are Az_t and El_t, whereas Az and El are azimuth and elevation of target object S.

4.2.3 Multibeaming receiver

The use of multibeaming receiver allows the characterization of the transit direction of the scattering object inside the FoV of the receiver. The beam illumination sequence indeed allows to discern the trajectory of the object in terms of right ascension and declination (or alternatively in terms of azimuth and elevation). Space debris observations were performed with the 7-horn receiver installed on the Effelsberg radar (100 mt dish antenna), using the TIRA L-Band radar (34 mt dish antenna) as transmitter [Rui06]. Both radars are located in Germany and are operated by the Max-Planck Institute for Radioastronomy and Fraunhofer Institute for High Frequency Physics and Radar Techniques respectively. The baseline of the bistatic radar configuration is approximately 20 km, resulting in a large shared observed volume, approximately 250 km in height. The bistatic radar is operated in beam-park mode. Tailored algorithms had to be developed to allow for the determination of the orbital parameter of the object transiting the FoV, using Least Square Estimation and Maximum Likelihood Estimation [Rui05]. The 2006 observation campaign set the detection threshold at object of 1.1 cm size at 1000 km range [Rui06].

Another multibeaming receiver has been developed for the BEST-2 array, a subset of 8 cylinder of the North-South arm of the Northern Cross antenna, located at the Medicina observatory, 30 km far from Bologna. A total of 32 receivers, 4 for each cylinder, have been installed as a test-bed for the Square Kilometer Array [Mon09]. The signal from the receivers is fed to a digital back-end [Fos14] and processed by means of an optimized Graphic Processing Unit (GPU) multibeam beamformer [Mag13] that

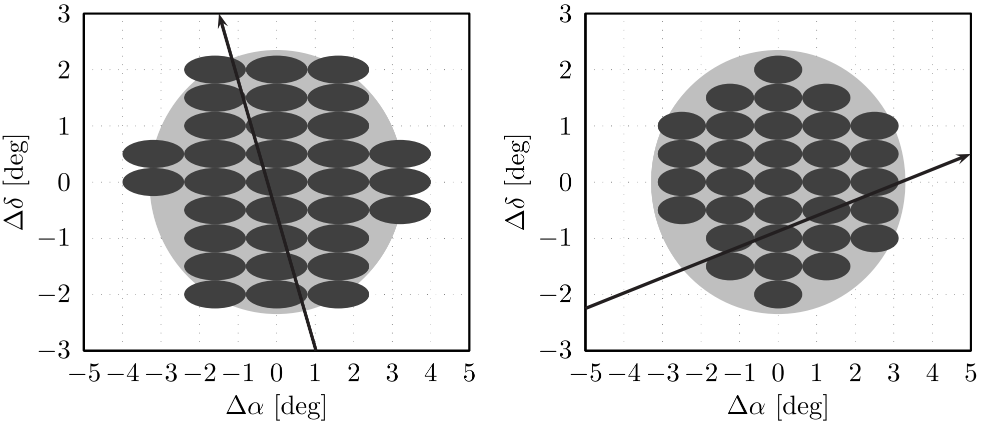

(a) Multibeam geometry for BEST-2 receiver

(b) Alternative multibeam geometry for BEST-2 receiver

Figure 4.11. Multibeam geometry for the BEST-2 receiver. The light gray ellipse in the background represents the antenna beam, modelled as an elliptic cone. The darker ellipse are the beams synthesized by the GPU beamformer. Measuring the time and received power at each beam the trajectory inside the FoV can be estimated.

generates 32 beams distributed across the array's primary FoV, as portrayed in Figure 4.11(a). Another possible distribution of the synthesized beams geometry considered in this work is given in Figure 4.11(b).

In the following section the orbit determination algorithms developed for the BEST-2 multibeaming receiver are described.

4.3 OD algorithms for bistatic radar with multibeaming receiver

In this section a novel algorithm for the orbit determination of RSO using a bistatic radar with a multibeaming receiver is described. This is the most innovative algorithm presented for orbit determination, due to the characteristics of the considered receiving antenna, the large number of beams synthesized in the field of view, and the scalibility of the proposed algorithm, that can used for different beams numbers, sizes, and distributions.

The orbit determination process is divided into two phases

1. Estimation of topocentric right ascension α and declination δ from SNR measurements
2. Estimation of object position and velocity via least square fit

In both cases it is assumed that the RCS is constant during the whole transit. In case the object is known or the observation can be univocally associated to a catalogued object, an estimation of its value is available from previous observations and can be used in the OD process.

The first step is tackled as a weighted curve fit. In most cases the relative motion of satellites and debris with respect to both receiver and target is fast enough to approximate the motion within the FOV of both radars as a straight line. As a consequence, the trail inside the FoV of the receiver can be expressed as a function of time as

$$\begin{cases} \Delta\alpha(t) = a_1\,t + a_0 \\ \Delta\delta(t) = b_1\,t + b_0 \end{cases} \tag{4.28}$$

The coefficients a_1, a_0, b_1, and b_0 of Eq. (4.28) are estimated in two steps. First, a curve fit that minimizes the angular displacement from each beam centre at the time of the maximum received power is performed. The right ascension and declination of each beam are indeed known from the radar pointing (azimuth and elevation) and the time at which the maximum SNR occurs can be determined from the simulated measures. Note that the number of residuals in this case equals the number of beams that are illuminated during the observation. The selected weights are the normalized values of the SNR: the maximum recorded value of the SNR among all beams is used taken as a reference and all SNR maximum of each beams are divided by this value. The higher the value of the normalized SNR, the more the object was closer to the beam axis.

Given the coefficients a_1, a_0, b_1, and b_0 obtained with the approach described above and the range and SNR measurements that are available at each sampled time instant[1] it is possible to obtain a more accurate fit of the trajectory. The algorithm starts with a guess of the right ascension and declination as function of time and the goal is to update this guess by minimizing the residuals between the measured SNRs and the estimated SNRs obtained with the $\alpha(t)$ and $\delta(t)$ guesses. The following operations are performed at each time step:

1. Compute azimuth and elevation of the target with respect to the receiver using right ascension and elevation from Eq. (4.28) and the nominal pointing of each beam.

2. Compute the look angle of the receiver, θ_r, by means of Eq. (4.27), using the azimuth and elevation of the target computed in the previous step and the azimuth and elevation of the transmitter.

3. Compute the receiver and transmitter range by means of Eq. (4.26) and (4.25), using the measured slant range $(\rho_r + \rho_t)$.

4. Compute the SNR for each beam correcting the gain in accordance to Eq. (4.24) and the estimated angular displacements with respect to the each beam axis.

Once all SNR values are recomputed for each beam and for each time step, the residuals with respect to the measured SNR are computed. The coefficients a_1, a_0, b_1, and b_0 are then updated to obtain a better fit. The above steps are repeated till when the changes in the coefficients is below the defined tolerance.

A comparison of the estimates of the right ascension and declination trajectories obtained with the simple weighted fit and the SNR least square is given in Figure 4.12. The blue trajectory is the coarse fit obtained considering the maximum SNR value for each beam, whereas the red trajectory is the refined one that considers also range information. The second is nearly superimposed to the black line, that is the true trajectory of the transiting object.

Pertaining the second step, it consists in a non-linear least square optimization to match the orbital trajectory with the range measurements, the right ascension and declination computed as above, and Doppler shift with the values recorder for the whole transit inside the FoV of the receiver.

---

[1] Sampling rate of the system is supposed to be 0.05 s.

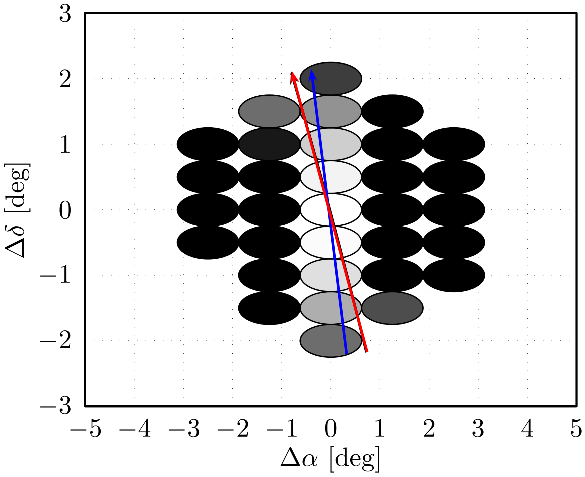

Figure 4.12. Determination of right ascension and declination from measured data. Black line is the true trajectory, blue line is the first guess obtained with the fit of the maximum SNR, and red line is the refined trajectory in the $\alpha - \delta$ plane.

4.4 Numerical simulations

In this section the results of a few orbit determination tests are given. The OD is first performed by considering optical observations only in Subsection 4.4.1. The case of radar only observations is instead tackled in Subsection 4.4.2, whereas the mixed case is in Subsection 4.4.3 and concludes this section.

The selected objects are reported in Table 4.1 where, in addition to the semi-major axis, inclination, and eccentricity of the orbit, the RCS value and the maximum visual magnitude $m_{\max}$ of the object are also given for each object. The maximum visual magnitude refers to a 100% illuminated object at the perigee[1]. The RCS values are instead obtained from Space-Track[2].

Sat. No.	**Sat. Name**	a [km]	e [-]	I [deg]	**RCS** [m^2]	$m_{\max}$ [-]
19046	SL-3 R/B	6946	3.96E-2	97.6	6.55	+1.5
25723	SL-8 R/B	6847	1.75E-3	48.4	4.93	+0.8
37820	Tiangong 1	6743	7.41E-4	42.8	20.54	-1.2

Table 4.1. Selected objects for orbit determination numerical tests.

The initial guess for the orbit determination process is always the orbital state of the object at the selected reference epoch, computed with SGP4 using the TLE closest to the first observation.

---

[1] Values taken from: www.heavens-above.com

[2] www.space-track.org

4.4.1 Orbit determination with optical observations

The results of the orbit determination routines, based on a non-linear least square fitting, for the case of optical observations only are here presented. For each OD a set of three angular measurements of the same object is considered. The observatory location used for the generation of the simulated observations is (44°51′57″ N, 11°00′11″ E) and the altitude is 14 m. The site is near Cavezzo (MO) and currently hosts the astronomical observatory "Geminiano Montanari". The characteristic of the (hypothetical) telescope are given in Table 4.2.

Diameter	400 mm
F-ratio	1.2
Focal length	480 mm
Field of view	4.3° × 4.3°
Resolution	5″
CCD size	3072 × 3072 pixels
Pixel size	11.7 μm
VLM	15.51

Table 4.2. Design parameters of telescope for space debris observation

The simulated optical observations are listed in Table 4.3, by considering the first two objects of Table 4.1. Pertaining the first object, three observations are performed during three consecutive days at dusk. The second object is instead observed three times in two consecutive days at dawn. The observations are usually performed when the object is at its maximum elevation, except for observation 2B that is performed right after the object is outside the Earth's shadow.

Obs. ID	**Sat. No.**	**Observation epoch**	**Observatory**	Az [deg]	El [deg]
1A	19046	2014/07/01 19:52:17	Cavezzo	75.6	84.5
1B	19046	2014/07/02 19:53:37	Cavezzo	74.2	87.5
1C	19046	2014/07/03 19:54:57	Cavezzo	265.2	89.6
2A	25723	2014/09/24 04:40:39	Cavezzo	346.9	60.0
2B	25723	2014/09/25 02:32:08	Cavezzo	98.0	26.0
2C	25723	2014/09/25 04:08:44	Cavezzo	345.4	62.6

Table 4.3. List of simulated optical observations. Exposure time of CCD for each observation is 1 s.

A sequence of illuminated pixels is generated for each observation and stored in a file that is then processed by the orbit determination algorithm. The generated observations include small random pointing errors for the telescope and discretization errors due to CCD imaging, since the resulting pixel sequence must be composed of integer numbers only. The right ascension and declination associated to the objects trails thus differ from the true value. As a result, these errors will produce a small deviation of the best fit line with respect to the true trajectory. Using the information on the azimuth Az and elevation El of each observation the right ascension and declination of the object can be reconstructed. The non-linear least square fit will then determine the initial conditions for AIDA that will minimize the residuals between the measurements and the numerically propagated trajectory. The observed trail is divided into 20 points, equally spaced in time. Since the exposure time is 1 s the time interval is 0.05 s. For each of these time steps the residuals between the observed right ascension and declination and the estimated one are computed. The perturbations considered during the OD process for AIDA are a 10×10 gravitational model, air drag, solar radiation pressure with dual-cone Earth shadow, and Moon and Sun gravitational attraction. The OD process is performed on orbital state only. The values of the area-to-mass ratio for both SRP and air drag are obtained from TLEs and are supposed to be known, thus becoming additional inputs for the propagator. The reference epoch for the propagation with AIDA is always the time of the last observation.

The estimated state for SL-3 R/B is listed in Table 4.4, together with the reference state and the uncertainties in the Earth Centred Inertial (ECI) J2000 reference frame, that is the default for AIDA. Note that the reference state is "true" in the sense that it is the reference epoch that is used to generate the simulated observations. There is a good accordance between the estimated and true state with errors of tens of meters in position and a few m/s for the velocity components. The uncertainties on position resulting from the OD process are of the order of a few hundreds meters for the position components and around 1 m/s for the velocity components.

	RX [km]	**RY** [km]	**RZ** [km]	**VX** [km/s]	**VY** [km/s]	**VZ** [km/s]
Ref. state	-3069.770	-3835.251	4872.005	2.189671	4.995551	5.297757
Est. state	-3069.893	-3835.364	4872.074	2.192780	4.997866	5.294026
St. dev. σ	±0.431	±0.529	±0.678	±0.916E-3	±1.134E-3	±1.361E-3

Table 4.4. Object 19046, estimated orbital states from three optical observations. Reference epoch: 03/07/2014 19:54:58.06 UTC

It is important to compare also the evolution of the error between the estimated and the reference trajectories to determine how effective the OD process is. In Figure 4.13 the position and velocity error is plotted for the 24 hours after the reference epoch of the estimated trajectory. The orbit propagation is performed with AIDA, using the same perturbations considered during the OD process. The position error is periodic and no drift between the two trajectory occurs in the considered propagation window. There is a bias of approximately 10 km in the error mean value and the maximum error is approximately 17 km. A similar trend is found for the velocity error, that has a mean value around 7 m/s.

The estimated state for SL-8 R/B is instead listed in Table 4.5, again provided

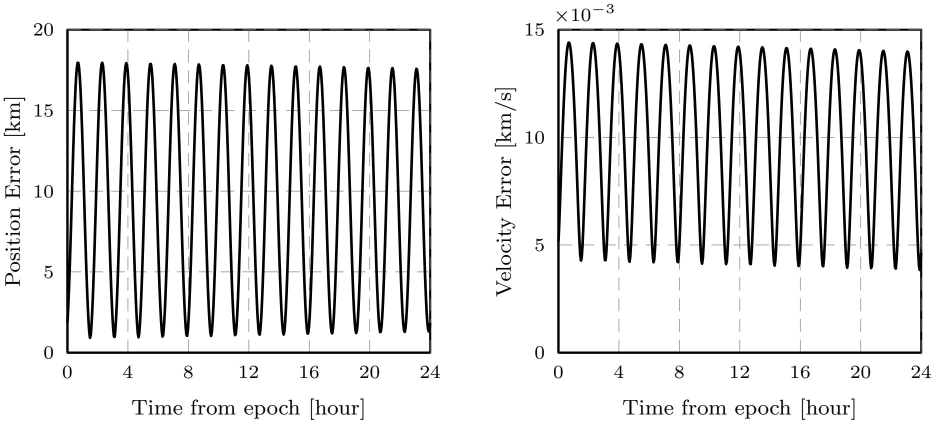

Figure 4.13. Position and velocity error between the reference and estimated trajectory of object 19046 for the 24 h following the last optical observation. The propagation of the estimated state is performed with AIDA.

together with the reference state and the uncertainties in the ECI J2000 reference frame. In this case the difference between the true trajectory and the estimated one is smaller and so are the uncertainties on the estimated orbital state, that are of the order of a few meters only for the position components and tens of mm/s for the velocity. The higher accuracy of the estimated state is probably due to the shortest time interval between the first and last observation for the second object and to the fact that the observations of the first object are all performed with similar conditions (pointing) and this could make the OD estimation ill-conditioned. The orbit of 19046 is nearly sun-synchronous, thus there is only a change of approximately 1 deg in right ascension between the different trails. For object 25723 instead the second observation is performed in different conditions and the change in right ascension and declination for the associated trail is much larger.

	RX [km]	**RY** [km]	**RZ** [km]	**VX** [km/s]	**VY** [km/s]	**VZ** [km/s]
Ref. state	1128.017	4559.876	4977.197	-7.501311	0.405709	1.343148
Est. state	1128.034	4559.913	4977.415	-7.501000	0.405227	1.343851
St. dev. σ	±0.003	±0.004	±0.016	±3.061E-5	±4.565E-5	±9.130E-5

Table 4.5. Object 25723, estimated orbital states from three optical observations. Reference epoch: 25/09/2014 04:08:44.63 UTC

The plot of the error between the estimated and the reference trajectory for a 24-h propagation is represented in Figure 4.14. In this case the maximum relative error on position and velocity are smaller, with a maximum of 1.2 km for the position and 1.2 m/s for the velocity. As before, the area-to-mass ratios are assumed to be known before the observation and are obtained from TLEs data.

According to the results reported in this section, three optical measurements of

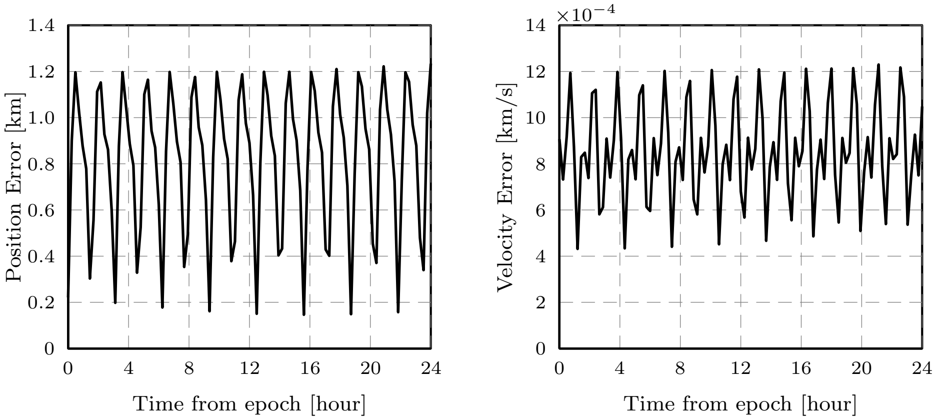

Figure 4.14. Position and velocity error between the reference and estimated trajectory of object 25723 for the 24 h following the last observation. The propagation of the estimated state is performed with AIDA.

an object are sufficient to compute an estimate of a RSO orbital parameters, which is in agreement with the classical OD methods. It was observed that when optical measurements of one object are performed from the same site and the azimuth and elevation of the telescope are similar, the error on the estimated state is higher. A good practice to reduce OD errors is thus to consider, if possible, measurements that are taken in different conditions (e.g. one at dusk and one at dawn), as for the second numerical simulation. Alternatively, the measurements of the same object could be performed from a different site.

To increase the accuracy of the estimated orbital state it is also important that observations do not spread over a period exceeding a few days. Due to perturbations, in particular air drag for low orbits, the residuals tend to increase with propagation time, resulting in larger state uncertainties.

4.4.2 Orbit determination with radar observations

In this section the results of the orbit determination for the case of a single bistatic radar observation are considered. For each OD a single observation is taken into account. Two different transmitters are considered, whereas the receiver is always the Northern Cross of the Medicina Observatory. The first transmitter is located approximately 20 km from the radioastronomical station of Medicina, whereas the second one is close to the Sardina Radio Telescope (SRT), located near San Basilio, Sardinia, Italy. Both transmitters are dish antennas with a diameter of 6 meters and their maximum transmitting power is 5 kW. The main characteristics and location of the antennas are given in Table 4.6. Pertaining the transmitters the aperture efficiency is assumed to be $k_a = 0.675$ and the resulting gain is $G = 667.8$ if the transmitting frequency is 411 MHz.

Antenna	Latitude	Longitude	Altitude	Diameter	Comp.	Max Power	Azimuth	Elevation
NC	44°31′14″N	11°38′49″E	25 m	52 m	Rx	-	0,180 deg	>45deg
Bagnara	44°23′31″N	11°49′57″E	15 m	6 m	Tx	5 kW	50-200 deg	>20 deg
SRT	39°29′34″N	09°14′42″E	650 m	6 m	Tx	5 kW	0-360 deg	>20 deg

Table 4.6. Main features of the antennas composing the ground-based bistatic radar system. The diameter for the Northern Cross is an equivalent circular diameter for BEST-2 array only.

A representation of the two bistatic geometries is given in Figure 4.15. The Northern Cross beam is the red one, whereas the transmitter beams are the blue ones. Note that the beams of transmitters and receiver are assumed to be elliptical cones, where the beamwidths are the angles between the the half-power (-3dB) points of the main lobe on two perpendicular axis. The location of the transmitter influences the crossover region of the bistatic radar: when the transmitter is located close to the receiver the two beams overlap on a wide altitude range, that extends over the whole LEO regime. The bistatic configuration with the transmitter in Bagnara could be thus classified as "quasi-monostatic". On the converse, when the transmitter is far from the receiver, as in the case of SRT, the crossover region has a limited extension in altitude. Note that the altitude bounds of the crossover region for a pure bistatic configuration is dependent on the target object location. When the antenna points towards the horizon the altitude range is higher than in the case in which the target object is at high elevation.

The simulated bistatic radar observations are listed in Table 4.7 with the azimuth and elevation of the receiver and transmitter. Note that the Northern Cross is a transit instrument and can be only pointed on the local meridian, with an azimuth of 0 deg or 180 deg. Two different layout are considered for the multibeaming receiver,

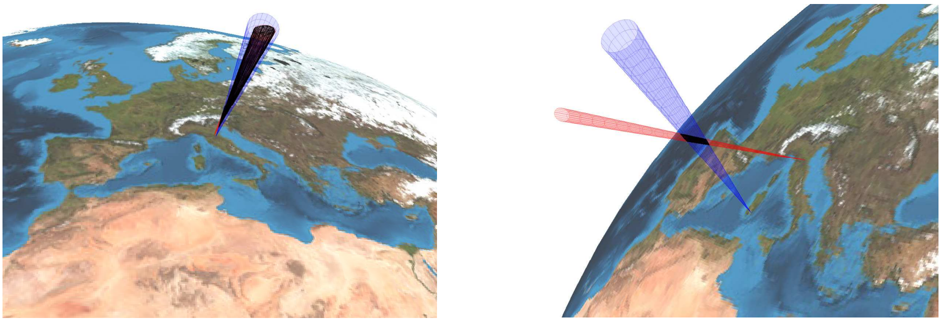

(a) Transmitter located in Bagnara **(b)** Transmitter located near SRT

Figure 4.15. Bistatic radar configuration. The red cone is the Northern Cross beam, whereas the blue cone is the transmitter beam. The crossover region is bounded by the black surface.

Obs.	**Object ID**	**Transit epoch**	**RX**	**Az [deg]**	**El [deg]**	**TX**	**Az [deg]**	**El [deg]**
1R	19046	2014/07/01 19:52:15	NC (A)	0.0	86.2	Bagnara	343.4	84.3
2R	19046	2014/07/01 19:52:15	NC (B)	0.0	86.2	Bagnara	343.4	84.3
3R	25723	2014/09/23 08:29:50	NC (A)	180.0	64.7	Bagnara	184.4	66.3
4R	25723	2014/09/23 08:29:50	NC (B)	180.0	64.7	Bagnara	184.4	66.3
5R	37820	2014/04/15 13:22:30	NC (A)	180.0	61.6	Bagnara	184.9	63.5
6R	37820	2014/04/15 13:22:30	NC (A)	180.0	61.6	SRT	27.9	39.0

Table 4.7. List of simulated bistatic radar observations.

both with 32 beams inside the FoV, as represented in Figures 4.11(a) and 4.11(b). The first layout, labelled NC (A), has slightly larger beams, equal to 1.6×0.5 deg in right ascension and declination, whereas the second layout is labelled NC (B) and its beams are 1.25×0.5 deg in right ascension and declination respectively. For each object two different configurations are considered for the same transit: the goal is to compare the performances of the system for the different possible configurations. The first four observations are targeted at determining whether the use of different beams geometry for the multibeaming have an impact on the orbit determination phase. Two simulated measures are generated for each object, using the different beams layouts for the receiver. The last observations instead are targeted at determining whether the location of the transmitter can affect the orbit determination process.

The tracklets, i.e. the trajectory covered by the satellite or debris inside the FoV of the antenna, for observations 1R and 2R are represented in Figure 4.16 as a black arrow. The estimated object trajectories inside the (α-δ) plane, obtained with the procedure described in Section 4.4.2, are also portrayed. Note that the estimates and

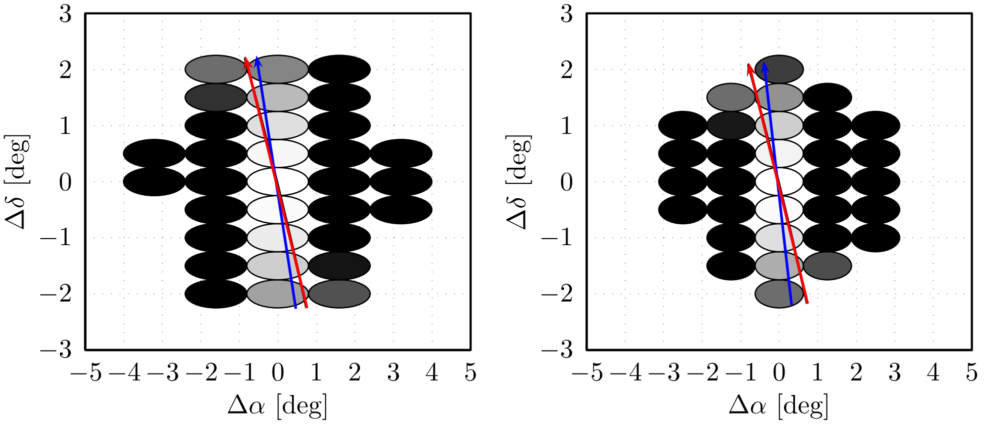

(a) Receiver tracklet for observation 1R **(b)** Receiver tracklet for observation 2R

Figure 4.16. Receiver tracklets for bistatic radar observations of object 19046. In both cases the transmitter is located in Bagnara. The black arrow is the reference trajectory, the blue line the first estimate of the trajectory in the α-δ plane, and the red line the refined trajectory. The receiver beams are coloured according to the measured SNR.

	RX [km]	**RY** [km]	**RZ** [km]	**VX** [km/s]	**VY** [km/s]	**VZ** [km/s]
Observation 1R, reference epoch: 01/07/2014 19:52:12.20 UTC						
Ref. state	-3208.888	-3746.830	4851.438	2.345987	4.901547	5.318343
Est. state	-3208.933	-3746.789	4851.440	2.347366	4.900858	5.318389
St. dev. σ	±0.014	±0.016	±0.021	±1.578E-3	±1.041E-3	±0.537E-3
Observation 2R, reference epoch: 01/07/2014 19:52:12.30 UTC						
Ref. state	-3208.654	-3746.340	4851.970	2.346372	4.901996	5.317759
Est. state	-3208.684	-3746.309	4851.974	2.348143	4.901026	5.317868
St. dev. σ	±0.013	±0.015	±0.020	±1.543E-3	±1.016E-3	±0.524E-3

Table 4.8. Object 19046, estimated states for observations 1R and 2R

simulated data are all obtained considering a constant and known RCS for the object as well as no noise on measures and no losses.

The reference and estimated orbital states for the radar observations 1R and 2R are listed in Table 4.8. These values are obtained by considering a 10×10 Earth gravitational model, air drag, SRP with dual-cone shadow model, and third body perturbations of the Moon and the Sun. As for the optical orbit determination, it was assumed that the area-to-mass values were known prior the OD. The reference epoch for the OD is the time of reception of the last echo. The error on the position components is equal to a few tens of meters, whereas the error on velocity components reaches 1 m/s for both observations. The uncertainty on position are on the order of a few tens of meters and the ones on velocity are again around 1 m/s.

The error between the estimated and the reference trajectory is plotted for the 24-h following the last observation in Figure 4.17. The black curve refers to the

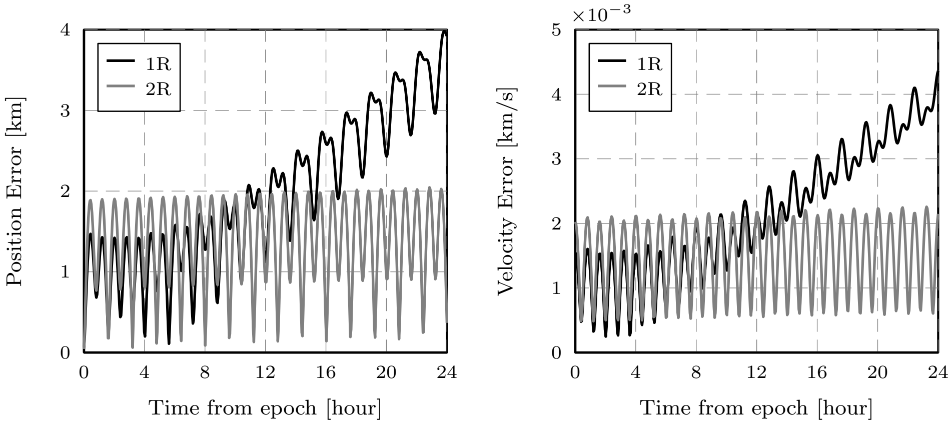

Figure 4.17. Position and velocity error between the the reference and the estimated trajectory of object 19046 for the 24 h following the radar observation. The propagation of the estimated states is performed with AIDA.

propagation of the orbital state with the first multibeaming layout and the gray curve with the second layout. In both cases the error on position and velocity is below 5 km and 5 m/s. When using the first multibeaming geometry the error increases with time, whereas for the second layout the maximum error remains constant. A possible explanation is the higher accuracy in terms of position (and velocity) for the second test case,where the smaller beam size could have a beneficial effect for the considered transit inside the FoV. It can be observed that the error has oscillations with a period close to the orbital one: this behaviour is explained by the fact that the OD is performed using only measurements from a small orbit segment. The error is thus small when the object is transiting in that portion of the orbit and increases when the object moves away from it.

The tracklets for the second object transit are represented in Figure 4.18. On the left the tracklet for the observation 3R, which employs layout NC (A), is represented, while on the right the tracklet referring to the observation 4R with the layout NC (B) is portrayed. The object moves in the opposite direction with respect to the previous one and has a lower inclination.

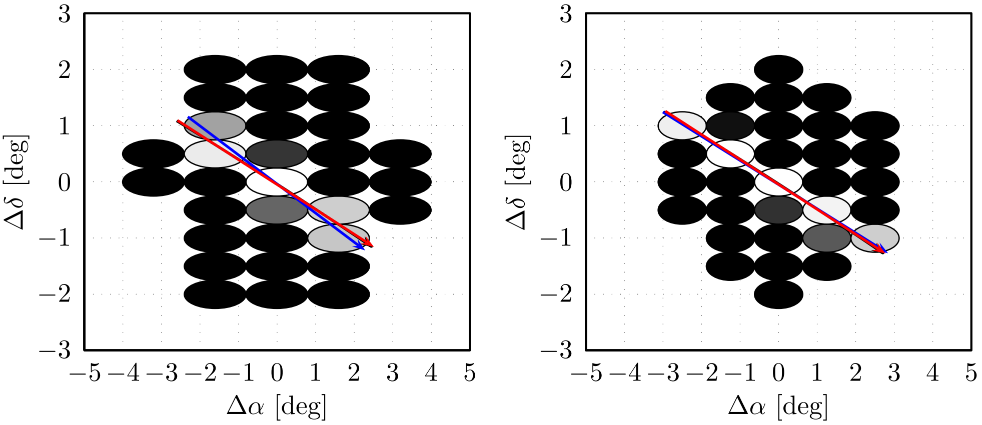

(a) Receiver tracklet for observation 3R **(b)** Receiver tracklet for observation 4R

Figure 4.18. Receiver tracklets for bistatic radar observations of object 25723. In both cases the transmitter is located in Bagnara. The black arrow is the reference trajectory, the blue line the first estimate of the trajectory in the α-δ plane, and the red line the refined trajectory. The receiver beams are coloured according to the measured SNR.

The orbital states obtained with the OD algorithm are listed in Table 4.9. The reference epoch is again the time of the last echo detection. In this case the uncertainties on position and velocity are comparable to those obtained for object 19046 but the difference between the reference and estimated velocity is larger, being around 5 m/s for the last two components. The reason is probably the geometry of the bistatic observation: the performances of a bistatic radar depend on the geometry, and are influenced by parameters such as the bistatic angle [Wil05].

The consequence in this case is that the error in the estimation of the velocity

	RX [km]	**RY** [km]	**RZ** [km]	**VX** [km/s]	**VY** [km/s]	**VZ** [km/s]
Observation 3R, reference epoch: 23/09/2014 08:29:52.80 UTC						
Ref. state	-3944.852	3166.151	4621.937	-6.052596	-3.927433	-2.460712
Est. state	-3944.852	3166.125	4621.962	-6.053030	-3.931060	-2.455444
St. dev. σ	±0.024	±0.019	±0.013	±0.467E-3	±1.333E-3	±2.105E-3
Observation 4R, reference epoch: 23/09/2014 08:29:53.15 UTC						
Ref. state	-3946.970	3164.776	4621.075	-6.050888	-3.928804	-2.462719
Est. state	-3946.996	3164.768	4621.062	-6.050103	-3.924708	-2.469463
St. dev. σ	±0.028	±0.023	±0.015	±0.501E-3	±1.412E-3	±2.222E-3

Table 4.9. Object 25723, estimated states for observations 3R and 4R

results in large position and velocity errors between the propagated and the reference trajectory, as can be observed in Figure 4.19. For both orbital states the error rapidly increases and reaches 140 km after 24 hours of propagation for the position and 0.15 km/s for the velocity.

In both comparison there is no evident advantage in choosing layout (A) and (B) for the multibeaming receiver. For the first object there is a slight improvement in the estimated state but the error for the second case becomes larger when layout (B) is used. For the last observation set it was thus decided to use the first multibeaming geometry. The resulting tracklets for simulated observations 5R and 6R are represented in Figure 4.20. On the left the tracklet is the one obtained with a transmitter located in Bagnara, whereas on the right the transmitter is located close to the SRT site. The tracklets are really similar, the only difference is the SNR measured by the beams.

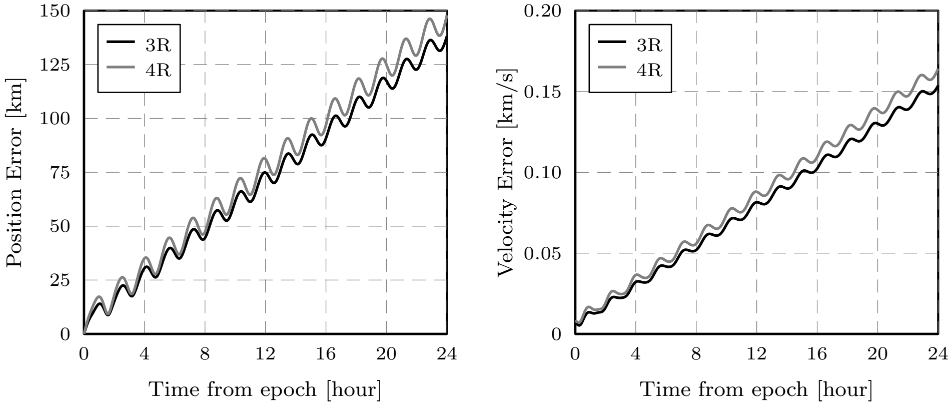

Figure 4.19. Position and velocity error between the the reference and the estimated trajectory of object 25723 for the 24 h following the radar observation. The propagation of the estimated states is performed with AIDA.

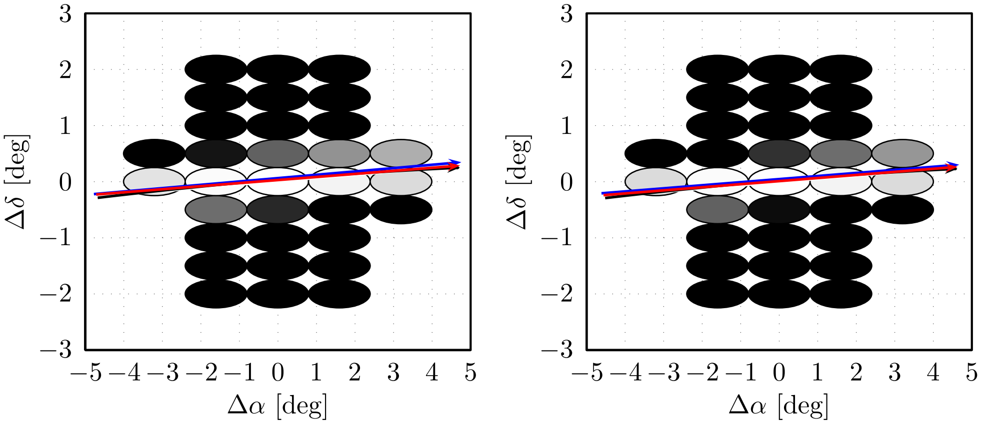

(a) Receiver tracklet for observation 5R (TX: Bagnara)

(b) Receiver tracklet for observation 6R (TX: SRT)

Figure 4.20. Receiver tracklets for bistatic radar observations of object 37820. The black arrow is the reference trajectory, the blue line the first estimate of the trajectory in the α-δ plane, and the red line the refined trajectory. The receiver beams are coloured according to the measured SNR.

The estimated orbital states for the two observations are listed in Table 4.10. The uncertainties are similar to the ones obtained for the previously presented ODs. The errors in position and velocity are larger than in the previous cases, in particular for what concerns the state estimated from observation 6R, where position components have errors of hundreds of meters.

As a result the displacement is even larger than for object 25723, as it can be observed in Figure 4.21. Besides that, another source of error is the lack of an appropriate estimation of the area-to-mass ratio for this observation. This increases the position and velocity error because the object is at a really low altitude (350 km) and has a large area, with an RCS of approximately 20 m^2.

	RX [km]	**RY** [km]	**RZ** [km]	**VX** [km/s]	**VY** [km/s]	**VZ** [km/s]
Observation 5R, reference epoch: UTC						
Ref. state	2828.978	4082.092	4562.402	-6.503424	4.077740	0.388543
Est. state	2828.943	4081.937	4562.536	-6.501331	4.084546	0.369195
St. dev. σ	±0.025	±0.034	±0.016	±0.604E-3	±0.685E-3	±1.995E-3
Observation 6R, reference epoch: UTC						
Ref. state	2828.003	4082.704	4562.460	-6.503975	4.076946	0.387652
Est. state	2827.834	4082.353	4562.477	-6.496159	4.088654	0.376651
St. dev. σ	±0.037	±0.050	±0.019	±1.405E-3	±1.599E-3	±1.643E-3

Table 4.10. Object 37820, estimated states for observations 5R and 6R

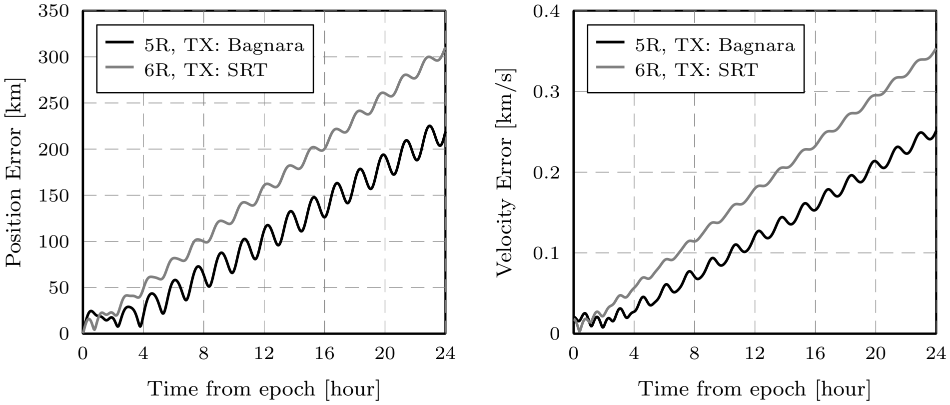

Figure 4.21. Position and velocity error between the the reference and the estimated trajectory of object 37820 for the 24 h following the radar observation. The propagation of the estimated states is performed with AIDA.

4.4.3 Orbit determination with radar and optical measurements

In this subsection the case of mixed optical and radar observation is tackled. The first two objects of Table 4.1 are considered for this analysis. The first numerical test considers object 19046, and takes into account the three optical observations of Table 4.3 and the radar observation of Table 4.7 for a total of four different observations. Three different orbit determinations are performed:

A. Three optical observations and one radar observation are used, the area-to- mass ratio is estimated in the orbit determination process.

B. Three optical observations and one radar observation are used, the area-to-mass ratio is computed by fitting a set of orbital states generated from the same TLE on a time window of 48 hours centred at the TLE epoch.

C. Three optical observations and one radar observation are used, the area-to-mass ratio is computed from the ballistic coefficient of the TLE closest to the first observation.

The resulting orbital states are listed in Table 4.11. First of all it can be noticed that the area-to-mass ratio computed from the ballistic coefficient of the TLE is one order of magnitude smaller than the reference value (obtained from a fit of the TLE states). The area-to-mass ratio estimated with OD A is instead close to the reference one, obtained by fitting the TLE states. Note that for the OD with both state and area-to-mass ratios estimation the uncertainty on position and velocity are quite high. The ill-conditioning caused by the similar optical observation is thus impacting the estimate of the area to mass. The estimate of position and velocity are in good accordance with the reference values apart from the last case. The reason is that the

	RX [km]	**RY** [km]	**RZ** [km]	**VX** [km/s]	**VY** [km/s]	**VZ** [km/s]	AoM [m^2/kg]	AoM SRP [m^2/kg]
Ref. state	-3069.770	-3835.251	4872.005	2.189671	4.995551	5.297757	8.888E-3	1.249E-3
OD A	-3069.765	-3835.222	4871.913	2.189603	4.995776	5.297703	9.971E-3	1.394E-4
St. dev. σ	±0.180	±0.226	±0.289	±0.319E-3	±0.201E-3	±0.319E-3	-	-
OD B	-3069.774	-3835.243	4871.884	2.189564	4.995735	5.297767	8.888E-3	1.249E-3
St. dev. σ	±0.015	±0.018	±0.022	±0.076E-3	±0.062E-3	±0.043E-3	-	-
OD C	-3069.853	-3835.417	4871.675	2.189279	4.995330	5.298300	4.573E-4	4.573E-4
St. dev. σ	±0.041	±0.049	±0.060	±0.211E-3	±0.173E-3	±0.121E-3	-	-

Table 4.11. Object 37820, estimated states for mixed radar and optical observations. OD A refers to the case of both state and area-to-mass estimation, OD B indicates the case in which the reference value for the area-to-mass ratios are used, and OD C uses instead the area-to-mass value computed directly from the ballistic coefficient of the TLE. Reference epoch: 03/07/2014 19:54:58.062 UTC

state is changed to compensate the mismodelled effect of the air drag, caused by a wrong choice of the associated area-to-mass ratio.

The error between the reference trajectory and the three estimated trajectories, each one propagated with AIDA for 24 hours, are plotted in Figure 4.22. The black curve refers to the orbit determination on both the orbital state and the area-to-mass ratios, for a total of nine variables. The dark gray curve, instead, is obtained propagating the state estimated by setting both area-to-mass ratio for SRP and air drag with the value computed from the ballistic coefficient of the TLE and the gray curve using the area-to-mass ratio estimated from the TLE states fit. The smallest error is obtained for this last case, being the area-to-mass ratios the one used by the reference trajectory. The largest error is obtained for the case where the area-to-mass

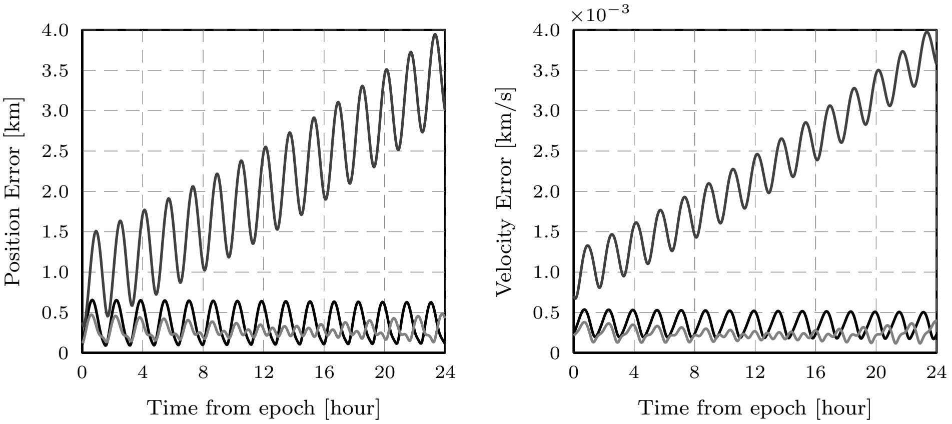

Figure 4.22. Position and velocity error between the the reference and the estimated trajectories of object 19046 for the 24 h following the last observation. The propagation of the estimated states is performed with AIDA. The black curve is obtained with the estimate of both orbital state and area-to-mass during the OD, the dark gray curve with the estimate of the orbital state and the area-to-mass from a TLE fit, and the estimate of the orbital state and the area-to-mass computed from the ballistic coefficient of the TLE.

ratio computed directly from the TLE is used, where the wrong estimate that it is used generates a drift between the two trajectories. The OD algorithm is capable of obtaining a good estimate of the area-to-mass ratios for air drag and SRP using three optical observations and one bistatic radar measurements.

The second numerical test takes into account the set of optical and radar observations of the object 25723 listed in Tables 4.3 and 4.7. Three orbit determinations are performed:

A. Three optical observations and one radar observation are used, the area-to- mass ratio is estimated in the orbit determination process.

B. Three optical observations and one radar observation are used, the area-to-mass ratio is computed by fitting a set of orbital states generated from the same TLE on a time window of 48 hours centred at the TLE epoch.

C. Only the first optical observation and one radar observation are used, the area-to-mass ratio is computed by fitting a set of orbital states generated from the same TLE on a time window of 48 hours centred at the TLE epoch.

The resulting orbital states for each observation are given in Table 4.12 for the first two tests, while the result of the third OD are in Table 4.13 since the reference epoch is different in this case. The estimated states are in good accordance with the reference values, with a maximum difference of 25 m for position components and 0.3 m/s for the full OD with both state and area-to-mass ratios. There is also a good accordance between the estimated area-to-mass ratio and the reference value for the full OD.

Pertaining the third orbit determination, that considers only one optical and one radar observation, it is worth observing that again there is a good correspondence

	RX [km]	**RY** [km]	**RZ** [km]	**VX** [km/s]	**VY** [km/s]	**VZ** [km/s]	AoM [m^2/kg]	AoM SRP [m^2/kg]
Ref. state	1128.017	4559.876	4977.197	-7.501311	0.405709	1.343148	6.617E-3	1.76E-3
OD A	1127.993	4559.851	4977.188	-7.501376	0.405403	1.343050	6.454E-3	2.219E-2
St. dev. σ	±0.008	±0.011	±0.020	±0.019E-3	±0.038E-3	±0.030E-3	-	-
OD B	1128.009	4559.865	4977.243	-7.501318	0.405470	1.343023	6.617E-3	1.76E-3
St. dev. σ	±0.009	±0.010	±0.021	±0.016E-3	±0.032E-3	±0.035E-3	-	-

Table 4.12. Object 25723, estimated states for mixed optical and radar measurements. OD A refers to the case of both state and area-to-mass estimation, while OD B indicates the case in which the reference value for the area-to-mass ratios are used. Reference epoch: 25/09/2014 04:08:44.63 UTC

	RX [km]	**RY** [km]	**RZ** [km]	**VX** [km/s]	**VY** [km/s]	**VZ** [km/s]	AoM [m^2/kg]	AoM SRP [m^2/kg]
Ref. state	561.846	4634.662	5005.796	-7.523969	-0.379063	1.209830	6.617E-3	1.76E-3
Est. state	561.898	4634.665	5005.839	-7.523931	-0.379061	1.209803	6.617E-3	1.76E-3
St. dev. σ	±0.012	±0.019	±0.070	±0.054E-3	±0.040E-3	±0.098E-3	-	-

Table 4.13. Object 25723, estimated states for one optical and one radar measurement. Reference epoch: 24/09/2014 04:40:40.18 UTC

between the estimated and the reference state. Note that in this case the area-to-mass ratio is equal to the reference value during the OD.

The errors between the estimated trajectories and the reference one are plotted in Figure 4.23. The black curve refers to the propagation of the state obtained with an OD aimed at estimating both the state and area-to-mass ratio, the dark gray curve to the state estimated using the area-to-mass ratios obtained from the TLE fit, and the gray curve using the same area-to-mass ratios but two measurements only. In the latter case the error increases with propagation time, reaching 5 km at the end of the propagation window. This is a significant improvement with respect to the case with a single radar observation, where the position error was nearly 150 km after 24 hours. As for object 19046, the difference between the state estimated using the area-to-mass ratio from the TLE fit and the one obtained with an OD on both state and area-to-mass is small, and the two curves are nearly undistinguishable.

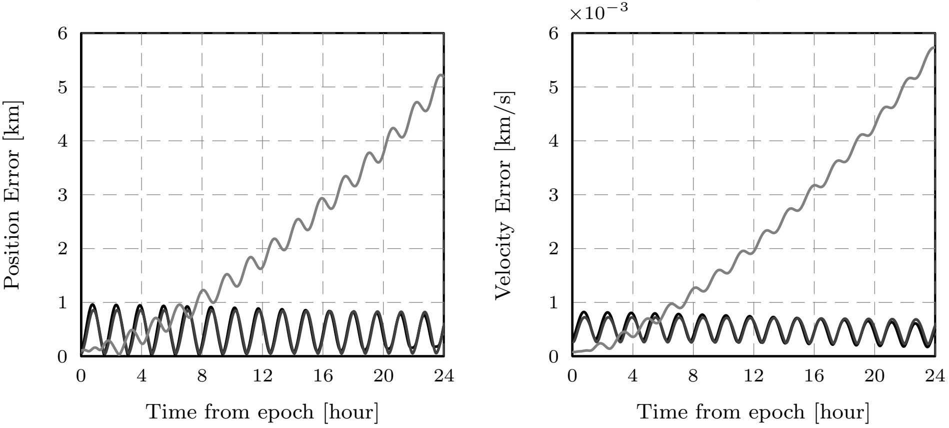

Figure 4.23. Position and velocity error between the the reference and the estimated trajectories of object 25723 for the 24 h following the last observation. The propagation of the estimated states is performed with AIDA. The black curve is obtained with the estimate of both orbital state and area-to-mass during the OD, the dark gray curve with the estimate of orbital state and the area-to-mass from a TLE fit, and the gray curve with an estimate obtained from one optical and one radar measurements only.

4.5 Conclusions

The orbit determination problem of space debris and satellites is tackled as a non-linear least square fit of the available observations. Two simulators to generate optical and bistatic radar observations were developed. The optical simulator considers a standard telescope, equipped with a CCD sensor. The produced observation consists in a sequence of illuminated pixel: knowing the azimuth and elevation at which the telescope was pointing it is possible to estimate the right ascension α, the declination δ and their rates $\dot{\alpha}$, $\dot{\delta}$.

The bistatic radar simulator is tailored for the Northern Cross, which is always employed as a receiver. The multibeaming capability of the BEST-2 array, an upgraded subset of 8 cylinders belonging to the N-S arm of the Northern Cross, are modeled. Different multibeaming geometry and transmitter can be modelled, making this simulator a powerful tool to study and compare the performances of different configurations. An algorithm that processes the measurement data generated by the bistatic radar was developed. The algorithm retrieves the trajectory of the observed object inside the receiver FoV in terms of right ascension and declination, using the information on beam illumination sequence, SNR, and range measurement. The set of observables from a bistatic radar observation after the data processing thus comprises time of observation, range, the sum of range-rates for transmitter and receiver, right ascension, declination and their rates.

Numerical simulations were performed to validate the orbit determination algorithms for RSO. Three sets of optical measurements were simulated for two LEO objects. The orbit determination algorithm was capable of reconstructing the orbital parameters of both object and the error between the reference and estimated trajectory is limited to a few kilometres. For the first object, orbiting in LEO on a nearly sun-synchronous orbit, it was observed that sets of observations taken at the same time for three consecutive days could degrade the accuracy of the OD. In that case the problem is nearly ill-conditioned since the right ascension and declination change is small between the observations.

The orbit determination algorithm developed for a bistatic radar in which the Northern Cross plays the role of a multibeaming receiver was tested on single radar measurements for three different objects. Two multibeaming geometries were compared, both with 32 beams inside the FoV of the antenna. In all cases the estimated position was compatible with the reference one and the uncertainties on the orbital state were a few tens of meters for the position and tens of mm/s for the velocity. The estimate of the velocity is instead influenced by the bistatic radar geometry, i.e. the satellite relative trajectory and transmitter location. For the third observation it was shown that the error on position after 24 hours changes significantly depending on the transmitter location. Further tests must be performed to assess the performances of the bistatic radar and identify the best configuration in terms of multibeaming receiver, transmitter location and antenna characteristics. In addition, the algorithms for the orbit determination should be tested in the presence of unknown RCS, which could have an impact on the measured range and SNR.

Finally, mixed orbit determination tests were performed using both radar and optical measurements. The estimates of the orbital state significantly improves in this case, in particular the large shift in position and velocity for the second object is drastically reduced even if just a single optical observation is processed together with the radar measurement. For what concerns the accuracy of the method, it was found that the uncertainties on the estimated position and velocity for the mixed orbit determination are usually a few tens of meters for the position and a few tens of mm/s for the velocity. When three optical and one bistatic radar measurements are available, an estimate of the area-to-mass ratio for air drag and SRP can also be obtained during the OD.

The case of mixed observations allows a better accuracy in the estimation of the orbital state of the observed object with respect to both radar-only and optical-only measurements. To reduce the uncertainty on the object state it is important to have observations available in a short time window, no longer than a few days. For what concerns the optical observation, it was found that the orbit determinations can be ill-conditioned when the observations are performed from the same observatory, at similar times during consecutive days, as the object tends to have close values of right ascension and declination in those observations.

As a consequence, the Northern Cross could represent a powerful instrument if operated in the stare-and-chase mode, provided that the radar ranging is available[1]. The large area of approximately 27,400 m^2 could provide a high sensitivity and the maximum FoV of 120 deg^2 could be "plastered" with up to 46,000 beams $4' \times 4'$ wide. Tests on this configuration will be performed to assess the improvements in the accuracy of the orbit determination and possibly determining whether a near-real-time OD process can be performed to allow a fast schedule of further observations for uncatalogued objects.

---

[1] currently the system was tested for continuous-wave only and ranging is not possible

5

Conjunction identification

The detection of orbital conjunctions between spacecraft and space debris is of fundamental importance in SSA programs. Once a potentially dangerous closest approach is identified, for instance by looking at the minimum distance between the objects, all information required to analyse the conjunction is provided to satellite operators that will compute the collision probability and evaluate the collision risk.

The collision risk depends on the geometry of the encounter and is considerably affected by the uncertainties of the orbital states at the Time of Closest Approach (TCA). These uncertainties, in turn, depend on the uncertainties on initial state and their evolution along the orbit. When the TCA is far away from the reference epoch of the initial state, nonlinearities can play an important role in the computation of collision probability, since the initial covariance ellipsoid stretches and deforms after each revolution.

In the past, the conjunction assessment procedures relied on the catalog of unclassified objects orbiting the Earth, maintained by the USSTRATCOM. The catalog is still available nowadays and contains all up-to-date TLE, that are intended for the use with the SGP4/SDP4 orbital model. The Center for Space Standards and Innovation (CSSI) produces daily reports of closest conjunctions for the upcoming week using the program Satellite Orbital Conjunction Reports Assessing Threatening Encounters in Space (SOCRATES)[1] [Kel05]. The conjunctions are identified using TLEs and SGP4/SDP4 and the tool also computes the maximum conjunction probability [Alf05b], which represents the upper bound of collision probability and is obtained assuming the worst-case orientation and size of the covariance matrices.

When using TLEs and the SGP4/SGP4 analytical propagator, it has to be taken into account that the TCA can vary up to tens of seconds and the Distance of Closest Approach (DCA) up to a few kilometers if more recent TLEs are considered for conjunction detection. Propagation accuracy of SGP4/SDP4 is indeed object dependent, and after a few days of propagation the errors can easily exceed tens of kilometres. In addition, potentially significant biases exist in TLE data [Kel07].

Nevertheless, when precise ephemeris of the chasers are not available, TLEs can represent a significant source of information. It is possible to estimate covariance

---

[1] The information is publicly posted at www.celestrak.com/SOCRATES/

information for TLEs by comparing states derived directly from the TLE data with states resulting from an orbit determination using pseudo-observations derived from TLE data [Ala04]. Alternatively, it is possible to derive a covariance matrix differencing a set of TLEs propagated up to a common time [Lap08, Val12].

Besides the publicly available TLE catalog, the Joint Space Operation Center (JSpOC) maintains an High-Accuracy Special Perturbation Catalog [Cof98] and releases Conjunction Summary Messages (CSM) to warn satellite operators of incoming close conjunctions [Aid12]. The CSM also provides the chaser covariance matrices at the TCA which can be used, together with satellite ephemeris, for accurate collision risk assessment.

The operational service for the assessment of collision risks of ESA satellites is based on the collision risk assessment software CRASS and the orbit determination software ODIN [Flo09a]. A daily automated screening is performed to identify close approached between covered missions and TLE from USSTRATCOM. When the estimated collision probability for an encounter exceeds a given threshold further data are acquired by the operator and processed by ODIN to improve orbit and covariance information. Methods were developed to estimate uncertainties associated with TLEs [Flo09b]. The process was adapted to take into account the CSM and analysis were performed to verify CSM against conjunction event analysis based on radar measurements [Flo13].

In this work, a method for the computation of the DCA and TCA for all the objects compatible with the initial orbital uncertainties (referred to as virtual debris or objects in the remainder of this work) with a single numerical integration is presented. The method is based on the high order Taylor expansion of the flow of the dynamics enabled by DA techniques. In particular, a DA-based integrator and a polynomial inversion algorithm are used to express the dependence of TCA and DCA on orbital uncertainties in terms of high order Taylor polynomials [Arm10a]. As a result, the multiple integrations required by a Monte Carlo based approach for the computation of TCA and DCA for all the virtual debris are substituted by fast polynomial evaluations. The computation of these polynomials and the study of their accuracy is the main focus of this Chapter. Their use for the fast and accurate computation of collision probability will be addressed in Chapter 6.

This Chapter is organized as follows: first a few facts concerning all-vs-all conjunction screening and the strategies to avoid unnecessary computation are briefly described. In Section 5.2 the computation of the TCA and DCA is introduced as global optimization problem. The algorithm for the expansion of the TCA and DCA is then introduced in Section 5.3. Some numerical examples are then provided: the strategy of Section 5.2 is first used to generate initial guesses for the TCA and DCA. Then, the algorithm of Section 5.3 is used to obtain the DA expansion of time and distance of closest approach using the polynomial maps generated with AIDA.

5.1 All-vs-all screening: a few remarks

One of the more challenging issues of conjunction identification is the necessity to deal with a huge number of possible threatening objects. The total number of RSO, according to Table 1.1, is $n_{\text{rso}} = 17129$. Thus, since the total number N of independent combinations in an all-vs-all screening is equal to

$$N = \frac{1}{2}\left({n_{\text{rso}}}^2 - n_{\text{rso}}\right), \tag{5.1}$$

there are nearly $N = 1.47 \times 10^8$ combinations to be analyzed each time. The above formula can be graphically explained by associating the RSO to rows and columns of a square matrix: each element (i, j) will then corresponds to a combination. The residual combinations, assuming that the order of elements is the same on the two dimensions, are represented by the upper triangular, colored in gray in Figure 5.1.

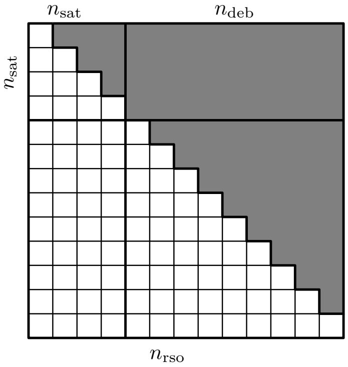

Figure 5.1. Graphical scheme for all-vs-all independent combinations

When the debris-vs-debris conjunctions are not of interest, the number of independent combinations reduces to

$$\tilde{N} = \frac{1}{2}\left({n_{\text{sat}}}^2 - n_{\text{sat}}\right) + n_{\text{sat}}\, n_{\text{deb}}, \tag{5.2}$$

where n_{sat} is the number of active satellites and $n_{\text{deb}} = (n_{\text{rso}} - n_{\text{sat}})$ is the number of debris. Even in this case the total number of combinations is still huge, with $\tilde{N} = 6 \times 10^7$ since the number of satellites is $n_{\text{sat}} = 3966$. It is thus evdent how important is the computational efficiency of the algorithms used for conjunction identification. For this purpose differents sets of geometrical and analytical filters were developed to quickly exclude objects combinations that will not result in close conjunctions [Hoo84, Ala02]. The sequential use of these filters can reduce the number of object combinations down to 10% of the total with a limited computational effort. The computation of TCA and DCA for each couple of objects is thus usually performed after an initial sieving to reduce computational time and enable the production of conjunction alerts on a daily basis.

5.2 Close conjunction identification as a global optimization problem

The computation of the TCA and DCA between two space bodies in a given time window is formulated as an optimization problem in which the global minimum of the square distance function between the two orbiting bodies is searched. The rigorous global optimizer COSY-GO is used for this task: since the the branch-and-bound algorithm works with TM, an analytical formulation for the objective functions is required. As a consequence, the DA implementation of SGP4/SDP4 is used to compute the position and velocity of the spacecraft. The square of the distance function is the objective function to be minimized

$$J_{GM}(t) = d(t)^2 = (\boldsymbol{r}_2 - \boldsymbol{r}_1) \cdot (\boldsymbol{r}_2 - \boldsymbol{r}_1). \tag{5.3}$$

For problems of practical interest the computation of all the minima of the square distance function can be important, as a local minimum occurring before the TCA can potentially represent a risky condition (this is particularly true when models accuracy and uncertainties on orbit determination are taken into account). When all the minima are searched for, firstly the time derivative of the square distance is computed

$$\frac{\mathrm{d}d(t)^2}{\mathrm{d}t} = 2d\dot{d} = 2(\boldsymbol{v}_2 - \boldsymbol{v}_1) \cdot (\boldsymbol{r}_2 - \boldsymbol{r}_1), \tag{5.4}$$

then the objective function is set to

$$J_{SP}(t) = [(\boldsymbol{v}_2 - \boldsymbol{v}_1) \cdot (\boldsymbol{r}_2 - \boldsymbol{r}_1)]^2. \tag{5.5}$$

Note that Eq. (5.5) is positive semidefinite, and its zeros (i.e. its global minima) are stationary points of the distance function. These stationary points are then classified by exploiting the high order derivatives included in the polynomial part of the Taylor model.

5.3 DCA and TCA expansion

Uncertainties in orbital measurements and orbital determination process result in uncertainties in the initial orbital state of the space objects. Consequently, each pair of virtual debris is characterized by a different value of TCA. In this section the procedure to obtain the Taylor expansion of TCA and DCA is described, provided that a first guess of TCA is available. The method described in Section 5.2 is here used to obtain an estimate of TCA and DCA, but any other method can be used for this purpose. In the remainder of the Chapter, the first guess values of TCA and DCA identified by this method are referred to as t^*_{FG} and d^*_{FG}, respectively.

5.3.1 TCA and DCA expansion algorithm

The aims of the algorithm presented in this section are:

1. Starting from t^*_{FG} and d^*_{FG}, compute the nominal value of TCA and DCA. These values will be referred to as t^* and d^*.
2. Compute the Taylor expansion of t^* and d^* with respect to the initial conditions of the two objects:

$$\begin{aligned} [t^*] &= t^* + \left(\delta \boldsymbol{x}_0^1, \delta \boldsymbol{x}_0^2\right) \\ [d^*] &= d^* + \left(\delta \boldsymbol{x}_0^1, \delta \boldsymbol{x}_0^2\right) \end{aligned} \tag{5.6}$$

   where $\boldsymbol{x}_0^1$ and $\boldsymbol{x}_0^2$ are vectors of six elements (any set of orbital elements, e.g. Keplerian elements, Delunay variables, position and velocity in any arbitrary reference frame, can be used).

The algorithm starts with the initialization of the initial orbital states and the final time as DA variables

$$\begin{aligned} \left[\boldsymbol{x}_0^1\right] &= \boldsymbol{x}_0^1 + \delta \boldsymbol{x}_0^1 \\ \left[\boldsymbol{x}_0^2\right] &= \boldsymbol{x}_0^2 + \delta \boldsymbol{x}_0^2 \end{aligned}, \tag{5.7}$$

$$[t_f] = t^*_{FG} + \delta t. \tag{5.8}$$

Note that the nominal value of the final time is set to the first guess TCA delivered by the global optimizer.

The resulting objects initial conditions are propagated forward with AIDA and, according to Section 2.4, the Taylor polynomials of the final state are obtained as function of time and initial uncertain states

$$\begin{aligned} \left[\boldsymbol{x}_f^1\right] &= \boldsymbol{x}_f^1 + \mathcal{M}_{\boldsymbol{x}_f^1}\left(\delta t,\, \delta \boldsymbol{x}_0^1\right) \\ \left[\boldsymbol{x}_f^2\right] &= \boldsymbol{x}_f^2 + \mathcal{M}_{\boldsymbol{x}_f^2}\left(\delta t,\, \delta \boldsymbol{x}_0^2\right). \end{aligned} \tag{5.9}$$

Note that the polynomial map can also be obtained using any other DA implementation of an orbital propagation, e.g. SGP4/SDP4. The algorithm does not need any modification to obtain the expansion of the TCA and DCA starting from polynomial maps that are not produced with AIDA.

In Eq. (5.9), $\boldsymbol{x}_f^1$ and $\boldsymbol{x}_f^2$ are the nominal final positions of the two objects at time t^*_{FG}, whereas $\mathcal{M}_{\boldsymbol{x}_f^1}\left(\delta t,\, \delta \boldsymbol{x}_0^1\right)$ and $\mathcal{M}_{\boldsymbol{x}_f^2}\left(\delta t,\, \delta \boldsymbol{x}_0^2\right)$ are the higher order terms of the

Taylor polynomials that describe how changes in both final time and initial conditions affect the final states.

After the integration, the squared relative distance can be computed in the DA framework, resulting in

$$[d^2] = d^2 + \mathcal{M}_{d^2}\left(\delta t,\, \delta \boldsymbol{x}_0^1,\, \delta \boldsymbol{x}_0^2\right), \tag{5.10}$$

which is a Taylor polynomial of 13 variables. By using the operator of differentiation implemented in COSY-Infinity, the Taylor polynomial

$$\left[\frac{\partial d^2}{\partial t}\right] = c_0 + \mathcal{M}_{\frac{\partial d^2}{\partial t}}\left(\delta t,\, \delta \boldsymbol{x}_0^1,\, \delta \boldsymbol{x}_0^2\right) \tag{5.11}$$

is computed. Note that the constant part c_0 is not zero as the numerical integration in AIDA is stopped at t^*_{FG}, which is the nominal TCA when SGP4/SDP4 is used for the propagation. By subtracting c_0 to (5.11), and defining $\delta\frac{\partial d^2}{\partial t} = \left[\frac{\partial d^2}{\partial t}\right] - c_0$, the following origin preserving augmented map can be built

$$\begin{bmatrix} \delta\frac{\partial d^2}{\partial t} \\ \delta \boldsymbol{x}_0^1 \\ \delta \boldsymbol{x}_0^2 \end{bmatrix} = \begin{bmatrix} \mathcal{M}_{\frac{\partial d^2}{\partial t}} \\ \mathcal{I}_{\delta \boldsymbol{x}_0^1} \\ \mathcal{I}_{\delta \boldsymbol{x}_0^2} \end{bmatrix} \begin{bmatrix} \delta t \\ \delta \boldsymbol{x}_0^1 \\ \delta \boldsymbol{x}_0^2 \end{bmatrix}, \tag{5.12}$$

where identities in the variation of the initial states are added. This polynomial map can then be inverted using suitable polynomials inversion techniques [Ber99b] obtaining

$$\begin{bmatrix} \delta t \\ \delta \boldsymbol{x}_0^1 \\ \delta \boldsymbol{x}_0^2 \end{bmatrix} = \begin{bmatrix} \mathcal{M}_{\frac{\partial d^2}{\partial t}} \\ \mathcal{I}_{\delta \boldsymbol{x}_0^1} \\ \mathcal{I}_{\delta \boldsymbol{x}_0^2} \end{bmatrix}^{-1} \begin{bmatrix} \delta\frac{\partial d^2}{\partial t} \\ \delta \boldsymbol{x}_0^1 \\ \delta \boldsymbol{x}_0^2 \end{bmatrix}. \tag{5.13}$$

The goal is to compute δt such that $\left[\frac{\partial d^2}{\partial t}\right] = 0$. This is obtained by evaluating (5.13) in $\delta\frac{\partial d^2}{\partial t} = -c_0$

$$\begin{bmatrix} \delta t \\ \delta \boldsymbol{x}_0^1 \\ \delta \boldsymbol{x}_0^2 \end{bmatrix} = \begin{bmatrix} \mathcal{M}_{\frac{\partial d^2}{\partial t}} \\ \mathcal{I}_{\delta \boldsymbol{x}_0^1} \\ \mathcal{I}_{\delta \boldsymbol{x}_0^2} \end{bmatrix}^{-1} \begin{bmatrix} -c_0 \\ \delta \boldsymbol{x}_0^1 \\ \delta \boldsymbol{x}_0^2 \end{bmatrix}. \tag{5.14}$$

Note that the first row of the map in Eq. (5.14) is a Taylor polynomial with 1) a constant part that is the correction to t^*_{FG} necessary to impose the stationarity of d^2 in the AIDA propagator 2) higher order terms that approximate how the TCA changes depending on the uncertainties in the initial conditions. By plugging the first row of Eq. (5.14) into Eq. (5.8) the following result is achieved

$$[t_f] = [t^*] = t^* + \mathcal{M}_{t^*}(\delta\boldsymbol{x}_0^1, \delta\boldsymbol{x}_0^2), \tag{5.15}$$

which is the high order Taylor expansion of the TCA evaluated with the numerical integrator AIDA. Similarly, the high order expansion of the squared distance is obtained by inserting the first row of Eq. (5.14) into Eq. (5.10), yielding

$$[{d^*}^2] = {d^*}^2 + \mathcal{M}_{d^{*2}}\left(\delta\boldsymbol{x}_0^1,\, \delta\boldsymbol{x}_0^2\right). \tag{5.16}$$

The main features of Maps (5.15) and (5.16) are

1. They are nonlinear and analytical.
2. Their accuracy can be suitably adjusted by tuning the expansion order.
3. They reduce the uncertainty analysis to the evaluation of Taylor polynomials.
4. They can be used to study the effect of uncertainties for arbitrary statistics.
5. They can be easily extended to include uncertainties on parameters other than initial orbital elements (e.g., Bstar for SGP4/SDP4).

For any perturbed initial condition of the two objects (i.e., for any pair of virtual debris) the evaluation of the Taylor polynomials in Eq. (5.15) and (5.16) delivers the associated values of TCA and DCA. Of course, these values are not exact: their accuracy depends on the selected expansion order, the propagation window, and the range of the uncertainties on the initial conditions.

5.4 Numerical simulations

In this section the methods for conjunction identification described in this chapter are tested. In Section 5.4.1 the method for the identification of all stationary points of the relative distance is applied to three test cases. One close conjunction is then selected for each of the three object combinations and is then used as an initial guess for the TCA and DCA expansion in Section 5.4.2. The accuracy of the TCA and DCA polynomial approximation is then assessed in Section 5.4.3.

5.4.1 Preliminary identification via global optimization

The method described in Section 5.2 for the computation of the stationary points of the relative distance using SGP4/SDP4 and global optimizer COSY-GO are applied to space objects combinations identified in Table 5.1. The objects are the same considered in Chapter 3 and the TLEs used for propagation are listed in Appendix A.1.

Test Case	Sat. No.	Sat. Name	a [km]	e [-]	I [deg]	Orbit
A	11510	COSMOS 1125	7161	1.15E-3	74.04	LEO
	21574	ERS 1	7149	3.49E-3	98.25	LEO
B	20237	COSMOS 2043	7787	4.19E-4	82.57	LEO
	23820	OPS 0856 DEB	9895	2.20E-1	87.62	HEO
C	36744	COMS 1	42165	7.88E-5	0.01	GEO
	28194	RADUGA 1-7	42166	1.21E-4	5.28	GEO

Table 5.1. Selected objects

LEO satellites

The first test case, labeled A, involves two LEO satellites, COSMOS 1125 and ERS 1. The orbits of the two satellites are plotted in Figure 5.2(a). The two objects orbits have the same altitude and the angle between the orbital planes is approximately 90 deg. The two satellites approaches twice for each revolution when transiting over the Earth's poles.

The stationary points are computed for one week starting from 25 January 2013, 14:09 UTC. The total number of stationary points found is 401 of which 200 are local minima. The computational time is 5.1 seconds using an expansion order $n = 2$. In Figure 5.2(b) the relative distance is plotted around the global minima that occurs on 26 January, 17:45 UTC. The stationary points are marked in gray, with local minima identified by a plus and local maxima by a diamond marker.

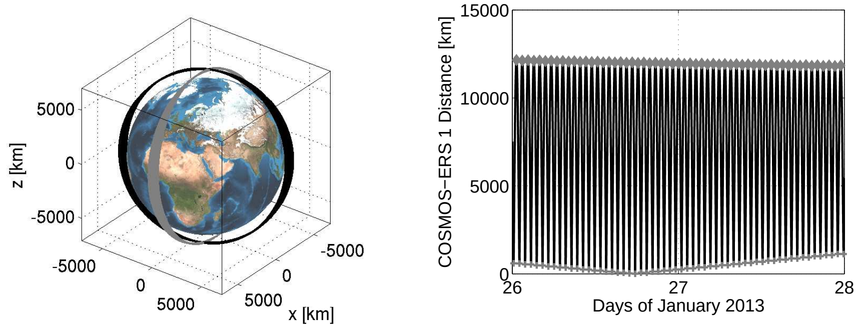

(a) Trajectories of COSMOS 1125 (in black) and ERS 1 (in grey) spacecraft.

(b) COSMOS–ERS 1 distance function. In grey the stationary points identified by COSY-GO.

Figure 5.2. COSMOMS 1125 and ERS 1 conjunction problem

LEO and HEO satellites

The second test case, labeled B, involves COSMOS 2043, a LEO satellite, and a debris from satellite OPS 0856 whose orbit is here classified as HEO. The trajectories of the two space objects are plotted in Figure 5.3(a). Due to the higher eccentricity of OPS debris the close conjunctions can occur only once in an orbit when both objects are transiting over the North pole. In this case the angle between the two orbital planes is lower than 90 deg, resulting in lower relative velocities at the conjunction.

The stationary points are computed for one week starting from 5 March 2013, 13:10 UTC. The stationary points found are 302, with 151 local minima. In this case the computational time is 5.8 seconds using an expansion order $n = 2$. The relative distance according to SGP4/SDP4 propagation and the corresponding stationary points, marked in gray, are plotted in Figure 5.3(b). The global minima is on 7 March 2013, 06:43 UTC. It is worth observing that the relative distance has a much more complex shape with respect to the LEO and GEO cases, where the periodicity of the function period can be immediately identified. Due to the different orbital periods and perturbations effects, the position and value of maxima and minima is less predictable. In addition, the value of the relative distance value between a local maxima and the subsequent local minima can be really small in some cases. This reflects in the slightly larger computational time with respect to test case A.

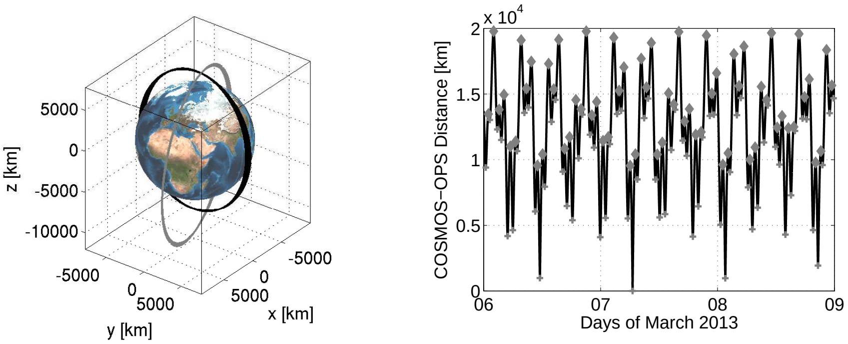

(a) Trajectories of COSMOS 2043 (in black) and OPS 0856 (in grey) spacecraft.

(b) COSMOS–OPS distance function. In grey the stationary points identified by COSY-GO.

Figure 5.3. COSMOMS 2043 and OPS 0856 conjunction problem

GEO satellites

The third test case considers the close approach between the satellites COMS and RADUGA 1-7 whose trajectories are propagated with SGP4/SDP4.

Figure 5.4 shows the conjunction problem between COMS and RADUGA 1-7 spacecraft. Figure 5.4(a) shows the orbits of two satellites. The Korean COMS satellite is in GEO at 128.2 deg East ±0.05 deg and the Russian RADUGA 1-7

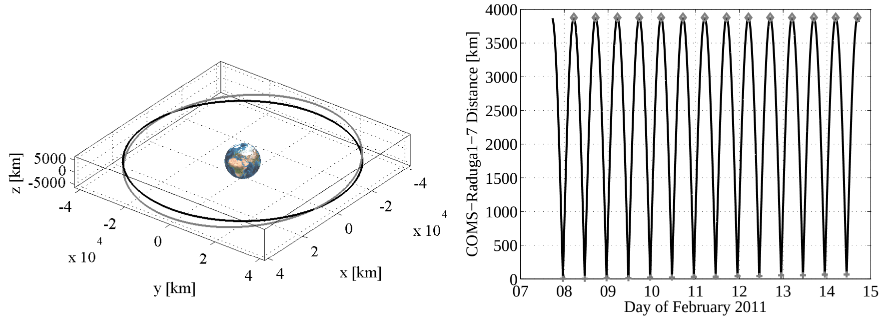

(a) Trajectories of COMS (in black) and RADUGA 1-7 (in grey) spacecraft.

(b) COMS–RADUGA 1-7 distance function. In grey the stationary points identified by COSY-GO.

Figure 5.4. COMS and RADUGA 1-7 conjunction problem

satellite is in inclined GEO at 128.0 deg East ±0.5 deg. When the RADUGA 1-7 satellite passes through the longitude of 128.2 deg East, close approaches of the two satellites happen two times a day during a few days. This effect is shown in Figure 5.4(b) where the distance function is plotted for one week starting from 7 February 2011, 17:28 UTC. In the same figure the stationary points of the distance function computed with COSY-GO are marked in grey.

In Table 5.2 the function evaluations and the computational time are reported for different expansion orders and interval widths in which the search space is initially subdivided. (Note that the number of initial intervals is the minimum value of function evaluations required by the optimizer to solve the problem). A minimum dimension of 10^{-4} hr is considered for the optimizer for all the simulations. It can be remarked that

1. For fine grids only few additional function evaluations are required by the optimizer to compute the global optimum

2. Increasing the expansion order reduces the number of function evaluations as tighter enclosures of the objective functions are obtained (this effect is magnified for large widths)

3. For moderately small widths the minimum value of function evaluations is already obtained with third order computations.

4. Small interval widths increase the number of function evaluations as unnecessary evaluations are imposed.

5. Large interval widths increase the number of function evaluations as many interval splittings are necessary.

Interval width (hr)	0.5	1	2	4
# of interval	336	168	84	42
order	Function evaluations (computational time)			
1 (J_{GM})	386 (0.33 s)	288 (0.48 s)	322 (0.67 s)	372 (0.67 s)
1 (J_{SP})	540 (1.29 s)	714 (1.60 s)	798 (1.73 s)	840 (1.73 s)
2 (J_{GM})	341 (0.27 s)	200 (0.28 s)	159 (0.42 s)	201 (0.43 s)
2 (J_{SP})	450 (1.43 s)	317 (1.05 s)	401 (1.26 s)	443 (1.26 s)
3 (J_{GM})	339 (0.29 s)	185 (0.32 s)	114 (0.40 s)	156 (0.40 s)
3 (J_{SP})	446 (1.91 s)	303 (1.47 s)	303 (1.57 s)	345 (1.57 s)
4 (J_{GM})	339 (0.37 s)	185 (0.43 s)	112 (0.48 s)	154 (0.47 s)
4 (J_{SP})	445 (2.67 s)	303 (2.07 s)	246 (1.78 s)	288 (1.78 s)
5 (J_{GM})	339 (0.44 s)	185 (0.55 s)	111 (0.60 s)	153 (0.61 s)
5 (J_{SP})	445 (3.50 s)	303 (2.72 s)	221 (2.06 s)	263 (2.06 s)

Table 5.2. Function evaluations as function of expansion order and interval width for objective function J_{GM} and J_{SP}

6. The computational time (in general) increases with the function evaluations and with the expansion order but, for a given expansion order, it is possible to have lower computational times associated to higher number of function evaluations. This is due to a different sequence of polynomial bounders used by the optimizer for the reduction of the search space.

The stationary points identified by COSY-GO are listed in Table 5.3 for an initial discretization of 2 hr and third order expansion. The values matches those reported in [Lee11] and that can be computed running the Matlab version of SGP4 released by David Vallado [1].

Figure 5.5 summarizes the results obtained with a Monte Carlo run of 50000 samples on the expansion maps (5.15) and (5.16) around the DCA. For both spacecraft the statistical analysis considers the following values of standard deviations for the mean orbital parameters: $\sigma_a = 1000$ m, $\sigma_e = 1 \times 10^{-5}$, $\sigma_i = 1 \times 10^{-2}$ deg, $\sigma_\Omega = 1 \times 10^{-2}$deg, $\sigma_\omega = 1 \times 10^{-2}$ deg, $\sigma_M = 1 \times 10^{-2}$ deg. These values do not have any practical justification (e.g., they are not derived by pseudo-observations derived from TLE data), but are assumed to show the capability of the method of managing large uncertainty sets. Figure 5.5(a) shows the distribution of the minimum distance between the two spacecraft, characterized by a 0 percentile of 3.948 m. Note that for the large uncertainties introduced on initial conditions, the set of TCA reported in Figure 5.5(b) has a width of the order of a minute. The CPU time required to run the algorithm of Section 5.3.1 at 5-th order is 0.19 s, and the Monte Carlo simulation

---

[1] downloadable from `http://celestrak.com/software/vallado-sw.asp`

Julian date	Distance [km]	Type
[2455607.199784, 2455607.199786]	[3878.274475, 3878.274477]	GMax
[2455606.950425, 2455606.950427]	[66.692821, 66.692824]	LMin
[2455606.701130, 2455606.701132]	[3877.560944, 3877.560946]	LMax
[2455606.451835, 2455606.451837]	[65.351702, 65.351704]	LMin
[2455606.202486, 2455606.202488]	[3878.272781, 3878.272783]	LMax
[2455605.953130, 2455605.953132]	[55.213738, 55.213740]	LMin
[2455605.703838, 2455605.703840]	[3877.513184, 3877.513186]	LMax
[2455605.454545, 2455605.454547]	[53.932389, 53.932391]	LMin
[2455605.205198, 2455605.205200]	[3878.171056, 3878.171058]	LMax
[2455604.955846, 2455604.955848]	[43.870709, 43.870711]	LMin
[2455604.706556, 2455604.706558]	[3877.361346, 3877.361348]	LMax
[2455604.457266, 2455604.457268]	[42.662315, 42.662317]	LMin
[2455604.207922, 2455604.207924]	[3877.971065, 3877.971067]	LMax
[2455603.958573, 2455603.958575]	[32.681655, 32.681658]	LMin
[2455603.709286, 2455603.709288]	[3877.124761, 3877.124763]	LMax
[2455603.459999, 2455603.460001]	[31.542157, 31.542159]	LMin
[2455603.210657, 2455603.210659]	[3877.705390, 3877.705392]	LMax
[2455602.961311, 2455602.961313]	[21.635605, 21.635607]	LMin
[2455602.712027, 2455602.712029]	[3876.844429, 3876.844431]	LMax
[2455602.462743, 2455602.462745]	[20.546279, 20.546281]	LMin
[2455602.213402, 2455602.213404]	[3877.418900, 3877.418902]	LMax
[2455601.964060, 2455601.964062]	[10.714866, 10.714868]	LMin
[2455601.714777, 2455601.714779]	[3876.565917, 3876.565919]	LMax
[2455601.465495, 2455601.465497]	[9.642766, 9.642768]	LMin
[2455601.216156, 2455601.216158]	[3877.156134, 3877.156136]	LMax
[2455600.966815, 2455600.966817]	[1.357918, 1.357920]	GMin
[2455600.717533, 2455600.717535]	[3876.332666, 3876.332668]	LMax
[2455600.468253, 2455600.468255]	[1.676237, 1.676239]	LMin

Table 5.3. Stationary points of the square distance function between COMS and RADUGA 1-7.

of 50000 samples takes 14.26 s (this is due to the evaluations of Taylor polynomials of 12 variables; the computational time reduces to 3.85 and 0.86 s for 4-th and 3-rd order computations, respectively).

5.4.2 Nominal TCA identification and time expansion accuracy

Three close approaches are selected among those identified in the previous section using TLEs and SGP4/SDP4 propagations. The selected TCA and DCA are reported in Table 5.4, together with the relative velocity Δv at the close approach. It can be observed that the relative velocity at the close encounter varies from more than 12 km/s for LEO to a few hundred m/s for the geosynchronous case. As a result, the close approaches can last from few seconds up to tens of seconds or even minutes.

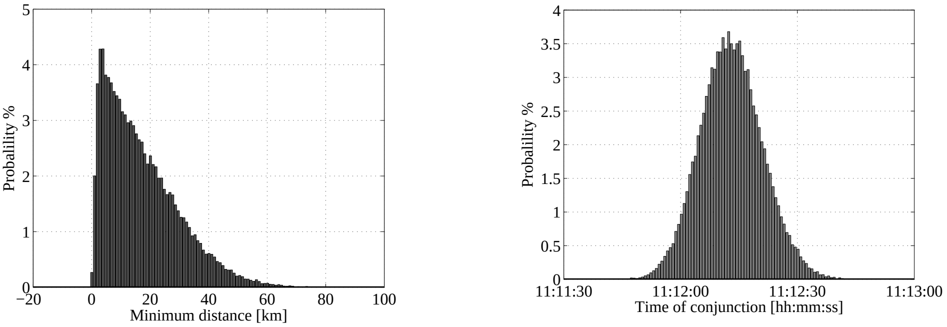

(a) Minimum distance statistical distribution

(b) Conjunction time distribution

Figure 5.5. Statistical analysis of COMS and RADUGA 1-7 conjunction

Test case	Sat. No.	Orbit	TCA [days]	TCA	DCA [km]	Δv [km/s]
A	11510	LEO	3.538	2013 Jan 26 17:45:19	1.149	12.472
	21574	LEO	3.805			
B	20237	LEO	4.125	2013 Mar 07 06:34:23	6.064	8.553
	23820	HEO	2.403			
C	36744	GEO	0.240	2011 Feb 07 23:14:17	1.676	0.283
	28194	GEO	0.431			

Table 5.4. Close approaches: first guesses with SGP4/SDP4

Figure 5.6 illustrates the relative distance as a function of time in the neighbourhood of TCA for the three close approaches. The dashed line refers to the relative distance between the two objects computed using TLEs and SGP4/SDP4 propagations; the grey dot is the identified minimum. The relative distance obtained with AIDA propagation is plotted on the same figure with a solid black curve. The TCA of Table 5.4 are used as first guesses for the algorithm described in Section 5.3, which uses the nominal positions and velocities listed in A.1 as inputs. The resulting minima of the relative distances are reported as grey dots on the solid black curves in Figure 5.6. The threshold value used to sieve potentially dangerous approaches, here set to 7.5 km, is indicated by the dashed-dotted lines.

As can be seen, the algorithm correctly identifies the minima of the relative distances computed with AIDA propagations. The differences between the two curves are due to the more accurate dynamical model implemented in AIDA and to the procedure adopted to estimate the initial conditions from TLEs. In particular, the error increases with the distance from the time windows on which the OD process is performed. The largest difference in TCA and DCA is obtained for test case B,

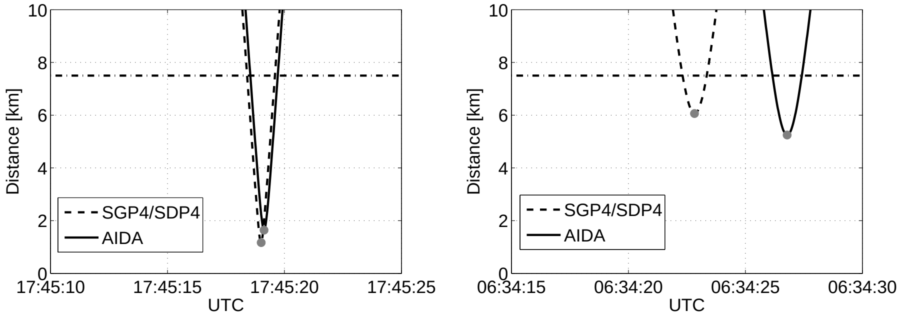

(a) Test case A **(b)** Test case B

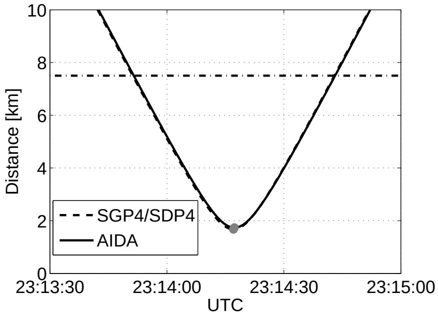

(c) Test case C

Figure 5.6. Comparison of the relative distances obtained with AIDA and SGP4/SDP4 propagations. Grey dots are identified local minima and the dashed-dotted line is the 7.5 km conjunction threshold.

probably due to slightly differences in the two orbital periods that caused a phase shift at the TCA with respect to SGP4/SDP4 propagation. For what concerns the GEO test cases, the TCA and DCA are the closest to the SGP4/SDP4 ones since the close conjunction occurs within the time window used for the OD process, i.e. less than 0.5 days from the reference epoch of both objects.

For the sake of completeness, the numerical values of TCA and DCA obtained with AIDA are reported in Table 5.5.

The analysis of the accuracy of the time expansions is performed on the square root of Map (5.10) evaluated in $-c_0 + \delta t$, and considering nominal initial conditions, i.e.

$$[d] = d + \mathcal{M}_d(\delta t). \tag{5.17}$$

The accuracy of Map (5.17) in a time window of 8 minutes around t^* is illustrated for the three conjunctions in Figure 5.7, where the relative distances computed with the DA approach are compared with pointwise propagations for samples equally spaced in the time domain. A third order expansion is used, following the considerations

Test case	Sat. No.	Orbit	TCA	DCA [km]	Δv [km/s]
A	11510 21574	LEO LEO	2013 Jan 26 17:45:19	1.641	12.471
B	20237 23820	LEO HEO	2013 Mar 07 06:34:27	5.248	8.553
C	36744 28194	GEO GEO	2011 Feb 07 23:14:17	1.739	0.283

Table 5.5. Close approaches: TCA, DCA, and relative velocities obtained with AIDA and TCA expansion algorithm

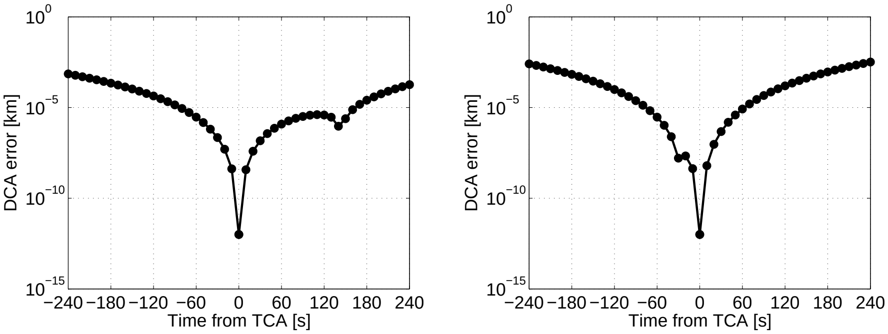

(a) Test case A **(b)** Test case B

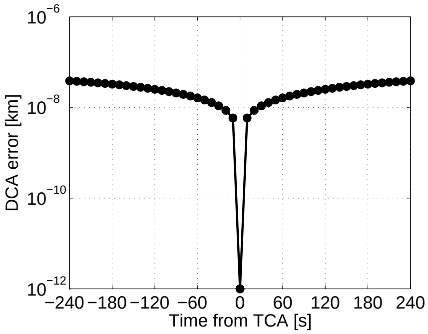

(c) Test case C

Figure 5.7. Comparison between pointwise numerical propagations and polynomial expansions for the relative distance d in the proximity of TCA

carried out in Section 3.3.1 about computational time and expansion accuracy.

The error reaches its minimum at the TCA and increases with the displacement from TCA. The maximum errors on the DCA are at the boundary of the considered time intervals, and are 108 m for test case A, 294 m for test case B, and $4\text{–}3 \times 10^{m}$ for test case C. The computational costs for each simulation are listed in Table 5.6. Most time is needed in the propagation of the two orbits, whereas the time required for the identification of the TCA is only a few milliseconds and is independent of the propagation period covered for each orbit. Note that the computational time for orbit propagation of the two GEO orbits is really low due to the short time interval between TCA and reference epoch.

Test case	1st orbit prop.	2nd orbit prop.	TCA expansion	Total time	
A	31.44	34.11	8.83E-3	65.56	s
B	33.05	12.85	8.51E-3	45.91	s
C	0.34	0.51	8.62E-3	0.85	s

Table 5.6. Computational time of TCA identification algorithm. In this case propagation with AIDA is performed only with one DA variable, time t_f.

5.4.3 TCA and DCA expansion accuracy

As already pointed out in Sect. 3.3.1, each virtual debris is characterized by a different trajectory evolution. Thus, each pair of virtual debris has its own value of TCA and DCA. If a pointwise method is used, the integration of two orbits and the use of a root-finding method would be required for each pair of virtual debris. The DA-based method introduced in this work allows replacing multiple propagation with faster evaluations of Taylor polynomials, after a single DA propagation of the two objects is carried out with AIDA. These maps can be used provided that they are sufficiently accurate for the aimed task: i.e., the identification of conjunctions and the computation of collision probabilities. As an example, when the computation of collision probabilities is of interest, the error on DCA expansion should be at least lower than the threshold adopted for the classification of a close conjunction as potentially dangerous. The accuracy analysis of these maps is the focus of this section.

As the expansion errors get bigger for larger uncertainties, the same method used for the selection of virtual debris in Sect. 3.3.1 is here used. Thus, 10^9 samples are generated and those with the largest displacement from the nominal initial position and velocity of the two objects are selected. Given a couple of virtual debris, the TCA and DCA computed with the evaluation of the Taylor polynomials (5.15) and (5.16) are compared with those obtained with AIDA pointwise integrations (i.e., two integrations and some root-finder iterations). The comparison of the times and associated distances of close approach for the three conjunctions are given in Figures 5.8(a), 5.8(c), and 5.8(e).

The black dots are the TCAs and DCAs obtained with the pointwise numerical

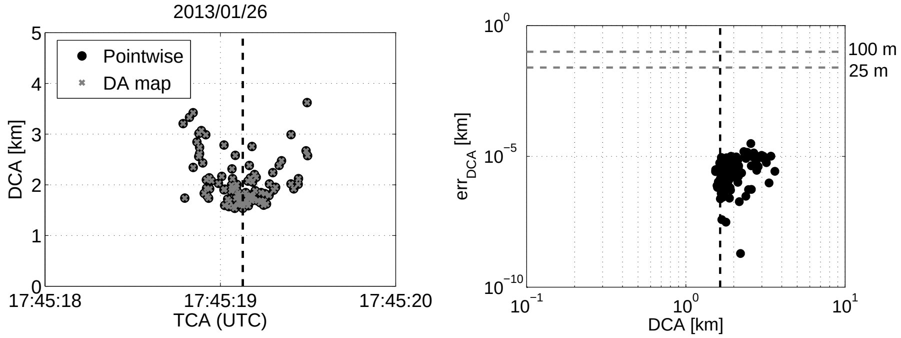

(a) Test case A: TCA vs. DCA **(b)** Test case A: DCA error

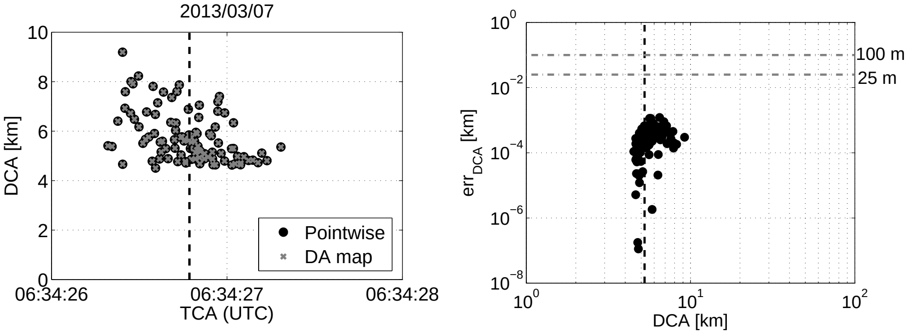

(c) Test case B: TCA vs. DCA **(d)** Test case B: DCA error

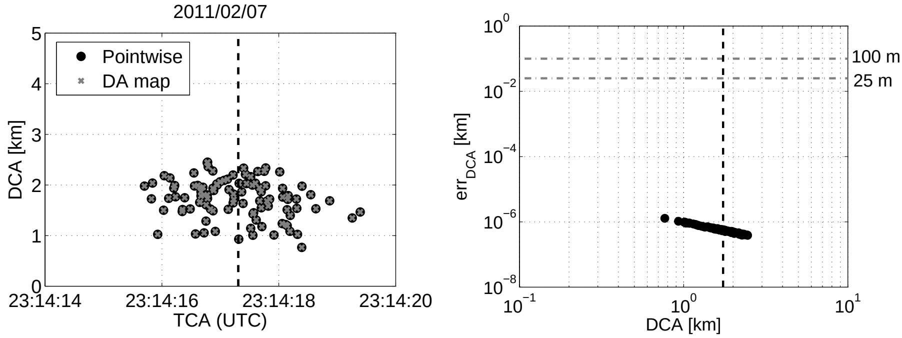

(e) Test case C: TCA vs. DCA **(f)** Test case C: DCA error

Figure 5.8. Comparison between pointwise numerical propagations and polynomial expansions for TCA and DCA with uncertain initial states

propagation of the set of virtual debris, whereas grey crosses are the values obtained with DA maps evaluations. The dashed line locates the nominal TCA value. In all cases the polynomial evaluation matches the numerical one. The difference between the polynomial evaluation of the perturbed TCA, t^*_{DA}, and the pointwise one, t^*_{PW}, is always lower than 10^{-4} seconds making them indistinguishable in Figure 5.8.

The error on the DCAs is defined as

$$err_{d*} = |d^*_{PW} - d^*_{DA}|\,, \tag{5.18}$$

where d^*_{PW} is the numerical DCA obtained with pointwise integrations, and d^*_{DA} is the one obtained with the evaluation of the Taylor expansions. This error is plotted versus the numerical DCA in Figures 5.8(b), 5.8(d), and 5.8(f). The data are compared with two thresholds, 100 m and 25 m. These two values represent estimates of the combined hard body radius that can be used for collision probability computation. The nominal DCA is indicated with a vertical dashed line.

In all cases the error on the DCA is well below the 25 m threshold, so the accuracy of the methods is suitable for a collision probability computation using a Monte Carlo method. The accuracy of the DA map can be related to the accuracy of the final position map with respect to propagation time analyzed in Sect. 3.3.1 and summarized in Figure 3.7(b). The maximum error for test case A is around 10^{-5} km and the TCA is 3.5 days after the reference epoch of satellite 1 and 3.8 days after the reference epoch of satellite 2. This is the same error of the final position map of the LEO orbit after 4 days of propagations. Similar considerations can be made for test case 2, where the TCA is 4.1 days after the reference epoch of satellite 3 and 2.4 days after the reference epoch of satellite 4, that is in HEO. The maximum error for these propagation times, according to Figure 3.7(b), is obtained for the HEO orbit and is nearly 10^{-3} km, which is compatible with the error obtained for the DCA expansion. The lower error is found for the GEO, also due to the short propagation time.

The computational times required for computing Map (5.15) and (5.16) are listed in Table 5.7. The higher number of variables results in higher computational cost with respect to the single variable DA propagations of Table 5.6. Note that these performances could be improved by running the propagation of the two orbits in parallel, reducing in this way the computational time to the one required by the most demanding orbit. In addition, in case of multiple conjunctions, the propagation of the two objects can be performed only once, whereas the TCA and DCA expansion algorithm is run on each conjunction.

Note that the evaluation of the d^* map takes 1.73×10^{-5} s on average (this number is obtained by evaluating the map for one million samples using the Horner scheme implemented in COSY INFINITY). If one considers that the reliable computation of collision probability requires a large set of virtual debris to be evaluated, it is apparent that the proposed approach allows large time savings with respect to pointwise propagations, with limited loss of accuracy.

Test case	1st orbit prop.	2nd orbit prop.	TCA&DCA expansion	Total time	
A	265.76	313.80	4.85E-2	579.60	s
B	262.44	101.53	3.99E-2	364.02	s
C	1.86	3.13	3.86E-2	5.03	s

Table 5.7. Computational time of TCA and DCA expansion algorithm. Each propagation with AIDA involves in this case 7 DA variables, i.e. time and initial states, since the aim is to obtain the polynomial approximation of $d^* = \mathcal{M}(\delta \boldsymbol{x}_0^1, \delta \boldsymbol{x}_0^2)$

5.5 Conclusions

A method for the analysis of close conjunctions between objects in Earth orbit has been presented. Differential algebraic (DA) techniques have been exploited to calculate the Taylor expansion of the time and distance of closest approach (TCA and DCA) with respect to initial orbital uncertainties. This reduces the problem of computing the TCA and DCA for the entire set of virtual debris to 1) two DA-based numerical propagations 2) polynomial manipulations to get maps of the time t^* and distance d^* of closest approach as function of uncertain initial states 3) multiple fast evaluations of these maps.

The numerical propagations are performed with AIDA (Accurate Integrator for Debris Analysis), a high-fidelity propagator written in the language COSY INFINITY. This allows us to compute, along with the trajectory, the high order expansion of the flow with respect to initial conditions in a limited amount of time. The resulting expansions are then used to build the map of the squared distance function. Partial inversion techniques and polynomial compositions are exploited to calculate the nominal values of TCA and DCA as well as their Taylor expansion with respect to uncertainties in the initial states. Thus, for each pair of virtual debris the computation of TCA and DCA reduces to polynomial evaluations. As a result, a drastic reduction in computational cost is achieved compared to classical pointwise methods: this paves the way to the development of efficient algorithms for the computation of collision probabilities.

The accuracy of the Taylor polynomials is suitable for the computation of a collision probability. An analysis is performed considering the 100 samples with the largest displacement from the nominal initial conditions among a set of 10^9 samples generated considering the full covariance matrix. The error between the polynomial evaluations of the DCA maps and a pointwise propagation are always less than 1 m for the considered orbits. It was also shown that the accuracy of the map of d^* is related to the accuracy of the maps of the final position of the objects. With order $k = 3$ and propagation window of 7 days, the error on the final position is less than 1 m for the orbits that are analyzed in this Chapter.

6

Collision probability computation

The risk of in-orbit collisions between operative satellites and space debris is a crucial issue in satellite operation. When a close approach is identified, it is necessary to define an indicator that can tell how risky the predicted conjunction is. It is common practice for space agencies and satellite operators to consider, together with conjunction geometry and miss-distance, the collision probability for this purpose [Kli05, Rig11].

The collision probability is computed by means of a multi-variate integral. The uncertainties in position and velocity coming from orbit determination can be translated into a probability density function (p.d.f.). The probability density function is then integrated over the volume swept out by the combined hard-body area of the satellite and colliding object, normal to the velocity vector, to retrieve the collision probability.

Different methods exist for the computation of this multi-dimensional integral. Most of these approaches [Ake00, Bèr99a, Pat01, Kli06] have the following assumptions in common:

- Position uncertainties of the two objects are not correlated;
- Objects move along straight lines at constant velocity during the conjunction;
- The uncertainty in the velocities is neglected;
- Position uncertainty during the whole encounter is constant and equal to the value during the conjunction;
- The uncertainties in the positions of the two objects are represented by three-dimensional Gaussian distributions.

These assumptions produce accurate results when the relative motion between the satellite and the object is rectilinear and the conjunction occurs close to the initial epoch so that the p.d.f. of the relative position of the two objects remains Gaussian. The probability density function in the proximity of the close approach, under the assumption that position error is Gaussian, is expressed as

$$p\left(\Delta\boldsymbol{r}\right)=\frac{1}{\sqrt{(2\pi)^3\det\boldsymbol{C}}}e^{-\frac{1}{2}\Delta\boldsymbol{r}^T\boldsymbol{C}^{-1}\Delta\boldsymbol{r}},\tag{6.1}$$

where $\Delta\boldsymbol{r}$ is the objects relative position vector. Integrating over the volume V swept out by the hard-body sphere with volume V_c, that is the combined volume of the colliding objects, yields the collision probability

$$P_c=\frac{1}{\sqrt{(2\pi)^3\det\boldsymbol{C}}}\iiint_V e^{-\frac{1}{2}\Delta\boldsymbol{r}^T\boldsymbol{C}^{-1}\Delta\boldsymbol{r}}\,dV.\tag{6.2}$$

Because of the assumption of rectilinear motion of both conjuncting objects, the volume V is a cylinder extending along the relative velocity direction. By integrating the p.d.f. along the cylinder axis from -∞ to +∞, the marginal two-dimensional p.d.f is obtained and the volume integral is reduced to a two-dimensional integral on the collision cross sectional area [Cha08]. Supposing that the combined covariance $\boldsymbol{C}$ is centred on the primary object and that the combined hard-body is positioned on the secondary object, the two-dimensional integral of the marginal p.d.f. on the collision cross-sectional area in the (x,y) encounter plane can be written as [Ake00, Kli06, Bèr99a]:

$$P_c=\frac{1}{2\pi\sqrt{\det\boldsymbol{C}}}\int_{-R_c}^{R_c}\int_{-\sqrt{R_c^2-x^2}}^{\sqrt{R_c^2-x^2}}e^{-A}\,dy\,dx.\tag{6.3}$$

The exponent argument A is

$$A=\frac{1}{2}\Delta\boldsymbol{r}^T\,\boldsymbol{C}^{-1}\Delta\boldsymbol{r},\tag{6.4}$$

where R_c is the combined radius of the two spherical objects and C now denotes the covariance in the marginal two-dimensional pdf. The analytical methods available in the literature differ in the way the two-dimensional integral is approximated. Chan transforms the two-dimensional p.d.f. into a one-dimensional Rician p.d.f. and uses equivalent areas to develop an analytical approximation of the double integral [Cha97]. A series expression to approximate Eq. (6.3) is derived by Alfano, using a combination of error functions and exponential terms [Alf05a] of the form

$$\begin{aligned}P_c=\frac{2R_c}{\sigma_x n\sqrt{8\pi}}\sum_{i=0}^{n}&\left[\operatorname{erf}\left(\frac{y_m+\frac{2R_c}{n}\sqrt{(n-i)\,i}}{\sigma_y\sqrt{2}}\right)+\right.\\&\left.+\operatorname{erf}\left(\frac{-y_m+\frac{2R_c}{n}\sqrt{(n-i)\,i}}{\sigma_y\sqrt{2}}\right)\exp\left(-\frac{\left(\frac{2i-n}{n}R_c+x_m\right)^2}{2\sigma_x^2}\right)\right],\end{aligned}\tag{6.5}$$

where σ_x and σ_y are the standard deviation of $\boldsymbol{C}$ in principal components and (x_m,y_m) are the coordinates of the secondary object again transformed in principal axis.

Patera performs an exact reduction of the two-dimensional integral of Eq. (6.3) to a one-dimensional contour integral over a general-shaped body [Pat01]. The method was then extended to use numerical quadrature for a simple one-dimensional integral [Pat05].

Methods that account for non-linearities, which are typical of GEO conjunctions, were also developed [Cha04, Pat03, Pat06]. An approach that uses a set of small consecutive linear segments to compute collision probability for non-linear conjunctions is presented in [Alf06, McK06].

The conflict probability, used for air-traffic control by the aviation community [Pai97], was proposed as an alternative to collision probability as a metric to quantify the collision risk even for space objects [Pat07a]. The conflict probability is computed similarly to collision probability, using a conflict volume instead of the combined hard-body region. It corresponds to the probability that a single conflict volume, centred on one space object, will be penetrated by the other space object. The conflict volume is large compared to space vehicle size and, as a result, conflict probability is higher than collision probability. In addition, no information on hard-body size, which is usually not available for space debris, is required. The conflict probability was extended to the case of ellipsoidal conflict volumes and tested against other metrics for the identification of risky conjunctions, showing good performances for the analyzed test cases [Pat07b].

Besides the analytical methods, the collision probability integral can be computed by means of Monte Carlo (MC) simulations [dV10, Sab11]. Despite being a general and flexible way to compute collision probability, the MC approach has the main drawback of requiring intensive computation, as each virtual satellite/debris trajectory has to be propagated. For this reason Monte Carlo methods are not suitable for daily collision probability computation, since results can be obtained in a timely manner only with simple dynamics, such as two-body propagators or SGP4/SDP4.

In recent times, techniques such as importance sampling [Dol11] or adaptive splitting [Pas11] have been introduced to cope with the high computational effort. Moreover, a method that couples Monte Carlo with orbital dynamics approximation, obtained by means of polynomial chaos expansion, was introduced to compute satellite collision probability with reduced computational effort [Jon13]. Monte Carlo methods were also used to study the impact of non-Gaussian probability density functions on collision probability computation [Ghr12].

New methods to reduce the computational effort related to collision probability computation are presented in this work. These methods are based on the Taylor expansion of the TCA and the DCA of the two orbiting objects. The occurrence of close approaches is first identified using the nominal initial orbital states. Then, DA techniques are used to propagate sets of initial conditions by computing the Taylor approximation of the final states at the nominal TCA. The polynomial expansion of the TCA with respect to uncertainties in the initial states is obtained by means of polynomial inversion tools and plugged into the DCA and final state maps to retrieve their dependence on initial uncertainties (see Section 5.3.1). The methods for collision probability computation can now take advantage of the availability of the resulting polynomial maps. More in detail, the initial positions and velocities are sampled according to their estimated uncertainties. For each pair of virtual objects, the associated DCA is computed through the fast evaluation of its Taylor expansion rather than running computationally intensive numerical integrations. The DCA is then compared with the collision threshold, i.e. the diameter of the sphere that envelopes the two objects. Three methods for the computation of collision probability are presented in this Chapter: a DA-based Monte Carlo simulation and the DA version of two advanced techniques, namely Line Sampling (LS) and Subset Simulation (SS) [Au01, Kou04]. A flowchart of the proposed procedure is represented in Figure 6.1, where the operated satellite is here identified as *target*, whereas the conjuncting object is the *chaser*. Note that the polynomial map obtained with the TCA and DCA expansion can be used for all DA-based Monte Carlo methods.

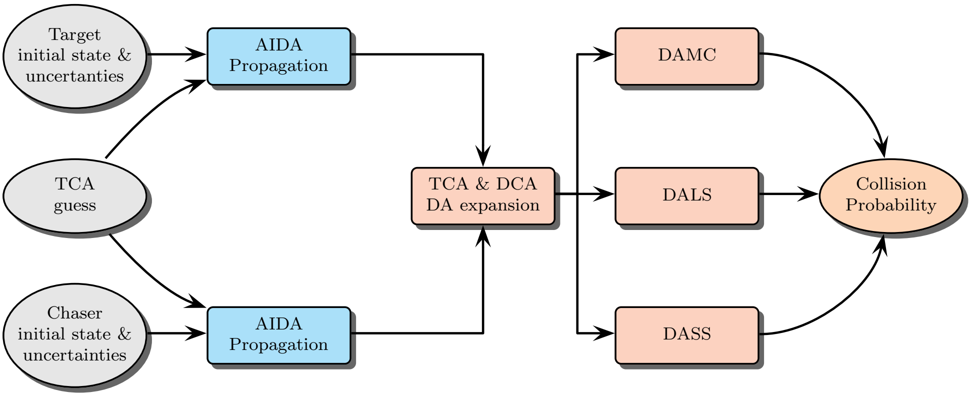

Figure 6.1. Collision probability computation: flowchart of the proposed procedure.

The Chapter is organized as follows. First the description of MC, LS, and SS methods in their standard version (i.e. not DA-based) is given in Sections 6.1.1, 6.1.2, and 6.1.3. Then, their formulation taking advantage of DA techniques is introduced in Section 6.2. Numerical examples and discussion of results are provided in Section 6.3, which is followed by conclusions.

6.1 Methods for collision probability computation

The two objects initial conditions are defined by the state vectors $\boldsymbol{x}_0^1$ and $\boldsymbol{x}_0^2$. Both vectors are uncertain due to the orbit determination process, and their statistics can be represented by a pdf. Typically, the initial statistics is assumed to be Gaussian, then the initial state is fully described by its mean and covariance matrix.

The methods for collision probability computation described in this section rely on the Performance Function (PF)

$$g\left(\boldsymbol{x}_0^1, \boldsymbol{x}_0^2\right) = D - d^*\left(\boldsymbol{x}_0^1, \boldsymbol{x}_0^2\right), \tag{6.6}$$

in which D is the collision threshold, and d^* is the function that maps each pair of initial conditions $\boldsymbol{x}_0^1, \boldsymbol{x}_0^2$ to the associated DCA. Note that, as D is a constant and d^* is the distance between the the objects centres of mass it follows that exact collision probabilities are computed for spherical space objects only. Exact collision probability could be computed for arbitrary shape objects by tailoring PF. However, this would be limited to cases of known and constant relative attitude along the whole encounter. According to the definition of the PF, the following conditions occur

$$g\left(\boldsymbol{x}_0\right) \begin{cases} < 0 & \Rightarrow \quad \text{no collision} \\ = 0 & \Rightarrow \quad \text{at limit state} \\ > 0 & \Rightarrow \quad \text{collision,} \end{cases} \tag{6.7}$$

where, for the sake of brevity, $\boldsymbol{x}_0 = (\boldsymbol{x}_0^1, \boldsymbol{x}_0^2)$.

The collision threshold D can be related to the dimensions of the two objects. Let L_i, for $i = 1, 2$, be the diameters of the spherical objects. Then, according to Figure 6.2, D is given by the sum of the radius of the two objects. In case of non-spherical objects without large appendages the same performance function could be used, by selecting the sphere that envelopes each object i. This is a conservative approach, which guarantees that the resulting collision probability is larger than its correct value since the collision condition will hold for a larger number of virtual objects. The shape of operative satellites or defunct satellite that did not experience a break-up is usually known or can be obtained from available data and information. In case the chaser is a debris generated by fragmentation or explosion, an estimate of the object area or diameter can be obtained from radar and/or optical measurements. Typical values of the collision threshold D ranges between a few meters up to 100 m.

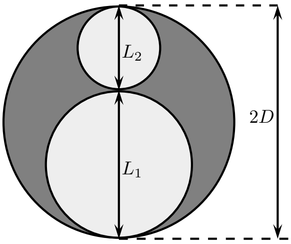

Figure 6.2. Collision threshold D definition. The diameters of the two conjuncting bodies are labeled L_1 and L_2.

6.1.1 Monte Carlo method

To compute the collision probability by means of MC simulation, the initial position and velocity of the two objects are sampled from their error covariance matrices (thus generating what are called virtual objects or debris). The initial orbital states, $\boldsymbol{x}_0^1$ and $\boldsymbol{x}_0^2$, are then propagated till the time derivative $\dot{d}$ of the relative distance d is zero, which happens in the surrounding of the nominal TCA. In this way, the TCA and DCA are identified for each pair of virtual objects. If the relative distance is below the threshold D a hit is counted. The number of samples N_c for which the collision condition is verified, i.e. $g_x\left(\boldsymbol{x}_0\right) > 0$, is divided by the total number of samples N_T to compute the collision probability

$$P(d^* < D) = \frac{N_c}{N_T}. \tag{6.8}$$

The standard deviation of the computed probability is given by

$$\sigma = \sqrt{\frac{P\left(1-P\right)}{N_T}}, \tag{6.9}$$

and is proportional to $1/\sqrt{N_T}$. For standard Monte Carlo methods the coefficient of variation (c.o.v.), i.e. the ratio between the standard deviation and the mean value, is thus defined as

$$\delta\left(P\right) = \frac{\sigma}{P} = \sqrt{\frac{1-P}{N_T\,P}}. \tag{6.10}$$

The collision probability between two spacecraft is usually very low since it exceeds 10^{-4} only for really close conjunctions. As a consequence, a large number of samples is required to obtain a sufficiently accurate estimate of its value. According to [Dag00], the number of samples N_T to be used in a Monte Carlo simulation when $\sigma^2 > \varepsilon P_c$ should be at least

$$N_T > \frac{4\left(e-2\right)\left(1-P_c\right)}{P_c\,\varepsilon^2}\log\left(\frac{2}{\beta}\right), \tag{6.11}$$

where P_c is the collision probability, $(1-\beta)$ is the desired confidence level, and ε is the relative error of the collision probability. The number of samples required to compute a given collision probability with a 95% confidence level is illustrated in Figure 6.3, where the dashed and a solid lines are computed with a relative error of 1% and 5%, respectively.

To compute a collision probability of 10^{-4} with a relative error of 5% at least 4.24×10^7 samples are required, whereas for $P_c = 10^{-6}$ the minimum number of samples increases to 4.24×10^9.

These considerations point out the main drawback of MC simulations, that is the high computational effort which is magnified when dealing with very low probabilities or when a computationally intensive simulation is required for each sample, such as a

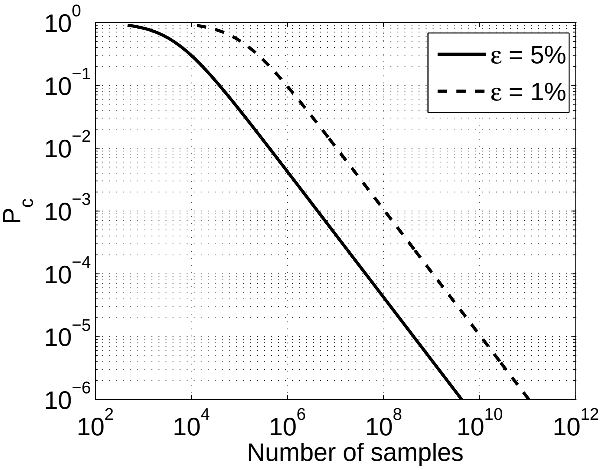

Figure 6.3. Number of Monte Carlo samples required to compute a probability P_c with a 95% confidence level and relative error ε

numerical integration of the equation of motion. Line Sampling and Subset Simulation algorithms, described in the next two subsections, were developed to reduce the number of samples required to compute low collision probabilities.

6.1.2 Line Sampling

The main idea behind LS is transforming a high dimensional problem into a number of conditional one-dimensional problems solved along an "important direction" $\boldsymbol{\alpha}$ [Kou04]. The key issue of the method is identifying this direction, that should point toward the region of failure, i.e. the hyper-volume of position and velocity deviations for which the collision criterion holds. The important direction tells which combination of states variations is more efficient to reach the failure condition.

In the LS approach, the vector of uncertain parameters $\boldsymbol{x}_0 \in \mathbb{R}^n$, where n is the number of uncertain parameters, has first to be transformed into the adjoint vector $\boldsymbol{\theta} \in \mathbb{R}^n$. This vector belongs to the so-called "standard normal space", where each variable is represented by an independent central unit Gaussian distribution. This is done using Rosenblatt's transformation [Ros52]

$$\begin{aligned} \boldsymbol{\theta} &= T_{x,\theta}\left(\boldsymbol{x}_0\right) \\ \boldsymbol{x}_0 &= T_{\theta,x}\left(\boldsymbol{\theta}\right), \end{aligned} \tag{6.12}$$

where the operator $T_{\cdot,\cdot}$ indicates the transformation, and applying it to the performance function

$$g\left(\boldsymbol{x}_0\right) = g_x\left(T_{\theta,x}\left(\boldsymbol{\theta}\right)\right) = g_\theta\left(\boldsymbol{\theta}\right). \tag{6.13}$$

A natural choice for the important direction is the normalized gradient of the PF at the nominal point in the standard normal space

$$\boldsymbol{\alpha} = \frac{\boldsymbol{\nabla}_{\boldsymbol{\theta}}\, g_\theta\left(\boldsymbol{\theta}\right)}{\left\|\boldsymbol{\nabla}_{\boldsymbol{\theta}}\, g_\theta\left(\boldsymbol{\theta}\right)\right\|_2}. \tag{6.14}$$

If not available analytically, this gradient can be numerically estimated. The more the estimate of the important direction is close to its true value, the lower will be the variance of the failure probability [Pra05]. For high-dimensional problems where the numerical computation of gradients can be time-demanding, it is possible to obtain an estimate by computing the normalized "centre of mass" of the failure domain. This is achieved by Monte Carlo Markov Chain (MCMC), using as seed a point belonging to the failure region or close to it and computing the mean of the N_α samples generated in the failure region [Zio09b].

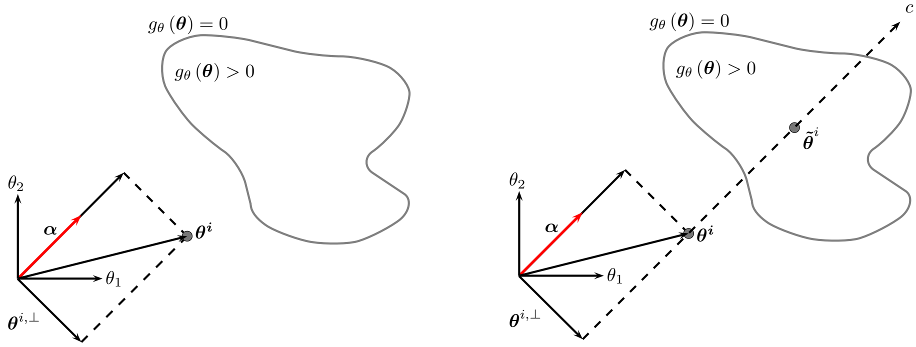

(a) Projection of the sample vector $\boldsymbol{\theta}^i$ on directions parallel and perpendicular to $\boldsymbol{\alpha}$ to obtain $\boldsymbol{\theta}^{i,\perp}$

(b) Graphical representation of the line with parametric equation $\tilde{\boldsymbol{\theta}}^i(c)$ used to identify the values of c for which $g_\theta(c) = 0$

Figure 6.4. Illustration of the Line Sampling procedure in a bi-dimensional space (θ_1, θ_2). The origin of the reference frame is in the nominal initial states and $\boldsymbol{\alpha}$ points in the direction of the gradient (i.e. greatest rate of decrease) of the relative distance. Failure region is surrounded by the grey line.

Once the important direction is identified, the LS method proceeds as follows

LS 1. Sample N_T vectors $\boldsymbol{\theta}^i$ from the normal multidimensional joint probability distribution.

LS 2. Estimate for each sample its conditional one-dimensional failure probability $\hat{P}^{1D,i}$ performing the following operations

   (a) Project the vector $\boldsymbol{\theta}^i$ onto the straight line passing through the origin and perpendicular to $\boldsymbol{\alpha}$ to obtain vector $\boldsymbol{\theta}^{i,\perp}$, as portrayed in Figure 6.4(a).

   (b) Write the parametric equation of samples along the important direction, $\tilde{\boldsymbol{\theta}}^i = \boldsymbol{\theta}^{i,\perp} + c\,\boldsymbol{\alpha}$, as sketched in Figure 6.4(b).

(c) Compute the values of c_j^i, $j = 1, 2$, for which the PF is equal to zero. (Here and in the remainder of the Chapter a maximum number of two zeros is considered.) This step requires evaluations of the PF, which involve numerical propagations or complex system simulations when g_θ is not known analytically. Note that when the failure region is infinite only one real solution is found whereas the other is $+\infty$.

(d) If the two values coincide or no solution is found then the ith one-dimensional probability $\hat{P}^{1D,i}$ is equal to zero; else, given the two solutions c_1^i and c_2^i, with $c_1^i > c_2^i$, the probability is

$$\begin{aligned} \hat{P}^{1D,i}(F) &= P\left[c_2^i \leq N(0,1) \leq c_1^i\right] = \\ &= \Phi\left(c_1^i\right) - \Phi\left(c_2^i\right) \end{aligned} \tag{6.15}$$

where $\Phi\left(c_j^i\right)$ is the standard normal cumulative distribution function, $N(0,1)$ is the standard normal distribution, with zero mean and unit standard deviation, and F indicates the collision condition $d \leq D$.

LS 3. Compute the unbiased estimator $\hat{P}^{N_T}(F)$, which is the sample average of the independent conditional one-dimensional probability estimate

$$\hat{P}^{N_T}(F) = \frac{1}{N_T} \sum_{i=1}^{N_T} \hat{P}^{1D,i}(F) \tag{6.16}$$

The variance of the collision probability in Eq. (6.16) is given by

$$\sigma^2\left(\hat{P}^{N_T}(F)\right) = \frac{1}{N_T\left(N_T - 1\right)} \sum_{i=1}^{N_T} \left(\hat{P}^{1D,i}(F) - \hat{P}^{N_T}(F)\right)^2 \tag{6.17}$$

The total number of system simulations is related to the number of PF evaluations required to compute, for each sample $\boldsymbol{\theta}^i$, the values c_j^i at step **LS** 2(c). When the PF is smooth and does not present oscillations along the important direction, the number of sample evaluations can be limited to the one necessary to obtain an approximation of the function in the region of interest [Zio09b]. For a short-term encounter between two space objects, the PF along the direction $\boldsymbol{\alpha}$ resembles a parabola. With three evaluations of the PF, it is indeed possible to obtain a second-order approximation and compute an approximate value of the intersections c_1^i and c_2^i with the line $g_\theta(c) = 0$, if they exists. Although reducing the computational effort when dealing with computationally demanding simulations, such an approach strongly depends on the choice of the c grid required to compute the approximation of the PF. A wrong spacing of the grid could result in erroneous estimations of the intersections with the failure region boundary. Thus, when this approach is selected, it is important to verify that the computed intersections are close to the true values for different close encounter geometries and relative velocities.

6.1.3 Subset Simulation

Subset Simulation (SS) is an adaptive stochastic simulation method to compute efficiently small failure probabilities [Au01]. The idea at the basis of the method is to compute the probability as a product of larger conditional probabilities. Thus, given a sequence of intermediate failure regions $F_1 \supset F_2 \supset \cdots \supset F_m = F$, the failure probability becomes

$$P(F) = P(F_m) = P(F_1) \prod_{l=1}^{m-1} P\left(F_{l+1}|F_l\right), \tag{6.18}$$

where $P(F_{l+1}|F_l)$ indicates the probability of F_{l+1} conditional to F_l. The method is initialized using a standard Monte Carlo simulation to generate samples at conditional level 0. Once the failure region F_1 is determined and the probability $P(F_1)$ computed, a MCMC algorithm [Met53] is used to generate samples conditional to the failure region F_1. Another intermediate failure region F_2 is then located and other samples are generated with MCMC. The process can be repeated till the failure region corresponding to objects collision is identified. The approach was originally developed to address structural failure, but it was also used in different research areas in reliability, e.g. to address the failure probability of thermal-hydraulic passive system [Zio09a].

The main issue of the algorithm is to identify the intermediate failure regions. This can be achieved by choosing a constant probability value p_0, and searching a threshold value of the relative distance at every conditional level for which $P(F_l|F_{l-1}) = p_0$. The PF changes accordingly: being D_l the collision threshold at conditional level l, it can be defined as

$$g_x^l\left(\boldsymbol{x}_0\right) = D_l - d^*\left(\boldsymbol{x}_0\right). \tag{6.19}$$

Similarly to Eq. (6.6), the following conditions occur

$$g_x^l\left(\boldsymbol{x}_0\right) \begin{cases} < 0 & \Rightarrow \quad \boldsymbol{x}_0 \text{ is out of } l\text{th conditional level} \\ = 0 & \Rightarrow \quad \boldsymbol{x}_0 \text{ is at limit state} \\ > 0 & \Rightarrow \quad \boldsymbol{x}_0 \text{ is in } l\text{th conditional level.} \end{cases} \tag{6.20}$$

Since the conditional probability is equal to p_0 at each iteration, the collision probability in Eq. (6.18) can be computed as

$$P(F) = P(F_m) = P\left(F_m|F_{m-1}\right) {p_0}^{m-1} \tag{6.21}$$

The resulting SS algorithm goes through the following steps (refer to Figure 6.5 for its schematic representation):

SS 1. Set $l = 0$ and generate N sample vectors $\boldsymbol{x}_0^{0,k}$, $k = 1, \ldots, N$, by standard MC simulation. The superscript 0 denotes that the samples are at "conditional level 0".

SS 2. Compute the values of the PF $g_x^l(\boldsymbol{x}_0)$ for the N samples $\boldsymbol{x}_0^{l,k}$.

SS 3. Sort the N samples in ascending order, according to their associated value of the performance function g_x^l. The samples closer to the failure region will be at the bottom of the list.

SS 4. Choose the intermediate threshold value D_{l+1} from the $(1-p_0)N$th value of the sorted list. The $(l+1)$th conditional level is then defined as $F_{l+1} = \{d^* < D_{l+1}\}$. The associated conditional probability is, according to the definition, $P(F_{l+1}|F_l) = P(d^* < D_{l+1} \,|\, d^* < D_l) = p_0$.

SS 5. If $D_{l+1} \leq D$ go to last step otherwise identify the p_0N samples $\boldsymbol{x}_0^{l,u}$, $u = 1, 2, \ldots, p_0N$, whose relative distance lies in F_{l+1}. All these samples belong to "conditional level $l+1$".

SS 6. Using MCMC, generate $(1-p_0)N$ additional conditional samples distributed as $p(\cdot|F_{l+1})$, so that a total of N conditional samples $\boldsymbol{x}_0^{l+1,k} \in F_{l+1}$, where $k = 1, \ldots, N$. Eq. (6.20) can be used to establish whether each sample belongs to conditional level $l+1$ or not.

SS 7. Set $l = l+1$ and return to step 2 above

SS 8. Stop the algorithm

The total number of samples generated is

$$N_T = N + (m-1)(1-p_0)N, \tag{6.22}$$

where m is the number of conditional levels required to reach the failure region. According to Eq. (6.21) the collision probability becomes

$$P(d^* < D) = {p_0}^{m-1} P(F_m \,|\, F_{m-1}) = {p_0}^{m-1} \frac{N_F}{N}, \tag{6.23}$$

where N is the total number of samples at each conditional level and N_F is the number of samples at conditional level m, whose relative distance is less than the collision threshold D.

The efficiency of the SS algorithm relies on the proper selection of its parameters: the conditional failure probability p_0, the number of samples of each step N, and the shape of the proposal probability density function for the generation of the Markov chain. A detailed analysis on the selection of these parameters is given in [Zue12], where it is shown that the optimal choice for p_0 is 0.2 (although similar efficiency is obtained for $p_0 \in [0.1; 0.3]$). For what concerns the proposal p.d.f. of MCMC, a univariate Gaussian distribution is used in this work. The variance σ_l of the proposal

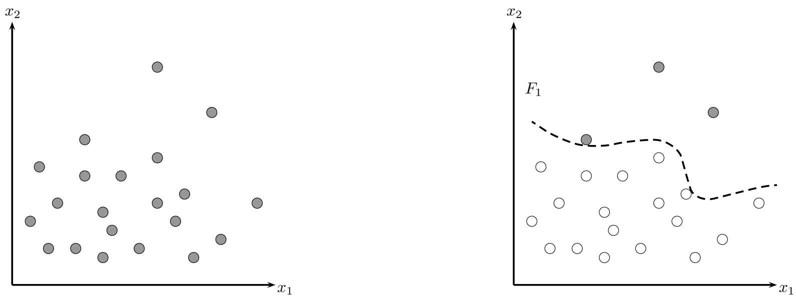

(a) Conditional level 0: Monte Carlo simulation. **(b)** Adaptive selection of samples in conditional level 1.

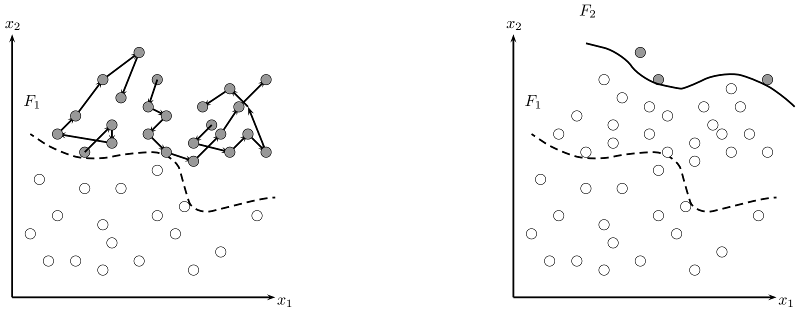

(c) MCMC simulation: generation of new samples belonging to conditional level 1. **(d)** Adaptive selection of samples in conditional level 2.

Figure 6.5. Illustration of the Subset Simulation algorithm for a bi-dimensional space (x_1, x_2). The dots are the generated samples and the lines identify the conditional levels. The grey dots are the samples belonging to the lth conditional levels and the arrows represent the MCMC path.

p.d.f. is changed dynamically at each conditional level l so that the acceptance rate of Markov Chain samples is kept between 30% and 50%. This solution is nearly optimal, i.e. the chain converges to stationarity nearly as fast as possible.

[Zue12] also suggest a Bayesian post-processor for Subset Simulation, SS+, to refine the computed failure probability and determine higher moments, allowing the computation of the failure probability variance. Defining

$$n_l = \begin{cases} p_0 N & \text{if } l < m \\ N_F & \text{if } l = m \end{cases} \tag{6.24}$$

the first moment of the distribution of the failure probability becomes

$$E_{SS+}\left[P(F)\right] = \prod_{l=1}^{m} \frac{n_l + 1}{N + 2}, \tag{6.25}$$

whereas the second moment is given by

$$E_{SS+}\left[P(F)^2\right] = \prod_{l=1}^{m} \frac{(n_l+1)(n_l+2)}{(N+2)(N+3)}. \tag{6.26}$$

The variance of the collision probability $P(F)$ can then be obtained using the definition

$$Var(P) = E[P^2] - (E[P])^2 . \tag{6.27}$$

The number of samples N to be used depends on the problem dimension and the expected failure probability. Furthermore, if the failure region is disconnected, the samples must be dense enough to lie in the proximity of each subregion at conditional level zero and then reach them at the subsequent conditional levels. The tests showed that a good choice is $N = 2 \times 10^3$ for collision probability computation.

To stress the advantages of the SS method over standard MC for low failure probability computation, two experimental cumulative distribution functions (c.d.f.) obtained with SS and MC for a close conjunction are compared in Figure 6.6. The solid black line is the distribution obtained with SS using 14000 samples ($p_0 = 0.2$, $N = 2000$ samples and 7 conditional levels), the dashed line is the c.d.f. obtained with MC using the same number of samples, and the solid grey line is the c.d.f. for a MC with 10^6 samples.

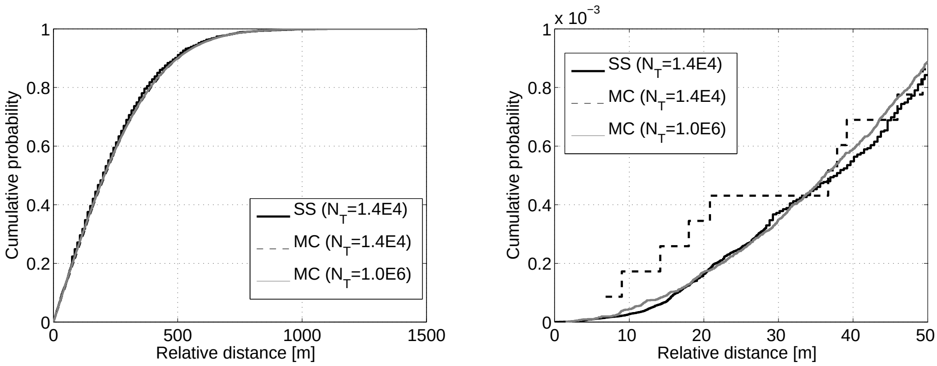

(a) Experimental c.d.f.

(b) Detail of experimental c.d.f. near failure region

Figure 6.6. Cumulative probability comparison between SS and MC

The three curves seem to agree over the entire set of relative distances. However, the detail reported in Fig. 6.6(b) shows the lack of accuracy of the MC simulation with fewer samples in the proximity of the failure region. As the maximum cumulative probability in Fig. 6.6(b) is about 0.001, only 14 samples out of 14000 lie, on average, in the associated range of relative distances in the MC simulation. In particular, only two samples have a relative distance below 10 m and no samples are located under 5 m. In contrast, SS generates nearly 5000 samples in the same region, which is five times more than the ones generated by MC with 10^6 samples. The samples generated by SS provide enough information to describe the c.d.f. accurately even at lower conditional probability level, i.e. closer to the failure region.

6.2 DA-based methods for collision probability

The methods described in the previous section are here modified to take advantage of the Taylor expansion of the DCA, described in Section 5.3. The Taylor expansions of the state vectors $\boldsymbol{x}_f^1$ and $\boldsymbol{x}_f^2$ of the two objects at the nominal TCA are here obtained by propagating their initial conditions with the DA-based numerical integrator AIDA (see Sect. 3.2).

It is worth observing that the presented methods are applicable only for cases with a single DCA and TCA. Nonlinear relative motion with multiple DCAs are not analyzed in this work and will be addressed in future works. In the following, the main modifications to the three proposed methods are summarized.

6.2.1 DAMC

For what concerns the Monte Carlo method, its DA-based counterpart is simply obtained by substituting each pair of numerical or analytical propagations necessary to compute the DCA with a single evaluation of the map in Eq. (5.16). In the following, the acronym DAMC-k is used to label the resulting DA-based Monte Carlo method, where k is the order used for the Taylor expansion of the TCA and DCA.

6.2.2 DALS

The availability of the DCA expansion is exploited for the computation of the important direction $\boldsymbol{\alpha}$ in the LS method. Once the polynomial map in Eq. (5.16) is available, the Taylor expansion of $g_\theta\left(\boldsymbol{\theta}\right)$ in Eq. (6.13) is obtained by evaluating Eq. (6.6) together with Eq. (6.12) in the DA framework. Then, the gradient of g_θ is readily obtained by extracting the twelve first order coefficients of its Taylor expansion and is used to compute $\boldsymbol{\alpha}$ using Eq. (6.14). In addition, similarly to DAMC, each numerical propagation of the standard algorithm is substituted by a polynomial evaluation of Eq. (5.16). Moreover, accurate methods for the computation of the parameters c_1^i and c_2^i can be developed since the evaluation of the polynomial approximation of g_θ is fast. More in detail, to further speed up the execution of a DA-based LS simulation, the algorithm described in Section 6.1.2 is slightly modified. The step **LS** 2(c) is divided in two parts. First, the maximum of the PF and the associated value c_{max}^i for the ith sample are identified. The two values c_1^i and c_2^i are then computed only if the maximum of the PF is positive. This is done by applying a secant method using two initial guesses that are close to c_{max}^i, one slightly larger and the other slightly smaller.

If the maximum of the PF is negative there is no need to compute intersections and $P^{1D,i} = 0$. Although this approach increases the complexity of the method, it avoids unnecessary polynomials evaluations increasing the robustness and efficiency of the DA-based LS. The acronym DALS-k is used in the following to indicate the DA-based Line Sampling with expansion order k.

6.2.3 DASS

Similarly to DAMC, in the DA-based Subset Simulation, the numerical propagations at step **SS** 2 are replaced by the fast evaluation of the polynomial map in Eq. (5.16). All other steps involve sorting and generation of samples through MCMC and do not require any modification. Hereafter this algorithm will be labelled as DASS-k, where k is again the order of the expansion.

6.3 Numerical Examples

In this section, the performances of the proposed approaches are assessed on the computation of collision probabilities for close encounters in LEO and GEO. All computations are performed on a Intel Core i5 2500 @3.30GHz, 8Gb RAM processor running Sabayon Linux (kernel version 3.11.0).

At first, the DA algorithms are compared against analytical methods and standard Monte Carlo simulations, using test cases in which the relative motion can be considered linear, non-linear and almost-linear, respectively. The test cases are taken from [Alf09], where simple Keplerian dynamics is used to compare a set of different methods for collision probability computation. The aim of this analysis is to validate the proposed methods and assess their performances in terms of accuracy and efficiency.

Then, the methods are tested using the high fidelity numerical propagator AIDA. The covariance matrices for each object are obtained after a pseudo orbit determination process, where observed states are obtained with TLEs propagation through SGP4/SDP4. The orbit determination is performed as a batch least-square optimization, yielding a full 6×6 covariance matrix. The goal of this analysis is to test the methods in real scenarios and assess their reliability.

Since the considered methods employs different number of samples, two figures of merit are used for comparisons [Zio09b]. The first figure of merit is the unitary coefficient of variation, Δ, and is defined as

$$\Delta = \frac{\sigma}{\hat{P}_c}\sqrt{N_T}, \tag{6.28}$$

where σ is the standard deviation of the collision probability from its estimated value $\hat{P}_c$, and N_T is the total number of samples used. The unitary c.o.v. does not depend on the number of samples, since for Monte Carlo methods $\sigma \propto 1/\sqrt{N_T}$. It is designed to enable the comparison of the different methods in terms of accuracy and number of samples required to reach that accuracy level. The lower is the value of Δ, the lower is the variability of the corresponding failure probability and, as a consequence, the higher is the efficiency of the method.

The second figure of merit, Ω, involves both variance and computational time t_c and does not depend on the number of samples N_T as well. It is defined as

$$\Omega = \frac{1}{\sigma^2 \, t_c}. \tag{6.29}$$

It is a measure of the computational efficiency and failure probability variability. The higher the value the higher is the efficiency of the method.

6.3.1 Validation of DA-based methods

In this section the methods for collision probability computation DAMC, DALS, and DASS are validated against an analytical method and standard Monte Carlo simulation. Three test cases are considered, one with linear relative motion between the two objects, one at the boundary of linear relative motion, and one with nonlinear relative motion. These are respectively test case 5, 6, and 7 of [Alf09]. The same labelling is used in this Section to ease comparison. The orbital state and covariance matrix are propagated using Keplerian dynamics [Her65, Der96] for the standard Monte Carlo method and Alfano's method. In this example, the Taylor expansion of the DCA given in Eq. (5.16) is then based on the propagation of Kepler's dynamics in DA environment.

The three conjunctions analyzed are detailed in Table 6.1, where the time, distance, and relative velocity at the closest approach, Δv_{TCA}, are listed. The reference value for collision probability, computed using a standard Monte Carlo simulation is given. For each trial, two sets of initial conditions are sampled from each initial covariance matrix and the associated DCA is searched in the proximity of the nominal TCA. The number of samples N_T for the computation of the reference P_c is selected to achieve a confidence level of 95% and 1% relative error according to Eq. (6.11). The collision probability obtained using Alfano's formula and its associated percentage relative error with respect to the reference collision probability are given in the last two columns.

The collision probability is then computed using the three DA-based methods and a standard Monte Carlo method. For DAMC and the standard Monte Carlo computations the number of samples is now selected to guarantee a relative error of 5% and a confidence level of 95%. The results are listed in Table 6.2, where for DAMC, DALS, and DASS the expansion order was set to $k = 3$. The relative error with respect to the reference P_c, number of samples used, computational time, coefficient of variation δ, and figures of merit Δ and Ω are also given.

The collision probability values are always in good accordance with the reference

Test case	TCA [days]	DCA [m]	Δv_{TCA} [m/s]	D [m]	P_c (Monte Carlo)	N_T (Dagum)	P_c (Alfano)	% err [-]
5	2.0	2.449	0.520	10	4.454E-02	2.30E+06	4.440E-02	-0.32%
6	2.0	2.449	0.173	10	4.340E-03	2.50E+07	4.324E-03	-0.36%
7	2.0	3.183	0.196	10	1.614E-04	6.71E+08	1.580E-04	-2.13%

Table 6.1. Time, distance, and velocity of closest approach for the Keplerian test cases and reference value for collision probability, computed with a standard MC method using N_T samples. The collision probability computed with Alfano's approach is given together with the relative error with respect to the reference P_c.

Test case	Method	P_c [-]	% err [-]	N_T	t_c [s]	δ [-]	Δ [-]	Ω [-]
5	MC	4.452E-2	-0.05%	1.0E+5	4.75	1.465E-2	4.63	4.949E+05
	DAMC-3	4.459E-2	+0.11%	1.0E+5	0.67	1.464E-2	4.63	3.503E+06
	DALS-3	4.451E-2	-0.07%	5.0E+3	2.53	7.662E-4	0.05	3.399E+08
	DASS-3	4.450E-2	-0.09%	2.0E+4	0.13	2.738E-2	3.87	5.183E+06
6	MC	4.339E-3	-0.01%	1.0E+6	43.21	1.515E-2	15.14	5.357E+06
	DAMC-3	4.350E-3	+0.24%	1.0E+6	6.67	1.513E-2	15.13	3.462E+07
	DALS-3	4.341E-3	+0.03%	5.0E+3	2.58	1.484E-3	0.11	9.340E+09
	DASS-3	4.328E-3	-0.27%	4.0E+4	0.27	3.586E-2	7.17	1.539E+08
7	MC	1.615E-4	+0.04%	2.7E+7	1155.36	1.514E-2	78.68	1.447E+08
	DAMC-3	1.612E-4	-0.15%	2.7E+7	179.34	1.516E-2	78.76	9.341E+08
	DALS-3	1.621E-4	+0.41%	5.0E+3	1.43	1.936E-2	1.37	7.103E+10
	DASS-3	1.626E-4	+0.72%	6.0E+4	0.43	4.580E-2	11.22	4.193E+10

Table 6.2. Computed collision probability for the Keplerian test cases. For each simulation the relative error with respect to the reference P_c, the number of samples used, the computational time t_c, coefficient of variation δ, and figures of merit Δ and Ω are listed.

value. In particular, the relative error for test case 7 is lower than the one obtained with Alfano's method, since nonlinear effects are captured by using a third-order polynomial approximation. The computational time of the DA-based methods is always lower than standard Monte Carlo. Among all methods DALS is the one that has the lowest Δ and the highest Ω, thus resulting to be the most efficient method. A comparison of the different methods is given in Figure 6.7. The collision probabilities are plotted as bars together with their 1-σ error. The reference probability value is represented by a solid black line and the 5% relative error lines are reported as two solid grey lines. For cases 5 and 6, DALS and DASS show the lowest and highest standard deviations of the collision probability, respectively. Standard Monte Carlo and DAMC provides similar results in terms of P_c and variance for all three test cases. In Figure 6.7(c) it can be observed that Alfano's method underestimates the collision probability for test case 7, when nonlinearities are relevant. The other methods

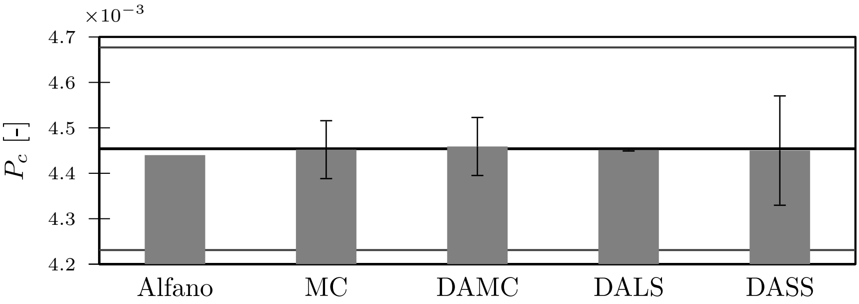

(a) Case 5

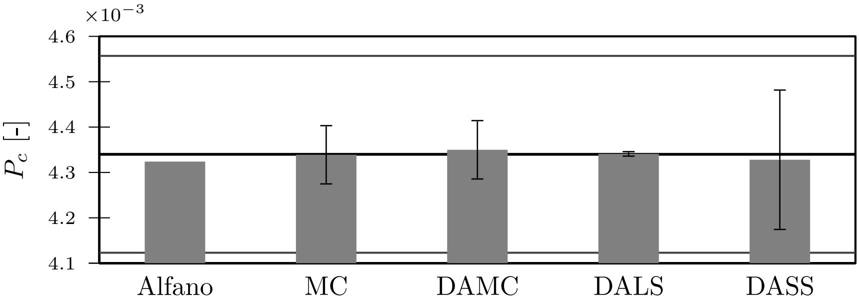

(b) Case 6

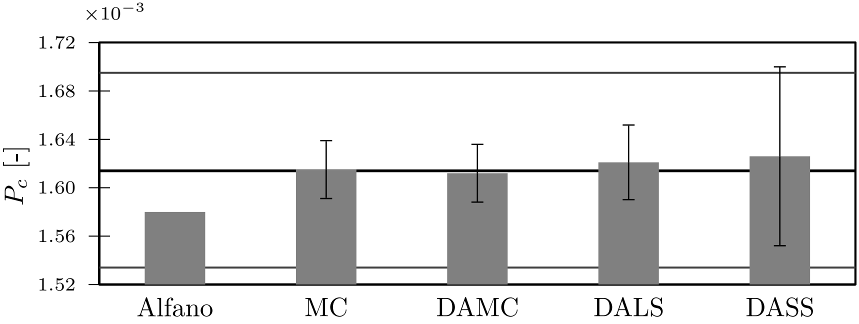

(c) Case 7

Figure 6.7. Comparison of the collision probability obtained with the tested methods for the Keplerian test cases. The DA expansion order is $k = 3$ for DAMC, DALS, and DASS. The solid black line is the reference value for collision probability and the gray lines are the 5% relative error bounds.

instead are much more closer to the reference probability.

The computational time for the three DA-based methods is plotted in Figure 6.8, normalized by the t_c obtained with the standard Monte Carlo method to highlight the computational gain. For each of the three DA-based methods a different marker is used: squares for DAMC, circles for DALS, and triangles for DASS. The computational time is plotted for expansion orders ranging from $k = 1$ to $k = 4$ and the markers are coloured accordingly using a gray scale, where black is used for $k = 1$ and light gray for $k = 4$. The computational time is usually lower than the one of the standard Monte Carlo method and increases with the expansion order for all methods. Using DAMC, the computational time can be reduced by a factor of 10 with an expansion order up to $k = 3$. Note that the computational gain is limited in this case as a simple dynamical model is used, thus there is only a little advantage when pointwise propagations are substituted by polynomial evaluations of Eq. (5.16).

For the higher probability value (test case 5) the computational time of the three DA-based methods are comparable and the one of DALS is even a bit higher than the one of DAMC and DASS, due to its higher complexity. In particular, it is worth noting that for order $k = 4$ it also exceeds the computational time of pointwise MC, that for test case 5 requires a lower number of samples. Nevertheless, the computational effort of DALS and DASS decreases for lower collision probability, becoming nearly 10^3 times lower than the one of a standard Monte Carlo method for test case 7.

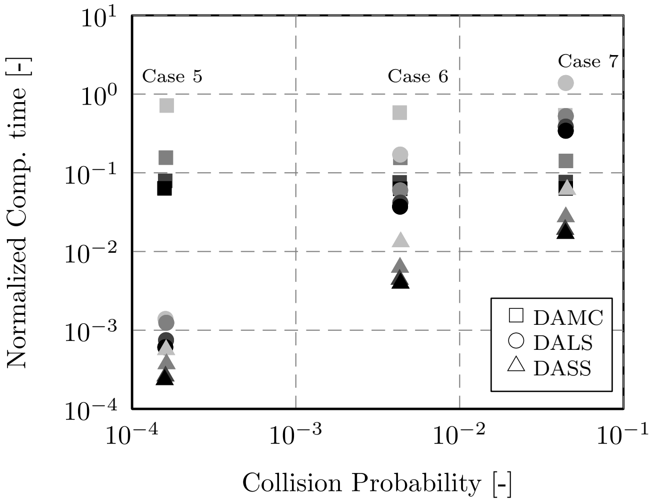

Figure 6.8. Normalized computational time of DAMC, DALS, and DASS for the Keplerian test cases vs. collision probability for different expansion orders. Markers are coloured using a grayscale, where black is used for the expansion order $k = 1$ and lighter gray for $k = 4$.

The figure of merit Δ, normalized for each test case with the value of the standard Monte Carlo method, is plotted against the collision probability P_c in Figure 6.9(a). The same criteria used in Figure 6.8 for markers colouring and shape is used, i.e. different markers are used for each method and they are coloured according to the expansion order using a gray scale. The normalized unitary c.o.v. is equal to 1 for the DAMC since the same number of samples of the standard Monte Carlo method is used. The lower value is achieved with DALS, which is two order of magnitude lower than DAMC. The efficiency of DASS increases for lower probabilities. The use of different expansion orders does not affect the final value of the normalized Δ, since points are overlapping and indistinguishable. The only exception is found for DALS in cases 5 and 6, where the normalized Δ is slightly higher when $k = 1$. This is probably due to a slightly lower accuracy of the first-order DCA expansion in those cases.

The figure of merit Ω is plotted versus the collision probability in Figure 6.9(b), again normalized with respect to the value obtained with the standard Monte Carlo method. Since the computational time increases with the expansion order as shown in Figure 6.8, the value of Ω decreases for higher order. The best performing among the three methods for the considered test cases is DALS, since the normalized figure of merit is at least 10 times larger than the one of DASS and 10^2 times larger than DAMC. For test case 7, where collision probability is lower, the efficiency of DASS in terms of Ω is higher than the other cases. Note that the value of Ω for an expansion order $k = 1$ is lower than the one obtained with $k = 2$ for DALS for test case 5 and 6. As stated before, the reason is the slightly lower accuracy of the map in this case, that is not mitigated by the lower computational time.

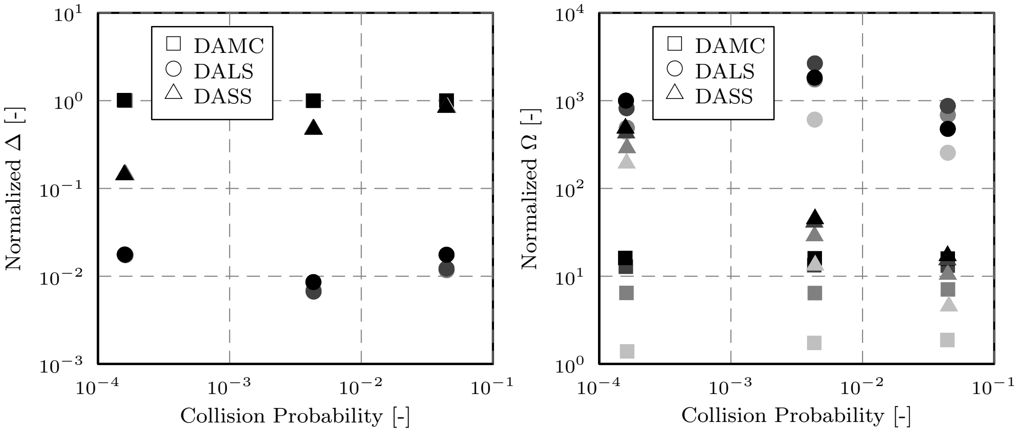

(a) Normalized figure of merit Δ **(b)** Normalized figure of merit Ω

Figure 6.9. Normalized figures of merit Δ and Ω of DAMC, DALS, and DASS for the Keplerian test cases vs. collision probability for different expansion orders. Markers are coloured using a gray scale, where black is used for the expansion order $k = 1$ and lighter gray for $k = 4$.

To conclude this analysis, the collision probability computed with Alfano's formula and the DA-based methods with an expansion order $k = 1$ are compared in Table 6.3. It can be observed that using a first-order DA expansion the percentage relative error is similar to that obtained using Alfano's method for test case 7, where the relative motion is no more linear. The DA-methods at first order are therefore equivalent to Alfano's analytical approximation.

Test case	P_c (Alfano)	% err [-]	P_c (DAMC)	% err [-]	P_c (DALS)	% err [-]	P_c (DASS)	% err [-]
5	4.440E-02	-0.32%	4.444E-02	-0.23%	4.448E-02	-0.14%	4.432E-02	-0.50%
6	4.324E-03	-0.36%	4.337E-03	-0.06%	4.332E-03	-0.18%	4.361E-03	+0.49%
7	1.580E-04	-2.13%	1.580E-04	-2.13%	1.568E-04	-2.87%	1.584E-04	-1.88%

Table 6.3. Comparison of the collision probability computed with Alfano's method and the DA-based methods for the Keplerian test cases with a DCA expansion of order $k = 1$

6.3.2 Comparison of the methods on real conjunctions

In this section four test cases are considered to test the algorithms for collision probability computation. The selected test cases include LEO and GEO close encounters with different relative velocity at TCA. The selected test cases are listed in Table 6.4: the satellites involved in each conjunction case and the associated orbital regimes are listed in the second and third column; the other columns report the TCA, DCA, the relative velocity at TCA, and the collision threshold D used for the computation of P_c. On the last column the collision probability computed using Alfano's formula is listed. The initial orbital states used for orbit propagation with AIDA are listed in A.2.

Test case	Sat. No.	Orbit	TCA [days]	TCA	DCA [m]	Δv_{TCA} [km/s]	D [m]	P_c (Alfano)
A	39152	LEO	2.831	2014 Feb 13 15:08:42	51.0	12.757	10	2.850E-3
	27580	LEO	2.950					
B	27453	LEO	1.820	2013 Nov 22 09:07:47	136.6	11.103	16	3.664E-5
	33692	LEO	1.837					
C	37838	LEO	2.707	2013 Nov 24 06:02:00	75.7	0.327	12	5.218E-3
	37840	LEO	3.909					
D	16199	GEO	1.535	2013 Nov 21 13:55:18	937.1	0.784	15	5.804E-4
	29648	GEO	2.007					

Table 6.4. TCA and DCA computed for the real conjunctions used as test cases

The orbits of the couples of objects listed in Table 6.4 are plotted in Figure 6.10. The orbital planes of the orbits involved in conjunctions A and B are almost perpendicular and consequently the relative velocity is higher than the other LEO close conjunction. For test case C indeed the planes are almost coplanar and the two satellites are orbiting in the same direction. For the GEO case the angle between the two orbital planes is higher but the slower orbital dynamics results in a lower relative velocity with respect to the LEO cases.

The collision probability is computed with DAMC, DALS, and DASS for each test case, and the results are listed in Table 6.5. Uncertainties on both position

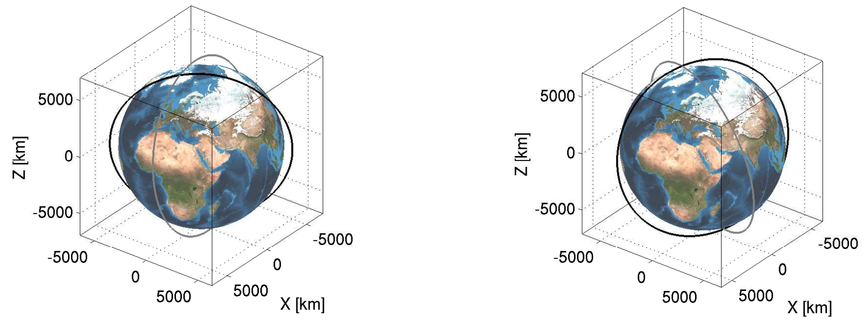

(a) Case A **(b)** Case B

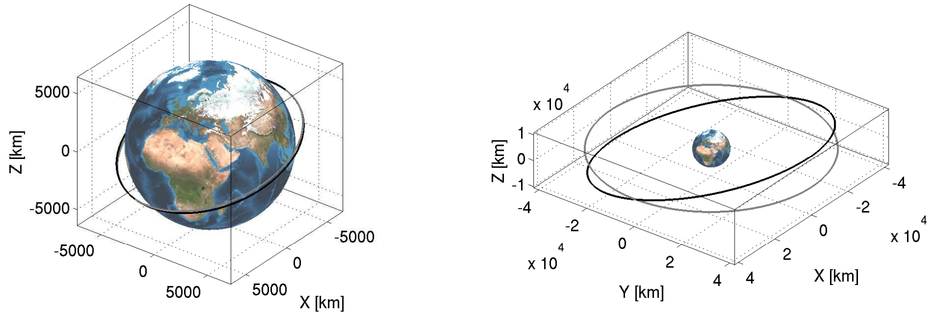

(c) Case C **(d)** Case D

Figure 6.10. Orbits of conjuncting objects selected as test cases. Black trajectory is referred to the first object involved in the conjunction, the gray one to the second object.

and velocity are considered in these simulations. The variance of the initial positions and velocities are estimated from pseudo observations generated using TLE and SGP4/SDP4 and are given in A.2. According to the results of Section 5.4.3, the error of a third order Taylor expansion of the DCA is lower than the collision threshold for a maximum propagation time of one week.

The number of samples of the DAMC are estimated using Eq. (6.11) considering a relative error $\varepsilon = 5\%$, whereas the number of samples for DALS is fixed to 5×10^3 and the samples for each conditional level of DASS is 10^4. Although the number of samples is much lower than in DAMC, both DALS and DASS can provide good estimates of the collision probability. Taking the value obtained with DAMC as reference P_c, it is possible to compare the three methods in terms of percentage relative difference. In all cases, the computed collision probabilities differ at most 3% from the DAMC value. The largest difference is obtained for test case B, where the collision probability is lower.

The computational time t_c required by DALS and DASS is lower than the one of DAMC. The latter is in turn significantly lower than the one of a standard Monte

Test case	Method	P_c [-]	% err [-]	N_T	t_c [s]	δ [-]	Δ [-]	Ω [-]
A	DAMC-3	2.869E-3	0.0%	1.5E+6	11.19	1.522E-2	18.64	4.686E+07
	DALS-3	2.891E-3	0.8%	5.0E+3	0.71	2.260E-2	1.60	3.300E+08
	DASS-3	2.875E-3	0.1%	4.0E+4	0.28	3.712E-2	7.42	3.141E+08
B	DAMC-3	3.597E-5	0.0%	1.2E+8	875.88	1.548E-2	166.73	3.682E+09
	DALS-3	3.511E-5	-2.3%	5.0E+3	0.42	3.858E-1	27.28	1.298E+10
	DASS-3	3.674E-5	2.1%	7.0E+4	0.54	4.975E-2	13.16	5.543E+11
C	DAMC-3	5.214E-3	0.0%	8.1E+5	6.06	1.535E-2	13.81	2.577E+07
	DALS-3	5.205E-3	-0.2%	5.0E+3	1.06	1.499E-2	1.06	1.549E+08
	DASS-3	5.190E-3	-0.5%	4.0E+4	0.28	3.541E-2	7.08	1.057E+08
D	DAMC-3	5.751E-4	0.0%	7.3E+6	55.16	1.543E-2	41.67	2.303E+08
	DALS-3	5.783E-4	0.6%	5.0E+3	0.63	3.452E-2	2.44	3.982E+09
	DASS-3	5.799E-4	0.8%	5.0E+4	0.36	4.215E-2	9.43	4.650E+09

Table 6.5. Computed collision probability P_c, computational time t_c, and figures of merit Δ and Ω. Percentage relative error is obtained taking DAMC-3 collision probability as reference.

Carlo method, in which the trajectory of each virtual object is numerically propagated up to the close encounter.

Let us consider the test case A for illustrative purposes. With our implementation of the dynamics, a standard MC simulation with 1.5×10^6 samples would require 1.05×10^8 seconds, as approximately 35 seconds are required to propagate each of the two objects to the TCA. The computational time of the DA methods is given by the time required to (1) perform the DA integrations (2) compute map (5.16) and (3) run the algorithms based on polynomial evaluations (labelled as t_c in Table 6.5). Each of the two third order propagations requires approximately 10 times a pointwise integration, and the DA manipulations to compute the DCA expansion requires only fraction of second (see Section 5.4.2). Thus, the additional cost associated to DA computations is equivalent to only 20 pointwise numerical propagations and this is irrelevant with respect to the gain obtained by substituting numerical integrations with polynomial evaluations. For test case A, the total computational cost (i.e. including DA orbit propagation, map inversion, and probability computation) of a DAMC-3 run is 492.38 s, which is 5 orders of magnitude less than the time that would be required by a standard MC (note that this value can be further reduced by a more efficient implementation of AIDA propagator). This gain in computational time can be higher for cases with lower computational probability (e.g., test case B) and when DALS and DASS algorithms are used.

Figure 6.11 summarizes the t_c of the three DA methods. Keeping in mind that the computational time of all the DA methods is orders of magnitude lower than that of standard MC, it can be noted that the computational effort of DAMC increases exponentially for decreasing collision probability, whereas the other two methods have drastically lower variations. The t_c of DASS slightly decreases for increasing collision probability, due to the lower number of conditional levels required to converge. On the contrary, the computational time of DALS increases with collision probability. This is a consequence of the control on the maximum value of the PF on the important direction: for test case B, that has the lowest probability, the relative distance between the two objects is higher and the intersection of the two ellipsoids is very small. As a result, most samples produce a one-dimensional collision probability that is zero since the maximum of the PF is negative and no computation of the intersections c_j^i is required, with a reduction of the computational time. To conclude, it is worth observing that the computational time of the methods can be further reduced as all methods can be classified as "embarrassingly parallel".

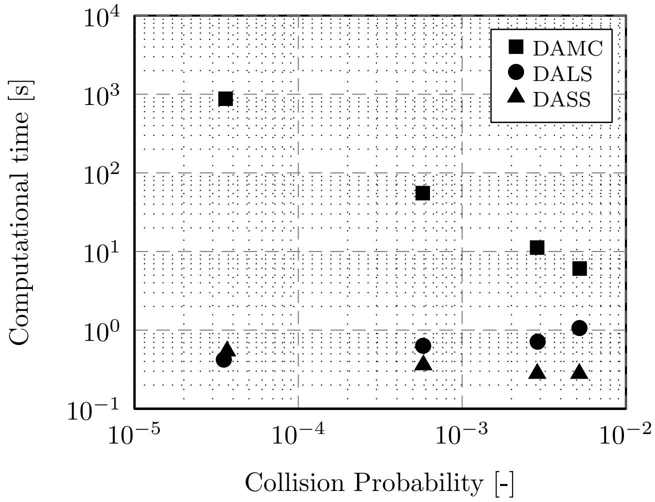

Figure 6.11. Computational time of DAMC, DALS, and DASS vs. collision probability.

The methods are compared in terms of accuracy and efficiency in Figure 6.12, where the figures of merit Δ and Ω are plotted against collision probability. For each test case the values of Δ and Ω listed in Table 6.5 are normalized with respect to the value obtained for the DAMC simulation.

According to Figure 6.12(a), both advanced methods lead to significant improvements in terms of unitary c.o.v. with respect to DAMC. DALS outperforms DASS for higher probability and its Δ is one order of magnitude lower than DAMC. The performance of DASS increases for lower probability, where it performs better than DALS. The variance of DASS is indeed lower than that of DALS. Nevertheless, DALS shows the lowest computational time.

The figure of merit Ω is plotted against the collision probability in Figure 6.12(b). For probability higher than 10^{-3}, DALS performs better than DASS and DAMC.

The value of Ω exponentially increases for decreasing probability and DASS reaches the same performances of DALS for test case D and outperforms DALS for test case B. The reason is mainly related to the lack of accuracy of DALS for case B, due to the low number of samples for which the one-dimensional probability is non-zero. An higher number of samples should be used with DALS to achieve a more reliable estimate of the collision probability in this case.

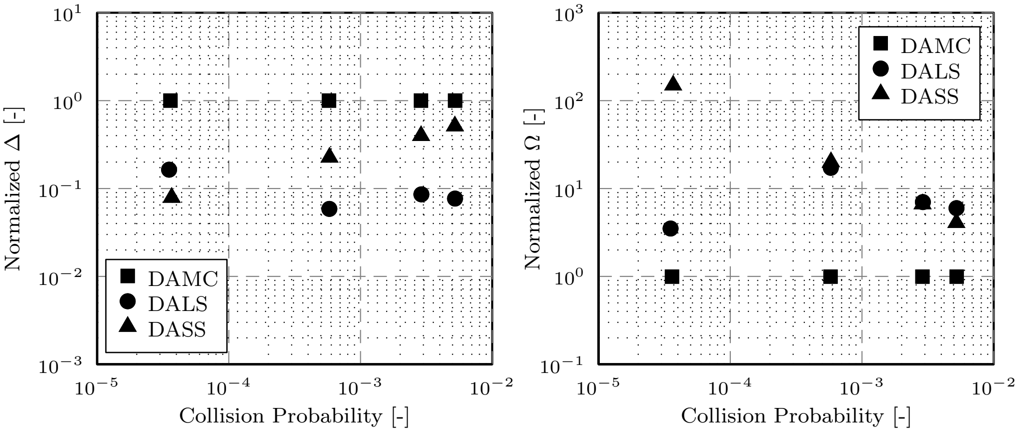

(a) Normalized unitary c.o.v. Δ **(b)** Normalized figure of merit Ω

Figure 6.12. Performance comparison with normalized figures of merit

6.3.3 Covariance scaling analysis

The collision probability depends on the shape, size, and orientation of the covariance matrix of the position and velocity at TCA. In this subsection a validation of DALS and DASS for varying initial covariance size is performed, using as a reference the values obtained with DAMC. This approach requires that the accuracy of the Taylor expansion of the DCA and TCA is high, with error below 1 meter for all initial covariance sizes. For each test case and covariance size, the accuracy of the Taylor expansion was verified by selecting, from 10^9 samples generated from the full covariance matrix, the 100 with largest displacement from the reference initial state. As the error on the DCA was below the selected threshold in all cases, the value obtained from the DAMC computation corresponds to the one of a pointwise Monte Carlo (for single DCA and TCA conjunctions). Thus, DAMC can be used to validate DASS and DALS.

The principal components of the initial covariance matrices of the two objects, accounting for both position and velocity, are scaled by a factor l and the collision probability is computed. Note that by using principal components it is guaranteed that all components are scaled by the same factor and the correlations coming from the orbit determination process are not altered. The collision probability computation is repeated for different values of the scaling factor l and the results are plotted in Figure 6.13. A good accordance between the values obtained with DALS and DASS (overlapping solid lines) and the reference DAMC (indicated with squares) is found for all test cases and scale factor l.

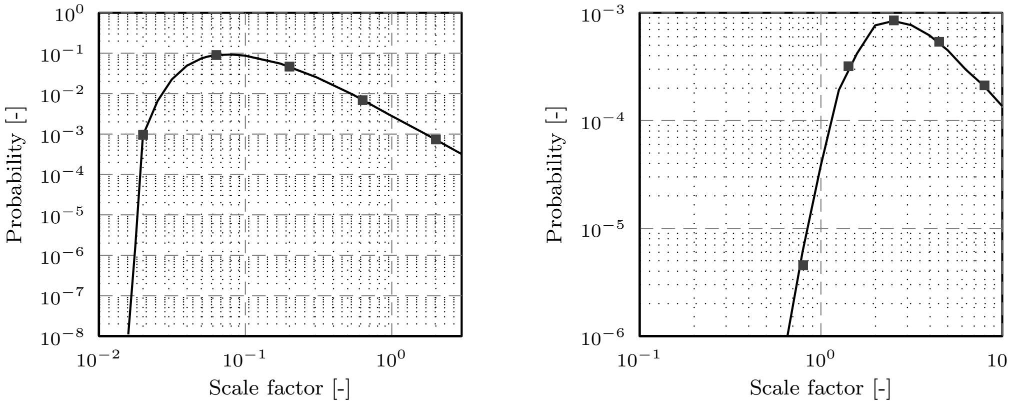

(a) Case A **(b)** Case B

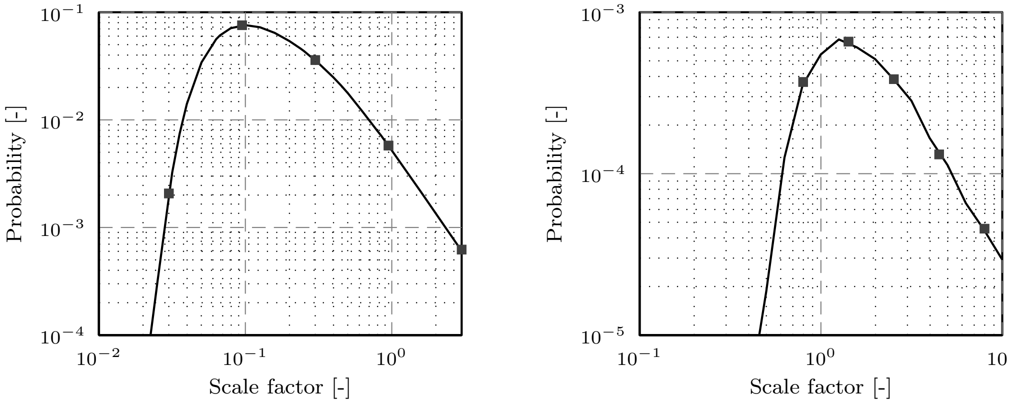

(c) Case C **(d)** Case D

Figure 6.13. Covariance scaling analysis: collision probability versus scaling factor l. Solid curves are obtained with DALS-3 and DASS-3, squares represent the reference values computed with DAMC-3.

Note that all curves show the same behaviour: for smaller initial uncertainties the collision probability is zero or very small, then it increases when the p.d.f. of the two objects at TCA start to overlap. After reaching its maximum value the collision probability decreases because the volume covered by the p.d.f. continues to grow while the hard-body region (over which the DALS and DASS ideally integrate the combined p.d.f.) remains constant.

6.3.4 Non-Gaussian distributions

Besides reducing computational time and managing nonlinearities by setting the expansion order $k > 1$, the DA-based methods can be modified to deal with non-Gaussian distributions. The DA-based propagation with AIDA does not depend on the initial distribution and so are the Taylor expansions of the DCA and TCA. Similarly, to evaluate the polynomials, only the displacement of the sample from the reference point is required. Thus, the samples can derive from any statistical distribution. The modification of the algorithms to work with non-Gaussian distributions is then straightforward and only requires only changing the sampling procedure to match the desired distribution of the initial position and velocity of the two objects.

Uniform Distribution

The case of a uniform distribution for the initial states is here analyzed and DAMC is used to compute the collision probability. Sampling is performed in principal components, since they are independent. After assembling the 12×12 global covariance matrix, where no correlations between the two colliding objects are considered, the eigenvalues and eigenvectors are computed. The range of each uniform distribution is selected so that its standard deviation σ_i equals the one of the original Gaussian distribution, i.e.

$$\begin{cases} \dfrac{\sqrt{3}}{6\,\sigma_i} & \text{for } x \in \left[-\sigma_i\sqrt{3}; +\sigma_i\sqrt{3}\right] \\ 0 & \text{elsewhere }. \end{cases} \tag{6.30}$$

The sampled 12-dimensional vector $\boldsymbol{u}$ is then transformed from principal components to J2000 reference frame by

$$\boldsymbol{z} = \boldsymbol{V}\boldsymbol{u} \tag{6.31}$$

where $\boldsymbol{z} = \left\{\boldsymbol{x}_0^1; \boldsymbol{x}_0^2\right\}$ and $\boldsymbol{V}$ is a 12×12 matrix, whose columns are the eigenvectors of the two covariance matrices. The obtained vector $\boldsymbol{z}$ is then used in DAMC algorithm to evaluate the Taylor expansion of the DCA, whose value is then compared with the collision threshold D.

The computed collision probabilities are listed in Table 6.6, where the order $k = 3$ is used for the DCA expansion. The collision probability decreases significantly for test case B, whereas it increases by a factor of about 10 for test case C. Smaller variations can be observed for the remaining test cases.

A detail of the resulting p.d.f. throughout the above process is portrayed in Figure 6.14. It can be observed how the principal component is uniformly distributed and the p.d.f. of the first component of $\boldsymbol{r}_0^1$ in J2000 has a trapezoidal shape. After the propagation, the p.d.f. resembles a triangular distribution.

This example shows the importance of considering the proper uncertainty distribution for the initial positions and velocity of the two objects. DAMC, DALS, and DASS have the maximum flexibility in these terms, as they can manage any com-

Test case	DCA [m]	D [m]	P_c (Gaussian)	P_c (Uniform)	N_T	t_c [s]
A	51.0	10	2.869E-3	2.591E-3	1.7E+6	12.86
B	136.6	16	3.597E-5	4.375E-6	1.2E+8	877.96
C	75.7	12	5.214E-4	4.783E-3	8.9E+5	6.74
D	937.1	15	5.751E-4	7.484E-4	7.5E+6	56.87

Table 6.6. Collision probability using DAMC-3 and uniform distribution for initial orbital states

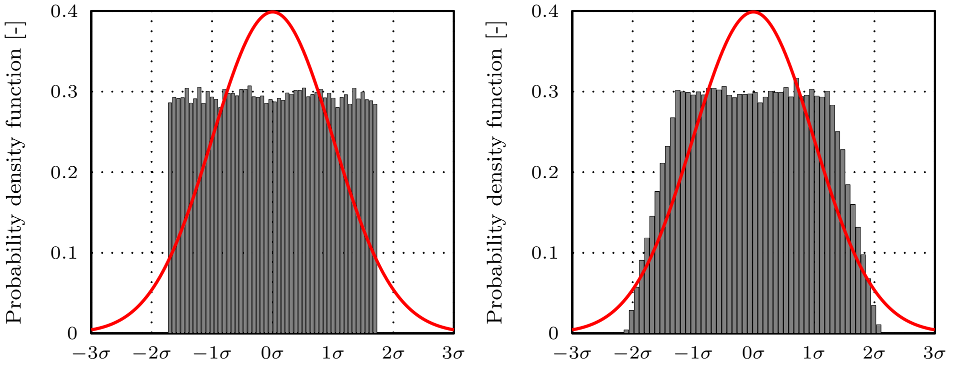

(a) Principal component $i = 1$ **(b)** J2000 position component

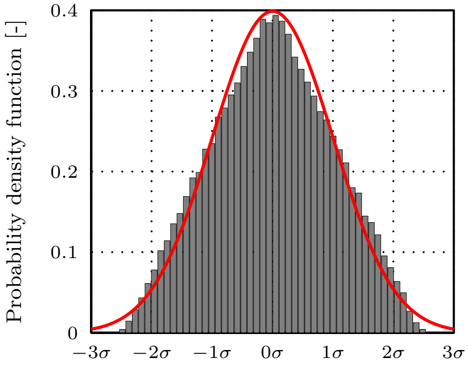

(c) Relative distance component

Figure 6.14. Probability distribution function for non-Gaussian initial state uncertainties. The p.d.f. are normalized by the current value of σ and a Gaussian distribution with the same standard deviation is plotted for comparison.

bination of initial distributions, which can also differ between target and chaser. In addition, the high-order polynomial approximation accounts for nonlinear effects on the p.d.f. resulting from orbital propagation.

Gaussian mixture

Non-Gaussian space objects uncertainties can be effectively represented by means of Gaussian mixture parametrization, i.e. using a combination of multivariate Gaussian distributions. The DA-methods are here used in presence of initial uncertainties described by Gaussian mixtures.

Conjunction geometry of test case C (see Table 6.4) is here used. The projection of the uncertainty distribution on the equatorial plane is represented in Figure 6.15. For both objects involved in the close conjunction the uncertainty at the reference epoch are obtained by considering two multivariate Gaussian distributions. For each of the two objects, the covariance matrices of Appendix A.2 are duplicated and shifted with respect to the nominal mean value.

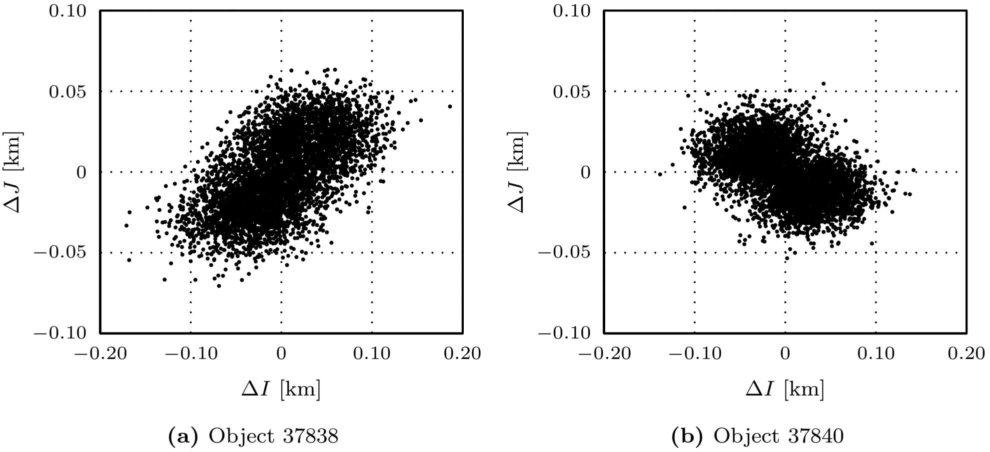

(a) Object 37838

(b) Object 37840

Figure 6.15. Gaussian mixture distribution of intial position on the equatorial plane IJ

The resulting collision probability is listed in Table 6.7. The probability is lower than the Gaussian reference value, mainly because the position of the four Gaussians is no more coincident with the reference mean values. As a consequence, a lower probability density is found inside the failure region and a lower number of samples for which collision condition occurs is generated.

Test case	DCA [m]	D [m]	P_c (Gaussian)	P_c (GaussMixt)	N_T	t_c [s]
C	75.7	12	5.214E-4	6.386E-5	6.6E+7	482.93

Table 6.7. Collision probability using DAMC-3 and gaussian mixture parametrization for initial orbital states

6.4 Conclusions

Three algorithms, based on the high order Taylor expansion of the DCA with respect to initial uncertainties, have been developed for the computation of collision probability. This approach enables significant savings in terms of computational effort, since the numerical propagation of the orbital dynamics is replaced by polynomial evaluations. The propagations account for the main sources of perturbation, using up-to-date models for spherical harmonics and air density. The procedure described for the expansion of the TCA and DCA can be adapted to any set of initial states and using any arbitrary reference frame, which widens the applicability of the method to data coming from any special perturbation catalogue. In addition, the probability distribution of the uncertain initial position and velocity is not required to be Gaussian. The algorithm for the identification of the TCA and DCA is insensitive to the initial conditions probability density function. Thus, the only modification to the method described here to work with non-Gaussian distributions is the sampling procedure (as shown by the uniform distribution and Gaussian mixture examples).

Besides a DA version of a standard Monte Carlo algorithm, here labelled DAMC, two advanced Monte Carlo methods for the computation of collision probability have been presented and adapted to DA techniques: Line Sampling and Subset Simulation. The resulting methods are named DALS and DASS respectively and both have better performances in terms of computational time and accuracy with respect to DAMC. For collision probability down to 10^{-4}, the DALS outperforms the other two methods, whereas for lower probabilities DASS turns out to be more accurate than the other methods. According to these results DASS is preferable when collision probability is below 10^{-4}, whereas DALS should be used for higher probabilities. The selection of the method to use could be translated in terms of DCA, selecting DALS when the relative distance is below a few hundreds metres and DASS on the other case.

Tests performed on both long-term and short-term encounters have shown that the collision probabilities computed with the three methods are in good accordance. Being based on the Taylor expansion of the TCA and DCA, and since no assumptions are made on the dynamics of the encounter, the presented methods are also suitable for close encounters with low relative velocity. It has been shown that, using an expansion order $k > 1$, the methods can capture the effects of nonlinear relative motion on collision probability.

7

Collision avoidance

In the case of a predicted high risk event, the possibility of a Collision Avoidance Maneuver (CAM) is considered. The classification of high-risk conjunctions depends on conjunction geometry, collision probability value, and satellite operator practice and procedures. These factors should be defined with the aim of avoiding all unnecessary CAM, to save fuel and in turn to guarantee satellite expected lifetime. When the driving parameters suggest that an event will exceed an admissible level of risk, a CAM is designed [Lap08, Flo09a]. The aim of the manoeuvre is to increase the separation between the objects, in order to reduce the collision risk. The fuel consumption should be as low as possible and the spacecraft must be kept in the operational window.

When the threatening conjunction occurs close to a designed station keeping manoeuvre, it can be sufficient to anticipate it to reach an acceptable level of risk. The advantage of this approach is that no extra fuel has to be used for an ad-hoc manoeuvre and mission constraints are not violated. In all other cases a CAM (and maybe a subsequent restitution manoeuvre) has to be designed. Using along-track burns it is possible to raise or decrease the altitude of the object at the time of the conjunction or, with lower Δv, to bring forward or delay the arrival at the conjunction location [Kli05]. The first strategy has to be applied with head-on conjunction, whereas the second is suitable for an oblique approach geometry.

CAM can be optimized by looking at the gradient of the collision probability with respect to velocity increment component and then using numerical methods to find the Δv that lowers the collision probability up to the desired value [Pat03]. Analytical expressions of the relative Keplerian dynamics of the two bodies on the B-plane can be obtained and used to set-up an optimization of the Δv to maximize the collision miss distance [Bom13].

The design of CAM can be also tackled as an optimization problem. Genetic Algorithm (GA) were used for the design of CAM for LEO and GEO objects, taking into account mission constraints and combining them into a single objective function to be minimized [Lee12]. More complex cases, such as the presence of multiple objects, can be tackled by GA optimization of the manoeuvre. In that case the use of an along-track manoeuvre can not be the optimal choice to reduce collision risk [Kim12].

In order to use classic optimization codes (i.e. gradient based methods) to solve a multi-objective optimization problem, a common practice is to merge the different objective functions into a single scalar objective function by means of weighting factors. This technique requires an accurate selection of the weights, and it has, as major drawback, the identification of a single optimal solution per run. It is clear that it is difficult to define a single objective function that takes into account many criteria, that for a CAM could range from fuel consumption minimization to separation distance maximization.

The use of multi-objective optimizers enables a more flexible approach in terms of optimal manoeuvre selection through the definition of the objective functions. This allows the operator to enrich the optimization problem with additional considerations and to obtain sets of optimal solutions rather then a single best solution. Thus, with respect to traditional methods, it it adds flexibility and it can be easily adapted to any satellite mission constraint and requirement. An innovative aspect of this approach is indeed the inclusion of mission constraints as separate objective functions. In this way it is possible, within the optimization, to understand whether or not a manoeuvre is compliant with mission constraints.

In this Chapter the CAM design as a multi-objective optimization problem, using a Multi-Objective Particle Swarm Optimizer (MOPSO) [Ken01]. In this way, it is possible to define a set of objective functions, each one targeted for a particular constraint (e.g. ground track repeatability), or optimization objective (e.g. minimum fuel consumption and collision risk reduction) without the need of combining all of them in a single one using scaling factors. Furthermore, the optimization will provide a set of solutions that are Pareto optimal, i.e. each CAM belonging to this set is such that any change in it will result in a worst performance in one or more objective functions. The set of all Pareto optimal solutions is usually referred to as “Pareto front”. The analyst can then select a CAM on the Pareto front, e.g. the one that guarantees a reduction of collision risk up to an acceptable level. This is not possible for a single-objective optimization that provides only one optimal solution that is strongly dependent on the scaling factors that are, in case, used to assemble objective functions.

This chapter is organized as follows: in Section 7.1 a few details on the population-based optimizer MOPSO are given, whereas Section 7.2 illustrates the optimization strategy and architecture for the evasive manoeuvre design. The CAM optimization is then applied to two test cases in Section 7.3.

7.1 MOPSO

Population-based optimizers can be easily modified to deal with a vector of objective functions delivering the entire set of Pareto optimal solutions. Furthermore, particle swarm optimization seems particularly suitable for multi-objective optimization mainly because of the high speed of convergence that the algorithm presents for single-objective optimization [Ken01]. In a multi-objective optimization problem the objective function is a M dimensional vector

$$\boldsymbol{f}(\boldsymbol{x}) = (f_1(\boldsymbol{x}), f_2(\boldsymbol{x}), \ldots, f_M(\boldsymbol{x})) \,. \tag{7.1}$$

In this frame, a criterion to compare vectors is necessary to identify the optimal solution set. The Pareto dominance is the appropriate criterion to serve this aim, enabling the solutions ranking [Deb99].

The MOPSO implemented for the solution of the problem at hand is based on the following algorithmic flow:

1. Randomly initialize a number of individuals or particles N within the design space.
2. Evaluate the objective function

$$\boldsymbol{y}_i = \boldsymbol{f}(\boldsymbol{x}_i) \quad \text{for} \quad i \ = 1, \ldots, N. \tag{7.2}$$

3. Update the personal best solution $\boldsymbol{p}_{\text{best}}$. The solutions are compared using the Pareto dominance criterion. Thus for each particle we have

$$\boldsymbol{p}_{\text{best}} = \begin{cases} \boldsymbol{x}_i & \text{if } \boldsymbol{x}_i \text{ dominates } \boldsymbol{p}_{\text{best}} \\ \boldsymbol{p}_{\text{best}} & \text{if } \boldsymbol{p}_{\text{best}} \text{ dominates } \boldsymbol{x}_i \\ \boldsymbol{x}_i \text{ or } \boldsymbol{p}_{\text{best}} \text{ randomly} & \text{in the other cases} \end{cases} \quad \text{for } i = 1, \ldots, N \,. \tag{7.3}$$

4. Update global best list $\boldsymbol{G}_{\text{best}}$. In the multi-objective problem $\boldsymbol{G}_{\text{best}}$ is the analogous of the scalar global best $\boldsymbol{g}_{\text{best}}$ and it represents the entire set of non-dominated solutions. This list is updated by processing the subset of non-dominated solutions $\boldsymbol{x}_j$ with $j = 1, \ldots, N^* \leq N$
   - If $\boldsymbol{x}_j$ is dominated by one of the solutions belonging to the list, do not updated the list
   - If $\boldsymbol{x}_j$ dominates one or more solutions belonging to the list, then add $\boldsymbol{x}_j$ to the $\boldsymbol{G}_{\text{best}}$ list and delete the dominated solutions
   - If $\boldsymbol{x}_j$ neither dominates nor is dominated by any solution belonging to the $\boldsymbol{G}_{\text{best}}$ list, then simply add $\boldsymbol{x}_j$ to the list
5. Update the global best solution $\boldsymbol{g}_{\text{best}}$. Note that the $\boldsymbol{g}_{\text{best}}$ is univocally defined for a scalar objective function, whereas it must be opportunely chosen within the $\boldsymbol{G}_{\text{best}}$ list in the multi-objective case. The selection of the $\boldsymbol{g}_{\text{best}}$ plays a key role in obtaining a uniform set of Pareto optimal solutions. For this purpose a uniform 30 cells grid in the objective space is defined at each iteration and the number of solutions belonging to each grid cell is calculated. Based on this

number, a roulette-wheel method is then applied to promote the selection of $\boldsymbol{g}_{\text{best}}$ in a low populated grid-cell.

6. Compute the new particles position by

$$\boldsymbol{x}_i^{k+1} = \boldsymbol{x}_i^k + \boldsymbol{v}_i^{k+1}\Delta t \quad \text{for} \quad i \ = 1, \ldots, N, \tag{7.4}$$

in which $\boldsymbol{v}_i^{k+1}$ is the velocity of the i-th particle at the $(k+1)$ iteration, given by

$$\boldsymbol{v}_i^{k+1} = w\boldsymbol{v}_i^k + c_1 r_1 \frac{\boldsymbol{x_i^k} - \boldsymbol{p}_{\text{best}}}{\Delta t} + c_2 r_2 \frac{\boldsymbol{x_i^k} - \boldsymbol{g}_{\text{best}}}{\Delta t}. \tag{7.5}$$

7. Repeat 2-6 until the convergence criterion is satisfied or the maximum number of iterations is reached.

The parameters c_1 and c_2 of Eq. (7.5) are considered constant and equal to 2 during the optimization, assuring a balance between local and global terms. A linear decrease of w with the iteration number in the interval $[0.4, 1.4]$ is adopted. In particular a greater value of the inertia enables a better exploration of the search domain in the first phase of the optimization, whereas a lower value allows a better analysis of the most promising areas of research space in the subsequent phases. Note that if the position of a particle goes outside the search space, the violated component of the decision vector takes the value of the corresponding boundary and its velocity component is multiplied by a random number between $[-1, 0]$.

The maximum number of particles belonging to the $\boldsymbol{G}_{\text{best}}$ is fixed to 100 units. The same procedure adopted for selecting the $\boldsymbol{g}_{\text{best}}$ is used to delete those solutions belonging to a highly populated grid-cell, if the maximum list size is exceeded.

The problem addressed with implemented MOPSO is characterized by the presence of inequality constraints necessary to control the time of execution of the CAM and limit the $\Delta\boldsymbol{v}$ in terms of module and direction. As the feasible domain inside the search space is sufficiently large the feasible solution method (FSM) is adopted for the constraints handling [Coa03]. More specifically the swarm initialization is performed randomly, but only feasible solutions are retained. This implies that the first step of the algorithm generally requires the evaluation of a number of solutions greater than the population size. Furthermore, only feasible solutions are counted for the $\boldsymbol{g}_{\text{best}}$ and $\boldsymbol{p}_{\text{best}}$ values during the optimization. The initial velocity of the particle is set to be 0.

The convergence criterion adopted is based on the comparison of the average position of the non dominated solutions in the objective space with the same average position of the previous 20 iterations. If the component-wise difference of this two vectors is lower than 1% the Pareto set of optimal solutions is assumed to have been found. Furthermore, a maximum number of iterations of 20 and a 50 particle swarm are considered. These values are chosen, on the basis of several experiments, to assure an acceptable repeatability of the Pareto optimal solution set with a limited computational time.

7.2 CAM optimization

The evasive manoeuvre design is tackled in two steps: first an optimal manoeuvre is searched using SGP4/SDP4 only, with the aim of retrieving quickly a CAM among those on the Pareto front. Then, a local optimization is performed using the numerical propagator AIDA and exploiting DA to obtain an expansion of the relative distance as a function of the optimization variables to avoid numerical propagations.

In both cases the following criteria are considered as driving factors for the CAM optimization

- Minimize fuel consumption
- Increase separation between the two objects
- Decrease collision risk below an accepted value
- Avoid that CAM increases the collision probability of other conjunctions in the week following the manoeuvre
- No violation of mission constraints for the target within a given time window

The last criterion is strictly connected to the satellite mission and has to be changed on each case accordingly. In the following subsections the optimization strategies for SGP4/SDP4 and AIDA based collision avoidance manoeuvre design are described.

7.2.1 Optimization strategy and architecture with SGP4/SDP4

Four free parameters are considered: the manoeuvre time t_m, the module of Δv, and its direction, expressed as a function of two angles λ and ϕ. The vector $\boldsymbol{\Delta v}$ is defined in the RTN reference frame as

$$\boldsymbol{\Delta v} = \Delta v \begin{Bmatrix} \cos(\phi)\cos(\lambda) \\ \cos(\phi)\sin(\lambda) \\ \sin(\phi) \end{Bmatrix} \tag{7.6}$$

A set of these variables, hereafter grouped in the vector $\boldsymbol{x}$, univocally identifies a possible manoeuvre. Under the hypothesis of an instantaneous burn the orbital state after the manoeuvre is given by

$$\begin{Bmatrix} \boldsymbol{r}(t_m^+) \\ \boldsymbol{v}(t_m^+) \end{Bmatrix} = \begin{Bmatrix} \boldsymbol{r}(t_m^-) \\ \boldsymbol{v}(t_m^-) \end{Bmatrix} + \begin{Bmatrix} \boldsymbol{0} \\ \boldsymbol{\Delta v} \end{Bmatrix} \tag{7.7}$$

where the vector $\boldsymbol{\Delta v}$ is in TEME reference frame. The original TLE is updated so that the orbital state is equal to the post-manoeuvre state at at time t_m^+. A new search for all minima of the relative distance in a time window of 7-days is then performed, starting from t_m. The search is performed as a global optimization problem with COSY-GO and using the SGP4/SDP4 analytical propagator as described in Section 5.2. This allows for the computation of collision probability with Alfano's formula in Eq. (6.5) for each minima whose associated relative distance is below a conjunction threshold. For this purpose the initial covariance matrix is propagated at conjunction epoch using the state transition matrix computed as in Section 3.1.3.

At this point, it is possible to define a set of objective functions, $\boldsymbol{f}(\boldsymbol{x})$, that are used by the optimizer to manage the plethora of design criteria. The objective function associated to propellant minimization is

$$f_1(\boldsymbol{x}) = \frac{\Delta v}{\Delta v_{\max}} \tag{7.8}$$

where $\Delta v_{\max}$ corresponds to the maximum amount of fuel that can be allocated for the manoeuvre.

The second figure of merit is designed to increase both the closest approach distance and the distances of other conjunctions that may occur within the time window of interest $[t_m, t_m + 7]$. The objective function is defined as follows

$$f_2(\boldsymbol{x}) = \frac{1}{2}\,\frac{R - \min\left(d(t)\right)}{R} + \frac{1}{2}\,\frac{R - \overline{d}}{R}, \tag{7.9}$$

where $\min(d)$ is the distance of closest approach after the manoeuvre, and $\overline{d}$ is the mean distance of all local minima below the conjunction threshold R. When both the minimum and the mean value are equal to R the objective function has value zero. In case no minima below R are found the value of $f_2(\boldsymbol{x})$ can be set equal to zero. This combination is chosen to correctly handle situations in which using only mean or minimum is not sufficient. As an example, let us consider the case in which a very low global minima is found together with many other local minima close to the threshold R. If only the second part of the objective function is considered the resulting value of f_2 will be zero, thus missing the risk associated to the global minima. By adding the first part the global minima the objective function will be close to 1/2, avoiding a good ranking for the associated manoeuvre during the optimization process.

The third objective function involves the collision probability of the global minimum, and is

$$f_3(\boldsymbol{x}) = \log_{10}\left(P_c + 1\right). \tag{7.10}$$

This function is close to zero for little collision probabilities and reaches $\log_{10} 2$ when the collision probability is maximum. The lower the probability, the lower the objective function, the more the probability is close to 1 the more the value gets close to $\log_{10} 2$.

It could be observed that the two objective functions $f_2(\boldsymbol{x})$ and $f_3(\boldsymbol{x})$ could be condensed in a single one, by computing the P_c for all minima and compute the sum of all collision probabilities. Anyway this would imply that a good knowledge of the orbital elements uncertainties is available during the considered time span for both the target and the chaser. This is usually not true when the chaser is a debris. In addition, the uncertainties grow with time if no other orbit determination is performed, resulting in possible underestimation of the actual collision probability. For this reason, the two objective functions are separated.

To handle mission constraints, another objective function is introduced. The design of such a function is not straightforward, since each mission has different requirements and constraints. As an example, a GEO satellite should lie in a well-defined latitude and longitude slot, whereas a LEO satellite can have requirements on ground-track evolution. To avoid the definition of an ad-hoc objective function for each case we used the following definition

$$f_i(\boldsymbol{x}) = \frac{n_v}{N} \tag{7.11}$$

where n_v is the number of violations of the mission constraint and N is the total number of time instants for which the violation of mission constraint is tested. In this way, the user has to verify when the mission constraints are violated, e.g. performing an orbit propagation and comparing the latitude and longitude with their limit values.

In case the maximum allowed fuel consumption or maximum allowed collision probability are exceeded all objective function are set to the value of f_1 or f_3. This workaround guarantees that all the points belonging to the Pareto front respect the desired thresholds for maximum $\Delta\boldsymbol{v}$ and maximum collision probability threshold.

To summarize, for each set of free parameters, the following steps are performed

1. Select the current particle $\boldsymbol{x}_i$
2. Update TLE of the target using the state after the implementation of the manoeuvre;
3. Perform a conjunction identification on a 7-days windows, starting from the manoeuvre epoch;
4. Find the global minimum and compute the mean of all minima below R;
5. Compute the collision probability using Alfano's method for the global minimum if below R;
6. Find the time for which mission constraints are violated, performing orbit propagation. The set of inequalities will change according to the mission constraints, which are different from mission to mission;
7. Compute the objective function vector $\boldsymbol{y} = \boldsymbol{f}(\boldsymbol{x_i})$. In case maximum allowed fuel consumption or collision probability are exceeded all components of $\boldsymbol{y}$ are set equal to f_1 or f_3 value respectively.

7.2.2 Optimization strategy and architecture with AIDA

The CAM optimization with AIDA is targeted to a single close conjunction. As in the previous subsection, four free parameters are considered: the manoeuvre time and the three components of the vector $\Delta\boldsymbol{v}$, that in this case is translated into the ECI J2000 reference frame. The search for all local minima of the relative distance is not performed and the second objective function is now defined as

$$f_2(\boldsymbol{x}) = \frac{R - d^*(t_m, \Delta\boldsymbol{v})}{R}, \tag{7.12}$$

where $d^*(t_m, \Delta\boldsymbol{v})$ is the Taylor expansion of the DCA as a function of manoeuvre time t_m and manoeuvre velocity vector. In this way it is possible to substitute each orbit propagation with a polynomial evaluation of d^*, thus reducing the computational effort. This polynomial map is free from singularities since in this case no angles are used to define the direction of the manoeuvre. In addition, since the module of the considered avoidance manoeuvre is small and the manoeuvre time is not allowed to vary too much from the reference value, all possible CAM are comprised in the convergence radius of the DA expansion. The behaviour of the DCA as a function of the manoeuvre Δv and manoeuvre time t_m is represented in Figure 7.1 for a close encounter in LEO. The availability of an analytical approximation of the manoeuvre can also help in the assessment of the robustness of the manoeuvre. It is indeed possible to determine whether a certain CAM lies in a region in which the relative distance has a maximum or, due to uncertainties in the manoeuvre execution, it can reach regions in which the relative distance decreases, thus limiting the CAM effectiveness. The constraint verification process is again performed using SGP4/SDP4, in order to avoid the numerical propagation for each sample at each optimizer step.

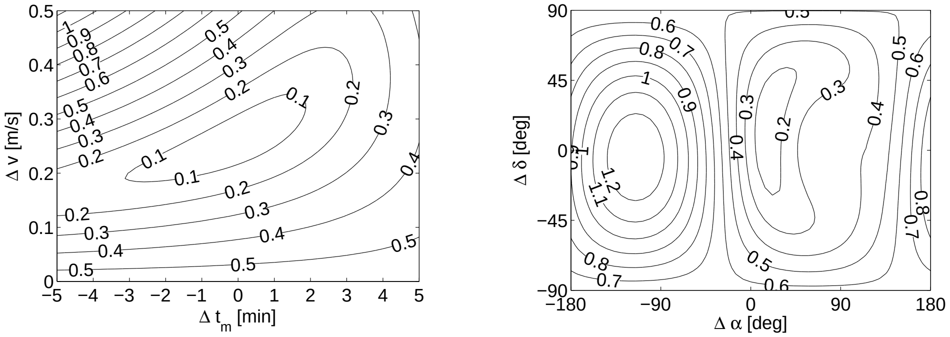

(a) Contour plot of d^* map on the (Δt_m, Δv) plane for $\alpha = 0$ and $\delta = 0$.

(b) Contour plot of d^* map on the (α, δ) plane for $\Delta t_m = 0$ and $\Delta v = 0$.

Figure 7.1. Contour plot of the polynomial approximation of the DCA map $d^*(t_m, \Delta\boldsymbol{v})$. Values on contour lines are in km.

The following steps are performed for the CAM optimization with AIDA:

1. Select the current particle $\boldsymbol{x}_i$

2. Evaluation of the polynomial map of the relative distance d^* to obtain the new DCA;

3. Compute the collision probability using Alfano's method for the new minima;

4. Find the time for which mission constraints are violated, performing orbit propagation with SGP4/SDP4. Again, the set of inequalities will change according to the mission constraints, which are different from mission to mission;

5. Compute the objective function vector $\boldsymbol{y} = \boldsymbol{f}(\boldsymbol{x_i})$. In case maximum allowed fuel consumption or collision probability are exceeded all components of $\boldsymbol{y}$ are set equal to f_1 or f_3 value respectively.

In the following section the approach is applied to two test cases, one LEO and one GEO orbit.

7.3 Numerical simulations

In this section the CAM optimization is applied to two orbital conjunctions, one in the LEO and the other in the GEO regime. In both cases the conjunction threshold is $R = 10$ km and the hard-body radius for collision probability computation is $D = 100$ m. The collision threshold D is not related to body size in this case but it guarantees that the collision probability for the nominal conjunction is above 10^{-4}. The upper and lower boundaries, u_b and l_b, of the optimization variables are listed in Table 7.1. No constraints on the manoeuvre direction are considered for these simulations and the time of the manoeuvre can occur up to one revolution before the targeted conjunction.

Variable		l_b	u_b
t_m	(rev.)	0	1
Δv	(m/s)	0	0.5
λ	(deg)	-180	180
ϕ	(deg)	-90	+90

Table 7.1. Upper and lower boundaries of optimization variables

All computations are performed on an Intel Core i5 2500 @3.30GHz, 8Gb RAM processor running Sabayon Linux 13 (kernel version 3.11.0), each run of the MOPSO lasts approximately 2 h for both LEO and GEO cases.

7.3.1 LEO case

The LEO test case considers a close conjunction between satellite Metop-A and a debris from Iridium-33 (NORAD ID 33874) occurring at 23:58:12 UTC on 2012/03/02 [Làz12]. Metop-A is on a sun-synchronous orbit, with an altitude of 820 km and an inclination of 98.7 deg, and its repeat cycle is 29 days and 412 revolutions. Iridium-33 debris instead is found at an inclination of 86 deg, and has an apogee of 890 km and a perigee of 750 km. According to last TLE data[1] before the event, the DCA is 590 m, with a radial, along-track, and out-of-plane separation of 451, 222, and 308 m respectively. The relative velocity at the TCA, again computed using SGP4/SDP4 and COSY-GO, is 12 km/s, mainly distributed on the along-track (9.7 km/s) and out-of-plane (7.1 km/s) components. The nominal collision probability for the close conjunction is $P_c = 5.118 \times 10^{-4}$.

A CAM optimization is performed, considering the upper and lower bound for the optimization variables of Table 7.1. Given that Metop-A is on a SSO, the following constraints were considered:

- Local solar time of the ascending node must be maintained within 15 minutes from the reference value;
- The cumulative error on the angular separation of tracks at the equator shall be less than $\Delta l = 360/R$ deg, where R is the number of revolutions per cycle. Since the resulting value is $\Delta l = 360/412 \approx 0.87$ deg, the threshold was lowered to 0.1 deg. In addition, it is assumed that the error on angular separation is zero before the manoeuvre.

For each of the two constraints an objective function of the form of Eq. (7.11) has been defined. The constraint on local solar time has been labelled f_4, whereas the constraint on Δl has been labelled f_5.

MOPSO optimization with SGP4/SDP4

The results of the simulation are represented in Figure 7.2, where each cross corresponds to a point on the Pareto front. The top left graph represents how the mean and minimum distance increases (i.e. $f_2(\boldsymbol{x})$ decreases) as a function of the manoeuvre Δv. The top right plot instead represents the Pareto front on the plane $(\Delta v, P_c)$. Note that in this case there is only one close conjunction in the considered time span. The two graphs at the bottom represent the objective function $f_5(\boldsymbol{x})$ with respect to the manoeuvre Δv on the left and collision probability on the right. No violations on the local time of the ascending node constraint are found for all manoeuvre on the Pareto front. It can be observed that the two graphs on the top convey similar results: the reason is that only one conjunction is found below the threshold R in this case for any CAM manoeuvre on the Pareto front.

---

[1] available from www.space-track.org

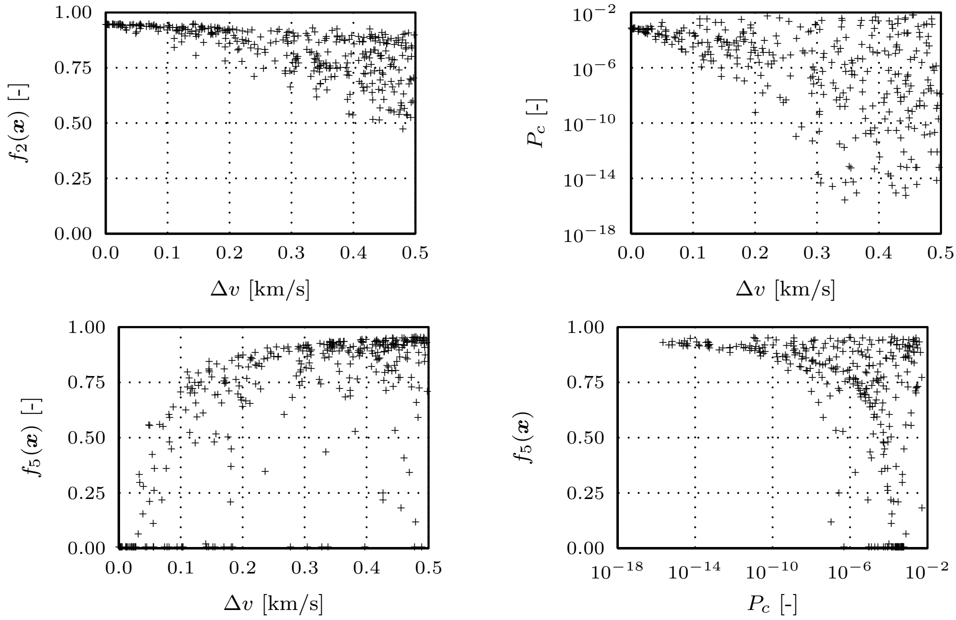

Figure 7.2. Pareto front for LEO collision avoidance manoeuvre optimization with MOPSO.

The solutions $\boldsymbol{x}$ on the Pareto front are represented in Figure 7.3. On the left the manoeuvre Δv is plotted against the manoeuvre execution time t_m. It can be observed that all manoeuvre capable of lowering the most collision probability have to be performed between 0.8 and 0.2 revolutions prior to the close conjunction[1]. In Figure 7.3(b) the direction and module of the associated $\Delta \boldsymbol{v}$ are plotted. The darkest vectors, which correspond to lower probabilities, are mostly directed towards the negative along-track direction with non-zero components on the normal and radial directions.

If a collision probability around 10^{-5} is deemed acceptable, then a suitable manoeuvre among those on the Pareto front is the one with $\Delta \boldsymbol{v} = [-7; -61; 24]$ mm/s to be performed 0.521 revolutions before the TCA. This CAM raises the relative distance up to 686 m, and lowers the collision probability down to 3.941×10^{-5}. The fuel consumption is equal to $\Delta v = 0.066$ m/s. This manoeuvre is the most performing also in terms of mission constraints: all manoeuvres that do not violate them are not capable of lowering the collision probability below 10^{-4}. Those that lowers P_c below 10^{-5}, instead, are less efficient in terms of fuel or guarantee shorter period within mission bounds. A representation of the behaviour of the Δl for the 29-days cycle of Metop-A is given in Figure 7.4 in case of CAM execution and for the nominal trajectory. Note that the constraint is not violated for the 12 days following the CAM.

---

[1] Note that $t_m = 0$ means executing the manoeuvre exactly at the TCA and $t_m = 1$ one revolution before

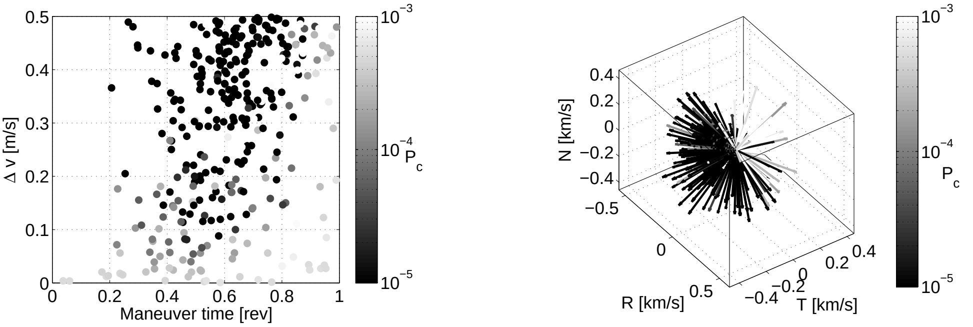

(a) Manoeuvre time and Δv **(b)** Manoeuvre $\Delta \boldsymbol{v}$ in Metop-A RTN frame

Figure 7.3. Pareto optimal collision avoidance manoeuvres obtained with SGP4/SDP4 for the LEO case. Colours of dots and vectors are associated with the corresponding collision probability

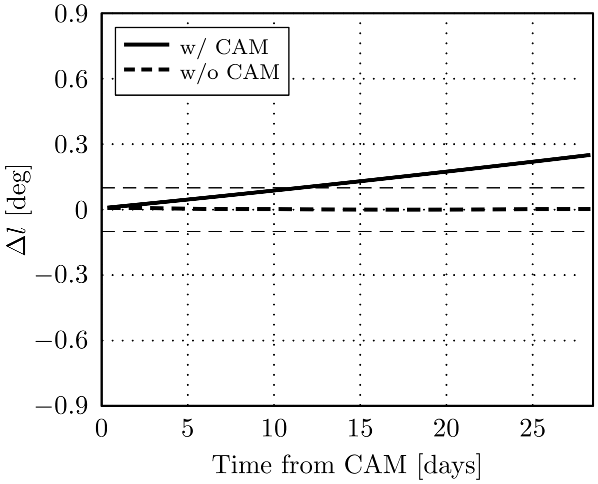

Figure 7.4. Cumulative error of the angular separation of tracks at the equator, Δl.

MOPSO optimization with AIDA

The solution obtained with SGP4/SDP4 can be further optimized using MOPSO and AIDA. The optimization is performed by considering the solution selected above. The Taylor expansion of the relative distance as a function of the free parameters Δt_m and $\Delta \boldsymbol{v}$ is thus computed 0.521 revolutions before the close conjunction. The obtained Pareto optimal CAM are graphed in Figure 7.5(a) and 7.5(b), where each dot and arrow is colored according to the collision probability value after the manoeuvre.

In Figure 7.5(a) it can be observed that all manoeuvres with $\Delta v > 0.2$m/s lower the collision probability below 10^{-6}. Thus, larger avoidance manoeuvres are required to lower collision probability with respect to the SGP4/SDP4 optimization. Also note that the manoeuvre execution is limited to a time window of 5 minutes around the reference manoeuvre epoch, i.e. 0.521 revolutions before the close conjunction. The direction of the Pareto optimal CAMs is represented in Figure 7.5(b). The direction of the manoeuvres is mainly between radial and along-track directions, whereas for SGP4/SDP4 the evasive manoeuvres were mainly directed towards $-\hat{\boldsymbol{t}}$.

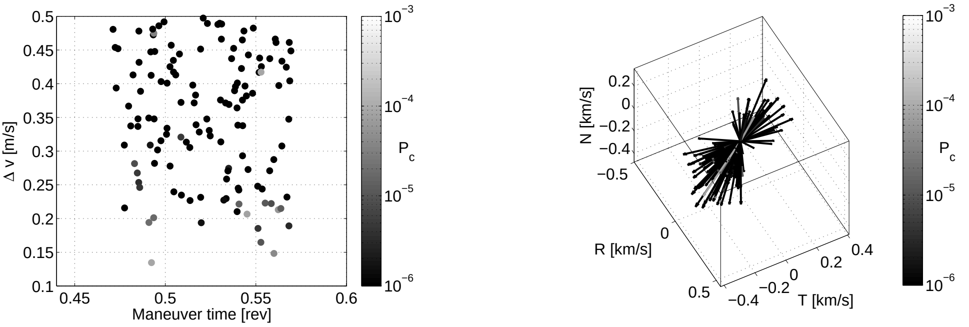

(a) Manoeuvre time and Δv **(b)** Manoeuvre $\Delta \boldsymbol{v}$ in Metop-A RTN frame

Figure 7.5. Pareto optimal collision avoidance manoeuvres obtained with AIDA for the LEO case. Colours of dots and vectors are associated with the corresponding collision probability

The selected manoeuvre has to be performed 0.558 revolutions before the close conjunction and is equal to $\Delta \boldsymbol{v} = [78; -190; -83]$mm/s. The collision probability is lowered to $P_c = 7.665 \times 10^{-6}$ and, according to SGP4/SDP4 propagation, the constraint on Δl is not violated for 12.45 days after the CAM execution. Anyway, this last estimation is not confirmed by the propagation with AIDA. The 0.1 deg maximum deviation from the nominal longitude separation of tracks is violated after only 5 days. In Figure 7.6 the cumulative Δl error, computed with AIDA, is plotted for both the nominal trajectory and the one for which the evasive manoeuvre is executed. The resulting error is larger not only for the trajectory with the CAM but also for the nominal trajectory: the 0.1 deg constraint is indeed violated at the very end of the propagation window, whereas when propagating with SGP4/SDP4 the error was close to zero (see Figure 7.4). The gray line is instead the resulting cumulative error using the CAM selected for the SGP4/SDP4 optimization and propagated with AIDA: even in this case the error is higher. The difference between the SGP4/SDP4 and AIDA propagation is magnified by increasing values of Δv, that result in larger displacements among trajectories. Nevertheless the cumulative error for the selected trajectory is below its nominal value that is $\Delta l = 360/412 \approx 0.87$deg.

7.3.2 GEO case

A conjunction between the GEO Korean satellite COMS and Russian GSO satellite Raduga 1-7 is analyzed. COMS occupies the 128.2 ± 0.05 deg E slot, whereas the

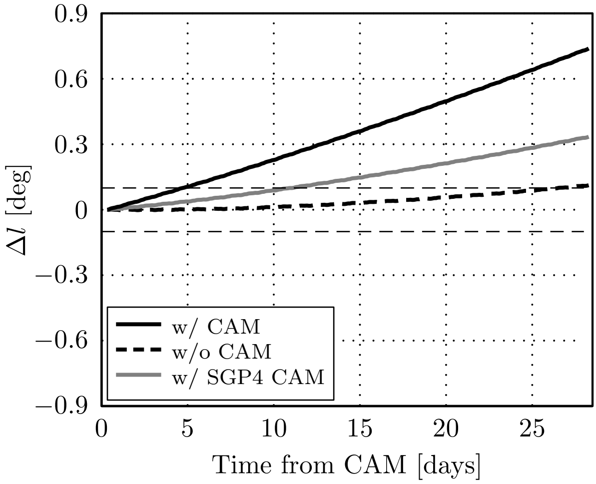

Figure 7.6. Cumulative error of the longitude separation of tracks at the equator, Δl, obtained with AIDA propagations. The solid black curve corresponds to the trajectory after the manoeuvre designed with AIDA is performed, the dashed curve to nominal trajectory (without manoeuvre), and the gray curve to the trajectory after the SGP4/SDP4 manoeuvre.

second is found inside the 128.0 ± 0.5 deg E region. Close conjunctions between the satellites can thus occur twice a day for a few days when, due to orbit evolution, the two are both around 128.2 deg E longitude. The close conjunction here analyzed occurred on 2011/07/02 at 23:14:17 UTC, one day after TLE epoch [Lee11]. Using TLE available from Space-Track the DCA is equal to 1.676 km, with a radial, along-track, and out-of-plane separation of 1.006, 1.339, and 0.062 km respectively. The relative velocity at the TCA is 282 m/s, in the out-of-plane direction with respect to COMS. The nominal collision probability for the close conjunction is $P_c = 6.228 \times 10^{-4}$.

The following constraints are considered for the CAM optimization

- Latitude of COMS should must within ± 0.5 deg
- Longitude of COMS should must within ± 0.5 deg

MOPSO optimization with SGP4/SDP4

The Pareto front obtained considering the objective function vector $\boldsymbol{f}(\boldsymbol{x})$ is represented in Figure 7.7. Due to the presence of multiple conjunctions the points are more spread: without the CAM there is indeed another close encounter occurring 12 h after, on 2011/08/02 at 11:12:13 with a relative distance of 1.358 km and $P_c = 1.236 \times 10^{-3}$. Since P_c is computed for the global minimum only, the value of $f_3(\boldsymbol{x})$ changes according to the global minimum, which can be either close to the first or second one based on the manoeuvre. Note that all collision probabilities below 10^{-6} were automatically set equal to that value during simulations.

The two graphs on the bottom take into account the constraints similarly to Figure 7.2 for the LEO case. The constraint on latitude was labeled $f_4(\boldsymbol{x})$, whereas the constraint on longitude $f_5(\boldsymbol{x})$. In this case the latitude constraint was not violated for all points on the Pareto front, so only f_5 is reported in Figure 7.7. It is interesting to notice how the manoeuvre can be truly effective not only in increasing miss-distance but also as a station keeping manoeuvre. According to the graph on the bottom left, for increasing Δv the number of violations of the longitude constraint decreases. Without any CAM or station keeping manoeuvre the satellite is estimated to remain into the GEO slot for 21.5 days only, whereas the manoeuvre can increase this time up to 55 days.

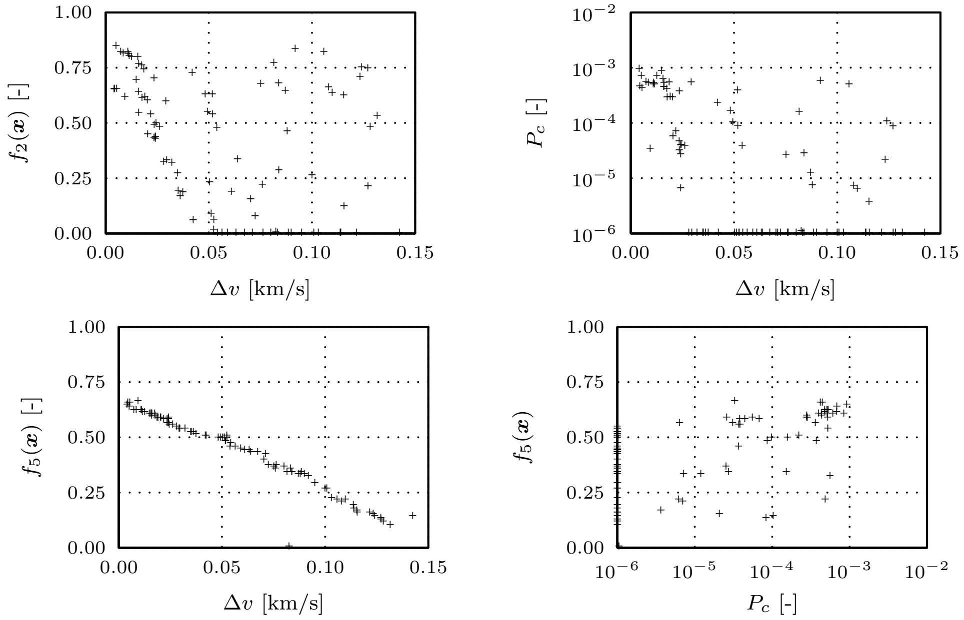

Figure 7.7. Pareto front for GEO collision avoidance manoeuvre optimization with MOPSO.

The Pareto efficient CAMs are plotted in Figure 7.8. It can be observed in Figure 7.8(a) that the Δv required to lower probability down to 10^{-5} increases as t_m gets closer to the close conjunction. Figure 7.8(b) shows that a burn in the $-\hat{\boldsymbol{t}}$ direction is more efficient, even if the other components are not negligible.

In this case two CAMs strategies can be selected from the optimization results: the first would be to perform a manoeuvre with the minimum consumption of fuel that guarantees a collision probability around 10^{-5} as for the LEO case. The CAM performed 0.736 revs. before the TCA with $\Delta\boldsymbol{v} = [0.5; -23; 0.8]$ mm/s meets this requirements since the collision probability becomes $P_c = 3.092 \times 10^{-5}$. Another possibility would be to perform a manoeuvre with a slightly larger Δv that guarantees a larger stay in the GEO slot. For example with a $\Delta\boldsymbol{v} = [-0.8; -114; 9]$ mm/s executed

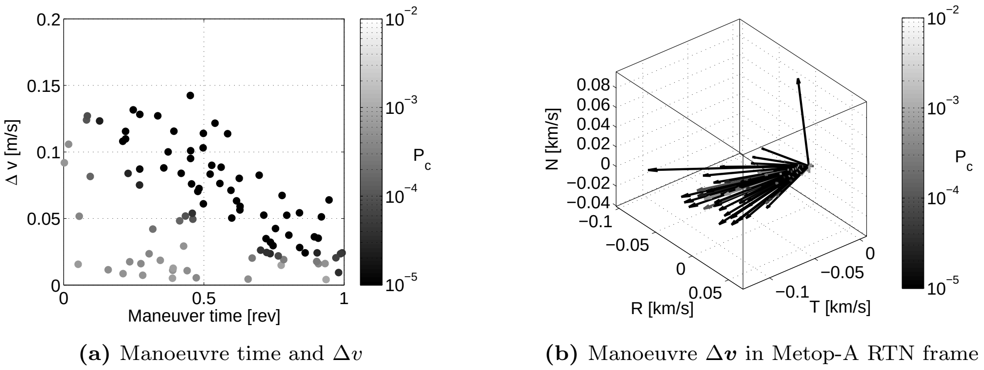

(a) Manoeuvre time and Δv **(b)** Manoeuvre $\Delta \boldsymbol{v}$ in Metop-A RTN frame

Figure 7.8. Pareto optimal collision avoidance manoeuvres obtained with SGP4/SDP4 for the GEO case. Colours of dots and vectors are associated with the corresponding collision probability

0.221 orbits before the close conjunction lowers collision probability to 3.641×10^{-6} and allows the spacecraft to remain into the latitude/longitude slot for 50.2 days instead of the 26.7 day of the previous CAM. The evolution of the latitude and longitude after the two CAM are plotted in Figure 7.9. It can be observed how the first CAM acts only marginally to the longitude shift behaviour, whereas the second one has a larger impact, inverting the drift of the satellite from East to West after the manoeuvre, thus increasing the time inside the GEO slot.

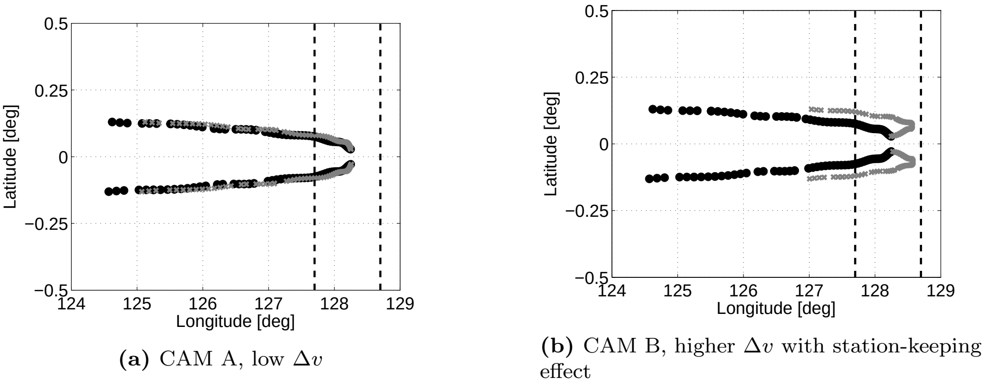

(a) CAM A, low Δv **(b)** CAM B, higher Δv with station-keeping effect

Figure 7.9. Evolution of latitude and longitude of COMS using SGP4/SDP4 inside ±0.5 deg GEO slot (dashed lines). Each point is computed at a latitude stationary point, black dots refer to the nominal trajectory whereas the grey crosses to trajectory after CAM execution.

MOPSO optimization with AIDA

A further optimization with AIDA was performed around the first CAM execution epoch. Again a set of Pareto optimal solutions was found and the resulting solutions are plotted in Figure 7.10. In this case almost all the CAM are capable of lowering the collision probability below 10^{-6}. The direction of the resulting evasive manoeuvre is again aligned with the along-track component, although in this case there are both manoeuvres in the $-\hat{\boldsymbol{t}}$ and $+\hat{\boldsymbol{t}}$ directions as can be observed in Figure 7.10(b).

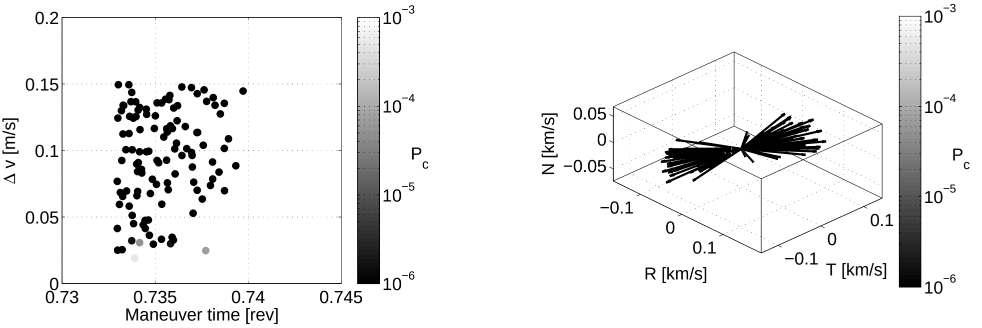

(a) Manoeuvre time and Δv

(b) Manoeuvre $\Delta \boldsymbol{v}$ in Metop-A RTN frame

Figure 7.10. Pareto optimal collision avoidance manoeuvres obtained with AIDA for the GEO case. Color of dots and vectors are associated with the corresponding collision probability.

Two solutions are selected: the first one has $\Delta \boldsymbol{v} = [-21; -66; 14]$ and has to be executed 0.736 revolutions before the close encounter. Collision probability goes to zero and the days inside the GEO slot are 34.9. The second solution instead has the aim of increasing the number of days within the latitude/longitude box and has to be performed 0.733 revolutions before the close approach with $\Delta \boldsymbol{v} = [-51; -122; -21]$. Again collision probability becomes zero but the days inside the GEO slot are now 52.4. The evolution of the stationary points of the latitude, computed using AIDA, are plotted in Figure 7.11. The black dots refer to the trajectory without the execution of a CAM, the dark gray plus to the trajectory that is obtained by applying the CAM determined with the SGP4/SDP4 optimization, and the gray crosses to the evasive manoeuvre obtained with AIDA optimization. For both manoeuvres there is an increase of the required Δv with respect to the SGP4/SDP4 manoeuvre that is anyway balanced by a longer time without violations of the latitude and longitude bounds. It is worth noting that the cost of the second manoeuvre is $\Delta v \approx 134$mm/s which is anyway lower than the total cost of the CAM and subsequent recover manoeuvre listed in [Lee11], that was equal to 180 mm/s.

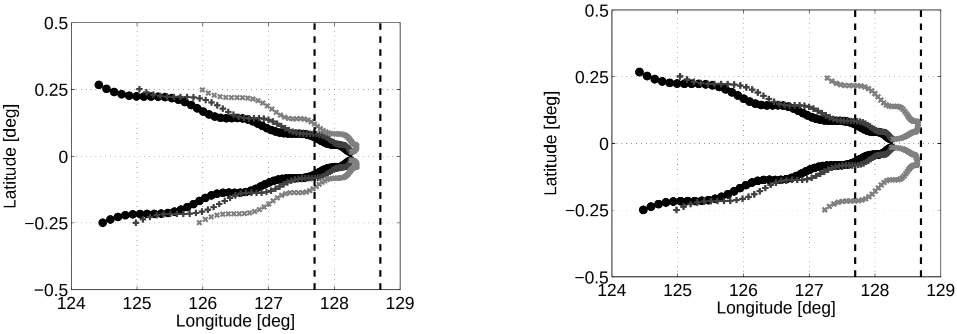

(a) CAM A, low Δv

(b) CAM B, higher Δv with station-keeping effect

Figure 7.11. Evolution of latitude and longitude of COMS using AIDA inside ±0.5 deg GEO slot (dashed lines). Each point is computed at a latitude stationary point, black dots refer to the nominal trajectory, the dark grey plus to trajectory after SGP4 CAM execution, and the gray cross to trajectory after CAM obtained with AIDA optimization.

MOPSO optimization with SGP4/SDP4 using cumulative collision probability

An additional test is performed to understand whether another set of objective functions can give better results when dealing with more than one close conjunction with the same object. In this case the objective function $f_2(\boldsymbol{x})$ was not considered and $f_3(\boldsymbol{x})$ is modified to take into account the cumulative collision probability of all conjunctions below threshold R. The resulting Pareto front is represented in Figure 7.12. As before it can be observed that the CAM are able to act as station keeping manoeuvres and a more clear trend is present in the graph relating collision probability and Δv with respect to the one in Figure 7.7. In this case it is indeed evident that increasing Δv guarantees lower collision probability.

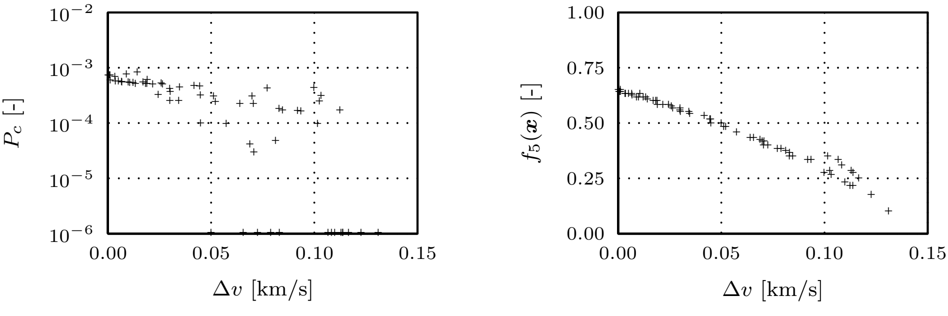

Figure 7.12. Pareto front for GEO collision avoidance manoeuvre optimization with MOPSO using cumulative collision proability.

The obtained solution $\boldsymbol{x}_i$ are plotted in Figure 7.13. In this case all CAM that are more effective in reducing collision probability must be executed at least 0.5 orbits before the close approach and all vectors have a prevalent along-track component. As before, two possible CAM can be identified. The one lowering to zero collision probability with the lowest fuel consumption has $\Delta \boldsymbol{v} = [18; -44; -15]$ mm/s and is executed 0.862 revolutions before the close conjunction. The second one, that requires more fuel but allows a longer stay in the GEO box (49.5 days instead of the 30 days achievable with the previous manoeuvre), has to be performed 0.557 orbits before the TCA with $\Delta \boldsymbol{v} = [-35; -116; -19]$ mm/s. It is worth noting that the two CAM, and especially the second, are similar to the ones obtained with the previous strategy with four objective functions. The two approaches seems equivalent, anyway it has to be taken into account that often collision probability estimates are not reliable, since no accurate estimation of debris uncertainties are available for TLE. For real satellite operations more accurate propagators and data coming from optical or radar tracking should be used for these estimations.

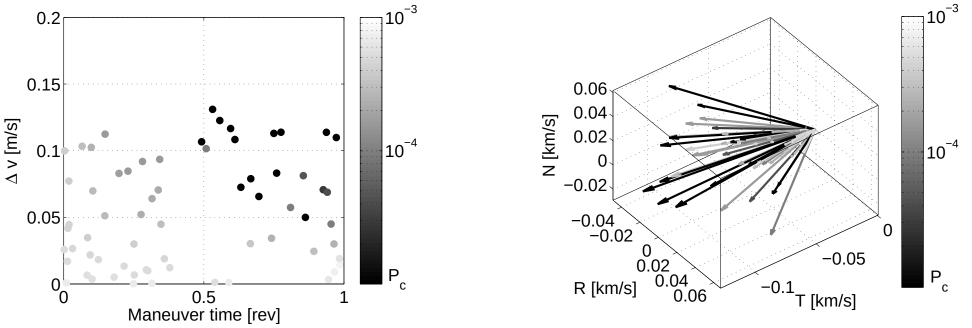

(a) Manoeuvre time and Δv

(b) Manoeuvre $\Delta \boldsymbol{v}$ in Metop-A RTN frame

Figure 7.13. Collision avoidance manoeuvre on the Pareto front for GEO. Colours of dots and vectors are associated with the corresponding collision probability

7.4 Conclusions

Two methods for CAM design using a Multi-Objective Particle Swarm Optimizer were developed. The first method relies on a conjunction identification algorithm, based on rigorous global optimizer COSY-GO and SGP4/SDP4 that computes all stationary points of the relative distance within a time window, and Alfano's method for collision probability computation. The second method, instead, relies on the numerical propagator AIDA and the Taylor expansion of TCA and DCA as function of the manoeuvre epoch and $\Delta \boldsymbol{v}$.

In both cases, three objective functions are defined to (1) minimize fuel consumption, (2) increase mean object separation, and (3) reduce collision probability at the same time. The mission constraints are handled by defining ad-hoc objective functions: the violations of the considered constraints is verified on a proper time grid and the goal is to reduce the number of violations in the time window of interest. The methods allow for the computation of optimal manoeuvre time and $\Delta \boldsymbol{v}$, which is not limited to the along-track direction but is free to vary.

Two close conjunctions, one in LEO and one in GEO, for which a collision avoidance manoeuvre was performed were tested. In both cases, it was possible to identify a CAM capable of reducing collision risk below a given threshold and maintaining the satellite inside the station keeping area when SGP4/SDP4 optimization is performed. For the GEO case, in particular, it was possible not only to increase the miss-distance but also to select a manoeuvre capable of performing some station keeping, increasing from 26.7 days to 50.2 days the time within the latitude-longitude box. For the AIDA optimization similar results were found, although in this case the different perturbation models showed that more intense manoeuvre must be performed to limit constraint violations.

An additional test involving the GEO close conjunction was performed to show how the algorithm can deal with multiple conjunctions. In this case, the cumulative collision probability is taken into account instead of the collision probability for the closest conjunction in the considered time window.

8

Conclusions and future developments

In this thesis new methods for orbit determination, uncertainty propagation, conjunction identification, collision probability computation, and collision avoidance manoeuvre design were introduced. The activities are framed into SST, with the aim of developing a complete set of innovative algorithms to manage all the aspects involved. The algorithms take advantage of Differential Algebra (DA) techniques with the exception of the ones for orbit determination, that use a simple batch least square. In this latter case the innovative aspect is the set of considered sensors, that requires tailored algorithms to process the measured data and estimate the orbital state.

In Chapter 3 the details on the implementation of the analytical and numerical propagators in a DA environment are described. In particular, the SGP4/SDP4 analytical propagator and the DA-based numerical propagator AIDA are introduced. Both propagators are written in the language COSY INFINITY. The two propagators can compute the polynomial approximation, up to an arbitrary order k, of the orbital state at any epoch with respect to the uncertain initial position and velocity. The Taylor expansion can be also computed for any additional uncertain parameter, such as the ballistic coefficient. The availability of the Taylor expansion allows us to propagate the uncertainty sets in a Monte Carlo fashion by means of fast polynomial evaluations. A set of samples is generated from the initial state statistics and, instead of propagating each of the resulting samples to the time of interest, the final distribution is obtained by evaluating the polynomials computed with AIDA or the DA version of SGP4/SDP4. Since the polynomials evaluations require only a few seconds and the cost of a DA propagation at order $n = 3$ with AIDA is more or less equal to 10 standard propagations, when 10^3 propagations are required the gain is of the order of 10^2. This approach has two main advantages: the initial distribution is arbitrary (Gaussian mixture or other distributions can indeed be used) and the propagation is performed at an high-order, thus taking into account all nonlinearities that can arise during the propagation. These effects are all neglected when the uncertainty propagation is performed using the state transition matrix and assuming that the initial uncertainty is normally distributed. Furthermore, the numerical propagator AIDA is the first DA-based high-fidelity numerical propagator ever written. The models for atmospheric drag and Earth's gravitational field are among the most recent and accurate and the position of celestial bodies is computed with JPL's ephemerides. A set of validation tests was performed to determine the expansion accuracy required to correctly represent the uncertainty distribution after a 7-days propagation.

In Chapter 4 the description of the optical and radar simulators is provided, together with the tailored algorithms for bistatic radars with a multibeaming receiver. For the latter the set of available measures includes bistatic range, Doppler shift, and SNR of each beam. These measurements are taken at regular intervals during the whole transit of the object inside the field of view of the instrument. The orbit determination algorithm first determines the right ascension and declination of the object during the transit, using the information on the nominal pointing direction of each beam and range measurements, and fitting the SNR history. Then, a batch least square fit is performed on the bistatic range, Doppler shift, and the previously estimated right ascension and declination for each available time instant. Numerical tests were performed to determine the performance of the proposed algorithm, using the bistatic radar measurements only and mixed measurements from both optical and bistatic radar sensors. The orbit determination with a single bistatic radar measurement can determine with good precision the position of the object during the transit. The uncertainty on position is very low, equal to a few tens of metres on each component, whereas the uncertainty on the velocity is high, between 0.5 and 1 m/s. Another drawback is the inability to compute an estimate of the area-to-mass ratio, which plays an important role for low-altitude objects. Nevertheless, it was shown that it could be possible to perform a follow-up observation of the object in the following 24 hours, since the error with respect to the reference trajectory could remain around a few tens of kilometres. This depends anyway on the bistatic triangle geometry and the type of transit. The case of mixed orbit determination, using both optical and radar measurements, showed a significant improvement in the accuracy of the estimated states. The uncertainty on position and velocity is of the order of a few metres and tens of mm/s respectively. It was also shown that a good estimate of the area-to-mass ratio can be obtained when three optical and one bistatic radar measurements are available.

Two conjunction identification algorithms have been developed and described in Chapter 5. The first is based on the DA-implementation of SGP4/SDP4 and the rigorous global optimizer COSY-GO. The objective function is defined using relative position and velocity of the object and it is such that all stationary points of the relative distance can be computed. The computation requires from few seconds to tens of seconds depending on the orbital regime. The second algorithm is instead based on the computation of the TCA and DCA Taylor expansion. Given a first guess of the TCA, the Taylor expansion of the relative distance as function of time is computed. By imposing the stationarity of the relative distance squared and using partial inversion techniques, the Taylor expansion of theTCA and DCA can be computed. Besides time, it is possible to add the dependence on the variation of the reference initial state and obtain the TCA and DCA polynomial approximation with respect to an initial position and velocity deviations. A set of numerical examples was performed to determine the accuracy of the two expansions, using the DA-based propagator AIDA to compute the polynomial approximations. Note that the proposed algorithm can be used with any other orbital propagator, numerical or analytical. The accuracy of the resulting DCA and TCA maps is comparable with the accuracy of the position map obtained with AIDA, with errors of only a few metres in LEO and a few millimetres in GEO. These results are obtained in a worst-case scenario were the largest 100 initial state deviations were selected among a set of 10^9 obtained from the uncertainty distribution.

In Chapter 6 three DA-based methods to compute the collision probability between two approaching objects are described. The three methods use a Monte Carlo approach and are all based on the DCA and TCA expansion obtained with the method described in Chapter 5. The three methods are the DAMC, which is a DA-based standard Monte Carlo, and two DA-based advanced Monte Carlo methods, DALS and DASS. The advantage of the proposed methods is the low computational effort, since polynomial evaluations are used to propagate each sample from the initial uncertainty set in place of numerical propagations. The computational time of the DALS is around 1 second, whereas it ranges from less than one second to about 10 seconds for DASS. The computational time for DAMC could reach a few hundreds of seconds depending on the number of samples required to meet the desired accuracy, which can be around 10^9 when collision probability is around 10^{-6}. The performed validation tests and comparisons with other analytical methods showed that all three methods

- can compute the exact collision probability for the case of spherical objects,
- are suitable to characterize single close conjunctions,
- can be used for both long-term and short-term encounters.

For collision probabilities down to 10^{-4} DALS outperforms the two other methods, both in terms of accuracy and computational efficiency. For lower values of the collision probability the performance of DASS is comparable or even better than that of DALS. An advantage of the proposed algorithms is their flexibility. Any uncertainty distribution for the initial state can indeed be used: tests with uniform distributions and Gaussian mixtures were presented in this thesis. In case other distributions are of interest the only modification to the algorithm is the sampling procedure, which must be modified to produce samples that are commensurate with the initial uncertainty distribution.

The collision avoidance manoeuvre design is tackled in Chapter 7. The proposed approach uses a Multi-Objective Particle Swarm Optimizer to determine a set of Pareto optimal manoeuvres in terms of fuel efficiency, miss-distance increment, collision probability, and mission constraints compliance. Two algorithms were developed: one considers SGP4/SDP4 and the conjunction identification algorithm based on COSY-GO, whereas the other uses the numerical propagator AIDA. In the second case, to speed up the computation, a DCA expansion is performed with respect to the manoeuvre parameters, i.e. execution time and $\Delta \boldsymbol{v}$, to replace the numerical propagations required for each particle with fast polynomial evaluations. The runtime of the optimization is about 2 hours for both the SGP4/SDP4 and AIDA algorithms: the computational times are, in general, compatible with the time interval between the issue of a conjunction warning and the conjunction epoch. Tests were performed on a LEO and a GEO conjunction: it was found that out-of-plane manoeuvres can be more effective in reducing the collision risk besides avoiding mission constraints violations. In certain cases, this approach could be preferred to the classical raise/decrease of altitude or phase shift, that is usually executed half-orbit prior the conjunction. The proposed optimization strategy can reduce fuel-consumption and increase the lifetime of a satellite, as it could avoid a recover manoeuvre since the resulting trajectory will guarantee that mission constraints are respected at least for the first few weeks following the manoeuvre execution. In addition, the optimization returns a set of manoeuvres. Thus the engineer can select the manoeuvre that best fits the mission requirements, giving in turn more importance to the miss-distance, fuel-consumption, or collision probability.

8.1 Future developments and final remarks

The proposed approaches are the first efforts to introduce DA in the framework of SST. Besides all advantages of the methods in terms of computational time with respect to classical Monte Carlo methods and demanding simulations in general (such as manoeuvre optimization), the drawback of the approach lies in the higher effort required for the single DA-based propagation that is necessary to compute the Taylor expansions. The collision probability computation and TCA and DCA expansion algorithm all require DA maps of the relative distance as function of 12 variables, which is obtained downstream of two numerical propagations, one for each object involved in the conjunction. It is worth highlighting that the additional effort is largely paid-back when the polynomials are used to propagate many samples, as in the case of spacecraft collision probability computation with a Monte Carlo simulation. Currently, an AIDA propagation requires ten times a standard propagation when it is performed at order $k = 3$ with $n = 6$ variables. Efforts should be thus devoted to optimize the code in order to increase the computational efficiency and, in turn, reduce the computational effort.

The applicability of DA methods for the orbit determination of RSO is another possible development. The techniques developed in [Val13b] could be used in presence of both optical and radar measures exploiting the already available DA-based propagator AIDA. The advantage of this approach, based on Kalman Filters, is on the update of the catalogue: when a new observation is available, the uncertainty distribution can be updated, without the need of maintaining old observations to perform a batch least square fit. In addition, since the estimation is nonlinear, it would be natural to use the DA-based methods for collision probability computation since, as stated in the previous section, they can handle this kind of uncertainty distribution.

For what concerns the conjunction identification algorithms, it is worth noting that the method based on SGP4/SDP4 and COSY-GO is not suitable for an all-vs-all daily screening. Although the computational time of a single run of the algorithm takes a few seconds, the total computational time in an all-vs-all conjunction identification could exceed one day due the high number of combinations to be taken into account, even after the use of geometry filters to exclude combinations that will surely not lead to a collision in the considered time window. Thus, future work should be devoted to study the applicability of the TCA and DCA expansion inside a Smart-sieve approach [Ala02]. The advantage of the Smart-sieve is that it carries out a propagation of all objects simultaneously (with a potential high level of parallelization) and could be adapted to a special perturbation catalogue. A DA-based AIDA propagation could be used and the TCA and DCA expansion could replace the root-finding algorithm for the "fine conjunction detection" phase. In this way, the DA maps required as inputs for the collision probability computation could be readily available to compute immediately an estimate of P_c with DALS, DASS, or DAMC. This approach could be particularly suitable for special perturbations catalogues, which are becoming of standard use because of the higher accuracy of the orbital state and lower uncertainty on the initial state.

The DAMC, DALS, and DASS could be improved to deal with objects of complex shape. In this way a more accurate estimate of the collision probability could be obtained when non-compact objects, e.g. satellites with long appendages or large solar panels, are considered. The modification of the algorithms is not trivial, since the DCA and TCA expansion cannot be used. The relative attitude of the objects must be taken into account during the whole encounter, thus increasing the computational effort because of the higher number of variables. Other efforts should be devoted to the parallelization of the algorithms to further reduce the computational time. Another interesting application of the developed method for collision probability could regard NEOs close approaches with the Earth.

Regarding the design of collision avoidance manoeuvres, future works should be focused on the case of multiple conjunctions with more than two objects. This situation could occur both in LEO and GEO, where an active satellite could experience more than one close conjunction with different chasers in a certain time window. In those cases it is important to schedule correctly the avoidance and orbit recover manoeuvre to ensure that the cumulative collision probability remains low and/or the miss-distance for each close conjunction is above a safety level.

Overall, if the proposed future developments are carried out a comprehensive DA-based SST tool could be assembled. The tool would be able to manage the uncertainties by considering the nonlinearities arising from orbit determination and orbit propagation and could produce accurate estimations of the collision probability to rank close conjunctions. The availability of such a tool will help in the management of space traffic, re-entry, and observation scheduling. In the scope of the mitigation guidelines, any improvement in handling such operations will have beneficial effects on space debris population control and the future exploitation of space.

Appendix A

Initial states

A.1 Conjunction identification

Object 1

Satellite ID
11510
Reference UT
23/01/2013 04:50:14.3891483545

# ECI J2000 Position (km)	ECI J2000 Velocity (km/s)
$-3.7721713215E+03$	$+2.0902060722E-01$
$+4.9994447579E+03$	$-4.1566598389E+00$
$+3.4596010085E+03$	$+6.2007675483E+00$

Covariance matrix (km^2, km^2/s, km^2/s^2)

$+3.3085138968E-03$	$+8.1569556907E-04$	$+6.3216213375E-04$	$+1.8594276250E-07$	$-6.8263129256E-07$	$+5.9476230591E-07$
$+8.1569556907E-04$	$+3.5565393379E-03$	$-2.0265346793E-03$	$-1.4711117793E-06$	$+2.4696267856E-06$	$+3.9897201273E-07$
$+6.3216213375E-04$	$-2.0265346793E-03$	$+5.2194974395E-03$	$+1.8751377639E-06$	$-2.0999712757E-06$	$-2.4422592051E-06$
$+1.8594276250E-07$	$-1.4711117793E-06$	$+1.8751377639E-06$	$+4.1301523076E-09$	$+1.5475454258E-10$	$+2.0530594462E-10$
$-6.8263129256E-07$	$+2.4696267856E-06$	$-2.0999712757E-06$	$+1.5475454258E-10$	$+3.3307135024E-09$	$+9.4333446860E-10$
$+5.9476230591E-07$	$+3.9897201273E-07$	$-2.4422592051E-06$	$+2.0530594462E-10$	$+9.4333446860E-10$	$+2.1401382330E-09$

Drag Area to mass ratio (m^2/kg), Cd = 2.2
$+7.9693388204E-07$
SRP Area to mass ratio (m^2/kg), eps = 0.31
$+7.2433066671E-02$
TLE used for nonlinear least square fit
1 11510U 79078A 13023.20155543 .00000103 00000-0 47518-4 0 1325
2 11510 074.0358 118.1525 0011496 088.5235 301.8268 14.32681184744812

Object 2

Satellite ID
21574
Reference UT
22/01/2013 22:26:54.0620023012

# ECI J2000 Position (km)	ECI J2000 Velocity (km/s)
$+3.0799289553E+03$	$-6.7335462784E+00$
$-1.1774790818E+03$	$+9.0909039658E-02$
$+6.3094366569E+03$	$+3.2876594254E+00$

Covariance matrix (km^2, km^2/s, km^2/s^2)

$+6.5110022394E-03$	$+1.1558082277E-04$	$-2.6158096782E-03$	$+2.7966467039E-06$	$-9.1277337669E-07$	$+4.6393449869E-06$
$+1.1558082277E-04$	$+3.4915733193E-03$	$+3.9873127221E-04$	$-2.0268510003E-07$	$+9.4972338534E-09$	$-4.9783742550E-09$
$-2.6158096782E-03$	$+3.9873127221E-04$	$+2.3878201022E-03$	$-2.8390289006E-07$	$+4.3116429054E-07$	$-2.7993620662E-06$
$+2.7966467039E-06$	$-2.0268510003E-07$	$-2.8390289006E-07$	$+1.9513723058E-09$	$-7.2082566955E-11$	$+1.6422454906E-09$
$-9.1277337669E-07$	$+9.4972338534E-09$	$+4.3116429054E-07$	$-7.2082566955E-11$	$+3.9810526042E-09$	$-2.2788964517E-10$
$+4.6393449869E-06$	$-4.9783742550E-09$	$-2.7993620662E-06$	$+1.6422454906E-09$	$-2.2788964517E-10$	$+4.5198732031E-09$

Drag Area to mass ratio (m^2/kg), Cd = 2.2
$+3.1525096930E-02$
SRP Area to mass ratio (m^2/kg), eps = 0.31
$+8.6998667752E-02$
TLE used for nonlinear least square fit
1 21574U 91500A 13022.93534794 .00000203 00000-0 83024-4 0 5448
2 21574 098.2460 355.3520 0034877 082.5971 341.2307 14.36304867126904

Object 3

```
# Satellite ID
20237
# Reference UT
03/03/2013 03:34:55.0660854578
# ECI J2000 Position (km)                ECI J2000 Velocity (km/s)
-6.9608504967E+02                        -7.1908922523E-01
+3.9447413218E+03                        -6.1667222531E+00
+6.6676677691E+03                        +3.5653521805E+00
# Covariance matrix (km^2, km^2/s, km^2/s^2)
+2.6282128459E-03  +4.9609574850E-04  -1.2472570972E-04  -4.6583233145E-08  +1.7868359512E-07  +4.6499234699E-07
+4.9609574850E-04  +5.1294297368E-03  -2.8175167448E-03  -2.6604126144E-07  +2.0213010498E-06  +3.1959036434E-06
-1.2472570972E-04  -2.8175167448E-03  +2.5231867160E-03  +2.3789204150E-07  -6.2505918713E-07  -2.4279044407E-06
-4.6583233145E-08  -2.6604126144E-07  +2.3789204150E-07  +2.1743122769E-09  -1.5519486573E-10  +3.4526380891E-11
+1.7868359512E-07  +2.0213010498E-06  -6.2505918713E-07  -1.5519486573E-10  +1.1046525934E-09  +1.0043646178E-09
+4.6499234699E-07  +3.1959036434E-06  -2.4279044407E-06  +3.4526380891E-11  +1.0043646178E-09  +2.6911031636E-09
# Drag Area to mass ratio (m^2/kg), Cd = 2.2
+1.2645425516E-03
# SRP Area to mass ratio (m^2/kg), eps = 0.31
+1.2072974147E-03
# TLE used for nonlinear least square fit
1 20237U 89074F 13062.14924845 .00000051 00000-0 22376-3 0 924
2 20237 082.5723 087.7657 0004186 082.5944 337.2822 12.63395421 82164
```

Object 4

```
# Satellite ID
23820
# Reference UT
04/03/2013 20:54:42.1015834808
# ECI J2000 Position (km)                ECI J2000 Velocity (km/s)
+8.7741400840E+03                        -1.4355103802E+00
+2.5174129938E+03                        -1.2478148630E-01
-1.1037130913E+01                        +6.7080731673E+00
# Covariance matrix (km^2, km^2/s, km^2/s^2)
+3.7365649111E-03  -1.8774896159E-03  -1.7756879090E-03  +1.1737797328E-06  +7.2965655117E-07  -1.9125787150E-06
-1.8774896159E-03  +8.4701814389E-03  +1.0368790267E-03  -3.6471225605E-07  -1.6589500283E-06  -4.7980730691E-07
-1.7756879090E-03  +1.0368790267E-03  +1.6075521088E-02  -7.5785218204E-06  -1.8780849958E-06  -6.5081630239E-07
+1.1737797328E-06  -3.6471225605E-07  -7.5785218204E-06  +4.4433848385E-09  -2.2730797064E-10  +2.1850803760E-10
+7.2965655117E-07  -1.6589500283E-06  -1.8780849958E-06  -2.2730797064E-10  +4.4757376092E-09  -1.2691331517E-10
-1.9125787150E-06  -4.7980730691E-07  -6.5081630239E-07  +2.1850803760E-10  -1.2691331517E-10  +1.4485851866E-09
# Drag Area to mass ratio (m^2/kg), Cd = 2.2
+2.9406164525E+00
# SRP Area to mass ratio (m^2/kg), eps = 0.31
+3.0085686833E+00
# TLE used for nonlinear least square fit
1 23820U 66077D 13063.87132062 .00020734 00000-0 60931+0 0 3081
2 23820 087.6151 016.1776 2204224 081.8477 302.4728 08.81977559657175
```

Object 5 (COMS-1)

```
# Satellite ID
36744
# Reference UT
07/02/2011 17:28:54.3233361840
# ECI J2000 Position (km)                ECI J2000 Velocity (km/s)
-4.1218586022E+04                        -6.4868868413E-01
+8.8973993544E+03                        -3.0052824298E+00
+6.5767406271E+01                        +1.1524550572E-03
# Covariance matrix (km^2, km^2/s, km^2/s^2)
+4.8684260805E-03  +2.8144019728E-03  +2.5855660862E-04  -2.9284545423E-07  -2.6416134160E-07  +4.7498191816E-10
+2.8144019728E-03  +2.1151760568E-02  -3.7731926146E-04  -8.9572939141E-07  +3.3550231926E-07  +1.4314764844E-09
+2.5855660862E-04  -3.7731926146E-04  +1.2383334290E-02  -1.5150684923E-08  -2.4339739820E-08  +1.8043084888E-11
-2.9284545423E-07  -8.9572939141E-07  -1.5150684923E-08  +5.3865847597E-11  -3.4214779531E-12  +1.8558767562E-14
-2.6416134160E-07  +3.3550231926E-07  -2.4339739820E-08  -3.4214779531E-12  +2.8061830734E-11  +7.0815634448E-15
+4.7498191816E-10  +1.4314764844E-09  +1.8043084888E-11  +1.8558767562E-14  +7.0815634448E-15  +6.5166338686E-11
# SRP Area to mass ratio (m^2/kg), eps = 0.31
+4.6465256622E-12
# TLE used for nonlinear least square fit
1 36744U 10032A 11038.72840652 -.00000340 00000-0 10000-3 0 956
2 36744 000.0086 088.0631 0000788 256.3015 183.5741 01.00269939 2416
```

Object 6 (RADUGA 1-7)

```
# Satellite ID
28194
# Reference UT
07/02/2011 12:53:03.5177153349
# ECI J2000 Position (km)              ECI J2000 Velocity (km/s)
−6.2997743088E+03                      −3.0273029590E+00
+4.1664952743E+04                      −4.6758259629E−01
+1.6017472390E+03                      +2.6224219851E−01
# Covariance matrix (km^2, km^2/s, km^2/s^2)
+2.4642428245E−02  +2.2712137544E−03  −6.4227590670E−04  −2.7598724396E−07  +1.0326836589E−06  +5.0508709424E−08
+2.2712137544E−03  +4.7804014798E−03  −5.3528868674E−04  +2.9818134924E−07  +2.3812269421E−07  −2.1062388599E−08
−6.4227590670E−04  −5.3528868674E−04  +1.3920101199E−02  +2.1358765258E−08  −9.7456008690E−08  −4.2449078518E−09
−2.7598724396E−07  +2.9818134924E−07  +2.1358765258E−08  +2.8385263365E−11  −3.0436486056E−12  +4.0211735020E−12
+1.0326836589E−06  +2.3812269421E−07  −9.7456008690E−08  −3.0436486056E−12  +6.1556025538E−11  −2.2819832001E−14
+5.0508709424E−08  −2.1062388599E−08  −4.2449078518E−09  +4.0211735020E−12  −2.2819832001E−14  +7.3295880653E−11
# SRP Area to mass ratio (m^2/kg), eps = 0.31
+4.0165085827E−02
# TLE used for nonlinear least square fit
1 28194U 04010A 11038.53684627 -.00000341 +00000-0 +10000-3 0 03215
2 28194 005.2813 074.4923 0001212 268.2646 116.0489 01.00265873025169
```

A.2 Collision probability

Test case A

```
# Satellite ID
39152
# Reference UT
10/02/2014 19:12:35.0844445825
# ECI J2000 Position (km)              ECI J2000 Velocity (km/s)
−3.6439539563E+03                      +9.1878920823E−01
+5.9878758060E+03                      +5.3316032714E−01
+4.9808066441E+00                      +7.4730343033E+00
# Covariance matrix (km^2, km^2/s, km^2/s^2)
+9.8237058494E−04  +3.8915942674E−04  +1.9571722596E−04  +1.6609615808E−07  −2.2559491098E−07  +1.9015667113E−07
+3.8915942674E−04  +5.7555444198E−04  +1.0303424759E−04  +4.0954623941E−08  −1.5338795992E−07  −3.0843253026E−07
+1.9571722596E−04  +1.0303424759E−04  +2.7558675605E−03  +1.1746412424E−06  −1.9215069558E−06  +1.1861317840E−08
+1.6609615808E−07  +4.0954623941E−08  +1.1746412424E−06  +1.5490440293E−09  −3.1617343607E−10  −1.0891636943E−10
−2.2559491098E−07  −1.5338795992E−07  −1.9215069558E−06  −3.1617343607E−10  +1.8659786917E−09  −8.3430324021E−11
+1.9015667113E−07  −3.0843253026E−07  +1.1861317840E−08  −1.0891636943E−10  −8.3430324021E−11  +4.1396922057E−10
# Drag Area to mass ratio (m^2/kg), Cd = 2.2
+1.2218479923E−02
# SRP Area to mass ratio (m^2/kg), eps = 0.31
+2.0694123476E−02
# TLE used for nonlinear least square fit
1 39152U 13018C 14041.80040607 .00002412 00000-0 34810-3 0 8423
2 39152 98.0284 121.5048 0018766 38.9612 321.2977 14.77065112 42877
```

```
# Satellite ID
27580
# Reference UT
10/02/2014 16:21:14.1030737758
# ECI J2000 Position (km)              ECI J2000 Velocity (km/s)
−3.8922004631E+03                      −6.2512439849E+00
−1.0438435353E+03                      +1.8465268478E−01
+5.7962513479E+03                      −4.1358463997E+00
# Covariance matrix (km^2, km^2/s, km^2/s^2)
+1.9547374453E−03  −9.8049890402E−05  +1.0580067225E−03  −1.1794923458E−06  −2.6119495220E−07  +1.3789927232E−06
−9.8049890402E−05  +1.1188760540E−03  +7.8137564847E−05  −1.1565590860E−08  +1.3391748522E−08  −7.1596458005E−08
+1.0580067225E−03  +7.8137564847E−05  +1.0336519655E−03  −4.2647489665E−07  −1.7889070361E−07  +1.1193578612E−06
−1.1794923458E−06  −1.1565590860E−08  −4.2647489665E−07  +9.1252134319E−10  +8.0369513444E−11  −7.6890339138E−10
−2.6119495220E−07  +1.3391748522E−08  −1.7889070361E−07  +8.0369513444E−11  +1.2941888854E−09  −6.9242035260E−11
+1.3789927232E−06  −7.1596458005E−08  +1.1193578612E−06  −7.6890339138E−10  −6.9242035260E−11  +1.4620365188E−09
# Drag Area to mass ratio (m^2/kg), Cd = 2.2
+1.7201681066E−05
# SRP Area to mass ratio (m^2/kg), eps = 0.31
+9.8460198665E−02
# TLE used for nonlinear least square fit
1 27580U 01049MY 14041.68141323 .00001359 00000-0 22429-3 0 5945
2 27580 97.8555 3.7377 0047446 330.9850 152.8019 14.71277121622316
```

Test case B

```
# Satellite ID
27453
# Reference UT
20/11/2013 13:26:25.8947440982
# ECI J2000 Position (km)             ECI J2000 Velocity (km/s)
−2.4979059959E+03                     −5.9504749387E+00
+3.0653803366E+02                     +3.8129647668E+00
+6.7181721934E+03                     −2.3755680897E+00
# Covariance matrix (km^2, km^2/s, km^2/s^2)
+1.8615176132E−03  −5.9371488217E−04  +5.7527411082E−04  −6.4855641668E−07  +1.4422052340E−07  +1.4063005261E−06
−5.9371488217E−04  +1.3880156120E−03  −2.8152360401E−04  +3.4638522095E−07  −3.9996702959E−08  −9.2455468978E−07
+5.7527411082E−04  −2.8152360401E−04  +5.8855927117E−04  +7.6250286311E−08  −1.6871676008E−07  +6.6170167678E−07
−6.4855641668E−07  +3.4638522095E−07  +7.6250286311E−08  +7.2731034077E−10  +2.4744622174E−10  −3.8539559873E−10
+1.4422052340E−07  −3.9996702959E−08  −1.6871676008E−07  +2.4744622174E−10  +9.1680701357E−10  +1.5038111950E−10
+1.4063005261E−06  −9.2455468978E−07  +6.6170167678E−07  −3.8539559873E−10  +1.5038111950E−10  +1.4968859391E−09
# Drag Area to mass ratio (m^2/kg), Cd = 2.2
+1.0075588399E−03
# SRP Area to mass ratio (m^2/kg), eps = 0.31
+2.7067261334E−02
# TLE used for nonlinear least square fit
1 27453U 02032A 13324.56002193 .00000354 00000-0 16975-3 0 3501
2 27453 98.3115 330.3370 0012692 70.4075 38.4024 14.24645909592980
```

```
# Satellite ID
33692
# Reference UT
20/11/2013 13:02:7.8791964054
# ECI J2000 Position (km)             ECI J2000 Velocity (km/s)
+2.7072504230E+03                     +1.1053867194E+00
+6.6185027866E+03                     −4.5872732420E−01
+6.5408784620E+00                     +7.3812411350E+00
# Covariance matrix (km^2, km^2/s, km^2/s^2)
+7.4456143946E−04  −2.1033418661E−04  +1.5630845774E−04  −9.5245718864E−08  −1.9436808166E−07  −9.0622152364E−08
−2.1033418661E−04  +3.1772267900E−04  −6.7843369616E−05  +1.9817261436E−09  +9.8865423604E−08  −2.2049290292E−07
+1.5630845774E−04  −6.7843369616E−05  +1.8524950529E−03  −5.4832073914E−07  −1.3392393107E−06  −2.2891164616E−09
−9.5245718864E−08  +1.9817261436E−09  −5.4832073914E−07  +9.1837031296E−10  +1.4156627714E−10  −9.0630235032E−11
−1.9436808166E−07  +9.8865423604E−08  −1.3392393107E−06  +1.4156627714E−10  +1.2051410084E−09  +3.8737522574E−11
−9.0622152364E−08  −2.2049290292E−07  −2.2891164616E−09  −9.0630235032E−11  +3.8737522574E−11  +2.6817511423E−10
# Drag Area to mass ratio (m^2/kg), Cd = 2.2
+6.1554384920E−01
# SRP Area to mass ratio (m^2/kg), eps = 0.31
+2.8921957815E−05
# TLE used for nonlinear least square fit
1 33692U 99025DGD 13324.54314675 .00015012 00000-0 56966-2 0 3993
2 33692 99.1407 67.9439 0028402 336.9020 23.1694 14.30917181292566
```

Test case C

Satellite ID
37838
Reference UT
21/11/2013 13:04:12.9898434877

# ECI J2000 Position (km)	ECI J2000 Velocity (km/s)
$-2.7064133232E+02$	$-6.9641618091E+00$
$+7.2375327257E+03$	$-2.6533008678E-01$
$+8.8144484510E-01$	$+2.5459684582E+00$

Covariance matrix (km^2, km^2/s, km^2/s^2)

$+1.4620065692E-03$	$+1.5096126850E-04$	$-3.4342152452E-04$	$+3.2500902338E-08$	$+1.1756166169E-06$	$-1.8919723104E-08$
$+1.5096126850E-04$	$+2.1171590357E-04$	$-5.6611199550E-05$	$+1.8808430093E-07$	$+1.5635248049E-07$	$-6.8748866154E-08$
$-3.4342152452E-04$	$-5.6611199550E-05$	$+7.3178022570E-04$	$-1.8310062662E-08$	$-4.5741482493E-07$	$+8.8305361044E-09$
$+3.2500902338E-08$	$+1.8808430093E-07$	$-1.8310062662E-08$	$+2.4930955928E-10$	$+5.3419271859E-11$	$+1.3816886668E-10$
$+1.1756166169E-06$	$+1.5635248049E-07$	$-4.5741482493E-07$	$+5.3419271859E-11$	$+1.0872884658E-09$	$-1.6378238816E-11$
$-1.8919723104E-08$	$-6.8748866154E-08$	$+8.8305361044E-09$	$+1.3816886668E-10$	$-1.6378238816E-11$	$+5.7539188515E-10$

Drag Area to mass ratio (m^2/kg), Cd = 2.2
$+1.3696048019E-03$
SRP Area to mass ratio (m^2/kg), eps = 0.31
$+1.1868850460E-03$
TLE used for nonlinear least square fit
1 37838U 11058A 13325.54459479 .00000586 00000-0 18131-3 0 5302
2 37838 19.9787 92.3179 0009179 164.4307 195.6381 14.09686725108936

Satellite ID
37840
Reference UT
20/11/2013 08:13:18.4635964036

# ECI J2000 Position (km)	ECI J2000 Velocity (km/s)
$-2.5924255453E+02$	$-6.9640911370E+00$
$+7.2375143678E+03$	$-2.5310140058E-01$
$+8.2501627159E-01$	$+2.5436846038E+00$

Covariance matrix (km^2, km^2/s, km^2/s^2)

$+8.9908619704E-04$	$+3.5482498530E-05$	$-1.5690448148E-04$	$-2.2950305574E-08$	$+6.7406759066E-07$	$-2.1839226852E-09$
$+3.5482498530E-05$	$+1.3622581555E-04$	$-8.5489681255E-06$	$+1.2828235413E-07$	$+3.7833918148E-08$	$-4.7743784534E-08$
$-1.5690448148E-04$	$-8.5489681255E-06$	$+5.2397255801E-04$	$+6.6104495832E-09$	$-2.4509570267E-07$	$+1.1577334597E-09$
$-2.2950305574E-08$	$+1.2828235413E-07$	$+6.6104495832E-09$	$+1.8248705329E-10$	$-8.7155540637E-12$	$+1.1263652901E-10$
$+6.7406759066E-07$	$+3.7833918148E-08$	$-2.4509570267E-07$	$-8.7155540637E-12$	$+6.0575620993E-10$	$-3.1320777230E-13$
$-2.1839226852E-09$	$-4.7743784534E-08$	$+1.1577334597E-09$	$+1.1263652901E-10$	$-3.1320777230E-13$	$+4.4991999269E-10$

Drag Area to mass ratio (m^2/kg), Cd = 2.2
$+1.6733308516E-02$
SRP Area to mass ratio (m^2/kg), eps = 0.31
$+2.6790857074E-02$
TLE used for nonlinear least square fit
1 37840U 11058C 13324.34257481 .00000265 00000-0 00000+0 0 5857
2 37840 19.9633 92.2212 0012886 173.2946 186.7632 14.10655180108878

Test case D

```
# Satellite ID
16199
# Reference UT
20/11/2013 01:04:17.9371109605
# ECI J2000 Position (km)          ECI J2000 Velocity (km/s)
−4.0984596292E+04                  −7.1565317033E−01
+9.3894851315E+03                  −2.8957835671E+00
+2.7224571229E+03                  −7.5321799039E−01
# Covariance matrix (km^2, km^2/s, km^2/s^2)
+2.0594892337E−03  +1.8379005001E−03  +4.7338792975E−04  −1.1332545815E−07  −9.2599726031E−08  −2.3507445814E−08
+1.8379005001E−03  +8.7961151778E−03  +8.4366722845E−04  −3.5906104057E−07  +9.8838124092E−08  +2.8114925162E−08
+4.7338792975E−04  +8.4366722845E−04  +5.4860265792E−03  −9.5190527137E−08  +2.7889672850E−08  +8.1851469305E−09
−1.1332545815E−07  −3.5906104057E−07  −9.5190527137E−08  +2.2266514440E−11  −3.2210326166E−12  −8.0528400269E−13
−9.2599726031E−08  +9.8838124092E−08  +2.7889672850E−08  −3.2210326166E−12  +1.1764972771E−11  −4.2665830474E−12
−2.3507445814E−08  +2.8114925162E−08  +8.1851469305E−09  −8.0528400269E−13  −4.2665830474E−12  +2.7035786499E−11
# SRP Area to mass ratio (m^2/kg), eps = 0.31
+1.1223807797E−06
# TLE used for nonlinear least square fit
1 16199U 85102A 13324.04465205 -.00000265 00000-0 10000-3 0 2554
2 16199 14.6620 1.3261 0008520 116.5622 48.8663 1.00297344105627
```

```
# Satellite ID
29648
# Reference UT
19/11/2013 13:45:33.4224164486
# ECI J2000 Position (km)          ECI J2000 Velocity (km/s)
+4.2091373228E+04                  +1.8931804031E−01
−2.5929194691E+03                  +3.0683059623E+00
−9.2251747965E+01                  +6.6909152476E−04
# Covariance matrix (km^2, km^2/s, km^2/s^2)
+1.4139689390E−03  +5.7834535594E−04  −5.2183084638E−05  −2.1498800482E−08  −1.0394009353E−07  +1.3075451281E−11
+5.7834535594E−04  +7.9198371095E−03  −1.5459818308E−04  −3.3496996136E−07  +1.2443268919E−08  +7.3094127670E−10
−5.2183084638E−05  −1.5459818308E−04  +4.5115226302E−03  −4.8657365415E−09  +4.6785900696E−09  +4.9130205025E−11
−2.1498800482E−08  −3.3496996136E−07  −4.8657365415E−09  +1.9350129603E−11  −1.1375786363E−12  +9.1002280124E−15
−1.0394009353E−07  +1.2443268919E−08  +4.6785900696E−09  −1.1375786363E−12  +8.6020208781E−12  −3.4871343335E−15
+1.3075451281E−11  +7.3094127670E−10  +4.9130205025E−11  +9.1002280124E−15  −3.4871343335E−15  +2.3739652425E−11
# SRP Area to mass ratio (m^2/kg), eps = 0.31
+4.0010579635E−06
# TLE used for nonlinear least square fit
1 29648U 06056A 13323.57330350 -.00000244 00000-0 10000-3 0 1373
2 29648 0.0702 90.3404 0001774 125.3902 140.9346 1.00270688 25513
```

Bibliography

[Aid12] S. Aida and M. Kirschner. *Collision risk assessment and operational experiences for LEO satellites at GSCOC*. J. Aerospace Eng., **4**(2):121 (2012).

[Ake00] M. R. Akella and K. T. Alfriend. *Probability of collision between space objects*. J. Guid. Control Dyn., **23**(5):769–772 (2000).

[Ala02] J. R. Alarcón Rodríguez, F. Martínez Fadrique, and H. Klinkrad. *Collision Risk Assessment with a 'Smart Sieve' Method*. In *Joint ESA-NASA Space-Flight Safety Conference*, volume ESA SP-486, 159–165 (2002).

[Ala04] J. R. Alarcón Rodríguez, F. Martínez Fadrique, and H. Klinkrad. *Development of a collision risk assessment tool*. Adv. Space Res., **34**(5):1120–1124 (2004).

[Alf05a] S. Alfano. *A Numerical Implementation of Spherical Object Collision Probability*. J. Astronaut. Sci., **53**(1):103–109 (2005).

[Alf05b] S. Alfano. *Relating Position Uncertainty to Maximum Conjunction Probability*. J. Astronaut. Sci., **53**(2):193–205 (2005).

[Alf06] S. Alfano. *Addressing Nonlinear Relative Motion for Spacecraft Collision Probability*. In *AAS/AIAA Astrodynamics Specialist Conference*, AIAA 2006-6760. Keystone, CO (2006).

[Alf09] S. Alfano. *Satellite conjunction Monte Carlo analysis*. Adv. Astronaut. Sci., **134**:2007–2024 (2009).

[Arm10a] R. Armellin, P. Di Lizia, F. Bernelli-Zazzera, and M. Berz. *Asteroid close encounters characterization using differential algebra: the case of Apophis*. Celest. Mech. Dyn. Astr., **107**(4):451–470 (2010).

[Arm10b] R. Armellin, P. Di Lizia, M. Berz, and K. Makino. *Computing the critical points of the distance function between two Keplerian orbits via rigorous global optimization*. Celest. Mech. Dyn. Astr., **107**(3):377–395 (2010).

[Arm12] R. Armellin, P. Di Lizia, K. Makino, and M. Berz. *Rigorous Global Optimization of Impulsive Planet-to-Planet Transfers in the patched conics approximation*. Eng. Optimiz., **44**(2):133–155 (2012).

[Au01] S.-K. Au and J. L. Beck. *Estimation of small failure probabilities in high dimensions by subset simulation*. Probabilist. Eng. Mech., **16**(4):263–277 (2001).

[Ber86] M. Berz. *The new method of TPSA algebra for the description of beam physics to high order*. Technical Report AT-6:ATN-86-16, Los Alamos National Laboratory, Los Alamos, NM (1986).

[Ber87] M. Berz. *The method of power series tracking for the mathematical description of beam dynamics*. Nucl. Instrum. Meth. A, **258**(3):431 – 436 (1987).

[Ber91] M. Berz. *High-Order Computation and Normal Form Analysis of Repetitive Systems*. In M. Month (Editor), *Physics of Particle Accelerators*, AIP 249, 456–489. American Institute of Physics (1991).

[Ber96] M. Berz, C. Bischof, G. Corliss, and A. Griewank. *Computational Differentiation: Techniques, Applications, and Tools*. SIAM, Philadelphia (1996).

[Bèr99a] N. Bèrend. *Estimation of the probability of collision between two catalogued orbiting objects*. Adv. Space Res., **23**(1):243–247 (1999).

[Ber99b] M. Berz. *Handbook of Accelerator Physics and Engineering*, chapter Differential Algebraic Techniques. World Scientific (1999).

[Ber99c] M. Berz. *Modern Map Methods in Particle Beam Physics*. Academic Press, New York (1999).

[Ber06a] M. Berz and K. Makino. *COSY INFINITY Version 9 Reference Manual*. Michigan State University, East Lansing, MI 48824 (2006). MSU Report MSUHEP-060803.

[Ber06b] M. Berz, K. Makino, and Y. Kim. *Long-term Stability of the Tevatron by Verified Global Optimization*. Nucl. Instrum. Methods, **A558**(1):1–10 (2006).

[Bom13] C. Bombardelli. *Analytical formulation of impulsive collision avoidance dynamics*. Celest. Mech. Dyn. Astr., 1–16 (2013).

[Cha97] K. Chan. *Collision Probability Analyses for Earth Orbiting Satellites*. Adv. Astronaut. Sci., **96**:1033–1048 (1997).

[Cha04] K. Chan. *Short-Term vs. Long-Term spacecraft encounters*. In *AIAA/AAS Astrodynamics Specialist Conference and Exhibit*, AIAA 2004-5460. Providence, RI (2004).

[Cha08] F. K. Chan. *Spacecraft Collision Probability*. Aerospace Press (2008).

[Coa03] G. Coath and S. Halgamuge. *A comparison of constraint-handling methods for the application of particle swarm optimization to constrained nonlinear optimization problems*. In *Congress on Evolutionary Computation CEC '03*, volume 4, 2419–2425 (2003).

[Cof98] S. L. Coffey, H. L. Neal, C. L. Visel, and P. Conolly. *Demonstration of a Special-Perturbation-Based Catalog in the Naval Space Command System*. Adv. Astronaut. Sci., **99**:227–248 (1998). Paper AAS 98-113.

[Dag00] P. Dagum, R. Karp, M. Luby, and S. Ross. *An Optimal Algorithm for Monte Carlo Estimation*. SIAM J. Comput., **29**(5):1484–1496 (2000).

[Deb99] K. Deb. *Evolutionary algorithms for multi-criterion optimization in engineering design*. Evolutionary Algorithms in Engineering and Computer Science, **2**:135–161 (1999).

[Der96] G. J. Der. *An elegant state transition matrix*. In *AIAA/AAS Astrodynamics Conference*, AIAA 96-3660. San Diego, CA (1996).

[DM12] K. De Mars, M. Jah, and P. Schumacher. *Initial Orbit Determination using Short-Arc Angle and Angle Rate Data*. IEEE Trans. Aerosp. Electron. Syst., **48**(3):2628–2637. ISSN 0018-9251 (2012).

[Dol11] J. C. Dolado, P. Legendre, R. Garmier, B. Reveling, and X. Pena. *Satellite Collision Probability Computation for Long Term Encounters*. Adv. Astronaut. Sci., **142** (2011).

[dV10] W. H. de Vries and D. W. Phillion. *Monte Carlo Method for collision probability using 3D satellite models*. Advanced Maui Optical and Space Surveillance Technologies Conference, **1**:1–11 (2010).

[Esc65] P. R. Escobal. *Methods of orbit determination*. Krieger Publishing Company, Malabar, FL (1965).

[Flo09a] T. Flohrer, H. Krag, and H. Klinkrad. *ESA's process for the identification and assessment of high-risk conjunction events*. Adv. Space Res., **44**(3):355–363 (2009).

[Flo09b] T. Flohrer, H. Krag, H. Klinkrad, B. Bastida Virgili, and C. Früh. *Improving ESA's Collision Risk Estimates by an Assessment of the TLE Orbit Errors of the US SSN Catalogue*. In *Proc. of the 5th Europ. Conf. on Space Debris*, volume ESA SP-672. Darmstadt, Germany (2009).

[Flo13] T. Flohrer, H. Krag, S. Lemmens, B. Bastida Virgili, K. Merz, and H. Klinkrad. *Statistical Look on ESA's Conjunction Event Predictions*. In *Proc. of the 6th Europ. Conf. on Space Debris*, volume ESA SP-723. Darmstadt, Germany (2013).

[Flu01] W. Flury and J. M. Contant. *The updated IAA position paper on orbital debris*. In H. Sawaya-Lacoste (Editor), *Space Debris*, volume 473 of *ESA Special Publication*, 841–849 (2001).

[Fos05] J. Foster, J. Benbrook, and E. Stansbery. *Detection of small radar cross-section orbital debris with the Haystack radar*. Adv. Space Res., **35**(7):1210 – 1213 (2005).

[Fos14] G. Foster, J. Hickish, A. Magro, D. Price, and K. Zarb Adami. *Implementation of a direct-imaging and FX correlator for the BEST-2 array*. Mon. Not. R. Astron. Soc., **439**(3):3180–3188 (2014).

[Fuj12] K. Fujimoto and D. J. Scheeres. *Correlation of Optical Observations of Earth-Orbiting Objects and Initial Orbit Determination*. J. Guid. Control Dyn., **35**(1):208–221 (2012).

[Ghr12] R. W. Ghrist and D. Plakalovic. *Impact of Non-Gaussian Error Volumes on Conjunction Assessment Risk Analysis*. In *AIAA/AAS Astrodynamics Specialist Conference*, AIAA 2012-4965. Minneapolis, MN (2012).

[Goo93] R. H. Gooding. *A new procedure for orbit determination based on three lines of sight (angles only)*. Technical Report 93004, Defence Research Agency (1993).

[Gri91] A. Griewank and G. Corliss. *Automatic Differentiation of Algorithms: Theory, Implementation and Application*. SIAM, Philadelphia (1991).

[Her65] S. Herrick. *Universal variables*. The Astronomycal Journal, **70**(4):309–316 (1965).

[Hoo80] F. R. Hoots and R. L. Roherich. *Spacetrack Report #3: Models for Propagation of the NORAD Element Sets*. Technical Report, U.S. Air Force Aerospace Defense Command, Colorado Spring, CO (1980).

[Hoo84] F. R. Hoots, L. L. Crawford, and R. L. Roehrich. *An analytical method to determine future close approaches between satellites*. Celestial Mechanics, **33**:143–158 (1984).

[Hoo04] F. R. Hoots, P. W. Schumacher, and R. A. Glover. *History of Analytical Orbit Modeling in the U. S. Space Surveillance System*. J. Guid. Control Dynam., **27**(2):174–185 (2004).

[Joh12] N. L. Johnson. *The Effects of Solar Maximum on the Earth's Satellite Population and Space Situational Awareness*. In *Proceedings of the 63rd IAC*. Naples, Italy (2012).

[Jon13] B. A. Jones and A. Doostan. *Satellite collision probability estimation using polynomial chaos expansions*. Adv. Space Res., **52**(11):1860 – 1875 (2013).

[Kea96] R. B. Kearfott. *Rigorous Global Search: Continuous Problems*. Kluwer Academic Publishers, Dordrecht (1996).

[Kel05] T. S. Kelso and S. Alfano. *Satellite Orbital Conjunction Reports Assessing Threatening Encounters in Space (SOCRATES)*. Adv. Astronaut. Sci., **120 (I)**:317–326 (2005). Paper AAS 05-124.

[Kel07] T. S. Kelso. *Validation of SGP4 and IS-GPS-200D against GPS precision ephemerides*. In *17th AAS/AIAA Space Flight Mechanics Conference*. Sedona, AZ (2007). Paper AAS 07-127.

[Ken01] J. Kennedy and R. C. Eberhart. *Swarm Intelligence*. Morgan Kaufmann Publishers Inc., San Francisco, CA, USA (2001).

[Kes78] D. J. Kessler and B. G. Cour-Palais. *Collision frequency of artificial satellites: The creation of a debris belt*. J. Geophys. Res-Space, **83**(A6):2637–2646 (1978).

[Kim12] E.-H. Kim, H.-D. Kim, and H.-J. Kim. *Optimal Solution of Collision Avoidance Maneuver with Multiple Space Debris*. Journal of Space Operations, **9**(3):20–31 (2012).

[Kli05] H. Klinkrad, J. R. Alarcón Rodríguez, and N. Sanchez. *Collision avoidance for Operational ESA satellites*. ESA SP, **587**:509–514 (2005).

[Kli06] H. Klinkrad. *Space debris - Models and risk analysis*. Springer Berlin Heidelberg. ISBN 978-3-540-3764-3 (2006).

[Kno04] E. Knott, M. Tuley, and J. Shaeffer. *Radar Cross Section*. Scitech Publishing (2004).

[Kou04] P. S. Koutsourelakis, H. J. Pradlwarter, and G. I. Schuëller. *Reliability of structures in high dimensions, part I: algorithms and applications*. Probabilist. Eng. Mech., **19**(4):409–417 (2004).

[Lap08] F. Laporte and E. Sasot. *Operational management of collision risks for LEO satellites at CNES*. In *SpaceOps 2008 Conference*, AIAA 2008-3409 (2008).

[Làz12] D. Làzaro and P. L. Righetti. *Evolution of EUMETSAT LEO conjunction events in handling operations*. In *SpaceOps 2012 Conference*, AIAA 2012-1287272 (2012).

[Lee11] B. Lee, Y. Hwang, H. Kim, and B. Kim. *GEO Satellite Collision Avoidance Maneuver Due to the Close Approach of an Inclined GSO Satellite*. European Space Surveillance Conference (2011).

[Lee12] S.-C. Lee, H.-D. Kim, and J. Suk. *Collision avoidance maneuver planning using GA for LEO and GEO satellite mainteined in keeping area*. International Journal of Aeronautical and Space Sciences, **13**(4):474–483 (2012).

[Mag13] A. Magro, J. Hickish, and K. Zarb-Adami. *Mulitbeam GPU Transient Pipeline for the Medicina BEST-2 Array*. J. Astron. Instrum., **2**(1) (2013).

[Mak98] K. Makino. *Rigorous Analysis of Nonlinear Motion in Particle Accelerators*. Ph.D. thesis, Michigan State University, East Lansing (1998).

[Mak99] K. Makino and M. Berz. *Efficient Control of the Dependency Problem Based on Taylor Model Methods*. Reliab. Comput., **5**(1):3–12 (1999).

[Mak03] K. Makino and M. Berz. *Taylor models and other validated functional inclusion methods*. Int. J. Pure Appl. Math., **4**(4):379–456 (2003).

[Mak05] K. Makino and M. Berz. *Verified Global Optimization with Taylor Model-based Range Bounders*. WSEAS Trans. Comput., **4**(11):1611–1618 (2005).

[Mar09] J. M. Maruskin, D. J. Scheeres, and K. T. Alfriend. *Correlation of Optical Observations of Objects in Earth Orbit*. J. Guid. Control Dyn., **2009**(1):194–209 (2009).

[McK06] D. McKinley. *Development of a Nonlinear Probability of Collision Tool for the Earth Observing System*. In *AIAA/AAS Astrodynamics Specialist Conference and Exhibit*, AIAA 2006-6295. Keystone, CO (2006).

[Meh97] D. Mehrholz. *Radar observations in Low Earth Orbit*. Adv. Space Res., **19**(2):203 – 212 (1997).

[Meh04] D. Mehrholz, L. Leushacke, and D. Banka. *Beam-park experiments at FGAN*. Advances in Space Research, **34**(5):863 – 871 (2004).

[Met53] N. Metropolis, A. W. Rosenbluth, M. N. Rosenbluth, A. H. Teller, and E. Teller. *Equation state calculation by fast computing machines*. J. Chem. Phys., **21**(6):1087–1092 (1953).

[Mil04] A. Milani, G. F. Gronchi, M. De' Michieli Vitturi, and Z. Knežević. *Orbit determination with very short arcs. I admissible regions*. Celest. Mech. Dyn. Astr., **90**(1-2):57–85 (2004).

[Mon00] O. Montenbruck and E. Gill. *Satellite Orbits - Models, Methods, and Applications*. Springer-Verlag (2000).

[Mon09] S. Montebugnoli, G. Bianchi, J. Monari, G. Naldi, F. Perini, and M. Schiaffino. *BEST: Basic Element for SKA Training Wide Field Science and Technology for the Square Kilometre Array*. In *Proceedings of the SKADS Conference*, 331–336. Château de Limelette, Belgium (2009).

[Moo66] R. E. Moore. *Interval Analysis*. Prentice-Hall, Englewood Cliffs, NJ (1966).

[Pai97] R. A. Paielli and H. Erzberger. *Conflict Probability Estimation for Free Flight*. J. Guid. Control Dyn., **20**(3):588–596 (1997).

[Pas11] R. Pastel. *Estimating satellite versus debris collision probability via the adaptive splitting technique*. Proceedings of the 3rd International Conference on Computer modeling and simulation, Mumbai, India (2011).

[Pat01] R. P. Patera. *General method for calculating satellite collision probability*. J. Guid. Control Dyn., **24**(4):716–722 (2001).

[Pat03] R. P. Patera. *Satellite Collision Probability for Nonlinear Relative Motion*. J. Guid. Control Dyn., **26**(5):728–733 (2003).

[Pat05] R. P. Patera. *Calculating collision probability for arbitrary space-vehicle shapes via numerical quadrature*. J. Guid. Control Dyn., **28**(6):1326–1328 (2005).

[Pat06] R. P. Patera. *Collision probability for larger bodies having nonlinear relative motion*. J. Guid. Control Dyn., **26**(6):1468–1471 (2006).

[Pat07a] R. P. Patera. *Space vehicle conflict-avoidance analysis*. J. Guid. Control Dyn., **30**(2):492–498 (2007).

[Pat07b] R. P. Patera. *Space vehicle conflict probability for ellipsoidal conflict volumes*. J. Guid. Control Dyn., **30**(6):1818–1821 (2007).

[Pav12] N. K. Pavlis, S. A. Holmes, S. C. Kenyon, and J. K. Factor. *The development and evaluation of the Earth Gravitational Model 2008 (EGM2008)*. J. Geophys. Res-Sol. Ea., **117**(B4) (2012).

[Pic02] J. M. Picone, A. E. Hedin, D. P. Drob, and A. C. Aikin. *NRLMSISE-00 empirical model of the atmosphere: Statistical comparisons and scientific issues*. J. Geophy. Res-Space, **107**(A12):SIA 15–1–SIA 15–16 (2002).

[Pra05] H. J. Pradlwarter, M. F. Pellissetti, C. A. Schenk, S. G. I., A. Kreis, S. Fransen, and A. Calvi. *Realistic and efficient reliability estimation for aerospace structures*. Comput. Method Appl. M., **194**(12–16):1597–1617 (2005).

[Rig11] P. Righetti, F. Sancho, D. Lazaro, and A. Damiano. *Handling of Conjunction Warnings in EUMETSAT Flight Dynamics*. Journal of Aerospace Engineering, Sciences and Applications, **3**(2):39–53 (2011).

[Ros52] M. Rosenblatt. *Remarks on a Multivariate Transformation*. Ann. Math. Stat., **23**(3):470–472 (1952).

[Rui05] G. Ruiz, L. Leushacke, and J. Rosebrock. *Algorithms for Multi-Beam Receiver Data Analysis*. In D. Danesy (Editor), *4th European Conference on Space Debris*, volume 587 of *ESA Special Publication*, 89 (2005).

[Rui06] G. Ruiz, L. Leushacke, R. Jehn, and R. Keller. *Improved FGAN/MPIFR Bi-Static Debris Observation Campaign: Experiment Outline, Analysis Algorithms and First Results*. In *57th International Astronautical Congress*. Valencia, Spain (2006).

[Sab11] C. Sabol, C. Binz, A. Segerman, K. Roe, and P. W. Schumacher Jr. *Probability of Collision with Special Perturbation Dynamics Using the Monte Carlo Method*. Adv. Astronaut. Sci., **142**:1081–1094 (2011).

[Sch07] T. Schildknecht. *Optical surveys for space debris*. Astron. Astrophys. Rev., **14**(1):41–111 (2007).

[Sri98] R. Sridharan and A. F. Pensa. *U.S. Space Surveillance Network capabilities*. In *Proc. SPIE*, volume 3434, 88–100 (1998).

[Sta98] E. M. Standish. *JPL Planetary and Lunar Ephemerides, DE405/LE405*. JPL IOM, **312** (1998).

[Tap04] B. D. Tapley, B. E. Schutz, and G. H. Born. *Statistical Orbit Determination*, chapter Fundamentals of Orbit Determination, 159 – 284. Academic Press, Burlington (2004). ISBN 978-0-12-683630-1.

[Tom07] G. Tommei, A. Milani, and A. Rossi. *Orbit determination of space debris: admissible regions*. Celest. Mech. Dyn. Astr., **97**(4):289–304 (2007).

[Tou57] R. Tousey. *Optical problems of the satellite*. J. Opt. Soc. Am., **47**(4):261–267 (1957).

[Val01] D. Vallado. *Fundamentals of Astrodynamics and Applications*. Springer-Verlag, 2nd edition. ISBN 0792369033 (2001). 205–231.

[Val06] D. A. Vallado, P. Crawford, R. Hujsak, and T. S. Kelso. *Revisiting SPACE-TRACK Report #3*. In *AIAA/AAS Astrodynamics Specialist Conference and Exhibit*, AIAA 2006-6753. Keystone, CO (2006).

[Val12] D. A. Vallado and P. J. Cefola. *Two-Line element sets – Practice and Use*. In *63rd International Astronautical Congress*. Naples, Italy (2012).

[Val13a] D. Vallado, B. Bastida Virgili, and T. Flohrer. *Improved SSA through orbit determination of Two-Line Element Sets*. In *Proc. of the 6th Europ. Conf. on Space Debris*, volume ESA SP-723. Darmstadt, Germany (2013).

[Val13b] M. Valli. *Nonlinear estimation and filtering for space applications*. Ph.D. thesis, Politecnico di Milano (2013).

[Val13c] M. Valli, R. Armellin, P. Di Lizia, and M. Lavagna. *Nonlinear Mapping of Uncertainties in Celestial Mechanics*. J. Guid. Control Dyn., **36**(1):48–63 (2013).

[Vei63] G. Veis. *Optical Tracking of Artificial Satellites*. Space Sci. Rev., **2**(2):250–296 (1963).

[Wil05] N. J. Willis. *Bistatic radar*. SciTech Publishing (2005).

[Zio09a] E. Zio and N. Pedroni. *Estimation of the functional failure probability of a thermal-hydraulic passive system by Subset Simulation*. Nucl. Eng. Des., **229**(3):580–599 (2009).

[Zio09b] E. Zio and N. Pedroni. *Functional failure analysis of a thermal-hydraulic passive system by means of Line Sampling*. Reliab. Eng. Syst. Safe., **94**(11):1764–1781 (2009).

[Zue12] K. M. Zuev, J. L. Beck, S.-K. Au, and L. S. Katafygiotis. *Bayesian post-processor and other enhancements of Subset Simulation for estimating failure probabilities in high dimensions*. Comput. Struct., **92**:283 – 296 (2012).

Acronyms

ADR	Active Debris Removal	3
AIDA	Accurate Integrator for Debris Analysis	44
CAM	Collision Avoidance Maneuver	137
CCD	Charge-Coupled Device	53
CSI	Commonewalth of Independent Sates	4
CSM	Conjunction Summary Messages	88
CSSI	Center for Space Standards and Innovation	87
DA	Differential Algebra	10
DCA	Distance of Closest Approach	87
ECI	Earth Centred Inertial	72
ESA	European Space Agency	2
FoV	Field Of View	54
GA	Genetic Algorithm	137

GEO	Geostationary Earth Orbit	3
GTO	Geosynchronous Transfer Orbit	4
GSO	Geosynchronous Earth Orbit	3
GO	Global Optimization	32
GPU	Graphic Processing Unit	67
HEO	Highly Elliptical Orbit	4
IA	Interval Arithmetic	27
IADC	Inter-Agency Space Debris Coordination Committee	2
JSpOC	Joint Space Operation Center	88
LDB	Linear Dominated Bounder	32
LEO	Low Earth Orbit	3
MC	Monte Carlo	109
MCMC	Monte Carlo Markov Chain	114
MEO	Medium Earth Orbit	3
MOID	Minimum Orbital Intersection Distance	34
MOPSO	Multi-Objective Particle Swarm Optimizer	138

NASA	National Aeronautics and Space Administration	4
NEO	Near-Earth Objects.	54
NSO	Navigation Satellite Orbit	39
OD	Orbit Determination	53
ODE	Ordinary Differential Equation	24
PRC	Public Republic of China.	4
QFB	Quadratic Fast Bounder	32
RCS	Radar Cross-Section.	61
RSO	Resident Space Object	1
RTN	Radial Transverse Normal	37
SGP4	Simplified General Perturbations #4.	38
SDP4	Simplified Deep Space Perturbations #4.	39
SNR	Signal-to-Noise Ratio	62
SRP	Solar Radiation Pressure	47
SRT	Sardina Radio Telescope	74
SSA	Space Situational Awareness	2

SSO	Sun-Synchronous Orbit	6
SST	Space Surveillance and Tracking	2
TCA	Time of Closest Approach	87
TLE	Two-Line Element set	11
TM	Taylor Model	26
UNCOPUOS	United Nations Committee on the Peaceful Uses of Outer Space	2
USA	United States of America	4
USSTRATCOM	United States Strategic Command	1
VLM	Visual Limiting Magnitude	58

Acknowledgments

Here we are...after three years of PhD, it is time to say thanks to all the people that supported me, helped me with advices and suggestions, and that supported me. First, I want to thank my supervisor, professor Bernelli, and my co-supervisors Roberto Armellin and Pierluigi Di Lizia. Needless to say that, without your support and timely advices (especially at the beginning of the PhD), I would have not been able to investigate all the topics described in this thesis. I also want to thank Klaus Merz and all the people of the ESA Space Debris Office (Holger, Tim, Benjamin, Quirin, Stijn, and Alexandra) for their availability and for the crucial insight on space debris research that they provided me during the internship at ESOC. A special thank goes also to Emma, Stelio, Germano, and Giuseppe of INAF-IRA: it was a pleasure to work with you and to have the opportunity to understand, “hands-on”, how to perform radar measurements of space debris. Finally, I want to acknowledge all the members of the GTOC7 team for the amazing effort put in place during the competition and results that we achieved.

Ed è arrivato il momento di passare anche all’italiano! E nel fare questo cambio drastico, dopo non so quante pagine scritte in inglese, il primo pensiero che ho è “quante cose sono cambiate negli ultimi tre anni”. E, come tutti quelli della “bassa”, penso di poter individuare, senza alcun margine di errore, il momento esatto in cui distinguere un “prima” ed un “dopo”, il 20 maggio 2012. Non è stato facile, soprattutto per uno come me che è così legato alla sua “terra”, passare gli ultimi due anni avanti e indietro tra casa e Milano. Voglio per questo ringraziare la mia famiglia che non mi ha mai fatto mancare il suo supporto e che, anzi, ha continuato a fornirmi le motivazioni necessarie per arrivare fino in fondo.

Ed ora passiamo alle cose serie...non ve lo meritate (soprattutto i primi in elenco e sapete perché) ma non posso fare a meno di tirare in ballo Alle, Mala, Prebby, Paoluc, Berek, Giulia, Marika, Silvia. Ci sono tanti aneddoti che potrei citare ma farei solo danni...quindi ricordo solo il paintball giocato in condizioni estreme. Dopo quello possiamo affermare che Bear Grills ha paura di noi. Sicuramente non hanno paura di noi (o forse si, ma per ora non ce l’hanno detto) Alice, Giulia P. e Anna. E no, non mi sono dimenticato di Giulia G. che merita un ringraziamento apposito perché ha avuto la pazienza di leggere tutta la tesi per correggere l’inglese!

Una menzione particolare va sicuramente alle pause pranzo nell’ufficio dottorandi del Grande Capannone, frutto di notevoli spunti critici ed alte speculazioni intellettuali. Soprattutto sui portachiavi. Un grazie quindi ai miei compagni di ufficio

Riccardo, Vincenzo, Kamal, Matteo e Alberto e agli altri dottorandi Michele, Barbara, Federica, Andrea, Fabio, Paolo, Valentina, Federico, Francesca, Chiara, Mirco, Claudio, Giulio, Marta, Jakub, Aykut e i “senatori” Seba, Tommy, Fabio, Parri, Monica, Francesco (che devo ringraziare anche per le birre e le tigellate durante lo stage in ESOC) e Giuseppe. Spero di essermi ricordato di tutti!

Infine voglio ringraziare il gruppo di amici con cui ho affrontato la laurea in ingegneria aerospaziale: se ci pensiamo è pazzesco che, nonostante siamo ormai sparsi per tutto il mondo, non abbiamo azzerato i contatti ma sfruttiamo ogni possibilità per organizzare una rimpatriata! Nicolò, Federico, Gianmarco, Daniele, Edoardo, Vincenzo, Stefania, Debora, Valerio, Giovanni, Gabriele, Vala, Carlo: ci si becca alla prossima!

Alessandro